Analysis of Core-Shell Leaky-Wave Lens Antennas based on a combination of Physical Optics and Asymptotic Techniques

Alexandros Bechrakis Triantafyllos

Student Number: 5499909

Supervisor: Prof. dr. Nuria Llombart

Faculty of Electrical Engineering, Mathematics and Computer Science
Delft University of Technology, The Netherlands
August 10, 2023

Analysis of Core-Shell Leaky-Wave Lens Antennas based on a combination of Physical Optics and Asymptotic Techniques (August 10, 2023)

TU Delft

THz Sensing Group

Preface

In the framework of this MSc thesis the analysis of core-shell leaky-wave lens antennas is presented, based on a combination of asymptotic and Physical Optics techniques. This study aims to develop an analysis approach which can be subsequently used for the optimization of the Fly's Eye antenna concept, through enabling the investigation of shaped variations of the core lens. The main difficulty of this prospect refers to the surface of the core lens being in the near field of the leaky wave feeding structure, since the evaluation of the near field is in general a computationally inefficient process. Adhering to this conclusion, a big part of this thesis elaborates on a very fast approach for the derivation of the near field, through asymptotically approximating the involved integral expressions. More specifically, the presented method exploits the nature of the near field in the examined stratification through introducing an approximation in the integral expressions, which in turn enables their asymptotic evaluation in a straightforward manner. Subsequently, the near field on the core lens is combined with a set of Physical Optics techniques in order to develop a model for the integrated lens architecture of the Fly's Eye antenna. Modelling the core-shell structure in such a manner enables its study in a much more computationally efficient fashion compared to the use of a full-wave simulator. In addition, it facilitates the investigation of structural alterations in the antenna concept, like shaped variations of the core lens. The derived model presented in this thesis also contributed to the measurement campaign of the Fly's Eye antenna prototype, through identifying a problematic component in the assembled prototype.

Acknowledgements

At this point I would like to express my sincere thanks to a number of individuals who each in his own way supported me throughout the last two years.

First and foremost, I owe my deepest gratitude to my supervisor Prof. Dr. Nuria Llombart. Your invaluable feedback and guidance throughout the duration of this project allowed me to gain deep insight into a challenging, yet fascinating topic. Thank you for always finding time for me. Furthermore, your advice as well as the overall mentorship during this year were indispensable. Our many discussions left an impact on me and contributed to the development of my way of approaching problems, which will certainly play a decisive role in my future. Working with you has been a great pleasure!

I would also like to extend my sincere thanks to the professors of the Terahertz Sensing group, whose enthusiasm during the courses of the MSc program inspired me to explore such interesting subjects and pursue this thesis.

Regarding my former colleagues in Greece, your mentorship and guidance played a decisive role in my choice of pursuing this MSc program. You helped me embark on this journey and I cannot thank you enough!

I have also benefited greatly from the support of my officemates, Robbin and Laurens, as well as many other members of the Terahertz Sensing group. I truly appreciate you taking the time to listen to my problems during the many difficult moments of this year.

To Alexandra, words cannot express my gratitude for the motivation you provide me to be the best version of myself. Your support during these years was essential for me to reach this point. I also greatly appreciate the time and effort you allocated to helping me with this project. Our work-related discussions provided me with a tremendous amount of input and helped me improve many aspects of this work.

Last but definitely not least, I want to thank my parents and sister for always being there for me during these years and making me feel appreciated.
Ειλικρινά ευχαριστώ για την υποστήριξή σας. Με βοηθάτε να αντιμετωπίζω κάθε πρόβλημα, ακόμα και στις πιο δύσκολες στιγμές! Δεν θα μπορούσα χωρίς εσάς.

ONASSIS FOUNDATION

This endeavor of pursuing an MSc degree in TU Delft had the generous support of the Alexander S. Onassis Public Benefit Foundation, who financed me through their scholarship program during the last two years [Scholarship ID: F ZR 040-1/2021-2022]. For that, I would like to express to them my sincere appreciation!

Analysis of Core-Shell Leaky-Wave Lens Antennas based on a combination of Physical Optics and Asymptotic Techniques

This thesis is submitted in partial fulfilment of the requirements for the degree of:

Master of Science

in

Electrical Engineering,

Track: Wireless Communication & Sensing

by

Alexandros Bechrakis Triantafyllos

The work presented in this thesis was performed at:
Tera-Hertz Sensing Group
Department of Microelectronics
Faculty of Electrical Engineering, Mathematics and Computer Science
Delft University of Technology

Delft University of Technology
Department of Microelectronics

The undersigned hereby certify that they have read and recommend to the Faculty of Electrical Engineering, Mathematics and Computer Science for acceptance the thesis entitled **"Analysis of Core-Shell Leaky-Wave Lens Antennas based on a combination of Physical Optics and Asymptotic Techniques"** by **Alexandros Bechrakis Triantafyllos** in partial fulfilment of the requirements for the degree of **Master of Science**.

Defense Date: August 18th, 2023

Chairman:

Prof. dr. Nuria Llombart

Advisor:

Prof. dr. Andrea Neto

Committee Member:

Dr. Marco Spirito

Contents

CHAPTER 1. Introduction

Taking into account the ever-increasing domain of applications that mobile communications can support, as well as the continuous demand for higher experienced end-user throughput, future communication networks are poised with several challenges in terms of wireless traffic, reliability, availability, latency and more [1], [2]. Among such a list of diverse requirements, arguably the most crucial refers to the need for increased capacity in order to support the expected surge in traffic volume density due to the rising number of connected devices and larger data rates requested by high-demand applications [3]. The required capacity to satisfy the expected increase in traffic volume density will become a formidable obstacle for wireless networks in places such as stadiums, open air festivals and other events that attract lots of people, where even today's users typically suffer from service denials due to network overload [4]. To properly address the connectivity requirements in such ultra-dense scenarios, which present the most demanding use case for modern and future communication networks in terms of simultaneous user connection, the Fly's Eye antenna concept has been proposed, envisioning a system with capacity capabilities above 10 Tbps [5].

Even though its specifications and requirements are extracted through considering the test case scenario of a sports stadium filled with spectators, the modular nature of the proposed antenna concept enables its scalability to a diverse range of ultra-dense deployment scenarios, such as shopping malls, open air festivals, offices and more.

1.1. Fly's Eye system overview

Given the saturation of employing advanced signal processing in small RF bandwidths, as well as the shortage of available spectrum at conventional cellular communication frequencies [6], arguably the most reasonable approach to cope with the required Tbps system capacity is to target higher carrier frequencies where large swaths of unused spectrum can be exploited. Assessing the trade-off between available bandwidth and power, while also aiming to exploit the recent advances in mm-wave and sub-THz integrated chips [7], a good compromise is established by targeting sub-THz carriers in the hundreds of GHz.

To further boost the overall system's capacity, apart from moving to mm-wave frequencies, a reuse scheme must be employed for the inherently limited spectral resource. However, instead of addressing the need for enhanced spectral efficiency through infrastructure densification, adhering to the cellular network architecture approach by deploying a very large number of base stations over the stadium and performing advanced interference rejection or exploiting local cooperation [4], [8]; the proposed concept adopts a much more energy efficient strategy. In particular, massive spatial division multiplexing from a single base station is employed through the use of directive antennas. At full scale, the designated area within the stadium will be covered by thousands of overlapping fixed beams, as indicated through Figure 1-1, each acting as a spatial cell and providing wireless connection to several spectators through Time Division Multiplexing. In conjunction with the two-dimensional spatial division multiplexing, to mitigate interference between adjacent spatial cells, the available bandwidth is partitioned into four sub-bands through the use of Frequency Division Multiple Access.

In terms of system specifications, moving to higher frequencies primarily requires the use of high-gain antennas in order to maintain the link budget and account for the square increase of the wave spreading factor with frequency. Considering that for a fixed aperture size the directivity is also increased with the square of the frequency, the wavelength size at the sub-THz band enables the design of high gain antennas even through moderate sized apertures. In addition to the aforementioned gain considerations, the limitations of transmitted power at higher frequencies due to the inefficiency of upconverting chains, stresses the need for highly efficient front ends and antennas.

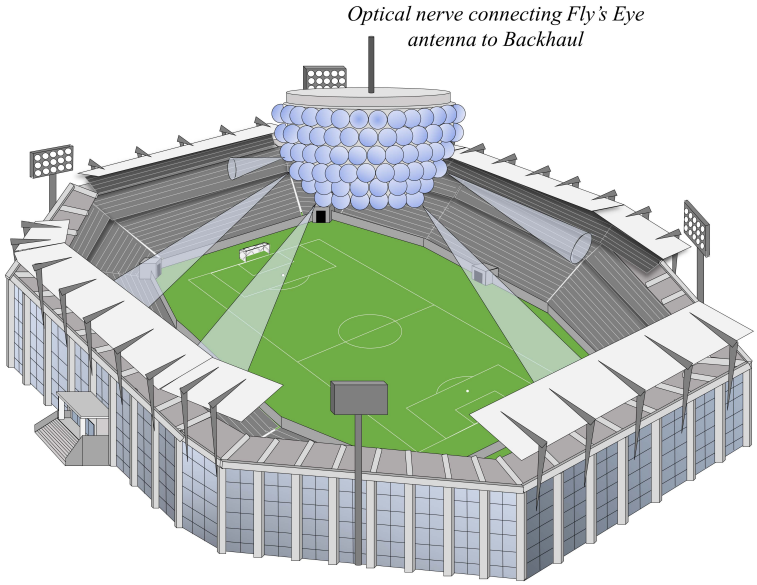

Figure 1-1. Simplified illustration of the Fly's Eye antenna concept.

Last but not least, the proposed antenna concept must be modular and compact, to facilitate both its scalability and its potential deployment to different communication scenarios with similar capacity requirements. For example, wideband and very directive antennas such as those proposed in the Fly's Eye antenna concept, can also be employed in ultra-high capacity line of sight use cases such as Fixed Wireless Access or Backhauling. In this manner, their possible utilization and exploitation in conjunction with a cellular network architecture is enhanced, providing an alternative to the use of labour-intensive fiber optics, as indicatively visualized through Figure 1-2.

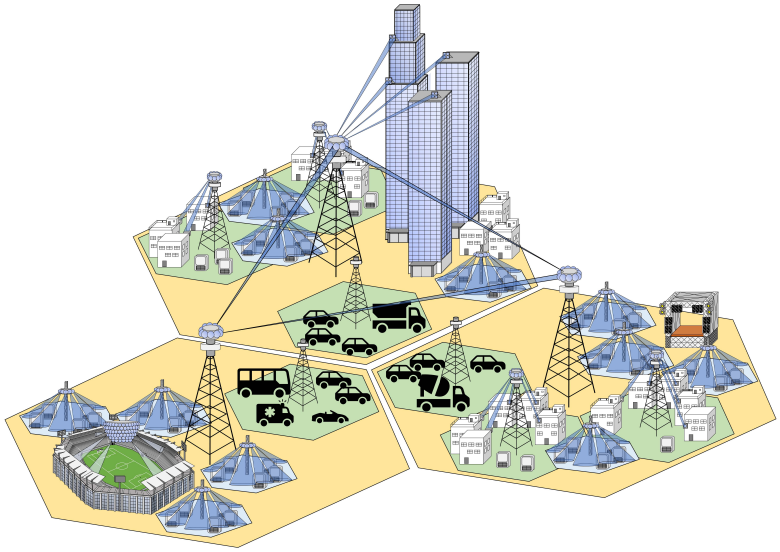

Figure 1-2. Wideband and directive antennas incorporated in a cellular network architecture, deployed in ultra-dense as well as high-capacity line of sight scenarios.

With the above system level requirements in mind, in the remaining of this section the background regarding the design of the Fly's Eye antenna array is going to be discussed.

Multibeam antennas

For the purpose of wideband operation above *100 GHz*, integrated lens antennas with leaky wave feeds stand out when compared to other more resonant antenna solutions such as Fabry-

Perot, metasurfaces or transmitarrays [9], [10], due to their capability of efficiently achieving large gain over a wide bandwidth. Furthermore, contrary to other multibeam solutions such as combining focal plane arrays of horns with reflectors, integrated lens antennas can be implemented in planar configurations, allowing for reduced complexity and size of the overall design. While even lower profile planar multibeam antennas can be implemented through the use of reflectarrays or transmitarryas, since their structure involves a single or multi-layered inhomogeneous array of printed resonant scatterers, their bandwidth performance is in general limited, being highly dependent on said element's resonance [11]. Several approaches have been explored to increase the bandwidth of reflectarrays [12], but even the more wideband designs [13], [14], [15], lack the aperture efficiency performance of integrated lenses with leaky wave feeds [16], [17]. Finally, apart from enhancing the radiation properties of planar antennas, lenses enable the integration of different beams under the same aperture. This is achieved through featuring a set of displaced feeds in their focal plane, which in turn generate a set of fixed independent beams in the far field.

It should be noted that another very popular multibeam antenna solution is the use of phased arrays. However, this is not well suited for the examined scenario since at frequencies in the hundreds of *GHz* the complexity and losses involved with implementing the required feeding network are significant.

Having showcased some of the benefits of integrated lenses as a multibeam antenna system solution, a brief discussion of the fundamental design considerations for lenses with leaky wave feeds will be presented below. Before doing so though, an indicative depiction of the above discussed multibeam antenna systems is presented through Figure 1-3.

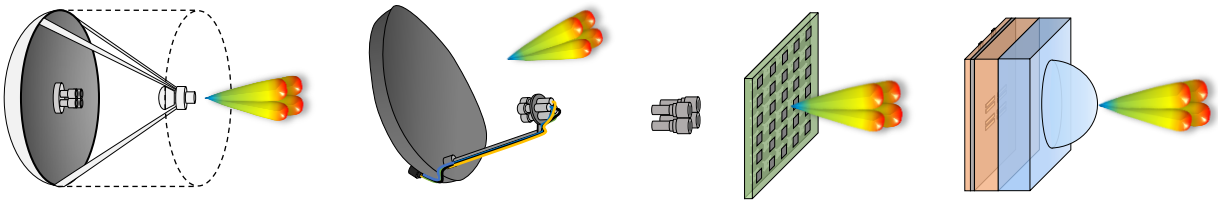

(a) *(b)* *(c)* *(d)*

Figure 1-3. Focal plane array of horns with (a) parabolic reflector, (b) elliptical reflector, (c) transmitarray and (d) integrated lens antenna with planar feeds.

Integrated lenses

Taking the above discussion into account, the goal of the Fly's Eye antenna concept is to develop a scalable integrated lens array in the form of modular planar panels operating from *140* to *170 GHz* [18] and capable of satisfying the requirements established for the targeted communication scenario [5]. For this purpose, each generated beam should feature a gain larger than *30 dB* over the desired bandwidth. Considering a reasonable estimate for the achieved aperture efficiency and losses of an individual lens, the desired gain is targeted with a radiating aperture of *3 cm* diameter.

In terms of design considerations, through basing the optimization of the lens feed in the analysis of antennas in reception, the aperture efficiency of the quasi-optical component can be evaluated in terms of field matching between the frequency independent Geometrical Optics (GO) fields and the field of the feed at a specified surface, usually the Fourier Optics (FO) sphere. In fact, the component's aperture efficiency is maximized when the GO and feed fields are conjugate matched. An extensive discussion for the analysis of antennas in reception which further elaborates on this field matching concept can be found in the appendix of [17], together with a thorough study of leaky wave feeds for integrated lenses in the rest of the document. Apart from the feed considerations though, there are some fundamental design limitations in terms of bandwidth, front-to-back ratio as well as steering capabilities, that are introduced by the leaky waves and lens structure themselves.

Primarily, integrated lenses were introduced to mitigate the impact of surface waves and enhance the radiation properties of printed antennas. As a matter of fact, the choice of material for the lens determines the front-to-back ratio of the feeding structure, since planar antennas printed on dense substrates radiated more energy into the denser medium. Consequently, the front-to-back ratio of the feed is increased with the permittivity of the lens material, as indicatively illustrated in Figure 1-4.

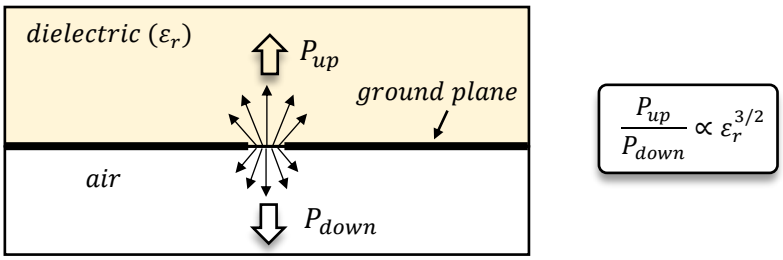

Figure 1-4. Front to back ratio for planar antenna printed on dielectric substrate.

It is worth pointing out that while any realistic printed antenna will be backed by a metallic reflector, forming a backing cavity, it is crucial to maintain a high front-to-back ratio for the feed itself. If this is not the case, a strong parallel plate waveguide mode can be excited inside the backing cavity, subsequently impacting the matching bandwidth and thus the performance of the feeding structure.

In order to enhance the optimization potential of the basic lens design, an air cavity can be introduced between the ground plane and the lens dielectric, forming a leaky wave structure. In a few words, such a structure enables the excitation of waves inside the cavity, which propagate radially away from the source in the form of cylindrical waves, through sequential bounces between the ground plane and the partially reflecting interface. Throughout their propagation inside the cavity, these waves feature an exponential attenuation as they couple their energy to the space wave, leading to them being labelled as leaky waves. In this manner, they can modulate the spectrum of the structure's Green's function around real angles and thus influence its radiation properties. The impact of these waves can be conveniently described through their propagation constants ($k_{\rho,LW} = \beta_{LW} + j\alpha_{LW}$), with its real part determining the angle around which the leaky wave influences the field ($\beta_{LW} = k_d sin(\theta_{LW})$), while the imaginary part expressing the attenuation constant and subsequently the directivity along said angle. In turn, these propagation constants ($k_{\rho,LW}$) correspond to the polar singularities of the respective spectral Green's function, with distinct leaky wave modes arising from different poles.

It should be noted that leaky wave supporting stratifications can also be formed with dielectric cavities, provided that their permittivity is smaller than that of the lens material. To conclude this brief discussion, several different structures can be designed to support leaky waves, with two indicative examples shown in Figure 1-5 *(a)* and *(b)*, featuring a dielectric slab and a semi-infinite dielectric medium respectively as a partially reflecting interface.

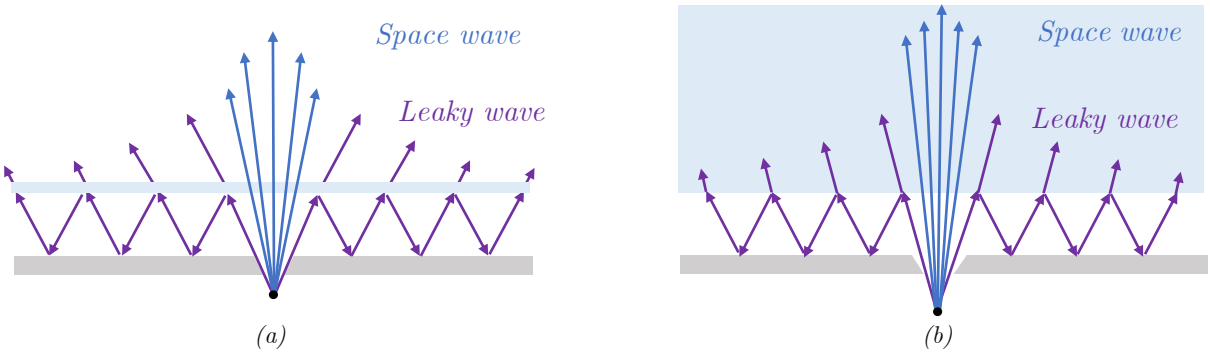

Figure 1-5. Leaky wave structure fed by an aperture in the ground plane featuring (a) a dielectric slab and (b) a semi-infinite dielectric medium as a partially reflecting interface.

Returning to the discussion regarding the fundamental limitations of lenses integrated with leaky wave feeds, considering a quasi-optical component such as a lens, its bandwidth must be evaluated in terms of aperture efficiency bandwidth, which in turn translates to the feed's pattern stability. As such, it is fundamentally limited by the frequency dispersion of the leaky wave modes excited in the cavity, which impacts the pattern of the leaky wave structure. Said frequency dispersion in turn depends on the dielectric contrast between the cavity and lens material. This is visualized through Figure 1-6, where the dispersion of the main leaky wave mode pair (TE_1, TM_1) is examined for a structure featuring a half-wavelength air cavity between a ground plane and a semi-infinite dielectric medium whose permittivity is varied.

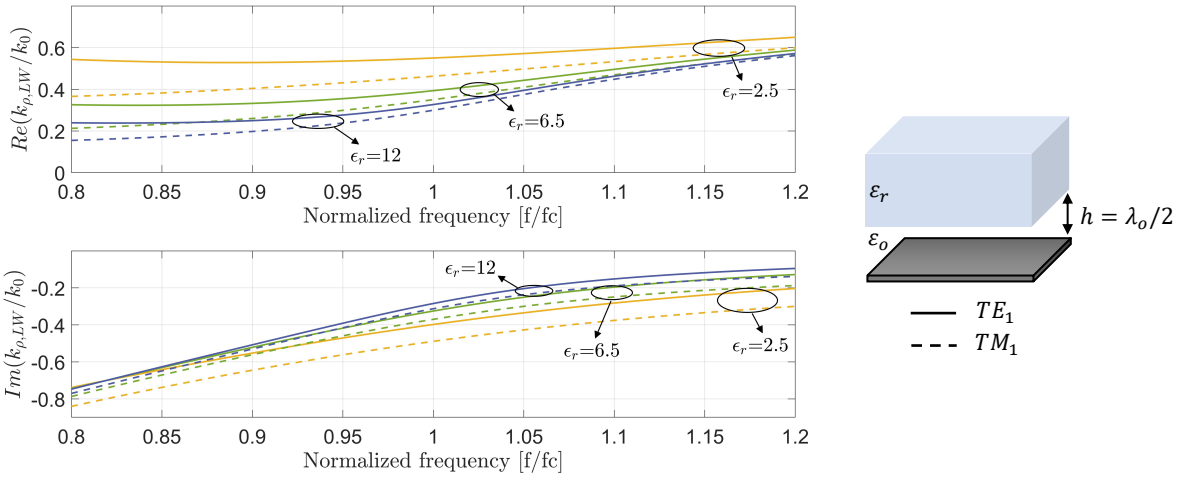

Figure 1-6. Frequency dispersion of main leaky wave mode pair (TE_1, TM_1) considering the leaky wave supporting stratification of the inset and varying the relative permittivity (ε_r) of the semi-infinite dielectric medium.

Another aspect of equal importance refers to the steering capability of the lens, which is limited by the maximum acceptable displacement of a feed in the ground plane in terms of the achieved aperture efficiency and thus gain of the steered beam. Given that denser materials lead to larger scanning angles for the same displacement (d_{feed}), one can deduce that high permittivity lenses feature an enhanced field of view when compared to low permittivity structures. This concept can be intuitively realized through considering the geometrical ray picture together with the Snell's law for the central ray, as shown in the inset of Figure 1-7.

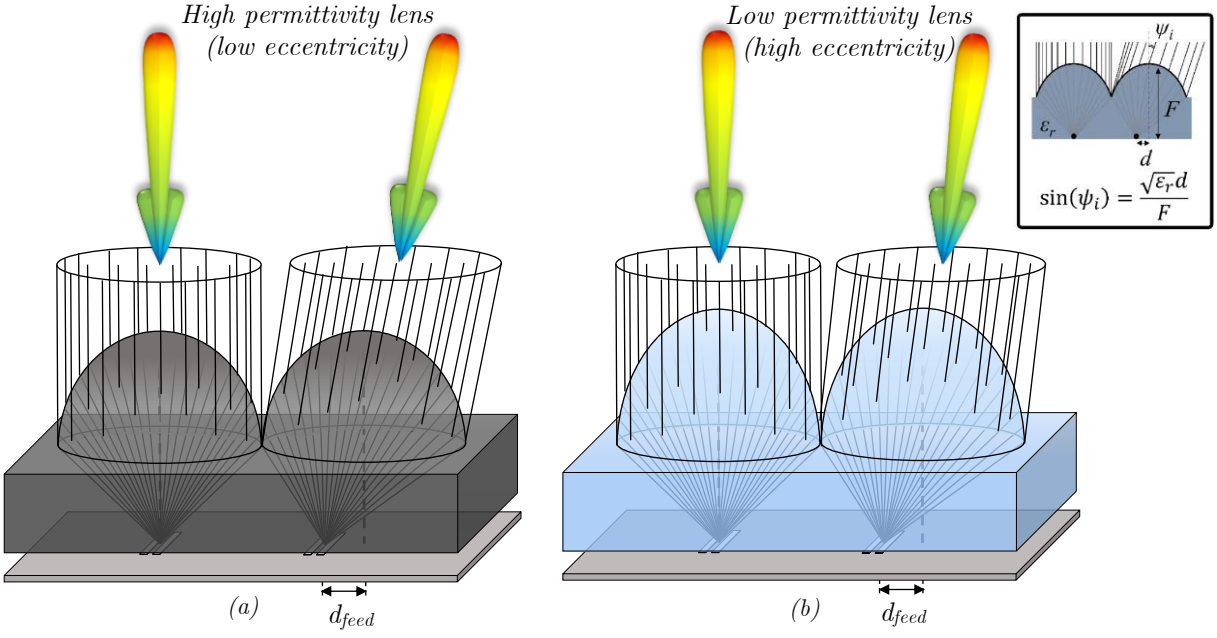

Figure 1-7. Illustration of broadside and steered beams for identical feed displacement in the ground plane (d_{feed}) and single dielectric elliptical lenses with (a) high and (b) low permittivity plastic.

Having introduced some of the basic considerations regarding the design of integrated lenses fed by leaky wave feeds, in the following subsection these concepts will be revisited in conjunction with the top-level requirements of the Fly's Eye antenna concept in order to introduce and justify the design choices for its lens geometry.

Core-shell lens structure

Regarding the implementation of a *3 cm* radiating aperture capable of satisfying the specified gain requirements [5], single high permittivity lenses would either be too costly (e.g., high resistivity Si) or lossy (e.g., PREMIX) for implementing the Fly's Eye planar panels. As such, the lens structure must be built by a material with very low loss tangent within the examined frequency range which can also be manufactured in a cost-effective manner. An ideal candidate satisfying the above is HDPE, which due to its low permittivity at the examined frequency range ($\varepsilon_{r,HDPE} \simeq 2.3$ [17]) does not feature significant reflections in the air interface, mitigating the need for a matching layer and thus reducing the overall complexity of the design. While a low permittivity lens made of HDPE integrated with a leaky wave feed, can satisfy both the bandwidth and gain requirements of the Fly's Eye concept, with some prototypes achieving an aperture efficiency higher than *80%* for bandwidths in the range of *40%* [16], [17], it does suffer both in terms of front-to-back ratio and steering capabilities. A design capable of enhancing the field of view of such a structure has been introduced in [19], where a wedge of dielectric gratings with modulated height is integrated inside the plastic lens, to improve the aperture efficiency of displaced feeds and thus reduce the scan loss of steered beams. While being an excellent design in all the remaining aspects, still the problem of chip integration remains, due to the poor front-to-back of the low permittivity lens.

To deal with this trade-off between the required scalability, bandwidth and front-to-back ratio, a double-lens structure has been proposed for the Fly's Eye concept, featuring a low permittivity shell and a high permittivity core lens integrated on a fused silica wafer [18]. As introduced above, the low permittivity shell enables the implementation of a large radiating aperture using low cost and low loss materials, essentially enabling the required gain while maintaining an acceptable cost to allow for the scalability of the design. At the same time, the high permittivity core lens improves the front-to-back ratio, facilitating chip integration, while also maintaining low contrast with the resonant dielectric (fused silica) cavity, thus preserving the bandwidth. An indicative illustration of the aforementioned core-shell lens structure is presented through Figure 1-8 *(a)* and *(b)*.

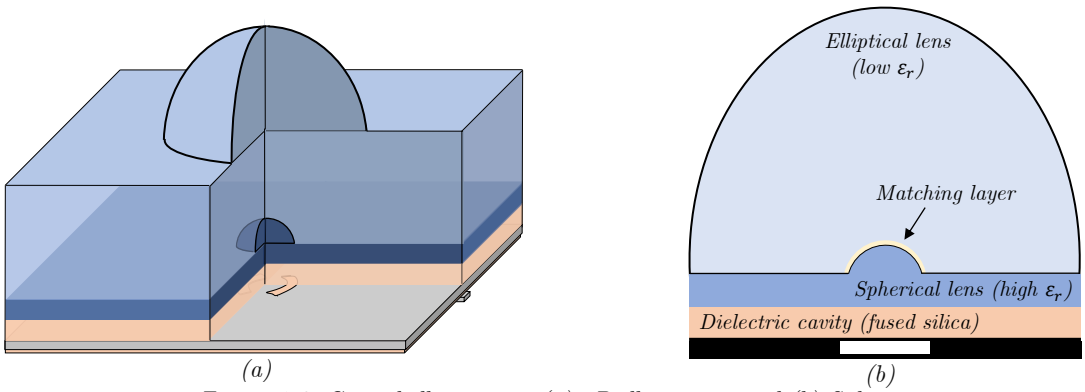

Figure 1-8. Core-shell structure (a) 3D illustration and (b) Side cut.

Depending on the desired impact of the lens component several shapes can be implemented exploiting the canonical properties of the respective geometries. As such, since its purpose is to form a directive beam, the shell lens shall feature an elliptical shape. On the other hand, to efficiently illuminate the high eccentricity elliptical structure ($e = 1/\sqrt{\varepsilon_{r,shell}}$), the core lens must act as an ideal transition between the different dielectric media, essentially simulating a leaky wave structure with high permittivity semi-infinite dielectric region. Considering the

observation made in [20], namely that given a proper definition of the phase center the field of a leaky wave structure resembles a spherical wave within a solid angle around broadside, even in the near field of the source, the shape of the core lens must be spherical. Furthermore, to reduce the level of reflections in the interface between the dense dielectric and low permittivity plastic material, the core structure must be coated with a matching layer, as indicated through Figure 1-8 *(b)*.

To summarize the above brief discussion, the proposed Fly's Eye antenna concept is comprised of planar panels of lenses, each featuring a number of simultaneous fixed independent beams, as showcased through Figure 1-9. All the lens feeds are placed over a flat ground plane in order to enable monolithic integration at high frequencies. Moreover, to simplify the design and avoid complexity and losses involved with implementing an array feeding network at the examined frequency band, each feed contributes to a single beam.

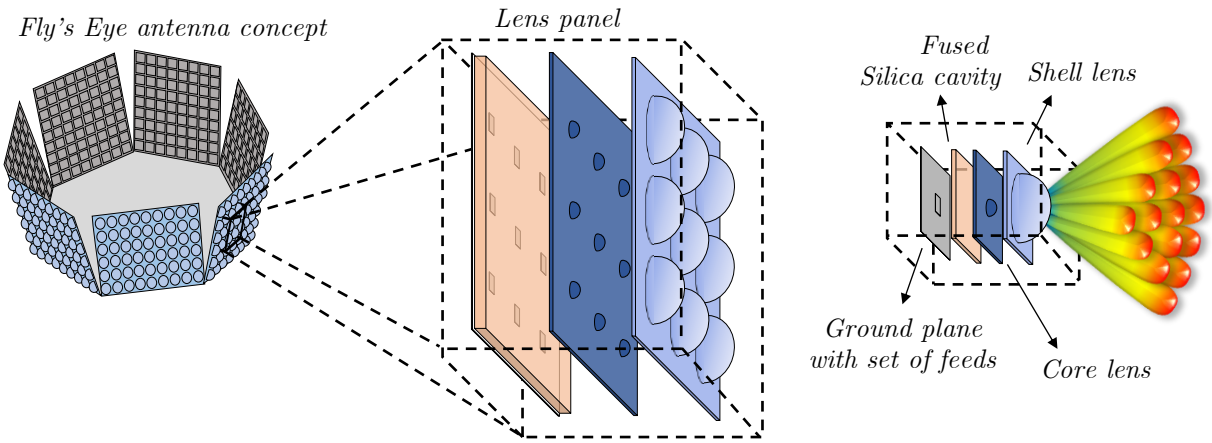

Figure 1-9. Fly's Eye antenna array comprised of planar lens panels.

1.2. Objectives of this work

Having presented the motivation as well as summarized the design considerations involved in the Fly's Eye antenna concept, in the current section the main aim of this work will be introduced.

Considering the previous discussion regarding the core-shell structure and with the aim of reducing the losses and cost introduced by the high permittivity material, the dimensions of the core lens should be maintained as small as possible. This inevitably brings the core lens surface in the near field of the leaky wave feeding structure. As a consequence, for the purpose of analysing and subsequently optimizing such a structure, the first step refers to developing a computationally efficient strategy for the derivation of the near field of a leaky wave structure.

Adhering to this conclusion, the initial stages of this work aim to present an asymptotic method for the derivation of the near field of a leaky wave structure, while also discussing its potential contribution in the optimization of the examined core-shell lens geometry. All things considered, this study offers the prospect of developing a fast tool for the evaluation of the near field of a leaky wave structure, which apart from speed can also provide insightful decomposition of the field into distinct components. This physical insight for the formation of the local phase-front in the near field, can contribute to the derivation of analytical geometries which optimize different aspects of the lens design. For example, in terms of shaping the lens, the latter can be made conformal to the incident field, thus acting as an ideal transition; or alternatively it can be shaped with the aim of enhancing the aperture efficiency for displaced feeds, in turn improving the scanning capabilities of the core-shell structure.

In order to enable the future study of such prospects, i.e., shaped variations of the core lens, another goal of this work refers to combining the derived near field with a set of Physical Optics (PO) techniques, with the aim of developing a model for the Fly's Eye antenna. Modelling the antenna concept in such a manner, enables its study in a much more computationally efficient fashion compared to the use of a full-wave simulator, while also facilitating the study of structural variants like lateral or vertical displacements, or even changes in the material dielectric properties. The versatility provided by studying the impact of such effects in the antenna performance can prove very useful especially when troubleshooting is required.

To summarize, one of the main objectives of this work is the derivation of a fast tool able to extract the field on the core lens through the asymptotic evaluation of the near field integral expressions. Prior to thoroughly discussing the asymptotic method employed in this work through subsequent chapters, a brief overview of the literature will be presented in the following section. In particular, this section will present an overview of some of the approaches encountered in the literature for the asymptotic evaluation of radiation integrals.

1.3. Literature overview – Asymptotics

A fundamental aspect in the analysis of stratified structures with unbounded cross sections is the derivation of the spatial domain Green's functions, i.e., the fields radiated by an elementary source. Since the Green's functions of layered media can be extracted analytically only in the spectral domain, their spatial counterparts can be obtained through the inverse Fourier transform of their spectral representation. However, the convergence of these complex integrals is slow due to the highly oscillatory nature of the integrands involved, making their numerical evaluation very computationally inefficient.

The most efficient techniques to improve the computational efficiency of complex integrals, are those which resolve the integral expressions through a finite number of analytical terms. To achieve this, the integrand functions are expressed in terms of simpler functions with similar properties in the relevant spectral region. This simplified representation is chosen such that it leads to closed-form expressions, allowing the evaluation of the complex integrals through a number of analytical terms. This process is referred to as asymptotic approximation of complex integrals.

The most frequently employed techniques for the case of radiation integrals utilize algorithmic processes in order to express the integrand in a way that allows the integral's asymptotic approximation. Some indicative approaches commonly encountered in the literature are the generalized pencil of function (GPOF) method or the total least square algorithm (TLSA), which are used to express radiation integrals as a summation of canonical forms. Examples of their use can be found in [21] and [22] respectively. Regarding the targeted canonical expressions, these can vary in each case depending on the integral's formulation. In several works concerning the radiation of field distributions [21], [23], [24] canonical forms based on the Sommerfeld identity are used. This enables the representation of the radiation integrals through a summation of beam-like wave objects, which in turn constitutes an efficient mean of analysing the interactions between parts of a system, like quasi-optical components [25].

One inherent aspect of the above discussed approaches arises from the treated integral expressions being evaluated on slow convergent integration paths. This essentially implies that a significant spectral region impacts the integral's evaluation, meaning that a large number of terms must be included in the representation of the integrand to maintain the accuracy of its asymptotic approximation. An alternative approach to the one discussed this far is to exploit the spectral properties of the integrand expression by identifying the dominant field contributions and the fastest convergent integration path. These refer to the integrand's saddle points and the steepest descent path (SDP) which includes this saddle point respectively. This approach can be used to improve the computational efficiency of the numerical field evaluation

while also providing physical insight through separating the field into distinct contributions. The resulting integral expressions, i.e., the SDP integrals, can be evaluated asymptotically through transforming their integrands into canonical forms in an auxiliary complex plane, labelled as s-plane. This process requires isolating the spectral singularities of the integrands in their simplest form and subsequently evaluating them asymptotically. An extensive overview of such techniques can be found in *section 4* of [26].

Given the properties of the employed integration path (SDP), the impactful spectral region around the integral's dominant contributions is minimized. This essentially implies that the integrand can be represented with fewer number of terms compared to the previously discussed approaches, leading to a more compact asymptotic approximation. However, what is different in this case is the dependence of the integration path on the observation point. Since the path of integration changes, this means that the integrand's representation must also be modified in response. Indicative examples for the asymptotic approximation of SDP radiation integrals can be found in [27] and [28], where the treatment of the integrand in each case varies depending on the impactful singularities and the nature of the field. One noteworthy aspect for the treatment employed in [27], refers to the use of the field decomposition provided by the SDP integration approach. In particular, the dominant contributions at different angular regions are identified and a distinct asymptotic treatment is employed for each region.

With the aim of asymptotically approximating the near field on the core lens of the Fly's Eye antenna, this work will focus on the asymptotic approximation of the SDP integral expressions presented in [20]. More specifically, the nature of the near field of a leaky wave structure featuring an infinite dielectric region and a cavity around resonance will be considered, in order to derive a simplified asymptotic evaluation of the involved integral expressions.

1.4. Outline of this Thesis

The remainder of this thesis is structured as follows.

- Chapter 2 extensively discusses the background in spectral analysis and numerical evaluation techniques for the near field of leaky wave structures, which is required for this work.
- In turn, Chapter 3 builds upon the background study of Chapter 2 and presents an approach which enables the asymptotic evaluation of the near field for leaky wave structures around resonance.
- Subsequently, Chapter 4 elaborates on the complications arising in the asymptotic approach when a current distribution is added in the ground plane and presents some indicative examples for small lenses in the near field.
- Following this, Chapter 5 describes the Physical Optics techniques employed to model the quasi-optical components of the Fly's Eye antenna (i.e., core and shell lenses) and elaborates on the validity of the approximations involved.
- In Chapter 6, the asymptotic evaluation of the near field presented through Chapter 3 and 4 is combined with the Physical Optics techniques discussed in Chapter 5, to develop a model for the Fly's Eye antenna. The contribution of this model in the measurement campaign of the assembled Fly's Eye antenna prototype is also discussed in this chapter.
- Finally, Chapter 7 draws conclusions and presents points of interest for future study, emphasizing on the possible improvements of the presented asymptotic near field evaluation approach as well as its potential utilization for shaping the core lens.

This thesis is supplemented by a number of Appendices, elaborating further on certain concepts which are deemed useful to facilitate the understanding of this work.

CHAPTER 2. BACKGROUND

2.1. General Considerations

The analysis of stratified media with unbounded cross sections constitutes an electromagnetic problem which can be conveniently approached in the spectral domain, since only in this manner the respective Green's functions can be derived analytically. Another aspect of spectral analysis with arguably equal importance, refers to the representation of the field as a continuous spectrum of plane waves. This way, dominant contributions can be identified and related to physical properties of the examined structure. Having said the above, prior to elaborating further on the analysis of stratified media in the spectral domain, the stratifications of interest will first be introduced.

2.1a. Examined stratifications

For reasons that will be explained through Chapter 5, referring to the Physical Optics methods employed to model the core-shell structure, the required near field evaluation for the modelling of the Fly's Eye antenna corresponds to the incident field on the core lens. Consequently, the stratification of the core lens can be simplified through extending the dense dielectric region to infinity. The resulting simplified stratification is illustrated through Figure 2-1 *(a)*, featuring a fused silica cavity and a semi-infinite dense dielectric region. While the case of the Fly's Eye antenna requires the examination of a wideband leaky wave structure with low dielectric contrast between the cavity and semi-infinite dielectric region, to provide a more complete study of the near field, a resonant stratification will also be considered in following chapter, as depicted in Figure 2-1 *(b)*. Both structures are examined around resonance, meaning that their cavity heights correspond to half the cavity wavelength ($h=\lambda_{cav}/2$) at the central frequency (*150 GHz*), while all planar layers are assumed infinite and untruncated. Furthermore, to simplify the analysis presented in the initial sections of this chapter, a y-oriented elementary magnetic current source will be considered in the ground plane for both structures.

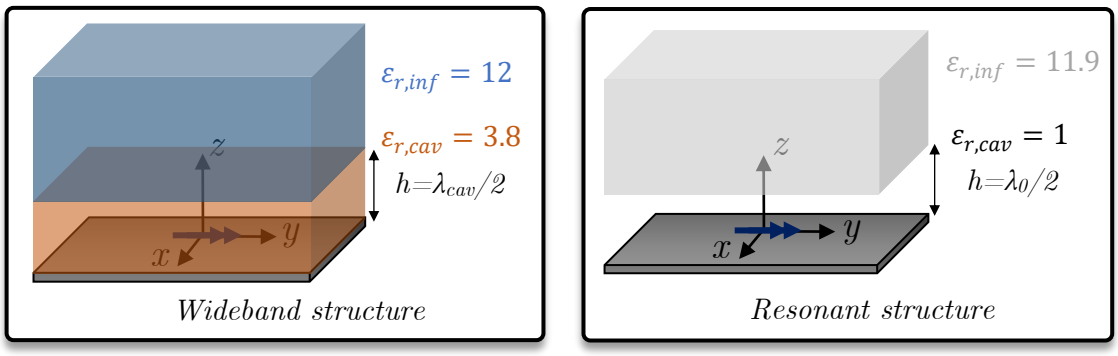

(a) *(b)*

Figure 2-1. Leaky wave structures with (a) low dielectric contrast (wideband) and (b) high dielectric contrast (resonant).

It should be noted that the region of interest for the derivation of the near field for both stratifications is the semi-infinite dielectric region. Consequently, for the remaining of this chapter, when dielectric medium properties are used in expressions (i.e., ζ_d and k_d), they will refer to those of the semi-infinite region, unless mentioned otherwise.

To employ the spectral Green's function for the above presented stratifications, first, one should solve their equivalent transmission line models for the voltage and current potential functions at the observation height of interest. To maintain the cohesion of the current discussion, this process will be thoroughly described through *Appendices A* and *B*.

2.1b. Significant leaky wave modes

One noteworthy comment regarding the structures of Figure 2-1 refers to the number of impactful leaky wave modes that they support. As briefly introduced in *section 1.2*, leaky waves are related to the polar singularities of the spectral Green's function, with their propagation constants ($k_{\rho,LW}$) extracted through the values of said poles. Since these singularities are attributed only to the examined geometry and its capability of supporting leaky waves, they must occur in the Green's function for all types of sources (either electric or magnetic) and for any planar orientation (either x or y). As such, their values can be derived as the zeros of the common denominator of the voltage and current potential functions and can subsequently be separated into *TE* and *TM* variants [29]. Even if several leaky wave modes can be excited inside the illustrated air/dielectric cavities, given their electrical height, only three modes will feature small enough attenuation constants in order to be impactful, namely TE_1, TM_1 and TM_0. The dispersion of these main modes for the two examined stratifications is depicted through Figure *2-2*, showcasing their pointing angles (θ_{LW}) and attenuation constants (α_{LW}), considering that $k_{\rho,LW} = k_d sin(\theta_{LW}) + j\alpha_{LW}$.

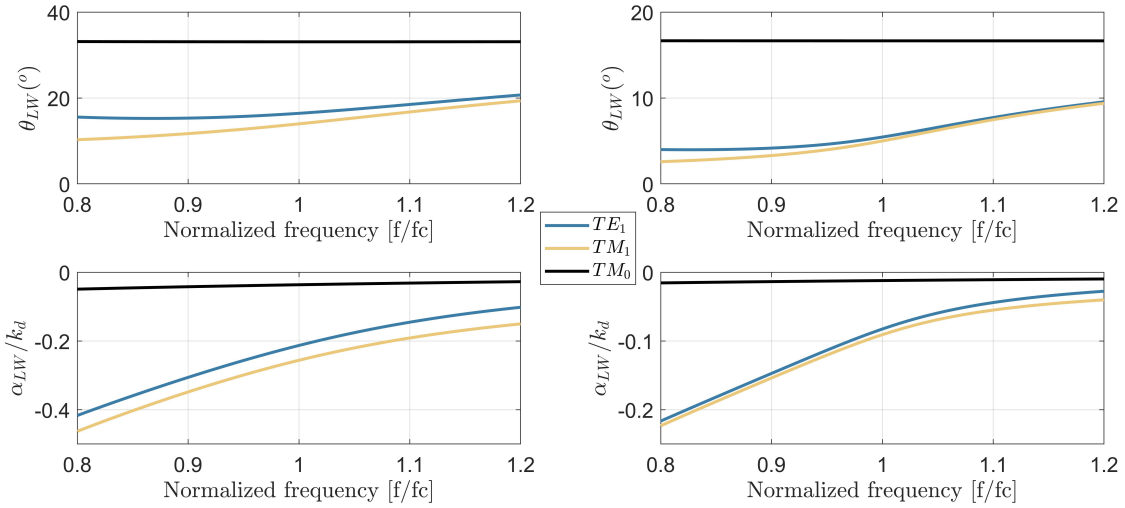

(a) *(b)*

Figure 2-2. Dispersion of dominant leaky wave modes (a) wideband and (b) resonant structure of Figure 2-1. The top figures refer to the leaky wave pointing angles ($\theta_{LW} = asin(Re(k_{\rho,LW})/k_d)$) while the bottom figures correspond to the attenuation constants (α_{LW}).

While the similar behavior of the TE_1, TM_1 mode pair leads to its frequent exploitation in order to enhance the radiation properties of small apertures through forming rotationally symmetric beams, TM_0 is usually undesirable. In fact, since it launches power at relatively larger angles off broadside and features small attenuation constant (α_{LW}), it constitutes a significant spillover loss when leaky wave feeds are integrated with lenses [17] or employed to illuminate reflectors [30], [31]. For this reason, a variety of methods have been explored for the suppression of this undesired mode. For example, in some more elegant designs, like [16], corrugations are introduced in the ground plane such that the attenuation constant for the propagation of TM_0 inside the cavity is increased and subsequently its impact in the field is reduced. Arguably the most common approach however, involves suppressing this polar singularity of the spectral Green's function (i.e., the TM_0) via forcing a null around the same spectral position ($k_{\rho,LW}^{TM_0}$), through the spectrum of the current source.

Having presented some fundamental aspects of the examined leaky wave supporting stratifications, the following section will elaborate on the required background for the asymptotic evaluation of the near field integral expressions.

2.2. Numerical near field evaluation

2.2a. Single complex integral formulation

Through analyzing stratified structures in the spectral domain, the evaluation of the field begins with the expression of the inverse Fourier transform of the convolution between the Green's function and the source's current distribution. For a y-oriented elementary magnetic current source, the resulting integral expression is expressed below.

$$\vec{E}(\vec{r}) = \frac{1}{4\pi^2}\int_{-\infty}^{+\infty}\int_{-\infty}^{+\infty}\bar{\bar{G}}^{em}(k_x,k_y,z,z_s)\cdot\hat{y}e^{-jk_x x}e^{-jk_y y}dk_x dk_y, \qquad (2.1\ a)$$

Where $\bar{\bar{G}}^{em}$ refers to the dyadic spectral Green's function relating electric fields with magnetic currents, z corresponds to the height of the observation point in the stratification and z_s refers to the position of the source.

Given the rotational symmetry of the examined stratified structures, the spectral variables (k_x, k_y) can be transformed into their cylindrical counterparts (k_ρ, α), where $k_x = k_\rho cos(\alpha)$ and $k_y = k_\rho sin(\alpha)$. The benefit of this step is that the total field can now be expressed in terms of a single infinite complex integral in k_ρ, while the finite α integral can be conveniently closed into a canonical form.

$$\vec{E}(\vec{r}) = \frac{1}{4\pi^2}\int_{0}^{+\infty}\int_{0}^{2\pi}\bar{\bar{G}}^{em}(k_\rho,\alpha,z,z_s)\cdot\hat{y}e^{-jk_\rho\rho\,cos(\alpha-\varphi)}k_\rho d\alpha dk_\rho, \qquad (2.1\ b)$$

To further progress with the integral evaluation, the projection of the spectral Green's function on $\hat{y}$, as given in equation $(A.1)$ of *Appendix A*, can be substituted in the above integral expression in terms of cylindrical spectral variables (k_ρ, α). Subsequently, the finite α integral can be closed through the identities presented below, with the resulting integral field expressions now formulated in terms of a single complex integral on k_ρ featuring *Bessel* functions. It should be noted that in all subsequent expressions the potential functions ($v_{TE/TM}$ and $i_{TE/TM}$) are expressed through the product of the respective wave amplitudes and the exponential relating to the propagation inside the semi-infinite dense medium ($e^{-jk_z z}$), as described through *Appendix A* and given in equations $(A.2)$ and $(A.3)$.

$$\begin{matrix}\int_0^{2\pi} cos(n\alpha)\,e^{-jk_\rho\rho\,cos(\alpha-\varphi)}d\alpha = j^{-n}2\pi\,cos(n\varphi)\,J_n(k_\rho\rho)\\ \int_0^{2\pi} sin(n\alpha)\,e^{-jk_\rho\rho\,cos(\alpha-\varphi)}d\alpha = j^{-n}2\pi\,sin(n\varphi)\,J_n(k_\rho\rho)\end{matrix}, \qquad (2.2\ a)$$

$$\begin{bmatrix}E_x(\vec{r})\\E_y(\vec{r})\\E_z(\vec{r})\end{bmatrix} = \frac{1}{4\pi}\int_0^{+\infty}\begin{bmatrix}-\left(\left(v_{TE}^{+}(k_\rho,z_s)+v_{TM}^{+}(k_\rho,z_s)\right)J_0(k_\rho\rho)+\left(v_{TE}^{+}(k_\rho,z_s)-v_{TM}^{+}(k_\rho,z_s)\right)cos(2\varphi)J_2(k_\rho\rho)\right)\\ sin(2\varphi)\left(v_{TM}^{+}(k_\rho,z_s)-v_{TE}^{+}(k_\rho,z_s)\right)J_2(k_\rho\rho)\\ -j\frac{2\zeta_d}{k_d}cos(\varphi)\,i_{TM}^{+}(k_\rho,z_s)J_1(k_\rho\rho)k_\rho\end{bmatrix}k_\rho e^{-jk_z z}dk_\rho, \qquad (2.2\ b)$$

Closing the complex integrals on α in the above presented manner does not constitute an approximation when elementary sources are examined, since expressions *(2.2 a)* refer to canonical integrals. However, for the more realistic scenario where an actual current distribution is considered in the ground plane, transforming the integral expressions into a formulation with a single complex integral requires additional considerations. This aspect of the near field evaluation resulting from the above steps in the integral manipulation will be revisited through *section 4.1*, where the inclusion of the source will be discussed.

2.2b. Singularities in the k_ρ complex plane

Apart from the capability of deriving analytical expressions for the Green's functions of stratified media, the analysis in the spectral domain also offers the potential of identifying

individual field components, which can in turn be related with spectral singularities of the Green's functions, namely branch points and poles.

Regarding the former, the Green's function's branch point singularities are a result of the odd nature of the transmission line solution in the semi-infinite regions of the stratified structure. Given that a single semi-infinite region exists in the examined geometries (Figure 2-1), namely $z > h$, only one pair of branch points appears in the k_ρ complex plane at $\pm k_d$. To make the definition of the double-valued function ($k_z = \pm\sqrt{k_d^2 - k_\rho^2}$) unique, a two-sheeted complex plane is required, with branch cuts providing the means of passing from one Riemann sheet to the other. While these branch cuts can be arbitrarily drawn in the complex plane, the most convenient choice is that which maintains the sign of the imaginary part of k_z constant in each of the defined Riemann sheets, i.e., the one illustrated through Figure 2-3 *(a)*, with the resulting expressions for k_z provided below.

$$\textit{Top Riemann sheet } (Im(k_z) < 0): \quad k_z = -j\sqrt{-(k_d^2 - k_\rho^2)}$$

$$\textit{Bottom Riemann sheet } (Im(k_z) > 0): \quad k_z = j\sqrt{-(k_d^2 - k_\rho^2)}$$

As already introduced through *section 2.1b*, besides branch point singularities resulting from the semi-infinite medium, the spectral Green's function also contains polar singularities which are directly linked to the leaky waves that can be exited in the cavity. More specifically, these polar singularities appear on the bottom Riemann sheet ($k_{z_{LW}} = j\sqrt{-(k_d^2 - k_{\rho_{LW}}^2)}$) and are only attributed to the examined stratification and its capability of supporting leaky waves. An indicative illustration of the polar singularities for the *TM* potential of a structure supporting the two main leaky wave modes (i.e., *TM₁* and *TM₀*), is given through Figure 2-3 *(b)*.

Considering the presence of the above singularities in the k_ρ complex plane, the integration path for the evaluation of the expressions of (*2.2 b*) commences at the origin and moves along the real axis, only slightly deformed to avoid the branch point at $+k_d$, as shown through Figure 2-3 *(c)*. It should be noted that for the integrand to remain bounded as k_ρ tends to infinity, the integration path must be maintained on the top Riemann sheet.

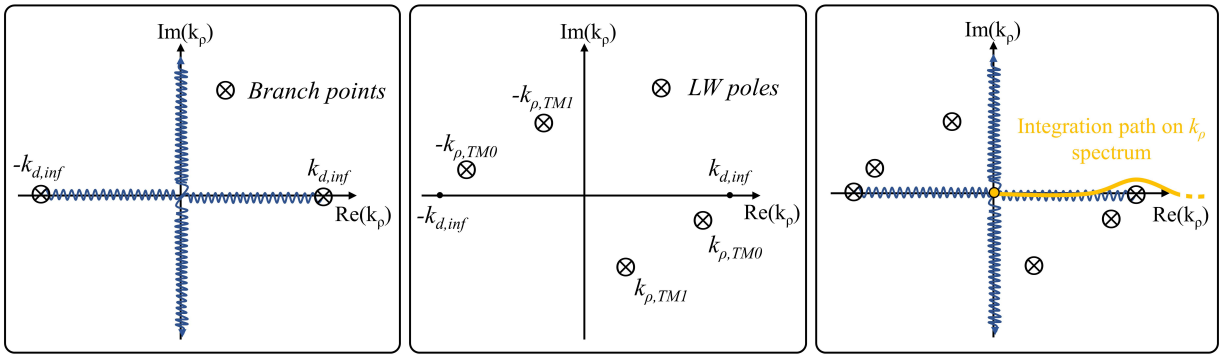

(a) *(b)* *(c)*

Figure 2-3. (a) Branch points and cuts for the stratifications of Figure 2-1. (b) Leaky wave poles in bottom Riemann sheet for TM potential of structure close to resonance. (c) Integration path for TM integrals of (2.2b).

While the equations of (*2.2 b*) and the integration path of Figure 2-3 *(c)* can be employed for the evaluation of the near field, their two main drawbacks refer to the slow convergence of the numerical integration, especially for observation points close to the source, as well as the lack of any insightful field decomposition. With the purpose of adopting alternative approaches for the numerical evaluation of the field integral expressions, in the following section, some fundamental concepts of complex analysis will be discussed.

2.2c. Integration path in the k_ρ complex plane

One powerful method for the evaluation of complex integrals arises from the integral's path independence. More specifically, the result of a complex integration remains unchanged between different integration paths, if they can be related through permissible path deformations.

Primarily, permissible path deformations require either the initial and deformed paths to feature identical end points or that the translated end points can be connected through integral section with negligible contribution. In conjunction to the end point consideration, the residue contributions of any singularities enveloped during the contour path deformation must be separately included in the resulting expression as defined by the Cauchy's theorem.

Employing these considerations, integral deformations to paths which provide faster convergence for the numerical evaluation as well as enable the identification of distinct field contributions related to the spectral singularities, can be implemented. To facilitate subsequent deformations however, it would be convenient to transform the k_ρ integrals of equation (*2.2 b*) into complex integrals along the real axis from negative to positive infinity. The latter is introduced to avoid complications that arise from maintaining the finite end point near the integral's dominant contributions and force the integral's end points to regions where it converges, e.g., at $k_\rho \rightarrow \pm\infty$ on the top Riemann sheet. The desired transformation can be performed through the identity presented below, which relates integrals of Bessel and Hankel functions of the second kind.

$$\int_0^{+\infty} F(k_\rho) J_n(k_\rho \rho) k_\rho dk_\rho = \frac{1}{2}\int_{-\infty}^{+\infty} F(k_\rho) H_n^{(2)}(k_\rho \rho) k_\rho dk_\rho, \qquad (2.3)$$

Introducing (*2.3*) into the integrals of (*2.2 b*) results into infinite complex integral expressions featuring Hankel functions. A comparison between the integration paths in the complex plane of these two formulations is depicted through Figure 2-4.

$$\begin{bmatrix} E_x(\vec{r}) \\ E_y(\vec{r}) \\ E_z(\vec{r}) \end{bmatrix} = \frac{1}{8\pi}\int_{-\infty}^{+\infty} \begin{bmatrix} -\left(\left(v_{TE}^{+}(k_\rho, z_s) + v_{TM}^{+}(k_\rho, z_s)\right) H_0^{(2)}(k_\rho \rho) + \left(v_{TE}^{+}(k_\rho, z_s) - v_{TM}^{+}(k_\rho, z_s)\right) cos(2\varphi)\, H_2^{(2)}(k_\rho \rho)\right) \\ sin(2\varphi)\left(v_{TM}^{+}(k_\rho, z_s) - v_{TE}^{+}(k_\rho, z_s)\right) H_2^{(2)}(k_\rho \rho) \\ -j\frac{2\zeta_d}{k_d} cos(\varphi)\, i_{TM}^{+}(k_\rho, z_s) H_1^{(2)}(k_\rho \rho) k_\rho \end{bmatrix} k_\rho e^{-jk_z z} dk_\rho, \qquad (2.4)$$

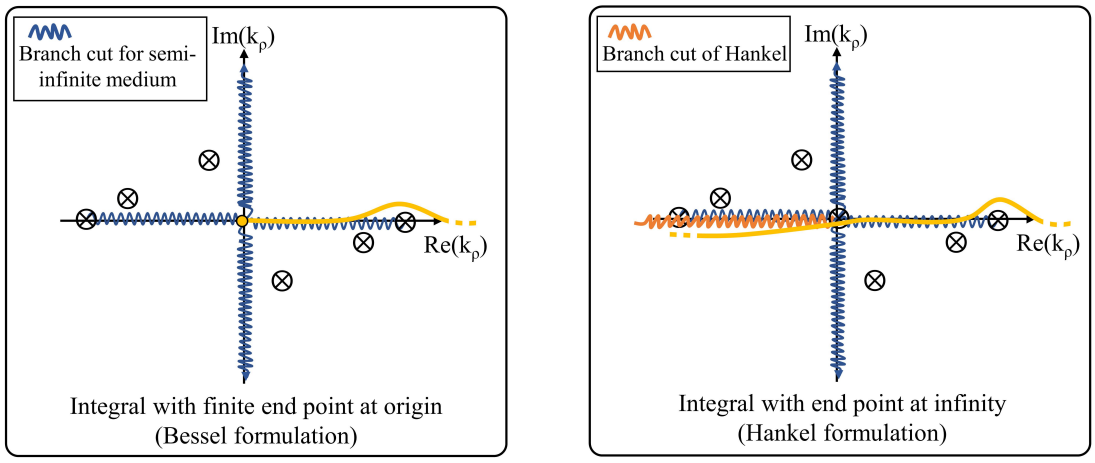

(a) *(b)*

Figure 2-4. Integration path and singularities for the TM integrals of (a) (2.2 b) and (b) (2.4).

One noticeable difference between the integrals of (*2.2 b*) and (*2.4*) refers to the singularities in the k_ρ complex plane. In particular, while the introduction of the Hankel functions of the second kind facilitates the subsequent path deformations, it also introduces a branch point at

the origin, with its respective cut drawn along the real axis towards negative infinity, as showcased through Figure 2-4 *(b)*. As will become apparent in *section 3.2c*, while the branch introduced by the Hankel function is irrelevant for numerical integral evaluations, since none of the implemented deformations envelopes the introduced branch cut, it will have a notable impact in the asymptotic integral evaluation. As such, it is deemed noteworthy to point out that the branch point at the origin is not related to the examined structure, i.e., the Green's function, but is purely attributed to the chosen representation which facilitates the desired path deformations.

2.2d. Saddle point (SP) and Steepest Descent Path (SDP)

Rectilinear (k_ρ) complex plane

Having presented the concept of path deformation, as a next step, the desired integration path must be determined. In order to identify the optimal path both in terms of faster convergence as well as potential field decomposition into wave components, the properties of the integrand's spectrum must first be examined. To facilitate this prospect, an indicative integral will be considered, featuring all the spectral dependencies of the integrals in (*2.4*). Without loss of generality, this integral employs the voltage wave amplitude of the *TE* variant and an n_{th} order Hankel function of the second kind. Considering the spectral dependence of the phase of the large argument approximation for the Hankel function (*2.5 a*), allows for the explicit separation of the phase of the examined integral, as expressed in (*2.5 b*), through the exponential $e^{-j(k_z z + k_\rho \rho)}$. Subsequently, the phase variance can be represented through a function $q(k_\rho)$.

$$H_n^{(2)}(k_\rho \rho) = \sqrt{\frac{2}{\pi k_\rho \rho}} e^{j\frac{\pi}{4}} e^{j\frac{n\pi}{2}} e^{-jk_\rho \rho}, \qquad (2.5\ a)$$

$$\int_{-\infty}^{+\infty} v_{TE}^{+}(k_\rho, z_s) H_n^{(2)}(k_\rho \rho) e^{jk_\rho \rho} k_\rho e^{-j(k_z z + k_\rho \rho)} dk_\rho, \qquad (2.5\ b)$$

$$q(k_\rho) = -j(k_z z + k_\rho \rho), \qquad (2.5\ c)$$

Having explicitly extracted the integrand's phase dependence on k_ρ, the points in the spectrum relating to dominant field contributions can be identified as stationary phase or saddle points of the function $q(k_\rho)$. These points are defined by the vanishing of one or more of the derivatives of $q(k_\rho)$, with the number of vanishing derivatives determining the order of the saddle point (SP). Using the above expression, together with the fact that the integration path remains on the top Riemann sheet (i.e., $I_m(k_z) < 0$), a first order saddle point can be identified for $q(k_\rho)$, as given below.

$$q'(k_{\rho SP}) = 0 \Rightarrow k_{\rho SP} = k_d \sin(\theta) \quad and \quad q''(k_{\rho SP}) \neq 0, \qquad (2.6\ a)$$

Where θ refers to the angle of the observation point ($\vec{r}$) with the z axis. Evidently, this saddle point changes with the observation angle (θ), moving along the real axis of the rectilinear k_ρ spectrum between the origin and k_d.

Given the identification of the integral's dominant contribution as the saddle point, the optimal path in terms of convergence would be the one on which the integrand's magnitude decays the fastest away from this point, such that only the vicinity of the saddle point is relevant. Deriving the expression for the path of fastest convergence begins by investigating the behaviour of $q(k_\rho)$ around its dominant contribution. This process commences by separating the real and imaginary parts of $q(k_\rho)$, as given below, where $k_\rho = x + jy$ with x, y being real numbers.

$$q(x, y) = u(x, y) + jv(x, y), \qquad (2.6\ b)$$

To identify the expression for the path on which the magnitude of the integrand decays the fastest away from the saddle point, one should start by seeking a criterion which defines that $u(x, y)$ and subsequently $e^{u(x,y)}$ change most rapidly. This behaviour of complex functions can be

evaluated through the use of the Cauchy-Riemann equations for the real ($u(x,y)$) and imaginary ($v(x,y)$) parts of $q(k_\rho)$, resulting in the argument that the real part changes the fastest when the imaginary part remains constant and vice versa. In other words, the magnitude of $e^{u(x,y)}$ decays the fastest in constant imaginary part paths, while paths of constant real part result in the most rapid imaginary part variation. Utilizing the above conclusions, the expression for the paths with the fastest amplitude variation passing through the first order saddle point can be derived by identifying the constant imaginary part paths which include the saddle point.

$$Im\left(q(k_\rho)\right) = Im\left(q(k_{\rho SP})\right), \tag{2.7}$$

It should be noted that the above expression defines the paths of fastest magnitude change and as such results into two expressions, indicating the fastest increase and fastest decrease away from the saddle point, namely the Steepest Ascend Path (SAP) and the Steepest Descend Path (SDP). Of course, for the purpose of enhancing the convergence of the numerical integration, the optimal path is the one for which the smallest possible section around its dominant contribution is relevant, i.e., the SDP. For a more detailed discussion regarding the introduction of the Cauchy-Riemann equations and the nature of the spectrum around an n_{th} order saddle point, the reader is referred to *section 4.1b* of [26].

Angular spectrum (β-plane)

Although complete in terms of the theoretical steps required for the derivation of the integral's dominant contributions as well as the path of fastest convergence, the previous discussion does not include any final expressions since the mathematical manipulations involved are more conveniently performed in the angular spectrum. In fact, introducing the complex angle variable β via the transformation given below, the branch pair related to the semi-infinite region is resolved and the subsequent calculations are facilitated.

$$k_\rho = k_d\, sin(\beta) \quad \& \quad k_z = k_d\, cos(\beta), \tag{2.8}$$

In a few words, due to the single valued nature of the above transformation ($sin(\beta)$), both Riemann sheets of the rectilinear spectrum (k_ρ) are mapped into adjacent regions of a single Riemann sheet in the angular spectrum (β). Furthermore, considering the periodic nature of the sine function ($sin(\beta + 2\pi) = sin(\beta)$), multiple values of β correspond to the same value of k_ρ. As a result, the entire k_ρ complex plane is periodically repeated into adjacent sections of width 2π in the angular spectrum. Even so, taking into account the chosen sign for the definition of k_z ($k_z = +k_d cos(\beta)$), the origin of the k_ρ spectrum is mapped into $\beta = 0$ and thus the principal strip is defined around the origin, from $-\pi$ to π. Transforming the indicative integral of (*2.5 b*) into the angular spectrum, its spectral phase dependence, first order saddle point and steepest descent path are expressed below.

$$q(k_d\, sin(\beta)) = q_B(\beta) = -jcos(\beta - \theta), \tag{2.9 a}$$

$$q'_B(\beta_{SP}) = 0 \Rightarrow \beta_{SP} = \theta, \;\; q''_B(\theta) \neq 0, \tag{2.9 b}$$

$$Im\big(q_B(\beta)\big) = Im\big(q_B(\beta_{SP})\big) \Rightarrow \beta_r = \theta \pm cos^{-1}\big(sech(\beta_i)\big), \tag{2.9 c}$$

Where $\boldsymbol{SDP} \rightarrow \beta_r = \theta + sgn(\beta_i)\, cos^{-1}\big(sech(\beta_i)\big)$ and $\boldsymbol{SAP} \rightarrow \beta_r = \theta - sgn(\beta_i)\, cos^{-1}\big(sech(\beta_i)\big)$.

To visualize the discussed nature of the saddle point as well as that of the paths of constant phase, the spectrum of the integrand of (*2.5 b*) will be depicted around the first order saddle point together with the two identified paths through Figure 2-5 *(a)* and *(b)* respectively; both corresponding to an observation point along the z axis ($\theta = 0^o$).

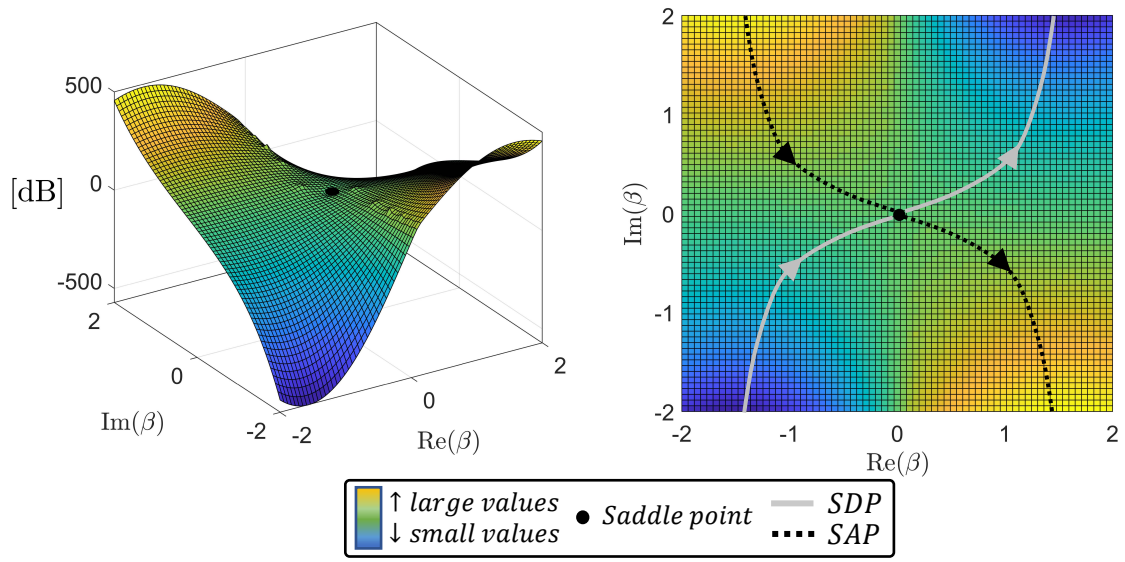

(a) (b)

Figure 2-5. Angular spectrum of integrand of (2.5 b) for observation points along z-axis (ϑ=0º) and z=λ_0. (a) Spectrum's nature around the saddle point (SP) and (b) illustration of the SDP and SAP passing through the SP.

The above definition for the expression of the SDP allows for the exact derivation of the observation angle above which the deformation from the initial integration path to that of steepest descent, envelops each leaky wave polar singularity. This angle, labelled as the shadow boundary angle for the respective leaky wave mode (θ_{SB}), determines the domain of existence of the leaky waves as the outer section of a conical region emanating from the reference system position. Inside this conical section the total field consists only of the space wave and is derived by the SDP integral, while outside it is obtained through the sum of the SDP integral and the respective residue contribution [20]. Assuming that the leaky wave polar singularities ($k_{\rho,LW}$) have been derived through solving for the zeros of the common denominator of the transmission line solution, the observation angle for which the SDP passing through the saddle point crosses a polar singularity (θ_{SB}), is presented below.

$$\theta_{SB} = Re(\beta_{LW}) - sgn\big(Im(\beta_{LW})\big)\, cos^{-1}\Big(sech\big(Im(\beta_{LW})\big)\Big), \qquad (2.10)$$

Where $\beta_{LW} = asin\left(\frac{k_{\rho,LW}}{k_d}\right)$.

Since for angles larger than θ_{SB} the residue contribution of the leaky wave pole must be included in the integral evaluation during the deformation from the initial path to that of the steepest descent, the field expression can be re-written as given below.

$$\vec{E}(\vec{r}) = \vec{E}_{SDP}(\vec{r}) + \sum_{i=1}^{3} U\big(\theta - \theta_{SB,i}\big)\vec{E}_{LW,i}^{TE/TM}(\vec{r}), \qquad (2.11)$$

Where *U(x)* corresponds to the Heaviside step function, $\vec{E}_{SDP}(\vec{r})$ refers to the integral expressions of (*2.4*) evaluated on the SDP path given in (*2.9 c*) and the finite sum of $\vec{E}_{LW,i}^{TE/TM}(\vec{r})$ relates to the residue field contributions of the polar singularities of the significant leaky wave modes, namely TE_1, TM_1 and TM_0. As such, by implementing the above described process, the near field can now be computed through a much faster convergent integral expression ($\vec{E}_{SDP}$) and a finite sum of analytical terms.

One interesting aspect that will be revisited in *section 4.2b* refers to the relative value of the shadow boundary angle when compared to the pointing angle of the respecive mode. In particular, while the shadow boundary angle is larger than the leaky wave pointing angle for all the examined modes, it approaches the latter ($\theta_{SB} \rightarrow \theta_{LW}$) the smaller is the attenuation constant of the respective mode. This can be visualized through Figure 2-6, which illustrates

the dispersion of the impactful leaky wave modes for the structures of Figure 2-1, through their pointing angles (solid-θ_{LW}), shadow boundary angles (dashed-θ_{SB}) and attenuation constants (α_{LW}).

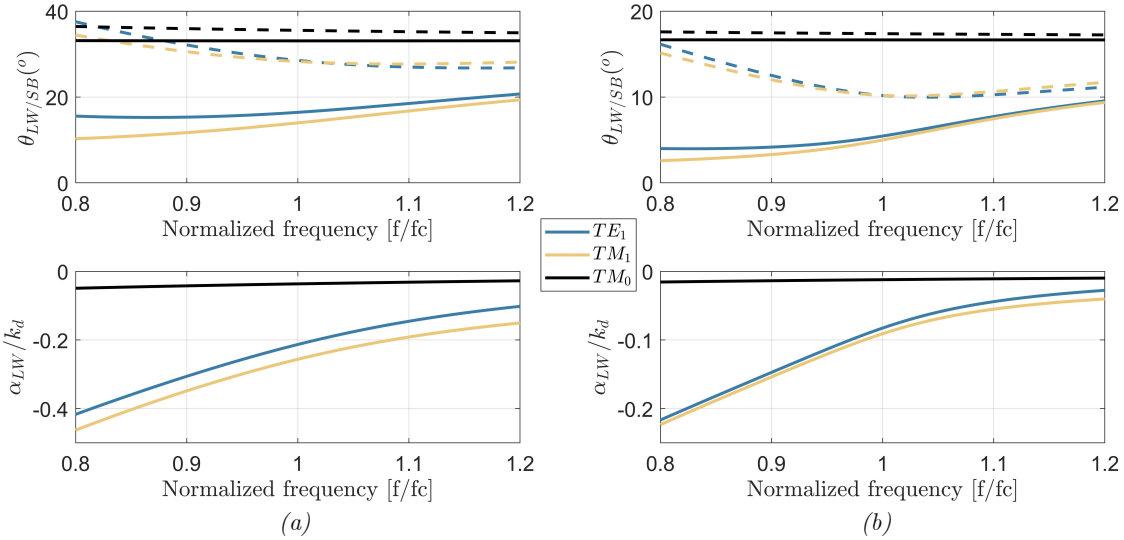

Figure 2-6. Dispersion of dominant leaky wave modes (a) wideband and (b) resonant structure of Figure 2-1. The dashed line on the top figures refers to the shadow boundary angles (θ_{SB}) while the solid lines correspond to the leaky wave pointing angles (θ_{LW}).

As a final note for the illustration of the aforementioned concepts, the initial integration path of (*2.5 b*) as well as the SDP for observation angle equal to the shadow boundary angle of the *TE₁* leaky wave mode are visualized through Figure 2-7 *(a)*, *(b)* in the rectilinear (k_ρ) spectrum and *(c)*, *(d)* in the angular (β) spectrum.

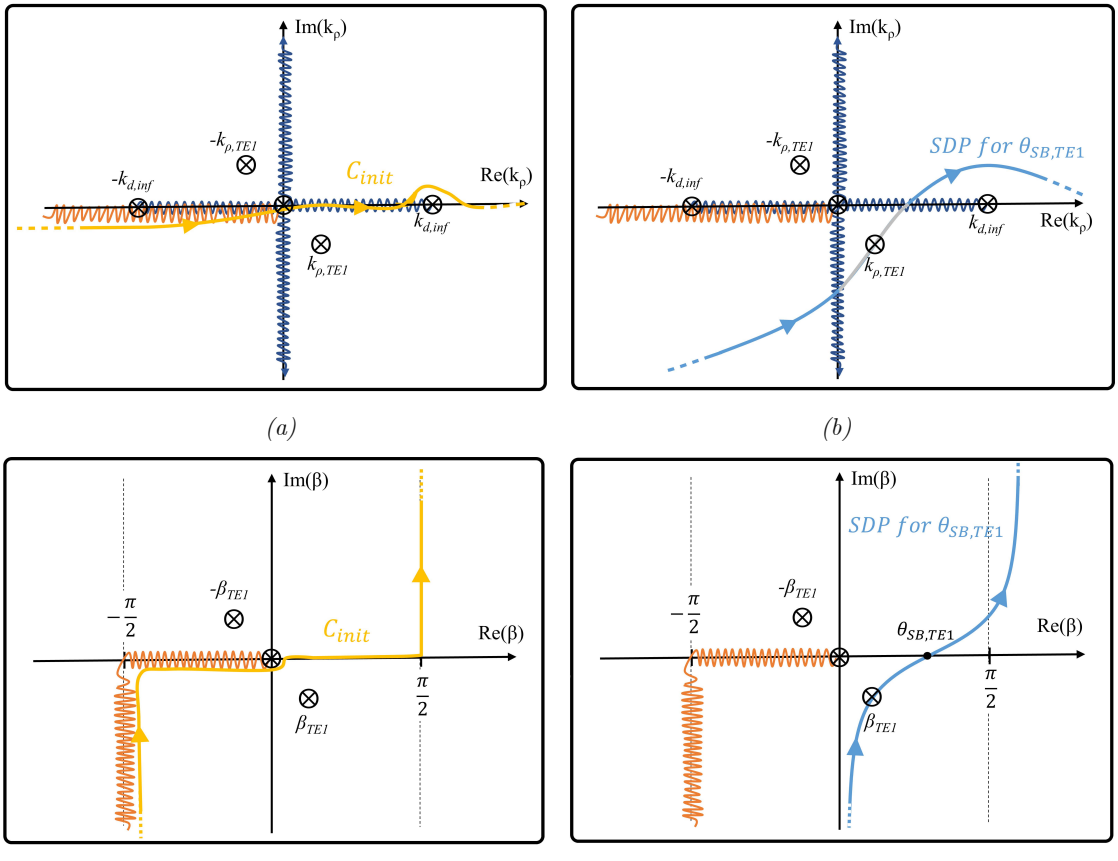

Figure 2-7. Initial and SDP integration paths of (2.5 b): (a),(b) in k_ρ spectrum and (c),(d) in angular spectrum.

To conclude this section, it is worth noting that the transformation to the angular spectrum is a very convenient step for integrals with similar form to that of (*2.4*), since it removes the branch pair at $\pm k_d$, facilitating substantially all the subsequent theoretical manipulations. Consequently, extensive discussions for the angular spectrum transformation can be found in several works, like *section 5.3c* of [26], *section 27* of [32] or *section 3.1* of [33] and their references therein. For the completeness of the current study, a brief discussion describing the mapping from the rectilinear to the angular spectrum will be included through *Appendix C*.

2.2e. Phase center choice

The necessity for a phase centre definition as the point of origin for the phase which minimizes the phase variance over a predefined solid angle, becomes apparent when quasi-optical components are implemented. As a matter of fact, to exploit the canonical properties of the involved geometry (e.g., parabolic reflector, elliptical lens, etc.) the phase origin point of the feeding component must coincide with a geometric point of the introduced structure.

Regarding stratified media capable of supporting leaky waves similar to those of Figure 2-1, the phase centre is not determined by the apertures in the ground plane. Instead, its position depends on the aperture field distribution formed by the leaky waves excited inside the cavity. Employing this concept, it has been shown that for an observation point in the semi-infinite dielectric region, the origin position for the phase appears to be displaced by Δ_z below the ground plane ($\Delta_z>0$) [20], [34]. This displacement of the reference system is illustrated through Figure 2-8 for both the wideband and resonant examined structures.

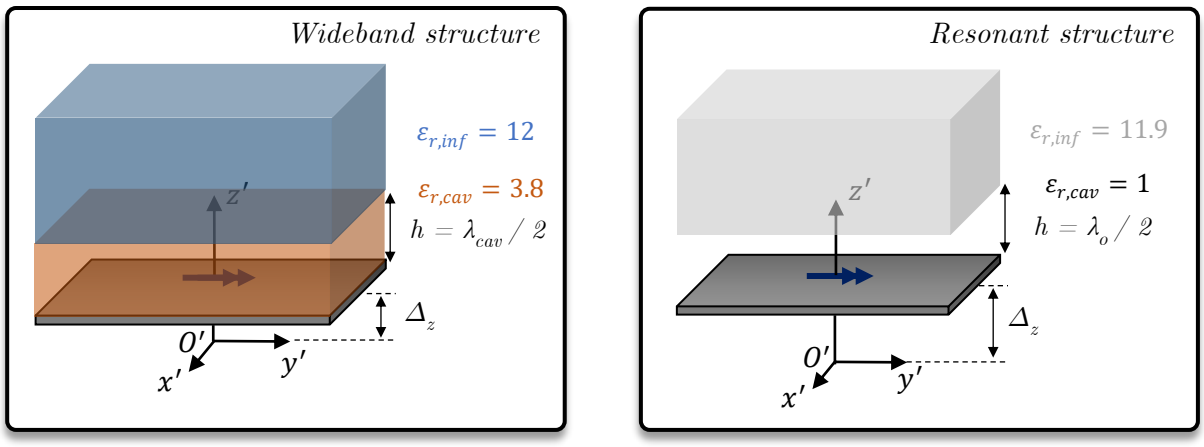

(a) *(b)*

Figure 2-8. Leaky wave structures with specified phase center positions below the ground plane, (a) wideband and (b) resonant case.

This reference system translation in turn modifies the equivalent transmission line model and subsequently impacts the expression of the potential functions in the semi-infinite region, as shown through Figure 2-9 and expressed below.

$$\begin{aligned} &For\ \Delta_z = 0:\ \ v_{TE/TM}(k_\rho, z, z_s = 0) = v^+_{TE/TM}(k_\rho, z_s = 0)e^{-jk_z z} \\ &For\ \Delta_z > 0:\ \ v_{TE/TM}(k_\rho, z', z_s = \Delta_z) = v^+_{TE/TM}(k_\rho, z_s = \Delta_z)e^{-jk_z z'} \end{aligned} \qquad (2.12\ a)$$

The complete derivation of the voltage and current wave amplitudes in the semi-infinite dielectric region for either the initial or the displaced reference systems is presented through *Appendix B*, with the final expressions given in (*B.8*) and (*B.10*). As evident through comparing the resulting expressions, the voltage wave amplitudes for the two structures can be related as follows. The same relation also holds for the current wave amplitudes.

$$v^+_{TE/TM}(k_\rho, z_s = \Delta_z) = v^+_{TE/TM}(k_\rho, z_s = 0)e^{jk_z \Delta_z}, \qquad (2.12\ b)$$

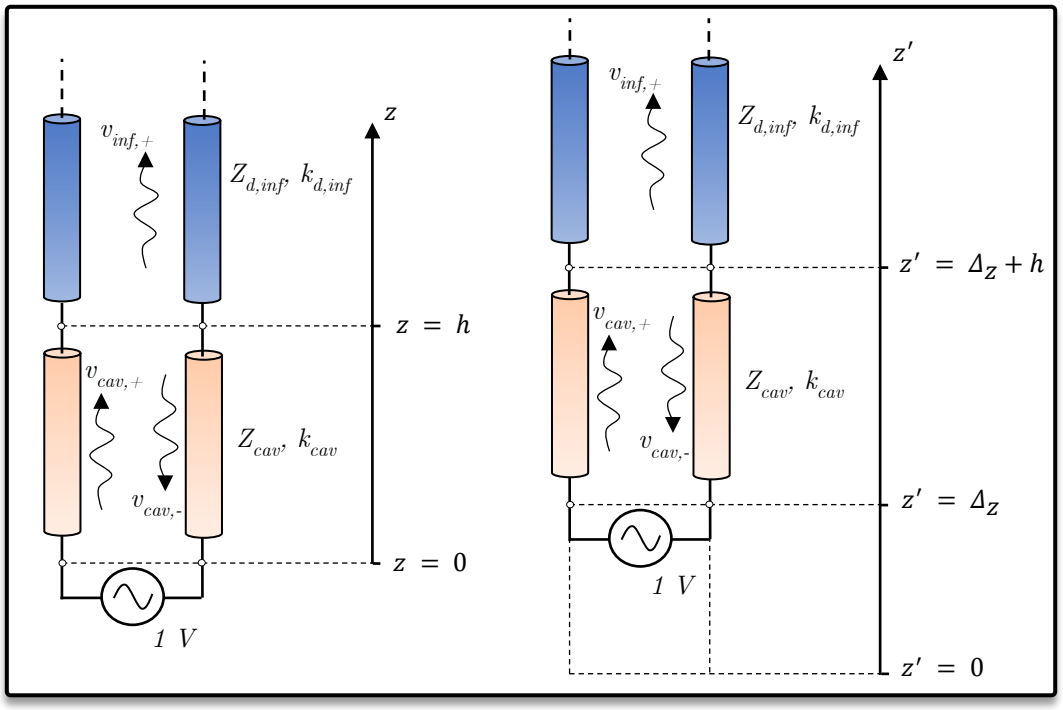

(a) (b)

Figure 2-9. Equivalent transmission line model of leaky wave structure, (a) reference system on the ground plane (Δ_z=0), (b) reference system displaced as in Figure 2-8.

Introducing this reference system displacement to the indicative integral expression that has been treated throughout this chapter *(2.5 b)*, results into the following, where z' corresponds to the displaced reference system of Figure 2-9 *(b)*.

$$\int_{-\infty}^{+\infty} v_{TE}^{+}(k_\rho, \Delta_z) H_n^{(2)}(k_\rho \rho) e^{jk_\rho \rho} k_\rho e^{-j(k_z z' + k_\rho \rho)} dk_\rho, \qquad (2.13)$$

Having presented the impact of displacing the reference system on the wave amplitudes and the near field integral formulation, the following section will elaborate on one of the most useful aspects of the above discussed reference system choice, that of identifying wave components in the near field. It should be noted that for the remaining of this document, prime notation in spatial variables, namely r' and θ', would signify that they refer to the displaced reference system below the ground plane.

2.3. Near field spherical wave formation

As shown in [20], choosing the phase center displacement such that it minimizes the phase variance of the wave amplitudes up to the smallest shadow boundary angle, enables the identification of the total field as a spherical wave up the aforementioned angle, even in the near field of the leaky wave structure. More specifically, utilizing the approximation for the phase of the co polarized component of a leaky wave structure extracted in [34], the phase center choice introduced in [20] is presented below.

$$\frac{\Delta_z^{TM/TE}}{\lambda_o} = \frac{atan\left(\frac{sin^2(\theta_{SB}^{TM/TE})}{2\left(a_{LW}^{TM/TE}\right)^2}\right)}{2\pi\sqrt{\varepsilon_r}\left(1-cos\left(\theta_{SB}^{TM/TE}\right)\right)} \quad and \quad \Delta_z = \frac{\Delta_z^{TM_1} + \Delta_z^{TE_1}}{2}, \qquad (2.14)$$

Using the above phase centre definition, the initial and corrected phase variance of the *TE* and *TM* voltage wave amplitudes in the semi-infinite region of the resonant and wideband examined structures, are illustrated through Figure 2-10 *(a)*, *(b)* and *(c)*, *(d)* respectively.

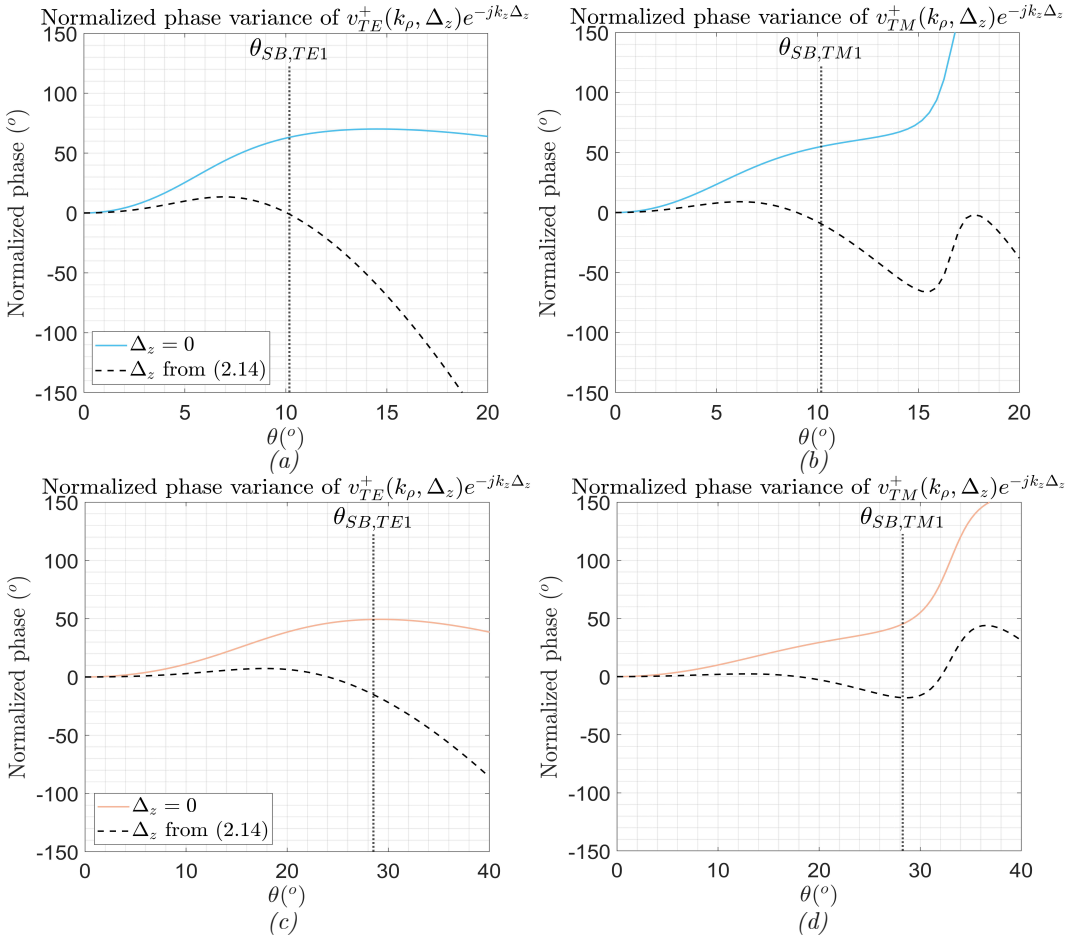

Figure 2-10. Phase variance of TE and TM voltage wave amplitudes (v_{TE}^{+} and v_{TM}^{+}) in the semi-infinite regions of the (a), (b) resonant and (c), (d) wideband structure of Figure 2-1.

The actual phase centre displacements below the ground plane ($\Delta_z>0$) for the examined structures resulting from expression (*2.14*), are given through Table 2-I in terms of the free-space wavelength of the central frequency (*150 GHz*).

Phase center displacement	**Wideband structure**	**Resonant structure**
Δ_z	$0.42\lambda_0$	$3.2\lambda_0$

Table 2-I. Phase center displacement at central frequency (150 GHz).

For the purpose of showcasing the spherical wave formation described above, the near field will be evaluated in spherical observation grids of different radii from the phase centre of the leaky wave structures. The evaluation of the near field is performed through the SDP numerical integration (*2.11*), where the reference system of the involved integrals is displaced below the ground plane as indicatively given in (*2.13*). In particular, the magnitude and phase of the co polarized component as well as the angle of the Poynting vector with the z axis will be examined. Regarding the Poynting vector angle, its derivation is performed as follows. It should be reminded that prime notation in spatial variables (i.e., r' and θ') indicates that they refer to the reference system translated below the ground plane.

$$\theta_{Poy}(\vec{r}') = acos\left(\hat{P}_{act}(\vec{r}')\cdot\hat{z}\right) = acos\left(\frac{\vec{P}_{act}(\vec{r}')}{|\vec{P}_{act}(\vec{r}')|}\cdot\hat{z}\right), \tag{2.15}$$

Where $\vec{P}_{act}(\vec{r}') = \frac{1}{2}Re\left(\vec{E}(\vec{r}')\times\vec{H}^{*}(\vec{r}')\right) = \frac{1}{2}Re\left(\begin{vmatrix}\hat{x} & \hat{y} & \hat{z}\\ E_x(\vec{r}') & E_y(\vec{r}') & E_z(\vec{r}')\\ H_x^{*}(\vec{r}') & H_y^{*}(\vec{r}') & H_z^{*}(\vec{r}')\end{vmatrix}\right)$.

The steps required for the derivation of the magnetic field, which is necessary for the evaluation of the Poynting vector, are identical to those presented in the previous chapter for the electric field and can be found in *Appendix D*. The only difference between the two cases arises from the expressions of the respective Green's functions ($\bar{\bar{G}}^{em}$ and $\bar{\bar{G}}^{hm}$). Having said the above, the resulting plots for the wideband structure are illustrated through Figure 2-11, with the co polarized component obtained using the Ludwig 3 definition.

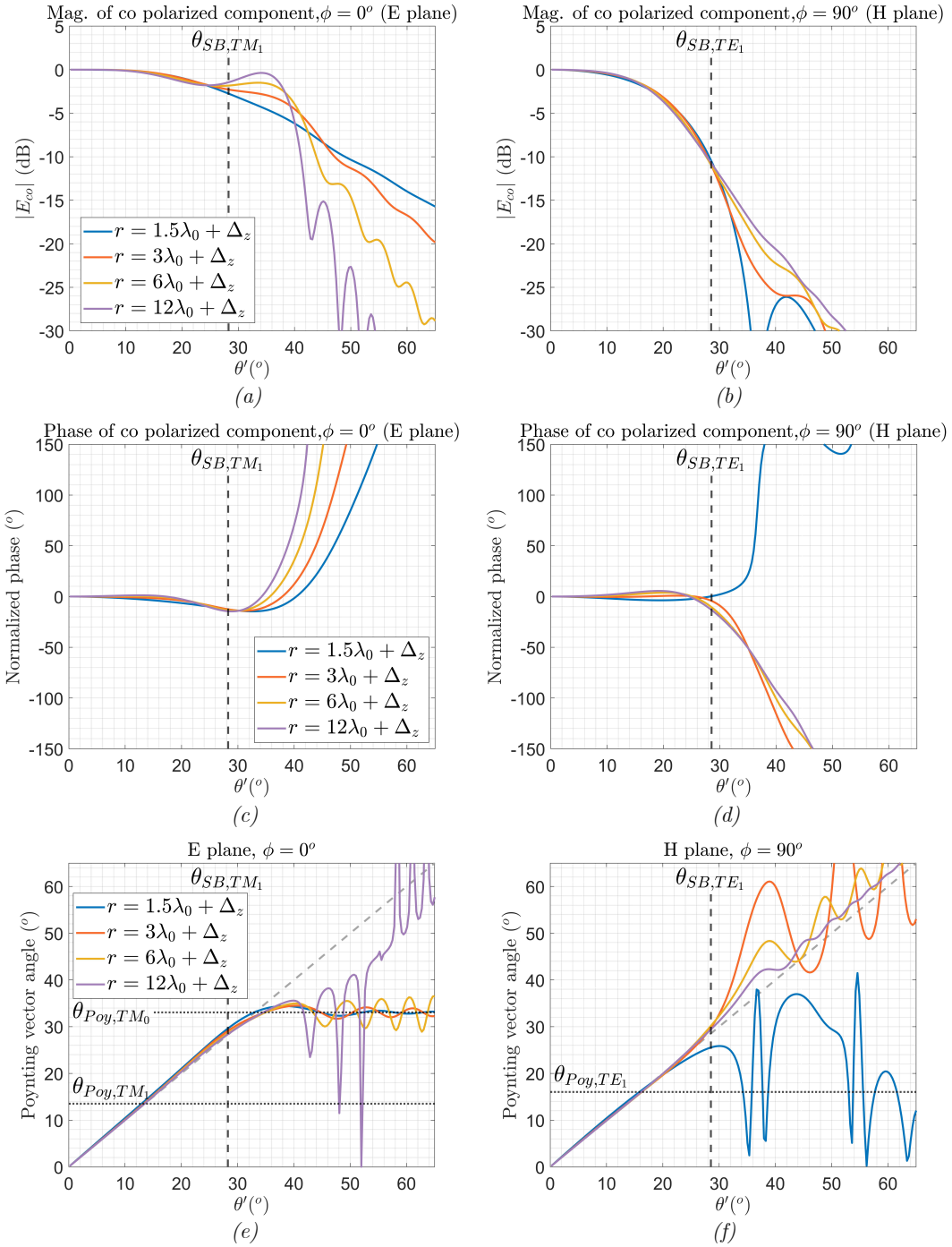

Figure 2-11. Co polarized component over observation sphere from the phase center of the wideband structure. Magnitude (a) E-plane and (b) H-plane. Phase variance (c) E-plane and (d) H-plane. Angle of Poynting vector with z axis (e) E-plane and (f) H-plane.

As evident from Figure 2-11 *(a)* and *(b)*, the shape of the pattern close to the source varies noticeably with distance for $\theta' > \theta_{SB}$, but is almost independent of the distance from the source

below the shadow boundary angle ($\theta' < \theta_{SB}$). Considering the presence of the TM_0 for the examined elementary source and its strong impact in the E-plane (around 35^o), the above is more evident in the H-plane. Together with the almost constant phase of the total field for $\theta' < \theta_{SB}$ even for spherical observation grids very close to the source, as seen through Figure 2-11 *(c)* and *(d)*, this means that the field within this solid angle ($\theta' < \theta_{SB}$) can be considered as a spherical wave [20].

To further illustrate the concept of the near field spherical wave formation, one can compare the Poynting vector angle of the total field in the main planes with the geometrical angle seen from the phase centre (dashed grey line), as shown through Figure 2-11 *(e)* and *(f)*. While for observation angles smaller than the shadow boundary the Poynting vector angle and the geometrical angle converge, beyond this point the near field is quite more complicated, since it is significantly influenced by the residue polar contributions. The only clear trend can be seen in the E-plane, where the strongly excited TM_0 dominates the near field above its shadow boundary ($\theta_{SB}^{TM_0}$), as visualized through Figure 2-11 *(e)*. The Poynting vector angles of the leaky waves, labelled as $\theta_{Poy}^{TE_1/TM_1/TM_0}$ in the figures, refer to the angles between the Poynting vector of the residue contributions and the z-axis, as given in *Appendix D*.

To conclude this discussion regarding the spherical wave formulation in the near field of a leaky wave structure, it is worth pointing out the difference between the resonant and wideband structures. In particular, while the same deductions can be made through Figure 2-12 *(a)-(f)* which correspond to the resonant structure, it can be observed that the higher the directivity of the structure, i.e., the more resonant the leaky wave stratification is, the furthest from the source this formation of a spherical wave occurs. This observation can be more easily visualized through the comparison of the Poynting vector angles shown through Figure 2-11 and Figure 2-12 *(e)-(f)*. This notion relating the directivity of the structure to the radial distance for which this near field spherical wave formation can be assumed, will be revisited in following sections due to its importance in determining the applicability region of the asymptotic approach.

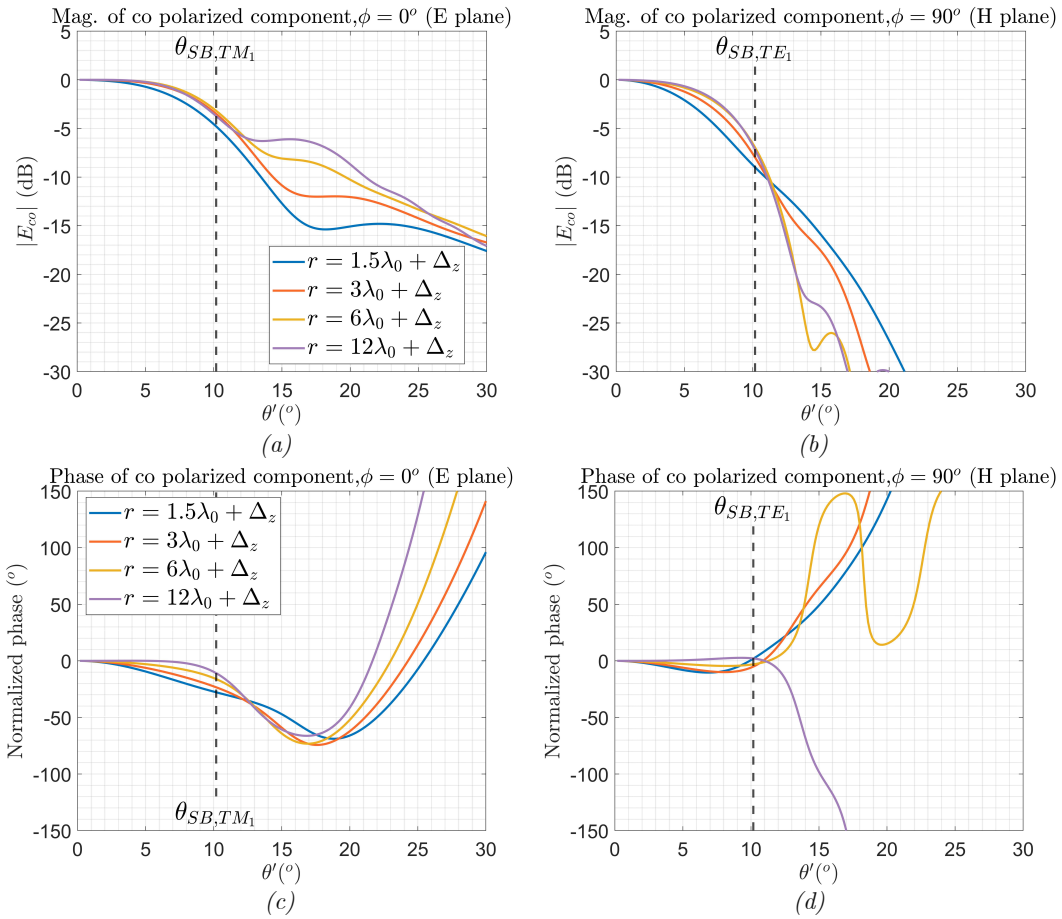

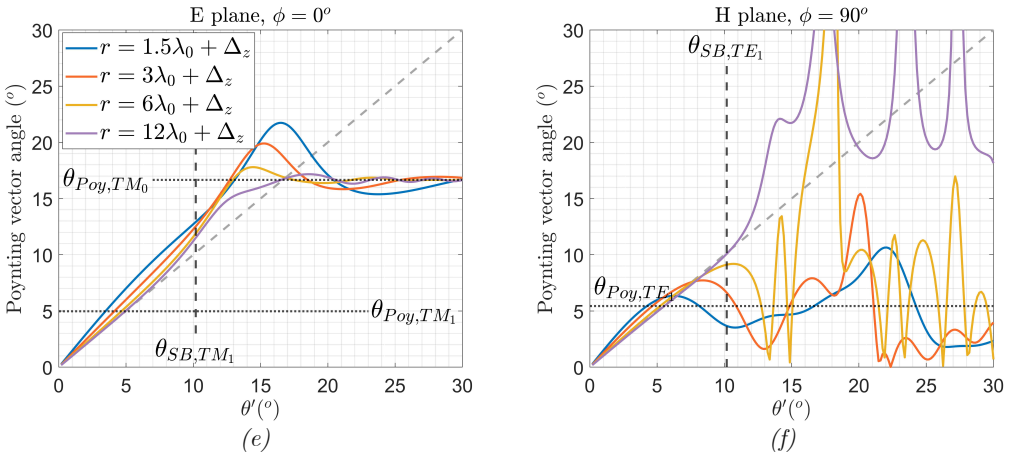

Figure 2-12. Co polarized component over observation sphere from the phase center of the resonant structure. Magnitude (a) E-plane and (b) H-plane. Phase variance (c) E-plane and (d) H-plane. Angle of Poynting vector with z axis (e) E-plane and (f) H-plane.

2.3a. Field decomposition

Having elaborated on the concept of the near field spherical wave formation enabled through the appropriate choice of phase centre, one final aspect that needs to be discussed prior to the introduction of the asymptotic techniques refers to the field decomposition provided by the SDP integration approach. In particular, as already discussed in previous sections, the definition of the observation angle for which each leaky wave polar singularity is captured during the deformation from the initial integration path to that of steepest descent (shadow boundary angle θ_{SB}), determines the region of existence of the leaky waves. More specifically, this angle defines a conical section for each leaky wave mode, emanating from the phase centre. While inside this cone the leaky wave does not exist and the total field is comprised of only the SDP integral; outside, the residue contribution of the polar singularity must be added to the SDP integral in order to obtain the total field. In fact, for strong residues, i.e., small attenuation constant for the mode in question and observation grids close to the source, the total field outside this cone can be dominated by the leaky wave [20]. To visualize the aforementioned nature of the field, a three-dimensional illustration of an indicative leaky wave geometry is presented in Figure 2-13, showing this conical region defined from the phase centre.

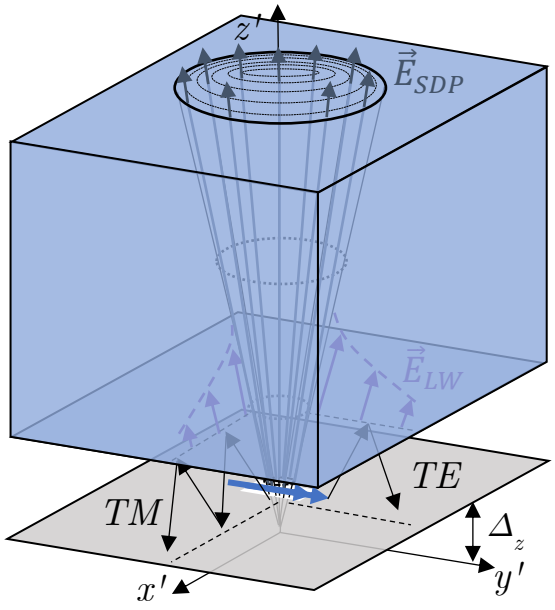

Figure 2-13. 3D view of leaky wave structure indicating the conical region emanating from the phase center which limits the domain of existence for the leaky wave.

Since the residue field contributions must be added only above the respective shadow boundary angles, in order to form a continuous total field, the SDP integral contribution must be discontinuous at the shadow boundaries with the exact level of said discontinuity accounted for by the respective residue contribution. This concept can be visualized through evaluating the co polarized component in the two main planes, as indicatively shown for the wideband structure through Figure 2-14 and Figure 2-15.

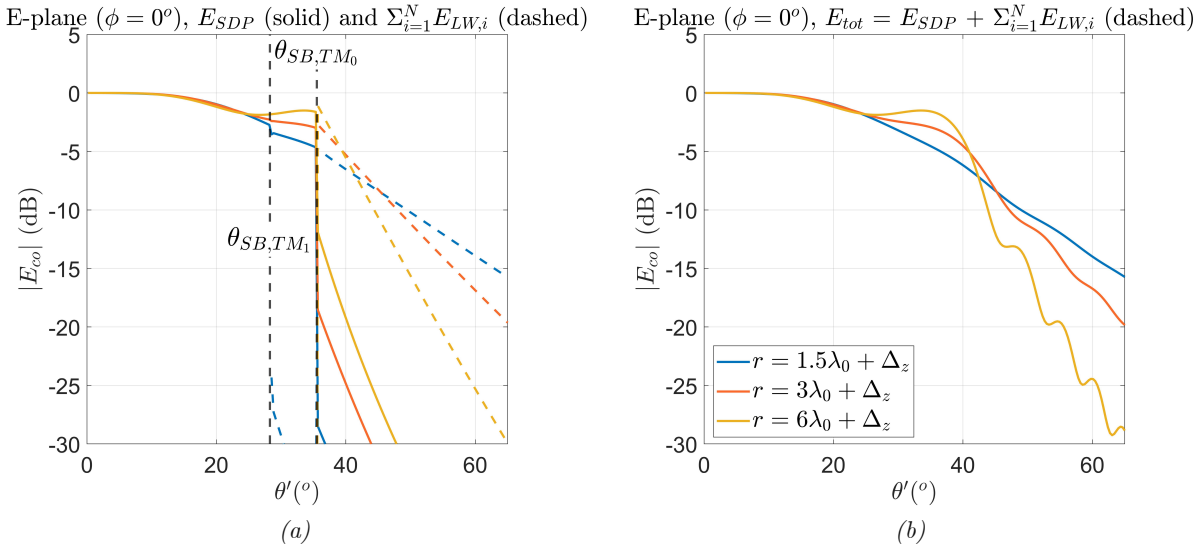

Figure 2-14. E-plane of co polar component, (a) decomposed, with the solid line referring to the SDP integral while the dashed to the polar residues and (b) total field (E_{SDP}+E_{LW}).

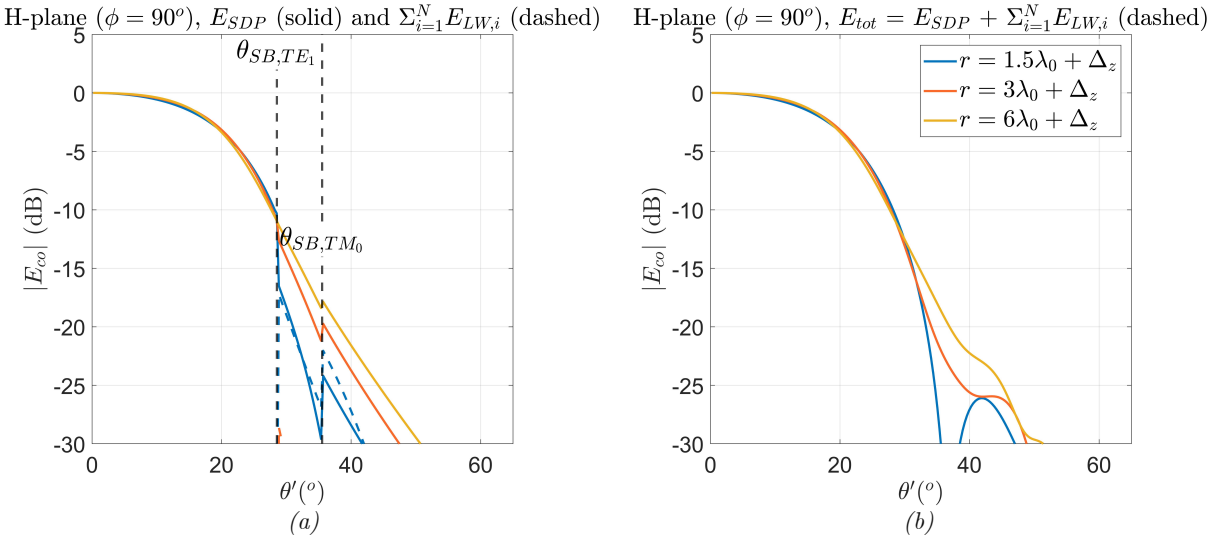

Figure 2-15. H-plane of co polar component, (a) decomposed, with the solid line referring to the SDP integral while the dashed to the polar residues and (b) total field (E_{SDP}+E_{LW}).

Apart from the discontinuous SDP integral at the shadow boundary angles, another important note that can be deduced from the above figures refers to the level of the residues, which decays rapidly as the observation point moves away from the source. In addition, given the relatively large attenuation constants of the main leaky wave mode pair (TM_1 and TE_1), their residue contributions do not dominate the total field above their respective shadow boundary angles, where the latter is comprised by the summation of the SDP integral and the residue. This of course is not the case for the TM_0 in its dominant plane, as can be visualized for $\theta' > \theta_{SB}^{TM_0}$ in Figure 2-14, due to its small attenuation constant. Another aspect of the leaky wave contributions visualized through the figures above, refers to the impact of each mode in its non-dominant (orthogonal) plane, i.e., E-plane for the TE and H-plane for the TM modes.

While far from the source the impact of the *TM* and *TE* leaky wave modes can be isolated in their respective dominant planes, i.e., E and H planes, the same cannot be said for observation points very close to the leaky wave cavity. Even so, for their impact to be noticeable in the orthogonal plane, a strongly excited leaky wave is needed (small α_{LW}). As such, for the present structure this occurs for observation grids very close to the source and only for the TM_0, as evident through the discontinuity at $\theta_{SB}^{TM_0}$ in Figure 2-15. Finally, even though both figures presented above correspond to the wideband structure, similar deductions can also be made for the resonant case.

Having allocated a big part of the above discussion on the insight for the nature of the near field provided by the SDP integration approach and the phase center choice, one aspect that has been only briefly discussed refers to the convergence of the near field integrals involved. This aspect is attributed to the exploitation of the integrands' spectral properties, as described through *section 2.2d*. In fact, through decomposition the field as given in (*2.11*), the near field can be derived through a number of fast converging integrals ($\vec{E}_{SDP}$) and a finite sum of analytical terms, resulting to its evaluation requiring a fraction of the time necessary for the integration of the initial expressions (*2.4*) over the real axis in the k_ρ complex plane. To showcase the latter, an indicative timing comparison has been performed for the nearest examined spherical grid, i.e., $r' = 1.5\lambda_o + \Delta_z$, and a mesh of *361* φ and *140* θ points. As indicated through Table 2-II, while the adaptive quadrature integration requires *9 minutes* for the k_ρ integrals over the real axis, the SDP is nine times faster.

Evaluation method	**Numerical** (integration path of Figure 2-4 b)	**Numerical** (SDP)
Time required	*9 min*	*1 min*

Table 2-II. Timing comparison between integration on k_ρ through the path shown in Figure 2-4 (b) and integration on the path of steepest descent.

CHAPTER 3. ASYMPTOTIC TECHNIQUES

To give an overview of the numerical field evaluation techniques showcased in the previous chapter, simple methods like the integration over the real axis of the rectilinear spectrum (k_ρ) have the advantage of versatility since they can be applied directly without consideration for the specific properties of either the integrand or the examined structure but do suffer in terms of computational time. Taking this into account, significant improvement in the computation efficiency can be achieved through exploiting the integrand's spectral properties and implementing the SDP method of integration described in *section 2.2d*. Having said that, the ideal scenario one could consider would be to replace each complex integral expression with a finite number of analytical terms. In this manner, the need for any spectral integration would be mitigated and thus the computational efficiency would be enhanced even further. This process of evaluating complex integrals through a finite number of analytical terms is essentially referred to as asymptotic approximation.

Arguably the simplest and most common method to asymptotically evaluate radiation integrals is the stationary phase point (SPP) approximation, which can be used to derive the far field of a radiating structure. In this case, given the consideration for an observation point far away from the source, the integrand's phase term oscillates very fast on the integration path compared to the much slower varying amplitude. This behaviour enables the evaluation of the slow varying amplitude at the stationary phase point (saddle point) and the subsequent closing of the remaining integral analytically. A thorough discussion regarding the SPP approximation and the derivation of the far field of a leaky wave structure similar to those of Figure 2-1, can be found in *Appendix F*.

Having introduced the concept of asymptotic approximation for complex integrals as well as an example for the case of the far field, the following chapter will elaborate on an asymptotic evaluation method that can also be applied for the near field of a leaky wave structure. Aiming for the cleanest asymptotic approach in the sense of requiring the smallest number of terms, the field decomposition introduced by the steepest descent path method will be exploited, essentially targeting the asymptotic evaluation of the SDP integrals ($\vec{E}_{SDP}$). Apart from its capability of enhancing the computational efficiency of the near field evaluation, the potential of extracting further insight into the wave phenomena which drive the radiation process through the asymptotic near field evaluation will also be explored.

3.1. General considerations

Integral representations play a fundamental role in spectral analysis, with the choice of representation enabling different approaches for the evaluation of the complex integrals involved. One indicative example of this concept has already been presented through the background *section 2.2c*. In particular, introducing the Hankel function of the second kind in the field representation, made it possible to resort to contour deformations, leading to the identification of the fastest convergence path and the subsequent field decomposition into the SDP integral and residue polar contributions. The price for enabling this approach though, is the introduction of the branch point at the origin of the complex plane and its respective cut, as depicted through Figure 2-4 *(b)*. In turn, this singularity introduces notable complications in the following asymptotic approach.

To begin approaching the asymptotic approximation of the near field integral expressions, first the field decomposition resulting from the SDP integration approach will be re-written below for clarity. The prime notation in the spatial variables (r', θ'), indicates that they refer to the displaced reference system of Figure 2-8.

$$\vec{E}(\vec{r}') = \vec{E}_{SDP}(\vec{r}') + \sum_{i=1}^{3} U\big(\theta' - \theta_{SB,i}\big)\vec{E}_{LW,i}^{TE/TM}(\vec{r}'), \qquad (3.1)$$

Taking into consideration the above decomposition, the derivation of the field in the semi-infinite region of a leaky wave structure can be reduced to the evaluation of the following integral expressions, evaluated on the path of steepest descent in the complex plane *(2.9 c)*.

$$\begin{bmatrix} E_{x,SDP}(\vec{r}') \\ E_{y,SDP}(\vec{r}') \\ E_{z,SDP}(\vec{r}') \end{bmatrix} = \frac{1}{8\pi} \int_{SDP} \begin{bmatrix} -\left(\left(v_{TE}^{+}(k_\rho, \Delta_z) + v_{TM}^{+}(k_\rho, \Delta_z)\right) H_0^{(2)}(k_\rho \rho) + \left(v_{TE}^{+}(k_\rho, \Delta_z) - v_{TM}^{+}(k_\rho, \Delta_z)\right) cos(2\varphi)\, H_2^{(2)}(k_\rho \rho)\right) \\ sin(2\varphi)\left(v_{TM}^{+}(k_\rho, \Delta_z) - v_{TE}^{+}(k_\rho, \Delta_z)\right) H_2^{(2)}(k_\rho \rho) \\ -j\frac{2\zeta_d}{k_d} cos(\varphi)\, i_{TM}^{+}(k_\rho, \Delta_z) H_1^{(2)}(k_\rho \rho) k_\rho \end{bmatrix} k_\rho e^{-jk_z z'} dk_\rho, \qquad (3.2)$$

Where the reference system displacement (Δ_z) is chosen as defined through *section 2.3*.

Similar to the previous section, in order to facilitate all the subsequent mathematic manipulations involved, an indicative integral will be treated instead of the complete expressions. As evident through (*3.2*), if a term-by-term integration is employed, all the SDP integrals consist of a Hankel function of the second kind of n_{th} order (with $n = 0, 1$ or 2) and a voltage or current wave amplitude (either *TE* or *TM*) multiplied by a power of k_ρ. As such, it will suffice within the present context to focus on the asymptotic evaluation of an integral of the type presented below, in terms of the rectilinear (k_ρ) as well as the angular (β) spectrum. Without loss of generality, the indicative integral examined features the *TE* voltage wave amplitude.

$$\int_{SDP} v_{TE}^{+}(k_\rho, \Delta_z) H_n^{(2)}(k_\rho \rho) e^{jk_\rho \rho} k_\rho e^{-j(k_z z' + k_\rho \rho)} dk_\rho, \qquad (3.3\ a)$$

$$\int_{SDP} v_{TE}^{+}(k_d\, sin(\beta), \Delta_z) H_n^{(2)}(k_d \rho\, sin(\beta)) e^{jk_d \rho\, sin(\beta)} k_d^2\, sin(\beta)\, cos(\beta)\, e^{k_d r' q_B(\beta)} d\beta, \qquad (3.3\ b)$$

Where $q_B(\beta) = -jcos(\beta - \theta')$.

At first glance, the above presented integral representations seem unable to be closed in an analytical manner. However, depending on the employed representation, certain manipulations can be introduced to transform the integrand into a function with similar properties but a simpler structure, which can be evaluated asymptotically through canonical integrals, many times also labelled as comparison integrals. This concept roughly constitutes the basis of the asymptotic approximation of complex integrals, where the targeted canonical form depends on the implemented representation. While potentially insightful in terms of field decomposition and beneficial in computational efficiency, transforming the integrands into canonical forms introduces certain limitations for the accuracy and applicability region of the resulting representation, requiring in turn additional considerations prior to the implementation of any asymptotic approximation.

Having elaborated on the dominant contributions of the examined integrals through *section 2.2d* ($k_{\rho SP} = k_d \sin(\theta')$ and $\beta_{SP} = \theta'$), as well as the deformation to the path of steepest descend that includes the latter, it is suggestive to approximate the SDP integrals only by the path section in the vicinity of the saddle point, since the contribution from the remainder of the path will be exponentially small in comparison. Considering the outline of all asymptotic approximations as introduced above, our purpose is to transform the integrand of (*3.3*) into a canonical form which describes in the simplest fashion the relevant behaviour around the saddle point. The first step of this process is the transformation from the angular spectrum (β) to the *s*-plane, which will be the topic of discussion in the following subsection.

3.1a. Transformation to the s-plane

Since only the vicinity of the saddle point traversed by the steepest descent path is relevant, it is unnecessary to deal completely with the exponent function $q_B(\beta)$. Instead, the latter is replaced by another function that describes in the simplest manner the relevant saddle-point

arrangement around $\beta_{SP} = \theta'$. This transformation will be phrased in terms of a new complex variable s, with the simplest function describing an isolated first order saddle point being the following polynomial $\tau(s)$.

$$q_B(\beta) = \tau(s) = c - s^2, \qquad (3.4\ a)$$

The constant c in the above expression is most conveniently chosen such that the saddle point is mapped in the origin of the s complex plane, that is when c is set equal to $q_B(\beta_{SP})$.

$$q_B(\beta) = -j - s^2, \qquad (3.4\ b)$$

Introducing the s-plane transformation to the test case integral of (*3.3 b*), results into the following integral expression.

$$\int_{SDP} F_B(\beta) e^{k_d r' q_B(\beta)} d\beta = e^{-jk_d r'} \int_{SDP} F_B(\beta) \frac{d\beta}{ds} e^{-k_d r' s^2} ds = e^{-jk_d r'} \int_{SDP} G(s) e^{-\Omega s^2} ds, \qquad (3.5)$$

Where $F_B(\beta) = v_{TE}^{+}(k_d\, sin(\beta), \Delta_z) H_n^{(2)}(k_d \rho\, sin(\beta)) e^{jk_d \rho\, sin(\beta)} k_d^2\, sin(\beta)\, cos(\beta)$, $G(s) = F_B(\beta) \frac{d\beta}{ds}$ and $\Omega = k_d r'$.

In order to facilitate the subsequent mathematical manipulations, the integrand excluding the exponential phase terms is defined in terms of a function $F_B(\beta)$ for the integral on the β plane and a function $G(s)$ for that on the s plane. Furthermore, while unnecessary for any step of the following asymptotic approach, defining the parameter Ω in the principal exponential of the integrand of (*3.5*) will enable an interesting discussion regarding the fundamental consideration for the asymptotic evaluation of complex integrals.

Having mapped the neighbourhood of the first order saddle point around the origin of the s-plane through the choice of constant in the transformation (*3.4*), the new integration path can now be considered. Given the phase dependence of the final integral in (*3.5*), the paths of constant imaginary part for the exponent can be identified in a simple manner as the real and imaginary axes of the s-plane. Moreover, since Ω is real and positive (assuming lossless dielectrics, i.e., k_d real), the distinction between the paths of fastest descent and ascent away from the origin is straightforward, corresponding to the real and imaginary axis respectively, with the *45°* and *135°* diagonals constituting the boundaries which divide the valley and mountain spectral regions. The above discussed nature of the spectrum in the s-plane is visualized through Figure 3-1 *(a)* and *(b)*, corresponding to the spectrum of the integrand of (*3.5*). Considering the range of the s-plane illustrated in the figures, what dominates the integrand's behavior is the exponent, namely $e^{-\Omega s^2}$.

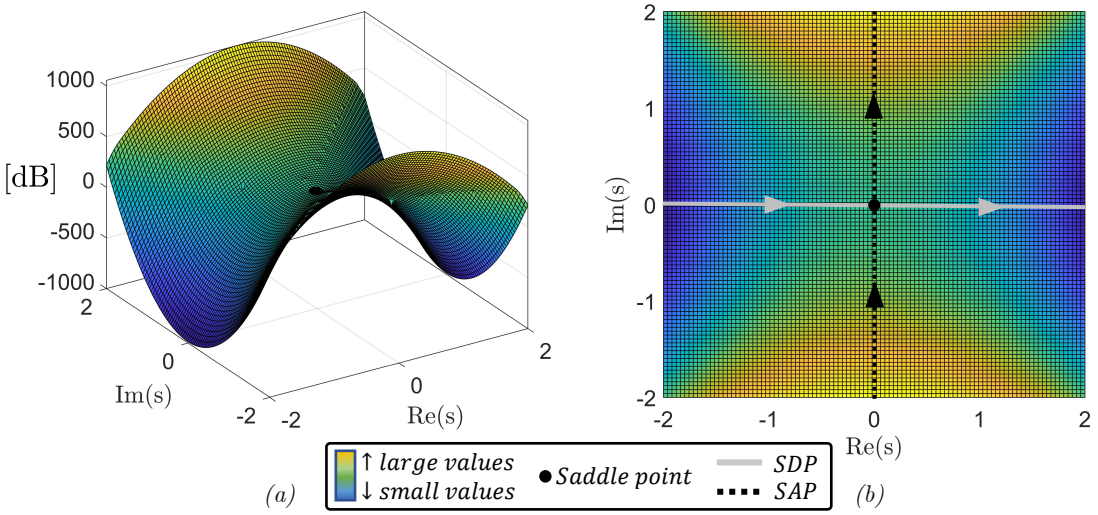

Figure 3-1. s-plane spectrum of integrand of (3.5). (a) Saddle point depiction and (b) Steepest Descent Path (SDP) - Steepest Ascent Path (SAP).

It should be mentioned that the Jacobian transform ($d\beta/ds$) incorporated in the definition of $G(s)$, does introduce additional critical points to the integral in question in the form of algebraic branch points. These singularities arise from all the other saddle points in the angular spectrum, apart from the one at $\beta_{SP} = \theta'$. More specifically, given the periodicity of the angular spectrum, $q'_B(\beta) = 0$ results in a multitude of saddle points at $\theta' \pm n\pi$ for n integer. While the choice of principal strip did define the operating saddle point as $\beta_{SP} = \theta'$, all other saddle points become branch points through the s-plane transformation. An extensive discussion for this argument can be found in *section 3.13* of [33]. Even if introducing additional critical points might seem worrisome, they are mapped far enough from the origin such that they do now impact the neighborhood of the saddle point and can thus be neglected.

Another aspect that should be discussed regarding the s-plane transformation, refers to the sign ambiguity introduced by the latter. In particular, given the multi-valued nature of the transformation presented in (*3.4*), the sign of the Jacobian transform ($d\beta/ds$) must be chosen such that $d\beta$ and ds denote elementary sections of the SDP in the respective complex planes. As a result, since at the saddle point the SDP in the angular spectrum forms a 45^o angle with the real axis (for $\beta_{SP} = \theta'$, $\measuredangle d\beta = 45^o$), as showcased through Figure 2-5, while in the s-plane the SDP always remains on top of the real axis (for $s_{SP} = 0$, $\measuredangle ds = 0^o$), the Jacobian transform must be defined as follows.

$$(3.4\ b) \Rightarrow \frac{d\beta}{ds} = \pm \frac{\sqrt{2j}}{\sqrt{1-j\frac{s^2}{2}}} \xrightarrow{\measuredangle\left(\frac{d\beta}{ds}\right)=45^o \ at\ s=0} \frac{d\beta}{ds} = \frac{\sqrt{2j}}{\sqrt{1-j\frac{s^2}{2}}}, \tag{3.6}$$

One fundamental difference between the s-plane and the angular (β) or rectilinear (k_ρ) spectrums which remains yet undiscussed, refers to the behavior of the spectral singularities for different observation points. Even so, to facilitate the understanding of the asymptotic approach, the presence of singularities in the integral will be neglected until *section 3.2b*, considering for the time being an isolated saddle point.

3.1b. Isolated Saddle Point

The transformation of the SDP integral passing through the first order saddle point to the s-plane, forms a Gaussian type phase ($e^{-\Omega s^2}$) in the integrand, which essentially filters the amplitude of the spectral content around the saddle point. While this integral formulation showcases once more that only the vicinity of the saddle point is relevant, it arguably introduces an even more important concept. Namely, it is the value of the real and positive parameter Ω which determines the sharpness of the filtering introduced by the exponent and thus the region around the saddle point that features noteworthy contribution. Having said the above, the process of asymptotically approximating complex integrals of forms similar to that of (*3.5*) is usually based on the presence of a large parameter in the exponential behaviour of the integrand. This in turn corresponds to a fast-decaying spectrum away from the saddle point, enabling the accurate approximation of the examined integral through substituting the integrand function $G(s)$ with a local representation around the origin. For the limiting case where $\Omega \to \infty$, this process tends to the SPP method, i.e., evaluating $G(s)$ on the saddle point and closing the remaining integral through a canonical form. Even so, one could suggest that what is in fact required to enable an asymptotic evaluation is not a very large parameter in the exponent, but an accurate representation of the integrand function $G(s)$ for a radius around the saddle point where the contribution of the spectrum remains significant. Although fundamentally intuitive, a more rigid formulation of this argument can be found in *section 3.13* of [33].

Returning to the evaluation of the integral in question and considering an isolated saddle point at $s = 0$, a representation for the spectrum's properties around the latter can be obtained through a power series expansion of $G(s)$ centred at the origin.

$$G(s) \cong G(0) + sG'(0) + \frac{s^2}{2}G^{(2)}(0) + \frac{s^3}{3!}G^{(3)}(0) + \cdots, \tag{3.7}$$

Assuming a regular function $G(s)$, i.e., featuring no singularities, the radius of convergence of this power series expansion is only determined by the number of terms included in the latter. Therefore, the larger the important spectral region around the saddle point (i.e., the smaller is Ω), more terms are required in the expansion to ensure the accurate representation of $G(s)$ and subsequently reduce the error introduced by the asymptotic approximation.

Given that the chosen representation is what determines the set of canonical integrals that can be employed in the asymptotic evaluation, for an isolated saddle point, the aforementioned Gaussian phase dependence results to integrals of the form presented below, which can be subsequently closed through gamma functions.

$$\int_{-\infty}^{+\infty} e^{-\Omega s^2} ds = \sqrt{\frac{\pi}{\Omega}} \;\; and \;\; \int_{-\infty}^{+\infty} s^n e^{-\Omega s^2} ds = \begin{cases} \frac{\Gamma[(n+1)/2]}{\Omega^{(n+1)/2}}, & n\ even \\ 0, & n\ odd \end{cases}, \qquad (3.8\ a)$$

Combining these concepts results into the asymptotic evaluation of an integral similar to (*3.5*), assuming a regular $G(s)$. As evident from the following equation, the odd terms of the power series expansion of $G(s)$ feature no contribution, due to the symmetrical end points of the integration and the even nature of the exponent.

$$\int_{-\infty}^{+\infty} G(s) e^{-\Omega s^2} ds = \int_{-\infty}^{+\infty} (G(0) + sG'(0) + \cdots) e^{-\Omega s^2} ds = \sum_{n=0}^{\infty} \left(\frac{G^{(2n)}(0)}{(2n!)} \frac{\Gamma\left[\frac{2n+1}{2}\right]}{\Omega^{\left(\frac{2n+1}{2}\right)}} \right), \qquad (3.8\ b)$$

Having discussed the treatment of an isolated saddle point as well as presented an intuitive concept to realize the impact of the value of Ω, a more realistic problem can now be approached where the integrand function ($G(s)$) features singularities in the spectrum.

3.2. Spectral singularities near the saddle point

When any spectral singularities of the integral function ($G(s)$) approach the saddle point, the above presented processes cannot be directly employed. More specifically, the radius of convergence of the power series expansion (*3.7*) is limited by the relative position of the singularities to the saddle point. This in turn requires a different approach to enable the asymptotic evaluation of the integral in question (*3.5*). Taking this into account, the following section will elaborate on the necessary treatment for different types of singularities of $G(s)$. Before doing so however, the mapping of those singularities and their properties in the s-plane will be discussed.

3.2a. Spectral singularities in the s-plane

As introduced through *section 2.2b*, in terms of singularities in the angular spectrum, the integrand of (*3.5*) features a branch point at the origin ($\beta = 0$) due to the presence of the Hankel function, as well as leaky wave polar singularities in the sections of the β-plane which correspond to the bottom Riemann sheet of the k_ρ complex plane. The mapping of these singularities in the s-plane is performed through solving (*3.4 b*) for s.

$$(3.4\ b) \xrightarrow{q_B(\beta) = -j\cos(\beta - \theta')} s = \pm\sqrt{2} e^{j\frac{3\pi}{4}} \sin\left(\frac{\beta - \theta'}{2}\right) \Rightarrow s_i = -\sqrt{2} e^{j\frac{3\pi}{4}} \sin\left(\frac{\beta_i - \theta'}{2}\right), \qquad (3.9)$$

The sign choice in the above expression is performed such that $s \to (\beta - \theta')/((d\beta/ds)_{s=0})$ for $\beta \to \theta'$, as in *section 4.4* of [26], whereas the subscript i can refer to either the leaky wave polar singularities of the Green's function or the branch point of the Hankel.

One notable aspect of the s-plane which was not discussed this far refers to the behavior of the singularities for different observation angles (θ'). While in the angular and the rectilinear spectrum the singularities remain fixed and the saddle point and its respective SDP change for

different observation angles (θ'), this is not the case in the s-plane. In particular, since the saddle point and SDP are always mapped to the origin and real axis of the s-plane respectively, the singularities must move in the spectrum for different θ'. Given that the implemented asymptotic approach will be determined by the type of singularities closest to the saddle point, in the remaining of this section the proximity of different types of singularities to the saddle point will be examined for different observation angles.

Mapping each of the critical points of the integrand of (*3.5*) to the s-plane by using (*3.9*), their relative position with respect to the saddle point and SDP for different observation angles is visualized through Figure 3-2 *(a), (c)* and *(b), (d)* for the β and s-planes respectively.

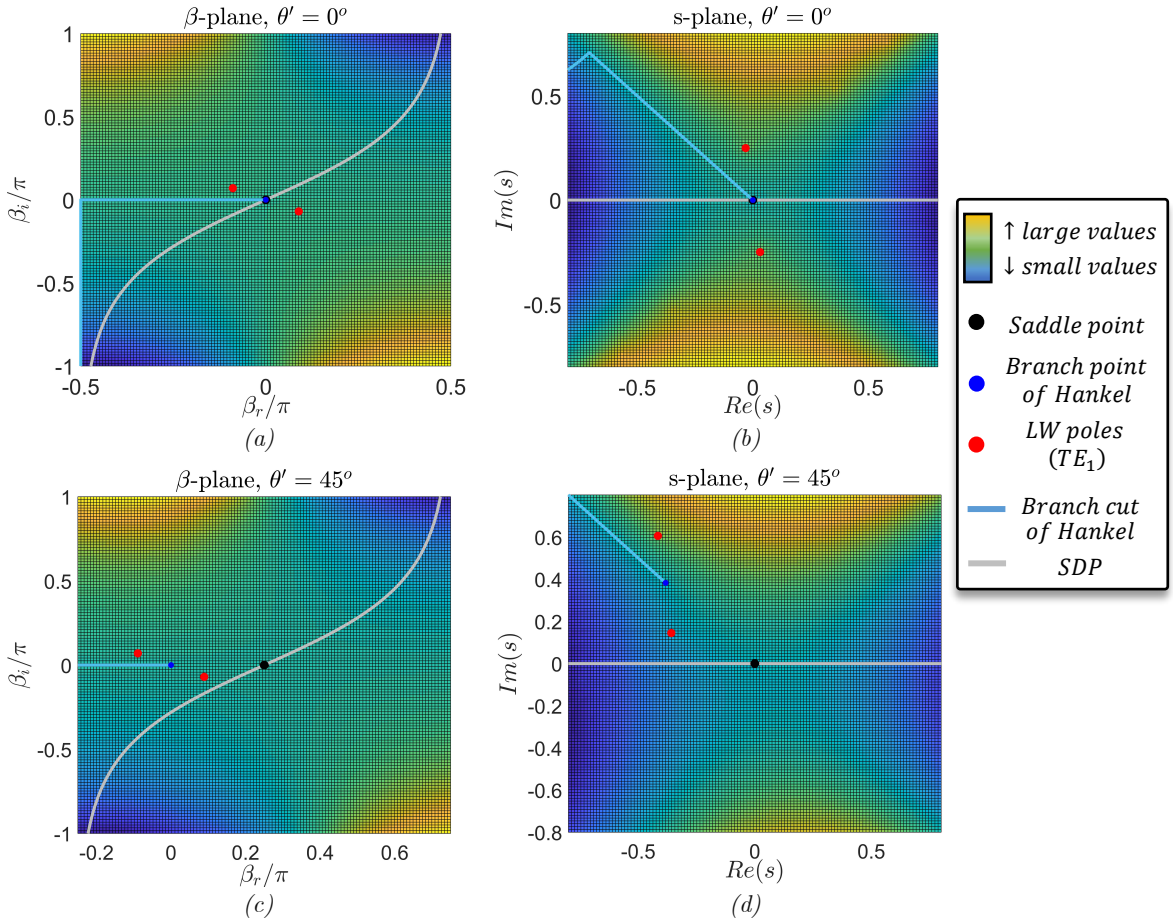

Figure 3-2. Relative position of saddle point and singularities in the spectrum for (a), (b) θ'=0° and (c), (d) θ'=45° for the β and s planes respectively.

As evident from the figures above, around broadside both poles of the leaky wave pole pair ($\pm k_{\rho,LW}^{TE_1}$) are equidistant from the saddle point, while for larger observation angles the one arising from $+k_{\rho,LW}^{TE_1}$ features a dominant impact, being much closer to the saddle point. To account for their equally significant contribution for small observation angles, both poles will be considered during the asymptotic integral evaluation, as will be discussed in the following section. However, apart from the impact of the leaky wave poles, the singularity nearest to the saddle point for observation points around broadside is the branch point of the Hankel function occuring at $\beta = 0$. In fact, for observation points along the z axis, the branch point coincides with the saddle point making its proper treatment crucial.

Adhering to the main idea behind the asymptotic evaluation of complex integrals, when the function $G(s)$ features singularities near the saddle point these must be isolated in their simplest form and subsequently evaluated through another class of canonical integrals. Taking the latter

into account, the following two sections will describe the treatment of the polar and branch point singularities present in the examined integrals.

3.2b. Polar singularities

Considering that the function $F_B(\beta)$ in expression (*3.5*), and subsequently $G(s)$, feature a set of simple poles near the saddle point, the radius of convergence for any expansion of the integrand function $G(s)$ is limited by the positions of said poles. As a result, for cases where Ω is not very large and thus the spectral region around the saddle point in which the properties of $G(s)$ must be maintained is significant, the approach presented through *section 3.1b* must be modified.

The first step in the method of treating polar singularities near the saddle point requires isolating them. This is achieved through decomposing the integrand function $G(s)$ into a regular part ($T(s)$), also referred to as the regularized part of $G(s)$, and a part containing all the poles, with this process labelled as regularization. Subsequently, the regular part can be evaluated through a power series expansion and term-by-term integration, as presented in *section 3.1b*. In turn, the integral of the polar contributions can be evaluated in closed form using either the error function (*erf*) or equivalently the Fresnel integral (F), once the poles have been separated into their individual contributions. The two main approaches for the regularization of $G(s)$ consist of an additive and a multiplicative pole treatment [35]. An extensive comparison of the two, which focuses on identifying their differences, is presented through *Appendix G*. Given the deductions of this comparison, for the remaining of this document the additive method will be employed for the regularization.

In the additive regularization approach, introduced by van der Waerden [36], a function $G_{pole}(s)$ containing all the polar singularities of $G(s)$ is added and subtracted from the latter, forming a regular part in the neighbourhood of the saddle point $T_{VdW}(s) = G(s) - G_{pole}(s)$. While the regular part can now be expanded around the saddle point, the function $G_{pole}(s)$ must be expressed as a combination of simple poles and zeros in terms of s. In this formulation $G_{pole}(s)$ can be evaluated through canonical integrals similar to those presented below for only a simple pole and a simple pole as well as a zero near the saddle point.

$$\int_{-\infty}^{+\infty} \frac{e^{-\Omega s^2}}{s-s_p} ds = \pm 2j\sqrt{\pi} e^{-\Omega s_p^2} Q\left(\mp j s_p \sqrt{\Omega}\right), \; Im(s_p) \gtrless 0, \qquad (3.10\ a)$$

$$\int_{-\infty}^{+\infty} \frac{s-s_z}{s-s_p} e^{-\Omega s^2} ds = \sqrt{\frac{\pi}{\Omega}} \pm 2j(s_p - s_z)\sqrt{\pi} e^{-\Omega s_p^2} Q\left(\mp j s_p \sqrt{\Omega}\right), \; Im(s_p) \gtrless 0, \qquad (3.10\ b)$$

Where $Q(x) = \int_x^{\infty} e^{-t^2} dt = \frac{\sqrt{\pi}}{2} erfc(x) = \frac{\sqrt{\pi}}{2}\left(1 - erf(x)\right)$ and $erf(x) = \frac{2}{\sqrt{\pi}} \int_0^x e^{-t^2} dt$.

Given the complex nature of the leaky wave polar singularities, i.e., $s_p \in C$, the definition of the error function (*erf*) required for the evaluation of Q and subsequently the showcased integrals, is expanded as discussed in [37] to account for complex input values.

The right-hand side of equations (*3.10*) corresponds to functions which uniformly describe the impact of poles as they approach the saddle point and are thus referred to as transition functions. One of their most notable aspects is that if the pole in question crosses the SDP for some observation angle (θ'), the imaginary part of s_p changes sign, making the transition function discontinuous at said angle. Similar to the properties of the SDP integral discussed in *section 2.3a* and showcased through both Figure 2-14 and Figure 2-15, the discontinuity introduced by the transition function is exactly equal to the resulting value by the capturing of the leaky wave pole through its residue contribution, making the total field continuous.

Before proceeding further, it should be noted that closing the integrals of (*3.10 a-b*) through the error function is one potential option, a thorough discussion of which can be found in *section 4.4a* of [26]. Another completely equivalent approach is to resolve the canonical forms using the Fresnel integral (F) as given below.

$$\int_{-\infty}^{+\infty} \frac{e^{-\Omega s^2}}{s-s_p} ds = s_p \int_{-\infty}^{+\infty} \frac{e^{-\Omega s^2}}{s^2-s_p^2} ds = -\frac{1}{s_p}\sqrt{\frac{\pi}{\Omega}} F\left(j\Omega s_p^2\right), \quad (3.10\ c)$$

$$F\left(j\Omega s_p^2\right) = \mp 2js_p\sqrt{\Omega} e^{-\Omega s_p^2} Q\left(\mp js_p\sqrt{\Omega}\right), \ Im(s_p) \gtrless 0, \quad (3.11)$$

To give an indicative example for the implementation of the additive regularization approach, the part of the integrand of (*3.5*) containing all the polar singularities will be considered. Taking into account that the poles of $G(s)$ are attributed to the zeros of the common denominator of the wave amplitudes, the integral of interest is expressed below.

$$\int_{SDP} v_{TE}^{+}(k_d\, sin(\beta), \Delta_z)\, cos(\beta)\, e^{\Omega q_B(\beta)} d\beta = e^{-jk_d r'} \int_{-\infty}^{+\infty} G_p^{TE}(s) e^{-\Omega s^2} ds, \quad (3.12)$$

Where $G_p^{TE}(s) = v_{TE}^{+}(k_d\, sin(\beta), \Delta_z)\, cos(\beta) \frac{d\beta}{ds}$ and $\Omega = k_d r'$.

For the leaky wave stratifications examined (Figure 2-8), the significant polar singularities of the v_{TE} potential, refer to $\pm k_{\rho,LW}$ for the TE_1 leaky wave mode. Therefore, for the implementation of the additive regularization method, a function describing the behaviour of the v_{TE} around the aforementioned polar singularities needs to be introduced. This is obtained through the following expression, as in [27].

$$v_{apr,TE}^{+}(k_\rho, \Delta_z) = \frac{2k_{\rho,LW}}{k_\rho^2 - k_{\rho,LW}^2} Res\left(v_{TE}^{+}(k_\rho, \Delta_z)\right)_{k_\rho = k_{\rho,LW}}, \quad (3.13)$$

To eventually showcase the impact of the regularlization, the spectrum of $G_p^{TE}(s)$ is initially depicted through Figure 3-3, in the bottom Riemann sheet sections of the k_ρ complex plane which contain the leaky wave poles.

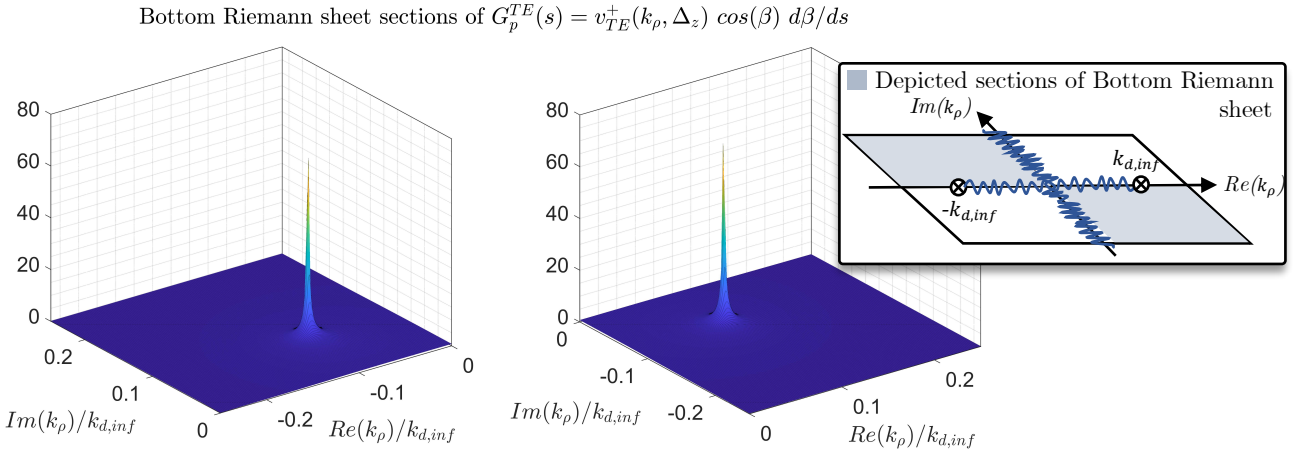

Figure 3-3. Bottom Riemann sheet of $G_p^{TE}(s) = v_{TE}^{+}(k_\rho, \Delta_z) cos(\beta) d\beta/ds$, depicted in the sections of the rectilinear (k_ρ) spectrum indicated in the inset on the top right.

The voltage wave function approximation introduced through (*3.13*), contains both leaky wave poles of the $\pm k_{\rho,LW}$ TE_1 pole pair. Consequently, the regularized part of $G_p^{TE}(s)$, presented below, is free of both polar singularities as can be visualized through the respective spectral regions in Figure 3-4.

$$T_{VdW_{TE}}(s) = \left(v_{TE}^{+}(k_d\, sin(\beta), \Delta_z) - v_{apr,TE}^{+}(k_d\, sin(\beta), \Delta_z)\right) cos(\beta) \frac{d\beta}{ds}, \quad (3.14)$$

It should be noted that while expressions (*3.12*) and (*3.14*) include both β and s variable dependence, this is done purely to maintain a compact form. In fact, these variables are related

through $s(\beta) = -\sqrt{2}e^{j(3\pi/4)}\,sin((\beta-\theta')/2)$ and its inverse, while the Jacobian transform $(d\beta/ds)$ is given by (*3.6*).

Bottom Riemann sheet sections of regularized (VdW) $T_{VdW_{TE}}(s) = (v^{+}_{TE}(k_\rho, \Delta_z) - v^{+}_{apr,TE}(k_\rho, \Delta_z))\,cos(\beta)\,d\beta/ds$

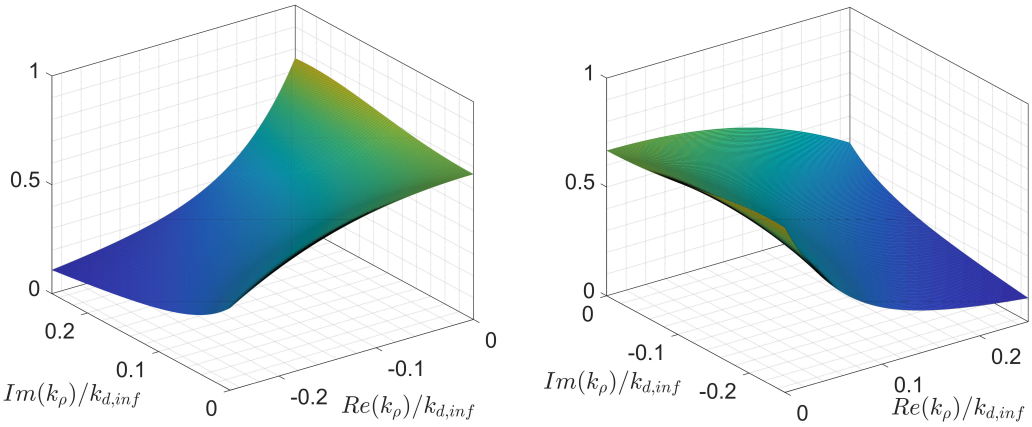

Figure 3-4. Bottom Riemann sheet of the regularized part through the additive method ($T_{VdW_{TE}}(s)$). The depicted sections of the rectilinear (k_ρ) spectrum are indicated in the inset of Figure 3-3.

Considering the integral of $G_p^{TE}(s)$ in (*3.12*), which below is labelled $I_{SDP}(\Omega)$, the previously discussed steps for the asymptotic evaluation using the additive regularization approach are given below.

$$I_{SDP}(\Omega) = \int_{-\infty}^{+\infty} G_p^{TE}(s)e^{-\Omega s^2}\,ds = \int_{-\infty}^{+\infty} T_{VdW_{TE}}(s)e^{-\Omega s^2}\,ds + \int_{-\infty}^{+\infty} G_{pole}^{TE_1}(s)e^{-\Omega s^2}\,ds \Rightarrow$$

$$\Rightarrow I_{SDP}(\Omega) = \int_{-\infty}^{+\infty}\left(T_{VdW_{TE}}(0) + sT'_{VdW_{TE}}(0) + \frac{s^2}{2}T^{(2)}_{VdW_{TE}}(0) + \frac{s^3}{3!}T^{(3)}_{VdW_{TE}}(0) + \cdots\right)e^{-\Omega s^2}ds + \int_{-\infty}^{+\infty} G_{pole}^{TE_1}(s)\,e^{-\Omega s^2}ds \Rightarrow$$

$$\Rightarrow I_{SDP}(\Omega) = T_{VdW_{TE}}(0)\sqrt{\frac{\pi}{\Omega}} + T^{(2)}_{VdW_{TE}}(0)\frac{\Gamma[3/2]}{2\Omega^{(3/2)}} + T^{(4)}_{VdW_{TE}}(0)\frac{\Gamma[5/2]}{4!\,\Omega^{(5/2)}} + \cdots + \int_{-\infty}^{+\infty} G_{pole}^{TE_1}(s)e^{-\Omega s^2}\,ds \Rightarrow$$

$$\Rightarrow I_{SDP}(\Omega) = \sum_{n=0}^{\infty}\left(\frac{T^{(2n)}_{VdW_{TE}}(0)}{(2n!)}\frac{\Gamma\left[\frac{2n+1}{2}\right]}{\Omega^{\left(\frac{2n+1}{2}\right)}}\right) + \int_{-\infty}^{+\infty} G_{pole}^{TE_1}(s)e^{-\Omega s^2}\,ds, \qquad (3.15)$$

Where $G_{pole}^{TE_1}(s) = v^{+}_{apr,TE}(k_d\,sin(\beta), \Delta_z)\,cos(\beta)\frac{d\beta}{ds}$ and $T_{VdW_{TE}}(s)$ as given in (*3.14*).

Number of terms in regularized expansion

Having showcased the integral decomposition resulting from the additive regularization approach through (*3.15*), the impact of higher order terms in the expansion of the regularized part ($T_{VdW_{TE}}(s)$) will now be more thoroughly examined. This process aims to evaluate the number of terms required in the expansion for different radial distances (r') and thus different values of Ω, in order to recover the complete integral of $T_{VdW_{TE}}(s)$ with sufficient accuracy. The utilized test case integral refers to the regularized part of the above presented example, with the comparison between the complete integral and an expansion with different number of terms presented through Figure 3-5. It should be noted that the number of terms indicated in the legends of the following figures refer to terms which contribute to the integral, thus even orders of s in the expansion of $T_{VdW_{TE}}(s)$. The showcased example refers to the wideband structure of Figure 2-8 for the central frequency and an observation grid of $2.5\lambda_0$ from its phase center.

$$I_{Reg}(\theta') = \int_{-\infty}^{+\infty} T_{VdW_{TE}}(s)e^{-\Omega s^2}ds = \int_{-\infty}^{+\infty}\left(\left(v^{+}_{TE}(k_d\,sin(\beta), \Delta_z) - v^{+}_{apr,TE}(k_d\,sin(\beta), \Delta_z)\right)cos(\beta)\frac{d\beta}{ds}\right)e^{-\Omega s^2}ds$$

(3.16 a)

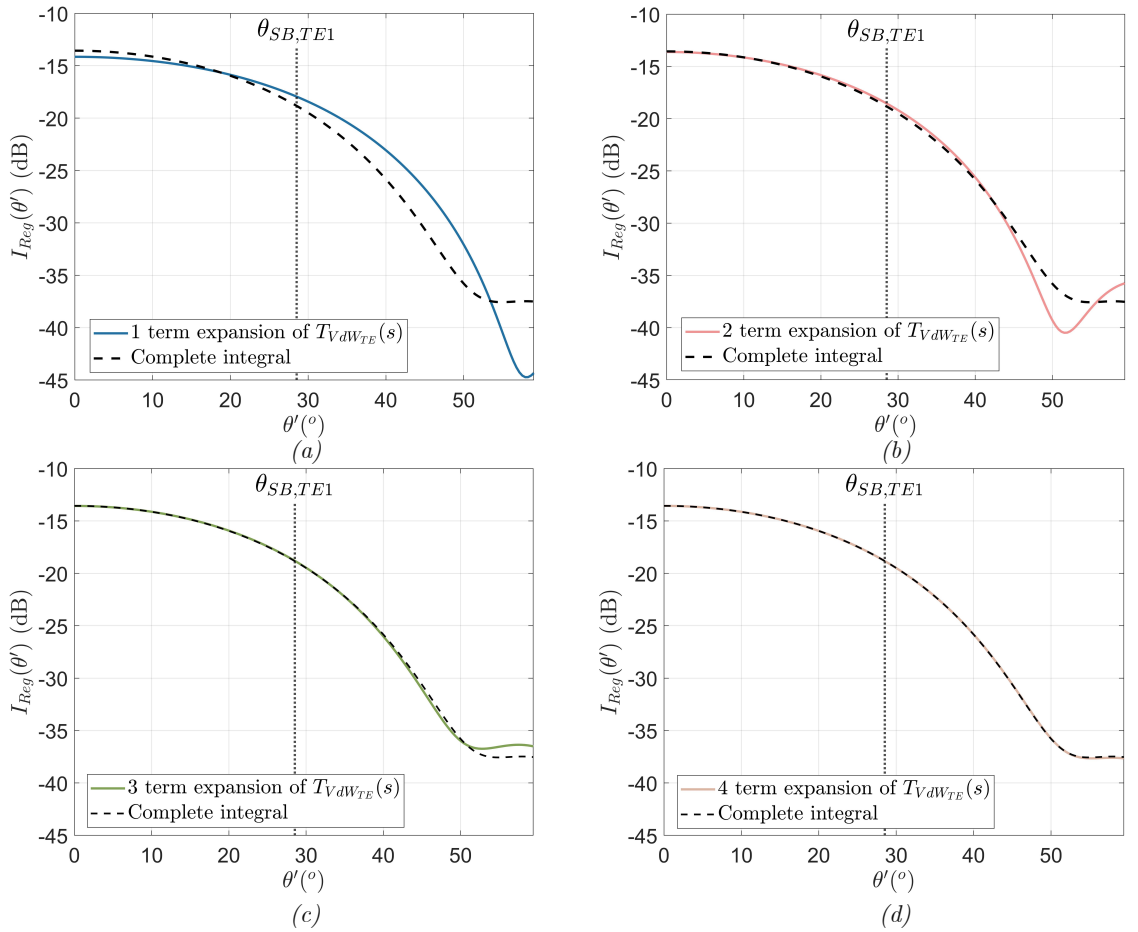

Figure 3-5. Comparison between the complete integral of the regularized part ($T_{VdW_{TE}}(s)$) and its expansion using a different number of terms, (a) one, (b) two, (c) three and (d) four terms.

It can be noticed through the figures above that the inclusion of higher order terms in the expansion of the regularized part ($T_{VdW_{TE}}(s)$) mainly impacts angular regions farther off broadside. In contrast, the region which would correspond to the main lobe of the resulting pattern (roughly $\theta' < \theta_{SB}$) is mostly recovered by the first couple of terms and only slightly influenced by the higher order terms of the expansion. Utilizing this observation, an estimate for the required number of terms in the expansion will be evaluated through obtaining the magnitude and phase errors between the results of the complete integral and that with $T_{VdW_{TE}}(s)$ expanded, as given through the following expressions.

$$E_{rror,mag}(\theta')\ [dB] = 20log_{10}\left(\left|I_{Reg}^{compl.}(\theta')\right|\right) - 20log_{10}\left(\left|I_{Reg}^{expans.}(\theta')\right|\right)$$
$$E_{rror,phase}(\theta')\ [deg] = \left|\left(\measuredangle I_{Reg}^{compl.}(\theta') - \measuredangle I_{Reg}^{compl.}(0)\right) - \left(\measuredangle I_{Reg}^{expans.}(\theta') - \measuredangle I_{Reg}^{expans.}(0)\right)\right| \quad (3.16\ b)$$

Subsequently, the maximum absolute errors within the angular region defined by the shadow boundary angle ($\theta_{SB} = \theta_{SB}^{TE_1}$) are computed and presented through Figure 3-6, for both the wideband and resonant structures. These errors are depicted in terms of the electrical distance between the observation spheres along broadside and the ground plane ($r' - \Delta_z - h$).

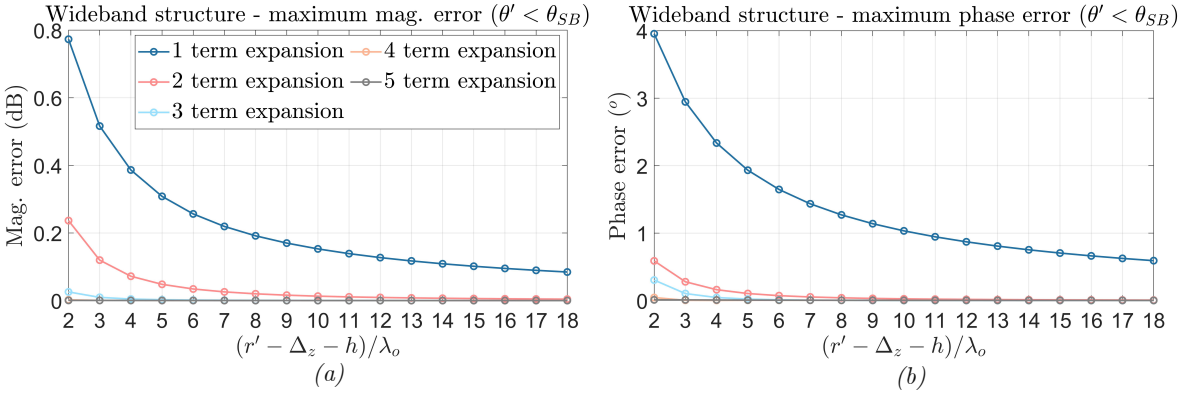

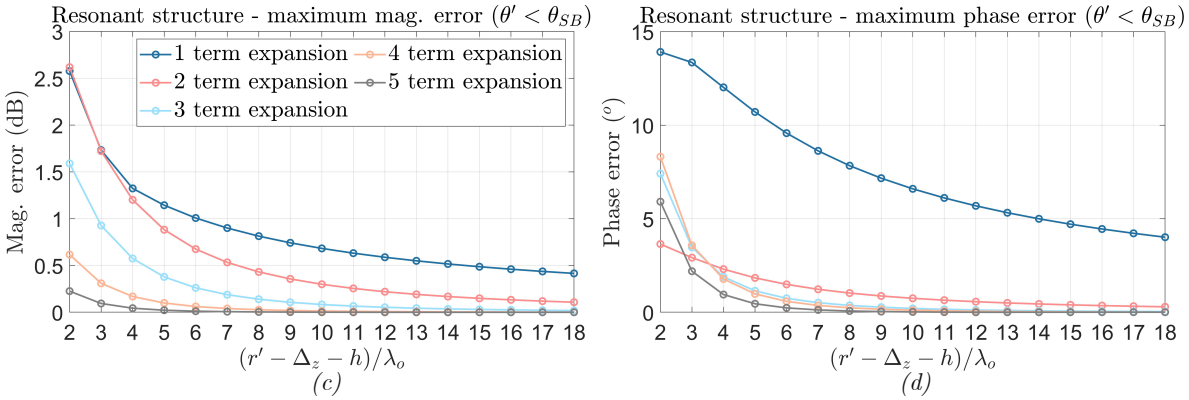

Figure 3-6. Maximum magnitude (a), (c) and phase errors (b), (d) between the complete integral of the regularized part and its expansion with different number of terms, (a),(b) wideband and (c),(d) resonant structure.

As can be visualized through the maximum error comparison presented above, using a three-term expansion for the regularized part allows the evaluation of the integral in question with sufficiently small magnitude and phase errors, even very close to the phase centre. Furthermore, it can be visualized that for smaller radial distances from the phase centre, i.e., small values of Ω, the filtering of the spectrum around the saddle point introduced by the Gaussian exponential term of the integrand ($e^{-\Omega s^2}$) is less sharp, therefore requiring more terms in the expansion of $T_{VdW_{TE}}(s)$ to enable its accurate representation.

Integral of polar contributions

Before concluding with this section, two concepts must still be discussed. Namely, the derivation of the power series expansion for the regular part ($T_{VdW_{TE}}(s)$) and most importantly the evaluation of the integral containing the polar contributions in (*3.15*). Regarding the former, the expansion of the regular part requires the use of the chain rule together with the finite difference method in order to numerically obtain the higher order derivatives of $T_{VdW_{TE}}(s)$, and is further discussed through *Appendix H*. In turn, the evaluation of the integral containing the polar contributions of the initial function, for this example $G_{pole}^{TE_1}(s)$, requires its separation into simple poles such that either of the canonical integrals given in (*3.10*) can be employed.

For this purpose, one must first identify the impactful poles of $G_{pole}^{TE_1}(s)$, i.e., those that approach the saddle point for some observation angle (θ'). Expressing the integral of interest through (*3.16 c*), distinguishing the impactful poles can be more conveniently performed by considering the angular spectrum. In particular, taking into account that the integral's saddle point moves in the real axis between *0* and $\pi/2$, the nature of the integrand's spectrum and the relative position of the poles and the saddle point is illustrated, through Figure 3-7.

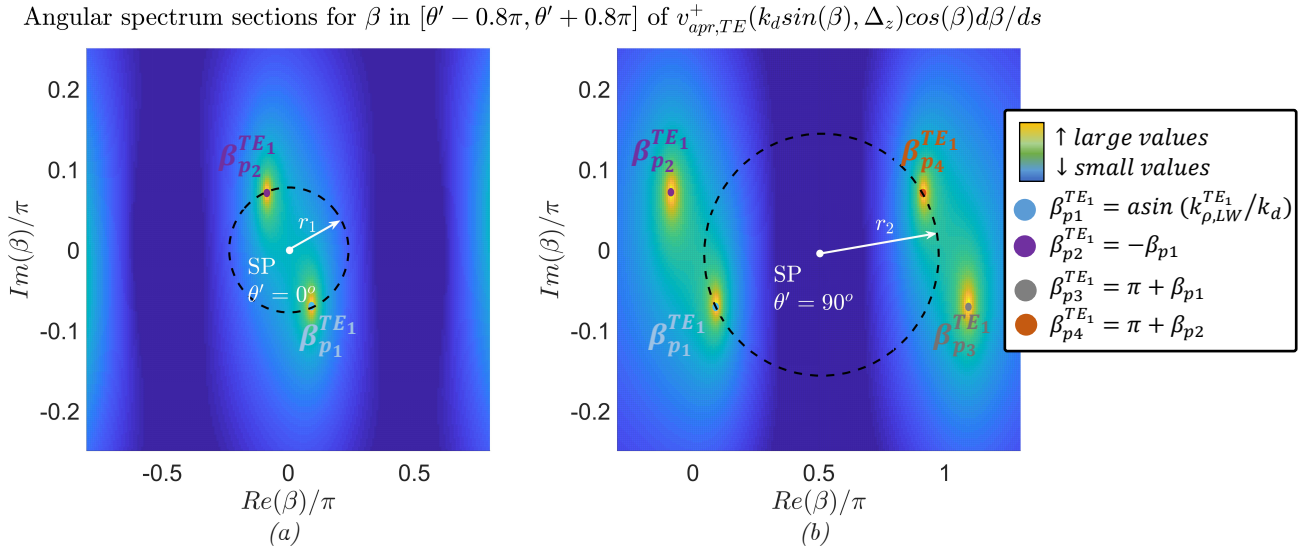

Figure 3-7. Angular spectrum of $G_{pole}^{TE_1}(s) = v_{apr,TE}^{+}(k_\rho, \Delta_z)cos(\beta)d\beta/ds$ for (a) θ'=0° and (b) θ'=90°.

$$I_{pole}(\theta') = \int_{-\infty}^{+\infty} G_{pole}^{TE_1}(s) e^{-\Omega s^2}\, ds = \int_{-\infty}^{+\infty} v_{apr,TE}^{+}(k_d\, sin(\beta), \Delta_z)\, cos(\beta) \frac{d\beta}{ds} e^{-\Omega s^2}\, ds, \qquad (3.16\ c)$$

As evident through the figure above, the $\pm k_{\rho,LW}^{TE_1}$ poles mapped to $\pm\beta_{LW}^{TE_1}$ (labelled $\beta_{p1}^{TE_1}$ and $\beta_{p2}^{TE_1}$ in the figure above), are equidistant from the saddle point for observation points at broadside, making them both necessary for the asymptotic evaluation of $G_{pole}^{TE_1}(s)$. Furthermore, the periodic nature of the angular spectrum leads the approximation of the potential function (*3.13*) to also feature poles at $\pi \pm \beta_{LW}^{TE_1}$ ($\beta_{p3}^{TE_1}$ and $\beta_{p4}^{TE_1}$ in the figure) which in fact approach the saddle point for large observation angles, near 90^o, as shown through Figure 3-7 *(b)*. As such, while their impact is negligible compared to that of the main poles ($\beta_{p1}^{TE_1}$ and $\beta_{p2}^{TE_1}$) for smaller observation angles, they need to be included for the accurate reconstruction of $G_{pole}^{TE_1}(s)$.

Employing the expressions for the positions of the polar singularities in the angular spectrum given in the inset at the bottom of Figure 3-7 ($\beta_{p1-4}^{TE_1}$), their mapping in the s-plane can be obtained through (*3.9*) and corresponds to ($s_{p1-4}^{TE_1}$). Subsequently, the function containing all the polar contributions $G_{pole}^{TE_1}(s)$ can be modelled through the summation of four simple poles as given below.

$$G_{pole}^{TE_1}(s) = \sum_{i=1}^{4} \frac{a_{pi}^{TE_1}}{s - s_{pi}^{TE_1}}, \quad \text{where } a_{pi}^{TE_1} = \lim_{s \to s_{pi}^{TE_1}} \left(s - s_{pi}^{TE_1}\right) G_{pole}^{TE_1}(s), \qquad (3.17\ a)$$

In this form, $G_{pole}^{TE_1}(s)$ can be evaluated asymptotically through the integral of (*3.10 a*)

$$\int_{-\infty}^{+\infty} G_{pole}^{TE_1}(s) e^{-\Omega s^2}\, ds = \sum_{i=1}^{4} \left(\int_{-\infty}^{+\infty} \frac{a_{pi}^{TE_1}}{s - s_{pi}^{TE_1}} e^{-\Omega s^2}\, ds \right) = \sum_{i=1}^{4} \left(\pm 2j a_{pi}^{TE_1} \sqrt{\pi} e^{-\Omega \left(s_{pi}^{TE_1}\right)^2} Q\left(\mp j s_{pi}^{TE_1} \sqrt{\Omega} \right) \right), \quad Im\left(s_{pi}^{TE_1}\right) \gtrless 0 \qquad (3.17\ b)$$

It should be mentioned that in the case where $G_{pole}^{TE_1}(s)$ also features a zero near the saddle point for some observation angle, (*3.10 a*) cannot be directly applied. Instead, the zero must be extracted as indicated in the following expression assuming $G_{pole}^{TE_1}(s_0)=0$, with the remaining part expanded as in (*3.17 a*) and the resulting canonical form evaluated through the integral of (*3.10 b*).

$$G_{pole}^{TE_1}(s) = (s - s_0) \left(\frac{G_{pole}^{TE_1}(s)}{s - s_0} \right) = (s - s_0) \sum_{i=1}^{4} \frac{b_{pi}^{TE_1}}{s - s_{pi}^{TE_1}} \qquad (3.17\ c)$$

In this specific example, this step could be employed for the zero of $cos(\beta)$ at $\pi/2$; however, its impact will be negligible except for observation angles very close to 90^o which are of little interest for the presented study. Aiming to evaluate the above discussed modelling process, the decomposition of $G_{pole}^{TE_1}(s)$ into four simple poles will be performed for the integral of (*3.16 c*). In particular, the impact of including the poles which lie outside the visible spectrum ($\beta_{p3}^{TE_1}$ and $\beta_{p4}^{TE_1}$ in Figure 3-7) will be compared to that of using only the main poles ($\beta_{p1}^{TE_1}$ and $\beta_{p2}^{TE_1}$), while the contribution of adding the zero arising from the cosine will also be shown. This is illustrated through Figure 3-8 *(a)* and *(b)*, which correspond to the asymptotic evaluation of (*3.16 c*) using the modelling described in the respective legends. The figures refer to the wideband leaky wave structure, the central frequency and a spherical observation grid of $2\lambda_0$ from the phase centre.

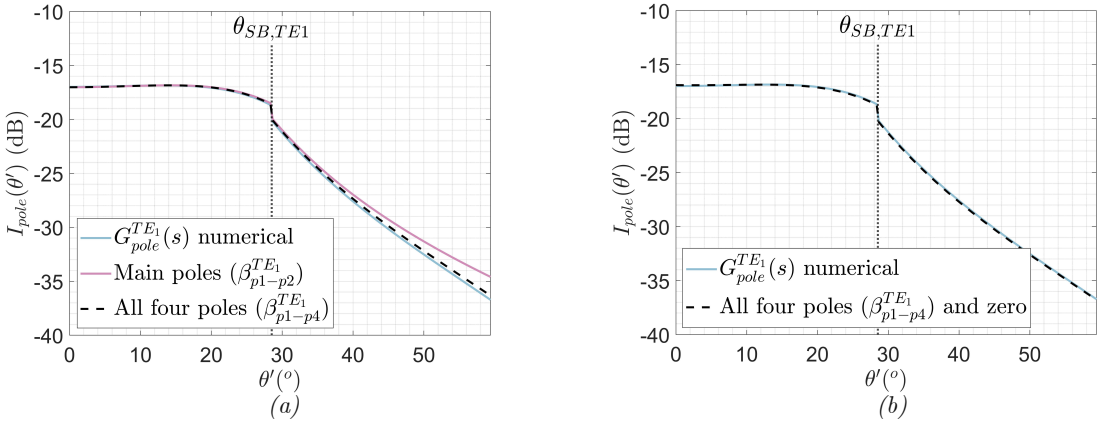

Figure 3-8. Comparing the integral of $G_{pole}^{TE_1}(s)$ in (3.16 c) when using (a) two or four simple poles and (b) four poles and adding the zero.

As visualized through the figures above, the poles which lie outside the visible region feature a small contribution only for large observation angles. In addition, the impact of the zero is negligible as anticipated by the previous discussion.

The steps described above can be employed in a similar manner for integrals featuring *TM* potentials with the only difference being the need for regularizing both the TM_1 and the TM_0 pole pairs and subsequently treating their polar contributions independently. To illustrate this process, the wave amplitude of the indicative integral (*3.12*) will be swapped to the *TM* variant and the necessary steps for the asymptotic evaluation of the resulting expression will be briefly presented below.

$$\int_{SDP} v_{TM}^{+}(k_d\, sin(\beta)\,, \Delta_z)\, cos(\beta)\, e^{\Omega q_B(\beta)} d\beta = e^{-jk_d r'} \int_{-\infty}^{+\infty} G_p^{TM}(s) e^{-\Omega s^2} ds, \qquad (3.18\ a)$$

$$I_{SDP}(\Omega) = \int_{-\infty}^{+\infty} G_p^{TM}(s) e^{-\Omega s^2}\, ds = \int_{-\infty}^{+\infty} T_{VdW_{TM}}(s) e^{-\Omega s^2}\, ds + \int_{-\infty}^{+\infty} G_{pole}^{TM_1}(s) e^{-\Omega s^2}\, ds + \int_{-\infty}^{+\infty} G_{pole}^{TM_0}(s) e^{-\Omega s^2}\, ds, \qquad (3.18\ b)$$

Where $T_{VdW_{TM}}(s) = \left(v_{TM}^{+}(k_d\, sin(\beta)\,, \Delta_z) - v_{apr,TM_1}^{+}(k_d\, sin(\beta)\,, \Delta_z) - v_{apr,TM_0}^{+}(k_d\, sin(\beta)\,, \Delta_z)\right) cos(\beta) \frac{d\beta}{ds}$,

$G_{pole}^{TM_1}(s) = v_{apr,TM_1}^{+}(k_d\, sin(\beta)\,, \Delta_z)\, cos(\beta) \frac{d\beta}{ds}$ and $G_{pole}^{TM_0}(s) = v_{apr,TM_0}^{+}(k_d\, sin(\beta)\,, \Delta_z)\, cos(\beta) \frac{d\beta}{ds}$.

In turn (*3.18 b*) can be treated through expanding the regularized part around the saddle point, similar to (*3.15*), and representing each of the polar contributions ($G_{pole}^{TM_1}(s)$, $G_{pole}^{TM_0}(s)$) through a sum of four simple poles. This process results into the following expression, where the remaining integrals can be closed with the use of (*3.10 a*).

$$I_{SDP}(\Omega) = \sum_{n=0}^{\infty} \left(\frac{T_{VdW_{TM}}^{(2n)}(0)}{(2n!)} \frac{\Gamma\left[\frac{2n+1}{2}\right]}{\Omega^{\left(\frac{2n+1}{2}\right)}} \right) + \sum_{i=1}^{4} \left(\int_{-\infty}^{+\infty} \frac{a_{pi}^{TM_1}}{s - s_{pi}^{TM_1}} e^{-\Omega s^2}\, ds \right) + \sum_{i=1}^{4} \left(\int_{-\infty}^{+\infty} \frac{a_{pi}^{TM_0}}{s - s_{pi}^{TM_0}} e^{-\Omega s^2}\, ds \right), \qquad (3.18\ c)$$

Where $a_{pi}^{TM_1} = \lim_{s \to s_{pi}^{TM_1}} \left(s - s_{pi}^{TM_1}\right) G_{pole}^{TM_1}(s)$ and $a_{pi}^{TM_0} = \lim_{s \to s_{pi}^{TM_0}} \left(s - s_{pi}^{TM_0}\right) G_{pole}^{TM_0}(s)$.

Finally, the impact of the individual poles for the TM_1 and TM_0 leaky wave modes will be presented through Figure 3-9 *(a)* and *(b)* respectively, similar to the comparison performed in Figure 3-8.

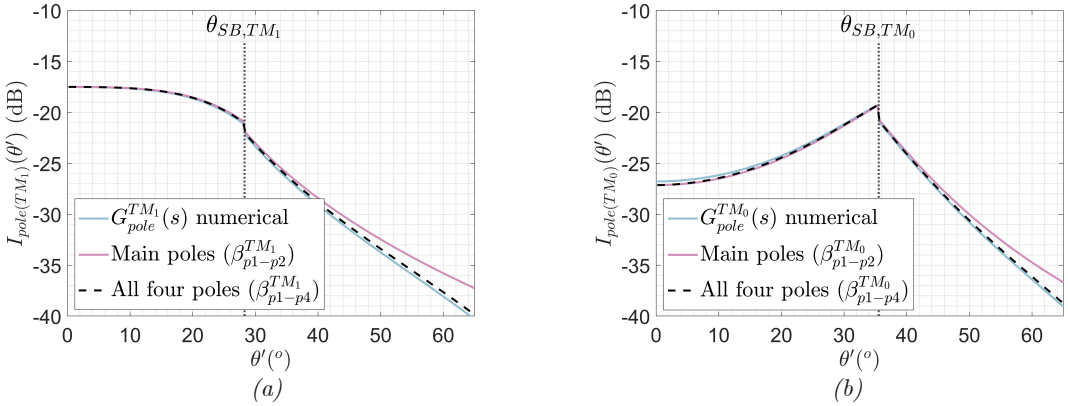

Figure 3-9. Comparing the integrals of (a) $G_{pole}^{TM_1}(s)$ and (b) $G_{pole}^{TM_0}(s)$ of (3.18 b), using only the main poles and using all four simple poles of the respective polar contributions.

While the deductions with respect to the importance of the individual poles are the same as those extracted for the TE_1 mode, the different nature of the polar contribution between the TE_1, TM_1 pole pair and the TM_0, will be discussed in *section 3.3a*.

3.2c. Branch point and Hankel considerations

Having described a method for the asymptotic approximation of integrals whose saddle point approaches polar singularities, still the evaluation of the test case integral of (*3.5*) cannot be performed. In particular, as introduced through *section 3.2a*, while the choice of representation using the Hankel function in our typical integral has made it possible to resort to contour deformations, it has also introduced the branch point and its respective cut, depicted through Figure 3-2. Consequently, for observation points around broadside the singularity nearest to the saddle point is precisely this branch point occuring in the origin of the angular spectrum. As such, specific considerations must be introduced for the treatment of this singularity in order to enable the asymptotic evaluation of the integrals of interest.

The first step in the subsequent deliberations refers to identifying the type of branch point to be treated. As a matter of fact, different types of branch points arise from different multivalued functions and in turn require distinct canonical forms for their asymptotic approximation. As an indicative example, algebraic branch points introduced by roots of any order, can be conveniently evaluated asymptotically through the use of parabolic cylinder functions, as discussed in *section 4.4c* of [26] or more thoroughly elaborated in [38]. Having said that, the branch point of the Hankel function of *0th* order (H_0) is of logarithmic nature and thus cannot be evaluated in the aforementioned manner.

Another complication related to the treatment of the Hankel function refers to the utilized representation. In particular, the most accurate approach would necessitate the use of the integral represenation for the Hankel function in (*3.3 b*) and the subsequent asymptotic evaluation of the resulting double integral. However, this step would contribute significant complication to the overall problem, since it results to integral expressions that cannot be transformed into the targeted one-dimensional integrals in the s-plane. Furthermore, given that the argument of the Hankel function is proportional to ρ, and thus $sin(\theta')$, if an asymptotic expansion is utilized, the employed expression would need to change between the large and small argument representation for the evaluation of the field over a spherical observation grid.

Considering all the above, together with the nature of the near field for the examined structures, two sequential approximations are introduced for the treatment of the Hankel functions in the integrals in question. First, the latter is substituted by its first order large argument approximation and subsequently, part of the integrand ($k_\rho H_n^{(2)}(k_\rho\rho)e^{jk_\rho\rho}$) is evaluated on the saddle point ($k_{\rho SP} = k_d sin(\theta')$). The impact of these two sequential approximations on the resulting integral expressions will be separately shown below. Before doing so however, it should be emphasized that these approximations do not aim to provide a generic method for the asymptotic treatment of Hankel functions; instead their applicability for the examined leaky wave structures is based in the nature of their near field and is enabled by the phase centre choice. Since the presented asymptotic study refers to the remaining integral term ($\vec{E}_{SDP}$) of the decomposition given in (*3.1*), the initial SDP integral expressions are presented below. To faciliate the subsequent observations, the cylindrical field components are treated.

$$\begin{bmatrix} E_{\rho,SDP}(\vec{r}') \\ E_{\varphi,SDP}(\vec{r}') \\ E_{z,SDP}(\vec{r}') \end{bmatrix} = \frac{1}{8\pi}\int_{SDP} \begin{bmatrix} -cos(\varphi)\left(v_{TM}^{+}(k_\rho,\Delta_z)\left(H_0^{(2)}(k_\rho\rho)-H_2^{(2)}(k_\rho\rho)\right)+v_{TE}^{+}(k_\rho,\Delta_z)\left(H_0^{(2)}(k_\rho\rho)+H_2^{(2)}(k_\rho\rho)\right)\right) \\ sin(\varphi)\left(v_{TE}^{+}(k_\rho,\Delta_z)\left(H_0^{(2)}(k_\rho\rho)-H_2^{(2)}(k_\rho\rho)\right)+v_{TM}^{+}(k_\rho,\Delta_z)\left(H_0^{(2)}(k_\rho\rho)+H_2^{(2)}(k_\rho\rho)\right)\right) \\ -j\frac{2\zeta_d}{k_d}cos(\varphi)\, i_{TM}^{+}(k_\rho,\Delta_z)H_1^{(2)}(k_\rho\rho)k_\rho \end{bmatrix} k_\rho e^{-jk_z z'}dk_\rho, \tag{3.19}$$

The first step of the introduced approximation refers to substituting the Hankel functions of the second kind with their first order large argument approximations.

$$H_n^{(2)}(k_\rho\rho) \cong \sqrt{\frac{2}{\pi k_\rho\rho}}e^{j\frac{\pi}{4}}e^{j\frac{n\pi}{2}}e^{-jk_\rho\rho}, \tag{3.20 a}$$

Doing so, transforms the integrals of (*3.19*) into the following expressions.

$$\begin{bmatrix} E_{\rho,SDP}(\vec{r}') \\ E_{\varphi,SDP}(\vec{r}') \\ E_{z,SDP}(\vec{r}') \end{bmatrix} \cong \frac{1}{4\pi}\int_{SDP} \begin{bmatrix} -cos(\varphi)\, v_{TM}^{+}(k_\rho, \Delta_z)\sqrt{\frac{2k_\rho}{\pi\rho}}\, e^{j\frac{\pi}{4}} \\ sin(\varphi)\, v_{TE}^{+}(k_\rho, \Delta_z)\sqrt{\frac{2k_\rho}{\pi\rho}}\, e^{j\frac{\pi}{4}} \\ -j\frac{\zeta_d}{k_d} cos(\varphi)\, i_{TM}^{+}(k_\rho, \Delta_z)\sqrt{\frac{2k_\rho^3}{\pi\rho}}\, e^{j\frac{3\pi}{4}} \end{bmatrix} e^{-jk_z z'} e^{-jk_\rho \rho} dk_\rho, \qquad (3.20\ b)$$

As evident by the above integral expressions, using the large argument approximation for the Hankel function leads to the decoupling of the *TM* and *TE* solutions of the transmission line equivalent problem to their respective dominant regions, which for a magnetic current source are visualized through Figure 3-10. This effect results directly from the relation between the large argument approximations of Hankel functions of the second king of 0_{th} and 2_{nd} order, namely $H_2^{(2)}(k_\rho\rho) = -H_0^{(2)}(k_\rho\rho)$, considering (*3.20 a*).

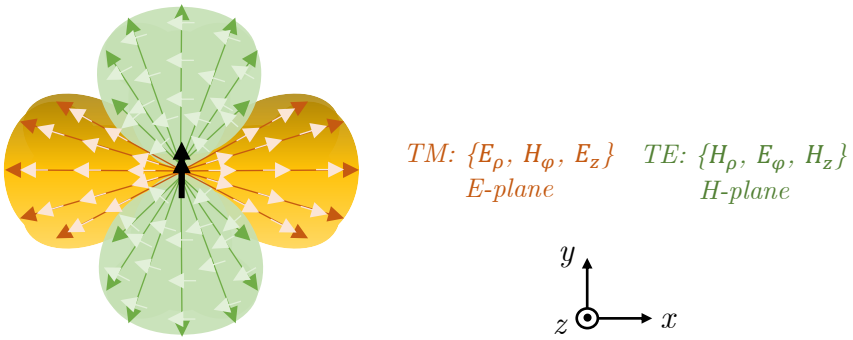

Figure 3-10. Dominant regions for the TE and TM transmission line solutions for a magnetic current source.

While this decoupling of the *TE* and *TM* parts of the transmission line solution in their respective dominant regions constitutes a very good approximation for most cases, it starts to fail as the observation point moves close to the source, as discussed through *section 2.3a* and shown in Figure 2-15. This difference might be negligible for the weaker modes, e.g., TE_1 and TM_1, but can be clearly noticed for modes with small attenuation constant (α_{LW}), like the TM_0. Even so, given that the impact of the TM_0 in its non-dominant plane (H-plane) is mostly described by its residue contribution and not the SDP integral, this approximation would not significantly influence the near field, as will be showcased in following sections.

Having discussed the resulting impact from using the large argument approximation for the Hankel function, the second part of the introduced approximation refers to evaluating part of the integrand, including the approximation of the Hankel function, on the saddle point. This is presented through the following equations, first substituting the Hankel function with its large argument approximation (*3.20 a*) and subsequently evaluating the resulting expression on the saddle point ($k_{\rho SP} = k_d sin(\theta')$).

$$k_\rho H_n^{(2)}(k_\rho\rho)e^{jk_\rho\rho} \underset{\cong}{\overset{H_n^{(2)}\ from\ (3.20\ a)}{}} \sqrt{\frac{2k_\rho}{\pi\rho}}\, e^{j\frac{\pi}{4}} e^{j\frac{n\pi}{2}} \underset{\cong}{\overset{k_\rho = k_{\rho_{SP}}}{\rho = r'\, sin(\theta')}} \sqrt{\frac{2k_d}{\pi r'}}\, e^{j\frac{\pi}{4}} e^{j\frac{n\pi}{2}}, \qquad (3.21\ a)$$

Introducing this step to the integral expressions of (*3.20 b*) transforms them as follows.

$$\begin{bmatrix} E_{\rho,SDP}(\vec{r}') \\ E_{\varphi,SDP}(\vec{r}') \\ E_{z,SDP}(\vec{r}') \end{bmatrix} \cong \frac{1}{4\pi}\sqrt{\frac{2jk_d}{\pi r'}}\int_{SDP} \begin{bmatrix} -cos(\varphi)\, v_{TM}^{+}(k_\rho, \Delta_z) \\ sin(\varphi)\, v_{TE}^{+}(k_\rho, \Delta_z) \\ \frac{\zeta_d}{k_d} cos(\varphi)\, i_{TM}^{+}(k_\rho, \Delta_z) k_\rho \end{bmatrix} e^{-jk_z z'} e^{-jk_\rho \rho} dk_\rho, \qquad (3.21\ b)$$

Since the approximated integrals of (*3.21 b*) feature only first order saddle points ($k_{\rho SP} = k_d \sin(\theta')$) and simple polar singularities through the wave amplitudes ($v_{TE/TM}^{+}$ and i_{TM}^{+}), they can

be transformed into the s-plane, using (*2.8*) and (*3.4*), and subsequently asymptotically evaluated as discussed in *section 3.2b*. In turn, combining the resulting asymptotic approximation of the SDP integral with the residue polar contributions (*3.1*), results to the total field in the semi-infinite region of the leaky wave structure.

One noteworthy aspect of the introduced approximation is that it is only employed on the SDP integrals ($\vec{E}_{SDP}(\vec{r}')$) of the decomposition given through (*3.1*). In other words, these approximation are not performed on the residue contributions. This is done to minimize the error involved, since for the residues the integrand is evaluated on the polar singularity in the complex part of the spectrum and not on the saddle point. On the other hand, the dominant contribution of the SDP integral is actually the saddle point, rendering the approximation of part of the integrand on this point (saddle point) sufficiently accurate. Considering that the nature of the SDP integral is being discontinuous at the shadow boundaries such that this discontinuity is exactly compensated by the residue polar contributions; employing different approximations for the SDP and the residues leads to slight discontinuities at all the shadow boundaries. As will be shown through *section 3.3c*, these discontinuities are not significant even for observation points very close to the source and are thus deemed acceptable.

To conclude this section, it must be emphasized once more that contrary to the considerations of *section 3.2b*, the above presented treatment of the Hankel function is based on the nature of the near field of the examined structures and thus it is specific to this problem. Its physical interpretation as well as its applicability to the leaky wave structures of interest will be the subject of discussion in the following section.

3.2d. Physical interpretation & phase center choice

As described in the previous section, to resolve the branch singularity of the Hankel function and subsequently enable the asymptotic approximation of the SDP integrals of interest, part of the integrand is evaluated on the saddle point (*3.21 a*). This approximation is applicable to the examined problem due to the spherical wave nature of the near field. As a result, it is very much dependent on the choice of reference system such that the near field spherical wave formation can be assumed, similar to what was discussed in [20].

The performance of the introduced approximation will be evaluated by considering the following example for the test case SDP integral of (*3.3 b*). In particular, the results of the numerical integration will be compared using three different reference system positions (Δ_z) with respect to the ground plane. In all cases, the wideband structure is examined at the central frequency, with the observation grid defined as a sphere of $1.6\lambda_0$ (or *3.2 mm*) from the reference system given through *section 2.3*, i.e., Δ_z=*0.42*λ_0. The three different reference system cases are illustrated through Figure 3-11 *(a)-(c)*, and correspond to Δ_z=*0.42*λ_0, Δ_z=*0.84*λ_0 and Δ_z=*0.*

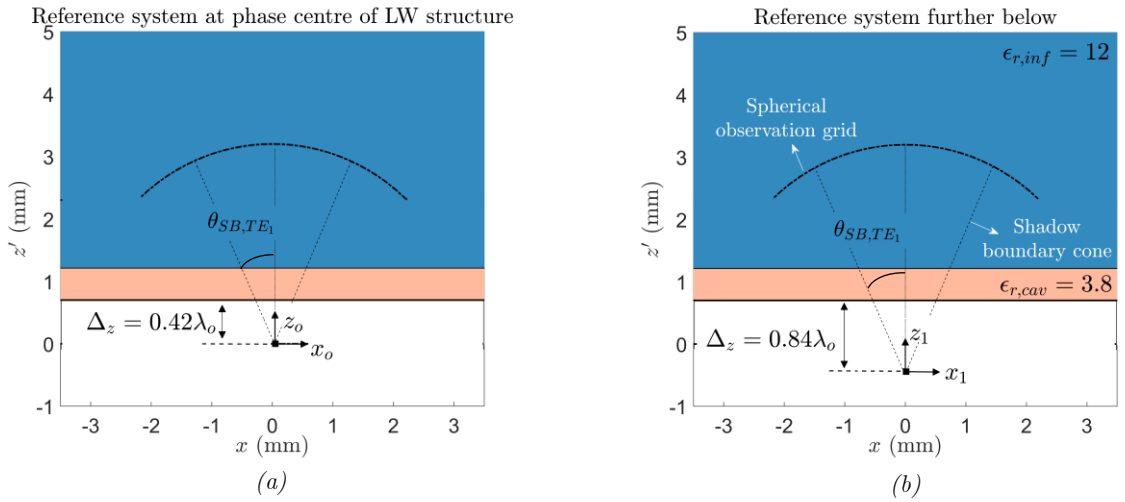

(a) *(b)*

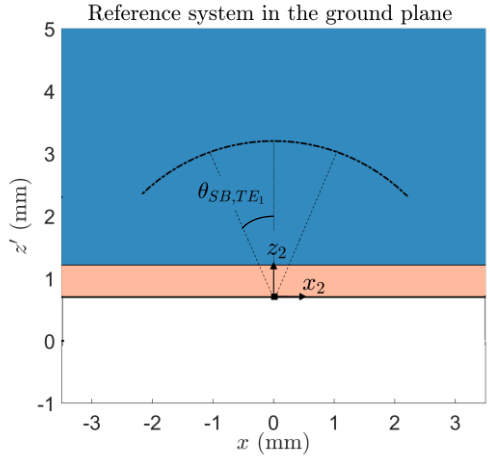

(c)

Figure 3-11. Different setups where the reference system is chosen at (a) Δ_z=0.42 λ_0, (b) Δ_z=0.84 λ_0 below the ground plane and (c) directly on the ground plane. The observation grid is the same for all three cases, corresponding to a sphere of 1.6λ_0 radius from the reference system of (a).

The order of the Hankel function of the second kind chosen for the examined SDP integral is that of 0_{th} order, with the two compared integrals (i.e., initial and approximated) re-written below for clarity. For the purpose of visualizing the impact of the introduced approximation at the shadow boundary angles, the residue contribution resulting from the capturing of the TE_1 leaky wave pole during the deformation to the path of steepest descent will also be included.

$$I_{SDP}(\theta') = \int_{SDP} v_{TE}^{+}(k_\rho, \Delta_z) H_0^{(2)}(k_\rho \rho)\, e^{jk_\rho \rho} k_\rho e^{-jk_\rho \rho} e^{-jk_z z'} dk_\rho, \qquad (3.22\ a)$$

$$I_{SDP}^{approx.}(\theta') = \sqrt{\frac{2k_d}{\pi r'}} e^{j\frac{\pi}{4}} \int_{SDP} v_{TE}^{+}(k_\rho, \Delta_z)\, e^{-jk_\rho \rho} e^{-jk_z z'} dk_\rho, \qquad (3.22\ b)$$

$$I_{Res}^{TE_1}(\theta') = -2\pi j U(\theta' - \theta_{SB}^{TE_1}) k_{\rho,LW}^{TE_1} H_0^{(2)}(k_{\rho,LW}^{TE_1}\rho) Res\left(v_{TE}(k_\rho, z, \Delta_z)\right)_{k_\rho = k_{\rho,LW}^{TE_1}}, \qquad (3.22\ c)$$

Considering the three cases visualized through Figure 3-11, the results of the numerical evaluation of the examined integrals are depicted through Figure 3-12 to 3-14. It should be noted that the illustrated angles on the horizontal axes of the following plots (θ_{0-2}) correspond to the observation angles from the respective reference system positions of each setup.

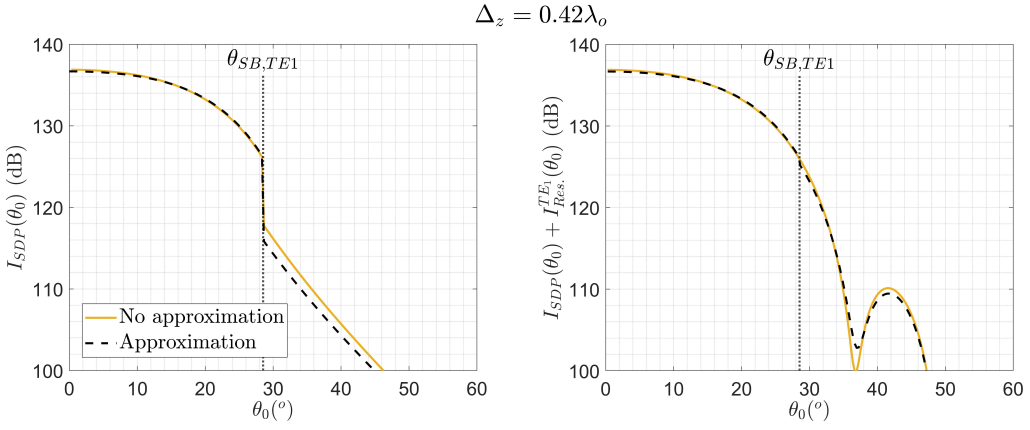

(a) (b)

Figure 3-12. Numerical comparison of the integrals of (3.22) using the reference system of Figure 3-11 (a). Where (a) refers to the comparison of only the SDP integrals while (b) includes the residue.

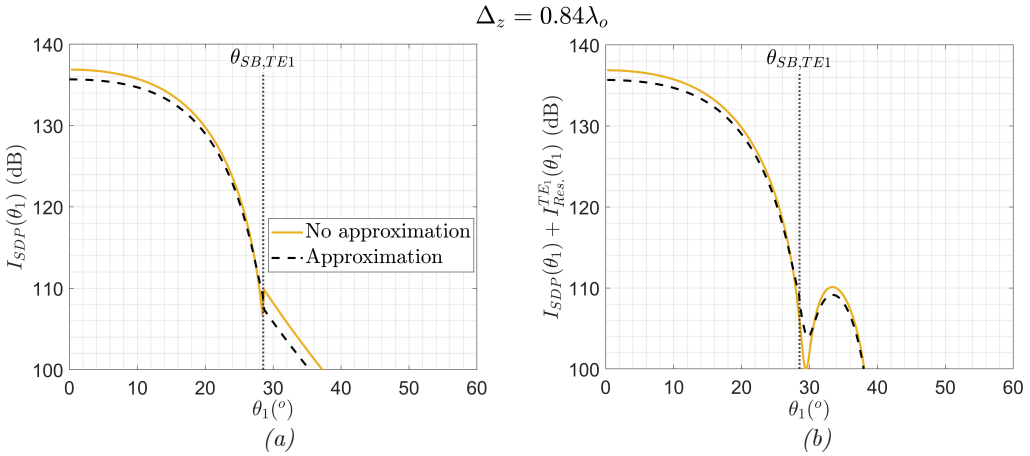

Figure 3-13. Numerical comparison of the integrals of (3.22) using the reference system of Figure 3-11 (b). Where (a) refers to the comparison of only the SDP integrals while (b) includes the residue.

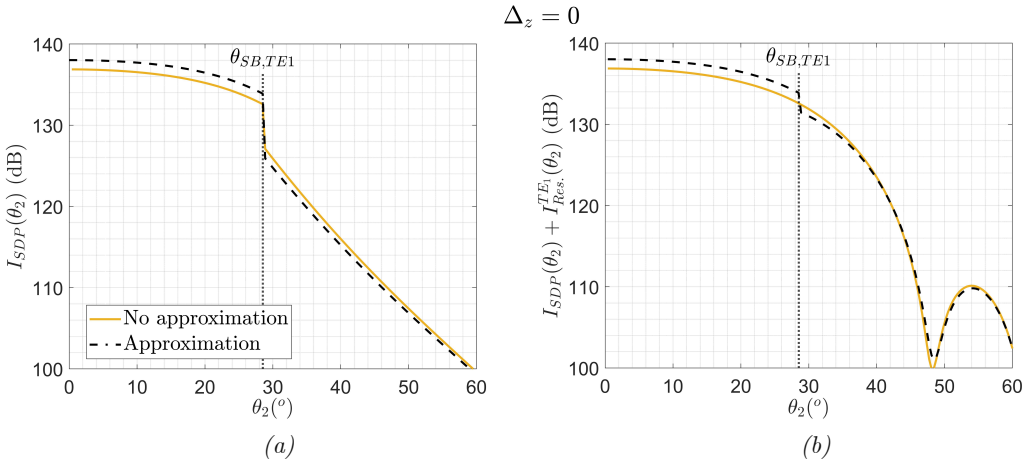

Figure 3-14. Numerical comparison of the integrals of (3.22) using the reference system of Figure 3-11 (c). Where (a) refers to the comparison of only the SDP integrals while (b) includes the residue.

As visualized through the comparisons presented above, the initial and approximated integrals feature very good agreement when the reference system with respect to which the approximation is performed is that from which the field resembles a spherical wave.

Within the shadow boundary cone (i.e., $\theta' < \theta_{SB,TE_1}$), this reference system choice refers to the phase centre for the near field spherical wave formation, i.e., the case of Δ_z=*0.42*λ_0 illustrated through Figure 3-12. Instead, it seems that for the region outside this cone ($\theta' > \theta_{SB,TE_1}$), the approximation's accuracy is improved when choosing the reference system for the integral's evaluation on the ground plane, i.e., Figure 3-14. This is a bit more evident through comparing the first sidelobe of the above figures. This effect can be justified due to the approximation being performed only on the SDP integrals. Above the shadow boundary angle, the space wave significantly contributes to the SDP term meaning that at this region the resulting field can be viewed as a spherical wave with its origin closer to the ground plane.

To further illustrate this concept regarding the different wave nature of the SDP integrals above and below the shadow boundary angles, the integral of (*3.22 a*) will be evaluated numerically over a 2D cut in the semi-infinite dielectric region of the wideband structure. Subsequently, the resulting phase profile over the examined plane will be visualized through Figure 3-15, together with the cross section of the shadow boundary cone referring to the *TE₁* leaky wave mode. As visualized through this illustration, while inside the shadow boundary cone the phase front of the SDP integral resembles that of a spherical wave originating from the displaced reference system below the ground plane (Δ_z=*0.42*λ_0), outside the shadow boundary cone this is not the case. In particular, for observation points close to the source, the

phase front of the SDP integral resembles that of a spherical wave originating from a point slightly above the ground plane.

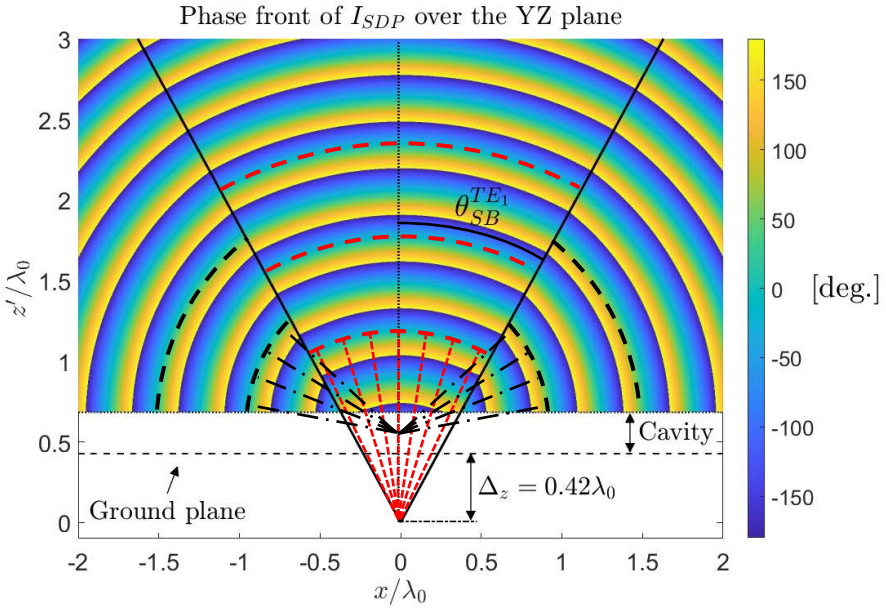

Figure 3-15. Phase front illustration for the SDP integral of (3.22 a).

Taking into account that the SDP integral is better represented as a spherical wave originating from the ground plane above the shadow boundary angle, the option of modifying the reference system choice with the observation angle (θ') will be considered. In particular, the reference system will be moved back to the ground plane after the shadow boundary, as given through the following expression. It should be noted that this option will make the representation of the near field non-uniform, since the field decomposition will change above and below the shadow boundary angle.

$$\Delta_{z_0}(\theta') = U(\theta_{SB} - \theta')\Delta_z^{(2.14)}, \tag{3.23}$$

Where $U(x)$ the Heaviside step function, $\theta_{SB} = min(\theta_{SB,TE_1}, \theta_{SB,TM_1})$ and $\Delta_z^{(2.14)}$ refers to the phase centre choice given in [20] and expressed through equation (*2.14*).

While this phase centre choice will improve the accuracy of the introduced approximation in regions where the SDP integral expressions resemble a spherical wave, this will not be the case for a small angular region around the shadow boundary angle. This is caused by the SDP integral being significantly influenced by the transition function of the respective leaky wave mode, as will be discussed in *section 3.3a*. As such, in a region around the shadow boundary angle the SDP integral cannot be purely described by a spherical wave.

It is also important to note that while the phase centre choice of (*3.23*) might perform adequately well for SDP integrals featuring *TE* potentials, like that of (*3.22*), some complications are indeed expected for integrals with *TM* potentials. This is attributed to the fact that the former are influenced by only one significant mode, namely TE_1, and thus feature a single shadow boundary. On the contrary, integrals featuring *TM* potentials are impacted by both the TM_1 and TM_0 modes, featuring two shadow boundaries. As such, it is expected that for such integrals the phase centre choice of (*3.23*) will create a somewhat problematic region around the shadow boundary angle of the TM_0. In this region, the nature of the near field would not be well represented by the approximation of *section 3.2c* and the phase centre choice of (*3.23*). This difference regarding the shadow boundaries for the *TE* and *TM* integrals can be visualized through Figure 3-16, which illustrates the shadow boundary cones of the significant leaky wave modes in their respective dominant planes.

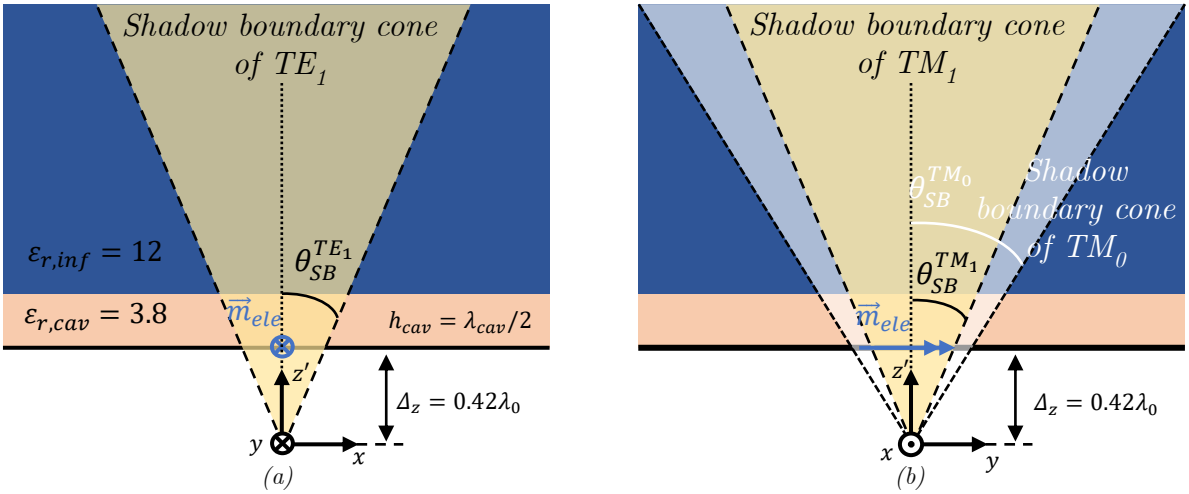

Figure 3-16. Shadow boundaries for y-oriented elementary source in the wideband structure, (a) H and (b) E-plane.

To further visualize this concept, the above presented example will be repeated where this time the wave amplitudes of the integrals given in (*3.22*) are swapped to those of the *TM* variant, as expressed below. The resulting comparisons for the three different reference systems positions presented of Figure 3-11 are visualized through Figure 3-17 to 3-19.

$$I_{SDP}(\theta') = \int_{SDP} v_{TM}^{+}(k_\rho, \Delta_z) H_0^{(2)}(k_\rho \rho)\, e^{jk_\rho \rho} k_\rho e^{-jk_\rho \rho} e^{-jk_z z'} dk_\rho, \qquad (3.24\ a)$$

$$I_{SDP}^{approx.}(\theta') = \sqrt{\frac{2k_d}{\pi r'}} e^{j\frac{\pi}{4}} \int_{SDP} v_{TM}^{+}(k_\rho, \Delta_z)\, e^{-jk_\rho \rho} e^{-jk_z z'} dk_\rho, \qquad (3.24\ b)$$

$$I_{Res}^{TM_1/TM_0}(\theta') = -2\pi j U(\theta' - \theta_{SB}^{TM_1/TM_0}) k_{\rho,LW}^{TM_1/TM_0} H_0^{(2)}(k_{\rho,LW}^{TM_1/TM_0} \rho) Res\left(v_{TM}(k_\rho, z, \Delta_z)\right)_{k_\rho = k_{\rho,LW}^{TM_1/TM_0}}, \qquad (3.24\ c)$$

$\Delta_z = 0.42\lambda_o$

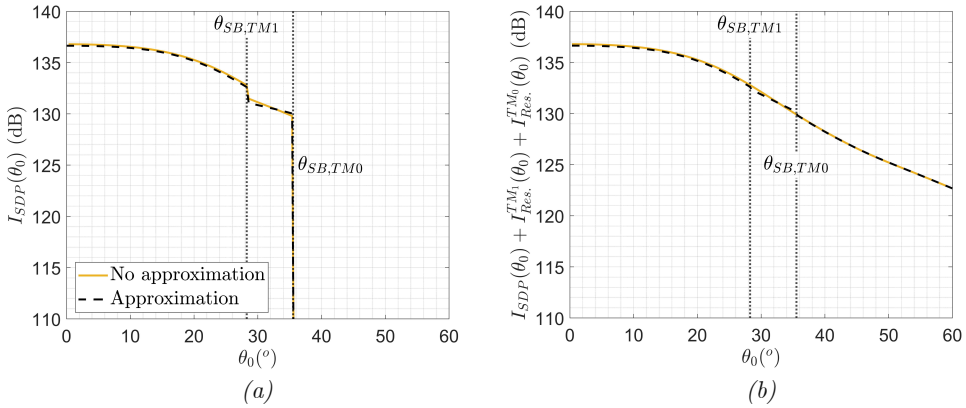

Figure 3-17. Numerical comparison of the integrals of (3.24) using the reference system of Figure 3-11 (a). Where (a) refers to the comparison of only the SDP integrals while (b) includes the residues.

$\Delta_z = 0.84\lambda_o$

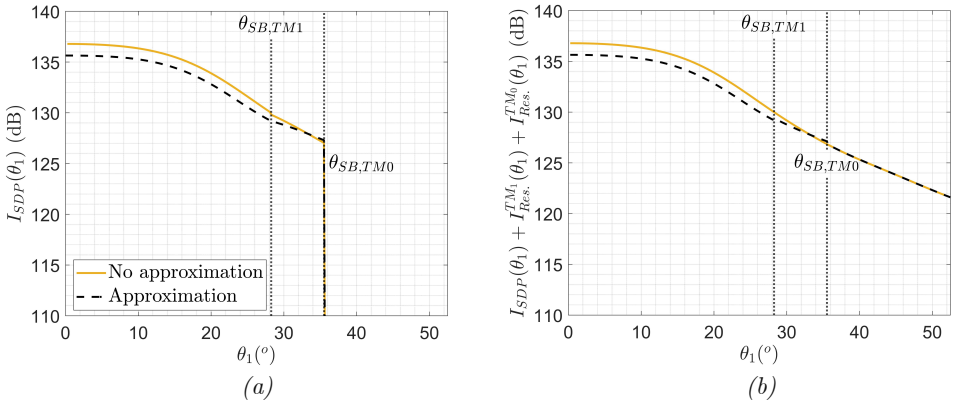

Figure 3-18. Numerical comparison of the integrals of (3.24) using the reference system of Figure 3-11 (b). Where (a) refers to the comparison of only the SDP integrals while (b) includes the residues.

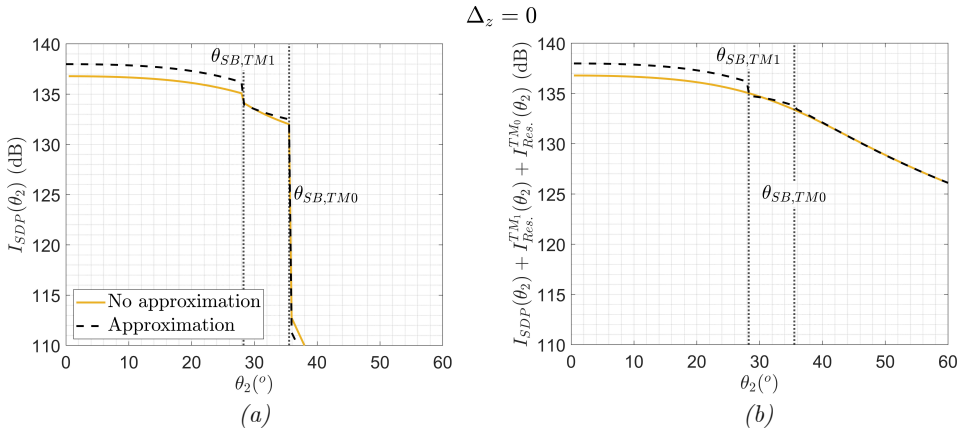

Figure 3-19. Numerical comparison of the integrals of (3.24) using the reference system of Figure 3-11 (c). Where (a) refers to the comparison of only the SDP integrals while (b) includes the residues.

As illustrated through the figures above, the improvement of moving the reference system back to the ground plane cannot be clearly seen in the total integral due to the residue of the TM_0 dominating the region above its shadow boundary ($\theta' > \theta_{SB,TM_0}$). However, what can be visualized through those figures is the region between the shadow boundaries of the TM_1 and that of the TM_0, where neither of the explored phase centre choices results into an exact recovery of the SDP integral.

Even though it would certainly be interesting to explore the possibility for an even more elaborate phase centre choice, differing between integrals with TE and TM potentials and including an additional region to account for the TM_0, for this study we will employ the somewhat simplified phase centre choice of (*3.23*). Potential improvements on this aspect with the concept of adjusting the phase centre choice in different angular regions such that the introduced approximation provides a good representation of the field's nature, are left as part of future work.

Non-uniform phase centre impact on the near field

To visualize the performance of the non-uniform phase centre choice in terms of improving the accuracy of the asymptotic approximation, the complete near field will be considered (*3.1*). For this purpose, the approximated SDP integral expressions of (*3.21 b*) are evaluated numerically, using the reference system displacements of (*2.14*) and (*3.23*) over the observation grid of Figure 3-11. Subsequently, the co-polarized component extracted through the use of the Ludwig 3 definition is compared to that obtained when the approximations of *section 3.2c* are not employed. The resulting comparison is visualized through Figure 3-20 and Figure 3-21.

$$E_{co}(\vec{r}') = E_\theta(\vec{r}')\cos(\varphi) - E_\varphi(\vec{r}')\sin(\varphi)$$
$$E_{cross}(\vec{r}') = E_\theta(\vec{r}')\sin(\varphi) + E_\varphi(\vec{r}')\cos(\varphi)' \qquad (3.25)$$

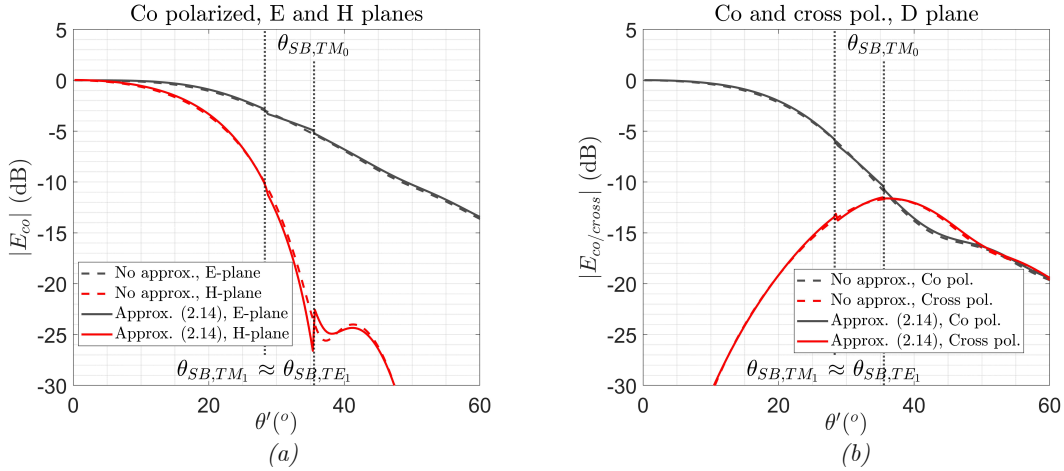

Figure 3-20. Comparison of numerical integration with and without approximation, with the uniform phase centre (2.14), (a) co pol., E and H planes, (b) co and cross pol., D plane. The observation grid is that of Figure 3-11.

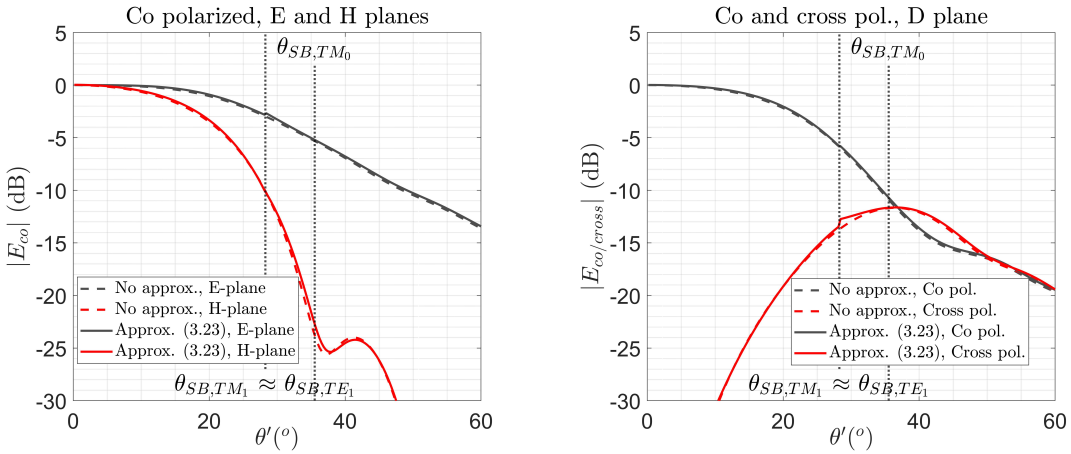

Figure 3-21. Comparison of numerical integration with and without approximation, with the non-uniform phase centre (3.23), (a) co pol., E and H planes, (b) co and cross pol., D plane. The observation grid is that of Figure 3-11.

As can be noted from the figures above, moving the reference system to the ground plane beyond the shadow boundary improves the approximation's accuracy. This is more clearly illustrated in the H-plane due to the residue contribution of the TM_0, which is not impacted by the phase centre choice, dominating the E-plane at larger angles.

Regarding the problematic region between the shadow boundaries of the TM_1 and TM_0 modes described above, it is not visible in the figures above due to the observation distance. In particular, considering the reference system change, this problematic region essentially corresponds to the non-overlapping sections of the shadow boundary cones of the TM_1 mode from the reference system below the ground plane and the shadow boundary cone of the TM_0 from the reference system on the ground plane, as visualized through the shaded region of Figure 3-22 *(a)*. To illustrate how this region's impact changes with the distance, the E-plane for the above example will be evaluated at progressively larger radial distances as illustrated through Figure 3-22 *(b)*. Regarding the observation angle θ' in the horizontal axis, it corresponds to the displaced reference system below the ground plane.

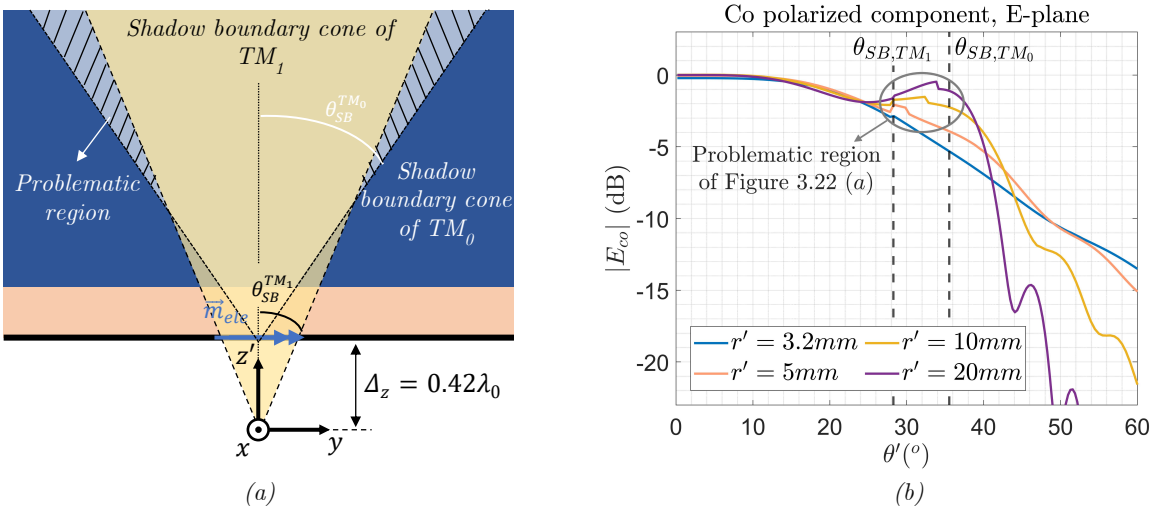

Figure 3-22. (a) E-plane of co polarized component at different radial distances and (b) illustration of problematic region for TM integrals in terms of the non-uniform phase centre choice of (3.23).

To summarize the above discussion, the phase centre choice of (*3.23*) provides adequately accurate representation of the field in all regions apart from that indicated through Figure 3-22 *(a)*. The performance of this simplified phase centre choice will be evaluated throughout the remaining of this document with further improvements in this aspect maintained as part of

future work. It should be noted once more that modifying the reference system choice over the observation grid makes the resulting representation non uniform. This essentially negates its potential use to study the resulting field components, since the field decomposition changes above and below the shadow boundary. Consequently, both phase centre options will be employed in subsequent sections with the uniform one (*2.14*) used to evaluate the near field decomposition and study the field components, while the non-uniform (*3.23*) utilized to accurately recover the field and evaluate the performance of the asymptotic approach.

To conclude, throughout this section an extensive overview of the theoretical aspects and mathematical manipulations involved in the asymptotic approximation of the SDP integrals has been presented. In the remaining of this chapter, the main implications of applying this process for the asymptotic evaluation of the near field will be described.

3.3. Near field asymptotic evaluation

It is without question that the asympotic approach described through *section 3.2* is more elaborate in terms of the mathematical steps required to formulate the near field integral expressions into canonical forms, compared to the numerical methods showcased in Chapter 2. Even so, the asymptotic approximation of the near field provides several benefits both in terms of computational efficiency as well as understanding of the wave phenomena which drive the radiation process. In the remaining sections of this chapter, these aspects of the asymptotic approach will be showcased and discussed. Furthermore, its applicability region arising from the nature of the near field implied by the approximation of *section 3.2c*, will also be assessed.

As a first step towards this goal, the conclusions of *sections 3.2b* and *3.2c* will be introduced into one vectorial field component to showcase the formulation of the asymptotically approximated field. The chosen component is E_φ, since with the introduced approximations (*3.21 a*) it is only influenced by the *TE* potential. As such, a single pole-pair regularization treatment is required ($\pm k_{\rho,LW}^{TE_1}$), making the overall analysis shorter and more compact. It should be noted that the same steps can be implemented for the remaining field components (E_ρ and E_z), with the difference of regularizing the wave amplitudes (v_{TM} and i_{TM}) for both TM_1 and TM_0 pole pairs.

Using the decomposition of the steepest descent path method (*3.1*) as the basis of the asymptotic approach, the steps for the evaluation of one of the SDP integrals of (*3.21 b*) will be briefly summarized below.

Step 1: The SDP integral is transformed into the s-plane, using (*2.8*) and (*3.4*), defining in the process the integrand function $G(s)$ and the parameter Ω.

$$E_{\varphi,SDP}(\vec{r}') \cong \frac{sin(\varphi)}{4\pi}\sqrt{\frac{2k_d}{\pi r'}}e^{j\frac{\pi}{4}}\int_{SDP} v_{TE}^{+}(k_\rho,\Delta_z)e^{-jk_z z'}e^{-jk_\rho \rho}dk_\rho \Rightarrow$$

$$\Rightarrow E_{\varphi,SDP}(\vec{r}') \cong \frac{sin(\varphi)}{4\pi}\sqrt{\frac{2k_d^3}{\pi r'}}e^{j\frac{\pi}{4}}e^{-jk_d r'}\int_{-\infty}^{+\infty} G(s)e^{-\Omega s^2}ds \qquad (3.26\ a)$$

Where $G(s) = v_{TE}^{+}(k_d\, sin(\beta)\,, \Delta_z)\, cos(\beta)\left({}^{d\beta}/_{ds}\right)$ and $\Omega = k_d r'$.

Step 2: The resulting integral is decomposed into the regularized part ($T_{VdW_{TE}}(s)$) and the part containing all the polar singularities of $G(s)$ ($G_{pole}^{TE_1}(s)$), employing the additive pole treatment discussed in *section 3.2b*.

$$E_{\varphi,SDP}(\vec{r}') \cong \frac{sin(\varphi)}{4\pi}\sqrt{\frac{2k_d^3}{\pi r'}}e^{j\frac{\pi}{4}}e^{-jk_d r'}\left[\int_{-\infty}^{+\infty} T_{VdW_{TE}}(s)e^{-\Omega s^2}ds + \int_{-\infty}^{+\infty} G_{pole}^{TE_1}(s)e^{-\Omega s^2}ds\right] \qquad (3.26\ b)$$

Step 3: By expanding $T_{VdW_{TE}}(s)$ around the saddle point and expressing $G_{pole}^{TE_1}(s)$ as a sum of simple poles (and, if necessary, zeros), the integral can be evaluated as a finite sum of terms using (*3.15*) and (*3.17 b*).

$$E_{\varphi,SDP}(\vec{r}') \cong \frac{sin(\varphi)}{4\pi}\sqrt{\frac{2k_d^3}{\pi r'}}e^{j\frac{\pi}{4}}e^{-jk_d r'}\left[\sum_{n=0}^{2}\left(\frac{T_{VdW_{TE}}^{(2n)}(0)}{(2n!)}\frac{\Gamma\left[\frac{2n+1}{2}\right]}{\Omega^{\left(\frac{2n+1}{2}\right)}}\right)+\sum_{i=1}^{4}\left(\pm 2ja_{pi}^{TE_1}\sqrt{\pi}e^{-\Omega\left(s_{pi}^{TE_1}\right)^2}Q\left(\mp js_{pi}^{TE_1}\sqrt{\Omega}\right)\right)\right] \quad (3.26\ c)$$

Where $a_{pi}^{TE_1} = \lim_{s\to s_{pi}^{TE_1}}\left(s-s_{pi}^{TE_1}\right)G_{pole}^{TE_1}(s)$ and the ± sign allocation is performed for $Im\left(s_{pi}^{TE_1}\right) \gtrless 0$.

Taking into account the existence of an inherent limitation for the approximations of *section 3.2c* in terms of the radial distance (r') from the phase centre where they can be employed, the expansion of the regularized part is limited to three terms. To put it simply, for radial distances where the value of Ω necessitates the use of more terms in the expansion in order to maintain acceptable accuracy, the approximations of section *3.2c* start to fail.

Step 4: Finally, the asymptotically approximated SDP integral is combined with the residue contributions of the component in question, resulting in the total field.

$$E_{\varphi}(\vec{r}') = E_{\varphi,SDP}(\vec{r}') + \sum_{i=1}^{3} U\left(\theta' - \theta_{SB}^{LW,i}\right)R_{es}^{LW,i}\left(E_{\varphi}(\vec{r}')\right), \quad (3.26\ d)$$

Where i=*1, 2, 3* corresponds to the *TE₁*, *TM₁* and *TM₀* leaky wave modes.

The above-described process can be employed in a similar manner either for the uniform case of the phase centre choice (*2.14*) or the non-uniform one (*3.23*). Having presented an indicative example for the formulation of the asymptotically evaluated field components, the first part of the following discussion regarding the asymptotic field evaluation will refer to the study of the individual terms of (*3.26*). This process will begin by taking a closer look to the transition functions which result from the asymptotic evaluation of the function containing the polar singularities of $G(s)$, for the above example $G_{pole}^{TE_1}(s)$. Since this essentially refers to the study of field components, the uniform representation in terms of Δ_z will be employed, i.e., that which uses a single reference system (*2.14*).

3.3a. Transition function

As briefly discussed in *section 3.2b*, expressions which result from the integral of polar singularities like those of (*3.10*), uniformly describe the impact of poles approaching the saddle point and are thus referred to as transition functions. These functions are concentrated around the observation point for which the distance between the polar singularities in question and the saddle point is minimized, while also featuring a discontinuity at the observation angle for which the pole crosses the SDP. Furthermore, in some cases, a transition region limited by the value of $|s_p\sqrt{\Omega}|$ can be identified, within which the field changes its wave structure in order to account for the discontinuity introduced by the pole crossing the SDP. This behaviour becomes easier to observe for strongly excited leaky wave modes, given that their respective transition regions are more concentrated, and their residue contributions dominate the field after the shadow boundary. One such example clearly illustrating the transition region within which the space-wave modifies its wave structure from spherical to conical (residue), can be found in [28].

Nature of transition function

In our case, the pole contributions are isolated through a double pole regularization (*3.13*), and subsequently expressed into a sum of four simple poles which are evaluated as given in (*3.17 b*). Some aspects of this approach which have not been treated this far refer to the shape of the transition functions as well as the impact of each individual pole included in the representation

of $G_{pole}(s)$. To showcase both of the above, the co-polarized component of the field resulting from the integral of the polar contributions of the TE_1 and TM_0 leaky wave modes are presented through Figure 3-23, in their respective dominant planes. The following results correspond to the central frequency and a spherical observation grid of *3mm* ($1.5\lambda_0$) radius from the phase centre of the wideband structure. In terms of the phase centre choice, the uniform asymptotic approximation is employed (*2.14*).

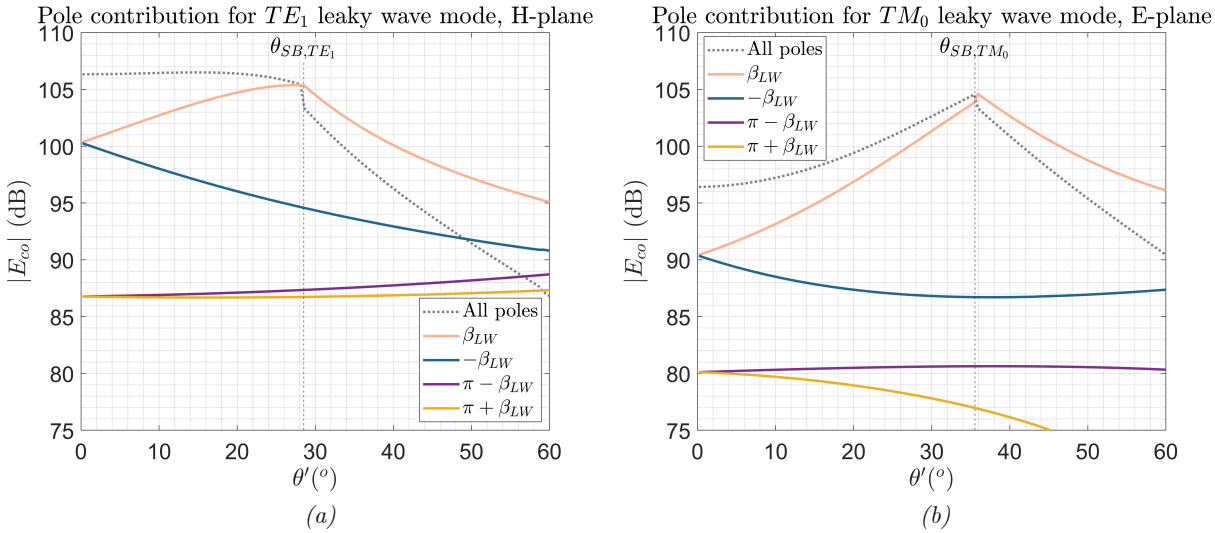

Figure 3-23. Complete pole contribution and its decomposition to foul simple poles for a spherical observation grid of 3mm radius from the phase centre. (a) TE_1 leaky wave mode in the H-plane and (b) TM_0 leaky wave mode in the E-plane.

As visualized through the figures above, the poles which lie outside the visible region feature a small contribution for large observation angles but otherwise their impact is negligible, as anticipated during the discussion in the final part of *section 3.2b*. Furthermore, while the contribution of the two main poles ($+\beta_{LW}$ and $-\beta_{LW}$) is equal along broadside (equidistant from the saddle point for $\theta' = 0^o$), as the observation angle increases, their relative impact changes substantially.

Another deduction that can be made through the above comparison refers to the different nature of the two examined leaky wave modes. Regarding the TM_0, its main pole pair ($+\beta_{LW}$ and $-\beta_{LW}$) is separated sufficiently in the spectrum such that the complete integral of the polar contribution peaks around its shadow boundary angle (θ_{SB,TM_0}). This is attributed to the large pointing angle (θ_{LW}) of the TM_0. On the other hand, the same cannot be said for the TE_1 leaky wave mode where the main pole pair ($+\beta_{LW}$ and $-\beta_{LW}$) coalesces around the saddle point, forming a broader shape as shown through Figure 3-23 *(a)*. It is noted that the TM_1 leaky wave mode behaves very similar to the TE_1 in complementary angular regions, as depicted through Figure 3-10. Consequently, through their transition functions one can visualize how the TE_1 and TM_1 leaky wave mode pair contributes towards enhancing the radiation along broadside, contrary to the TM_0 which launches power towards larger angles.

Transition function shape

Having described the above, the shape of the transition function can also be derived, in an identical fashion to that described in [28] and [39]. More specifically, considering one single pole which crosses the SDP (i.e., $k_{\rho,LW}^{TE_1}$, $k_{\rho,LW}^{TM_1}$ or $k_{\rho,LW}^{TM_0}$) and as such its transition function peaks around its shadow boundary angle, the shape of its transition region results to be elliptical, with the parameters given in Table 3-I. In those expressions, ε' refers to an arbitrarily small number used to define the elliptical contour.

Major axis angle (θ')	Major axis length (a)	Minor axis length (b)	Centre (ρ_o, z'_o)
$\theta' = Re(\beta_{LW})$	$a = \frac{\pi(\varepsilon')^2 \cosh(Im(\beta_{LW}))}{4k_d(\cosh^2(Im(\beta_{LW})) - 1)}$	$b = \frac{\pi(\varepsilon')^2 \sqrt{\cosh^2(Im(\beta_{LW})) - 1}}{4k_d(\cosh^2(Im(\beta_{LW})) - 1)}$	$\rho_o = \frac{\pi(\varepsilon')^2 \sin(Re(\beta_{LW}))}{4k_d(\cosh^2(Im(\beta_{LW})) - 1)}$ $z'_o = \frac{\pi(\varepsilon')^2 \cos(Re(\beta_{LW}))}{4k_d(\cosh^2(Im(\beta_{LW})) - 1)}$

Table 3-I. Parameters of the transition region elliptical shape derived as defined in [39].

An indicative illustration of the two-dimensional cross-section of the elliptical transition region is visualized through Figure 3-24 *(a)*. As depicted, the major axis direction is along $\theta' = Re(\beta_{LW})$, the lower focus is located at the origin and the shadow boundary is tilted with respect to the ellipse orientation, intersecting it at the level of its minimum waist. To supplement this figure, the co-polarized components of the complete asymptotic evaluation of $G_{pole}(s)$ (including all four poles) for the TE_1 and TM_0 leaky wave modes will be presented into two *2D* plots in their respective dominant planes through Figure 3-24 *(b)* and *(c)*.

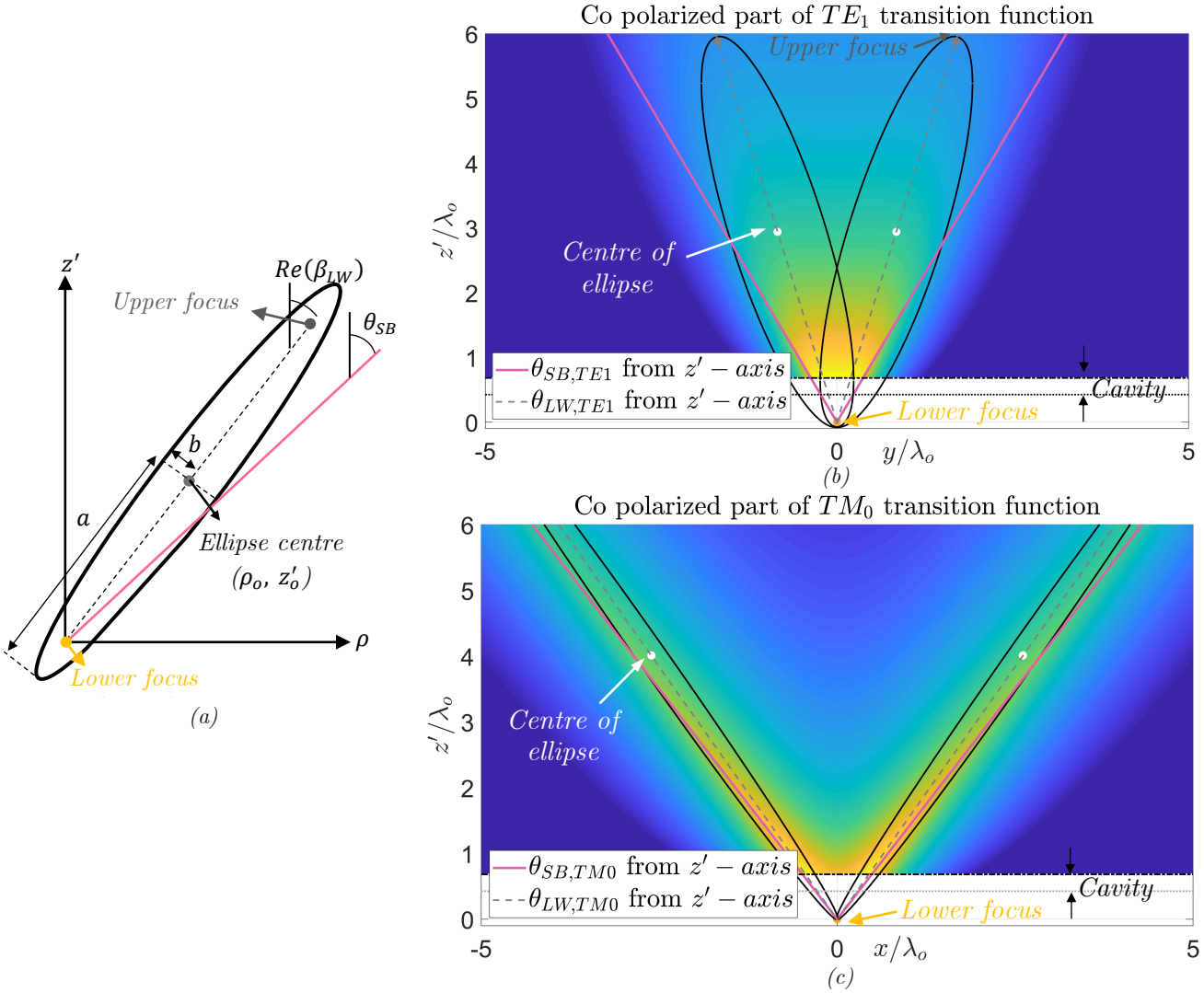

Figure 3-24. (a) Illustration of elliptical cross-section of transition function, (b) 2D plot of co polarized component of all four poles for TE_1 leaky wave mode in the H-plane and (c) 2D plot of co polarized component of all four poles for TM_0 leaky wave mode in the E-plane.

As already noted above, contrary to the case of the TM_0 where the contributions of the $k_{\rho,LW}$ and $-k_{\rho,LW}$ poles are distinguishable, for the TE_1 leaky wave mode this pole pair coalesces around broadside forming a broader structure as visualized through Figure 3-24 *(b)* and *(c)*. While the above discussion for the shape referred to the dominant planes of the respective

modes, it should be noted that the transition functions are also shaped in φ through either a sine or cosine function, as given by (*3.21 b*) and shown through Figure 3-10.

To conclude this discussion on the transition functions, the impact of using the non-uniform phase center choice of (*3.23*) will be showcased. This will be performed by comparing the complete pole contributions of Figure 3-23, with those obtained in the same setup by modifying the reference system choice to that of (*3.23*). The resulting comparison for the TE_1 and TM_0 leaky wave mode is presented through Figure 3-25.

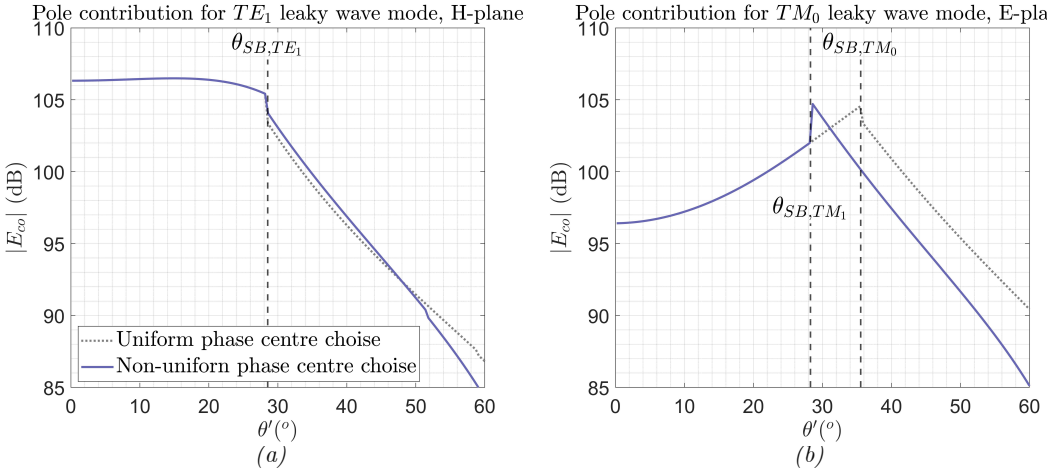

Figure 3-25. Complete pole contribution comparison between uniform (2.14) and non-uniform (3.23) phase centre choice (a) TE_1 leaky wave mode for the H-plane and (b) TM_0 leaky wave mode for the E-plane.

While for the case of the TE_1/TM_1 leaky wave modes the change is not significant, for the TM_0 this is not the case. More specifically, in the non-uniform approach, its transition function does not peak around its shadow boundary angle (θ_{SB,TM_0}). This is attributed to the nature of the shadow boundary; each time being defined from the utilized reference system. As such, by altering the reference system prior to the shadow boundary of the TM_0 ($\theta_{SB,TM_1} < \theta_{SB,TM_0}$), one might end up in a region after this shadow boundary in the new reference system. To facilitate the understanding of this concept, the pole contribution of the TM_0 leaky wave mode is evaluated from two reference systems, one on the ground plane and another displaced as given in (*2.14*), with the resulting plots illustrated through Figure 3-26. To briefly explain the depicted results, until the shadow boundary angle of TM_1, the reference system from (*2.14*) is utilized (yellow color in Figure 3-26), while after the shadow boundary angle, the reference system from the ground plane is used (purple color in Figure 3-26). In this manner, for the examined observation grid the shadow boundary angle of the TM_0 is not crossed in any region.

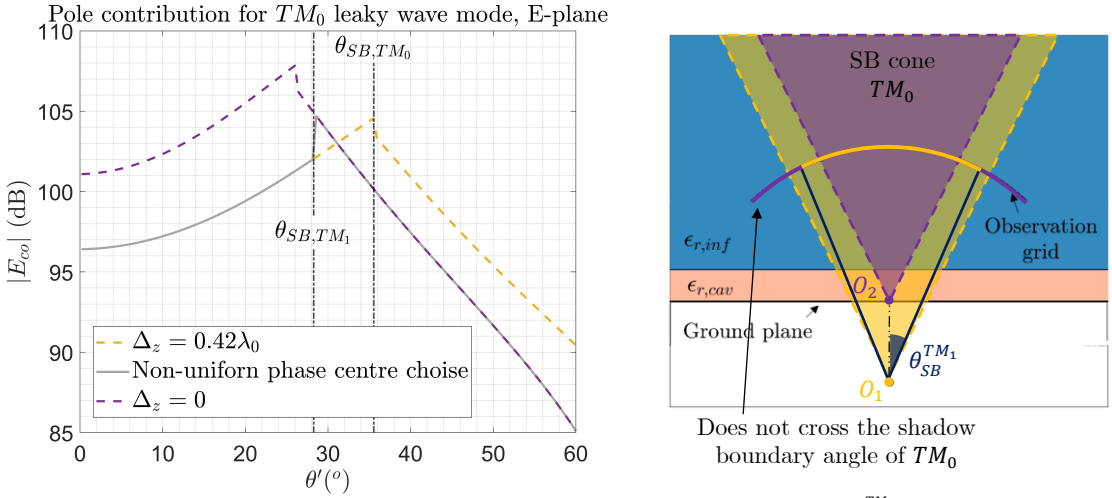

Figure 3-26. Co polarized field component resulting from the complete integral of $G_{pole}^{TM_0}(s)$, evaluated from a displaced reference system (yellow) until $\theta_{SB}^{TM_1}$ and from the ground plane (purple) after this angle. The angle θ' refers to that between the observation vector ($\vec{r}'$) and the z-axis from the displaced reference system (O_1).

Whether this behavior occurs for the TM_0 depend on the overlapping of the shadow boundary cones illustrated through Figure 3-22 *(a)* for the examined observation grid.

3.3b. Regularized component

Having showcased the asymptotic approximation of the SDP integrals through a finite sum of terms in (*3.26*), as well as explored the nature of the transition function resulting from the integral of the polar singularities in the previous section, now the regularized component will be examined. To facilitate this process, the expansion of $T_{VdW_{TE}}(s)$ is explored further, substituting the actual expression for the parameter Ω $(k_d r')$ and separating the resulting terms by their spreading factors $(\frac{1}{(r')^n})$.

$$E_{\varphi,Reg}(\vec{r}') \cong \frac{sin(\varphi)}{4\pi}\sqrt{\frac{2k_d^3}{\pi r'}}e^{j\frac{\pi}{4}}e^{-jk_d r'}\sum_{n=0}^{2}\left(\frac{T_{VdW_{TE}}^{(2n)}(0)}{(2n!)}\frac{\Gamma\left[\frac{2n+1}{2}\right]}{\Omega^{\left(\frac{2n+1}{2}\right)}}\right) = E_{\varphi,Reg_1}(\vec{r}') + E_{\varphi,Reg_2}(\vec{r}') + E_{\varphi,Reg_3}(\vec{r}') + \cdots \quad (3.27)$$

Where $E_{\varphi,Reg_1}(\vec{r}') = \frac{\sqrt{2j}k_d\, sin(\varphi)}{4\pi}\frac{T_{VdW_{TE}}^{(0)}(0)}{r'}e^{-jk_d r'}$, $E_{\varphi,Reg_2}(\vec{r}') = \frac{\sqrt{2j}\, sin(\varphi)}{16\pi}\frac{T_{VdW_{TE}}^{(2)}(0)}{(r')^2}e^{-jk_d r'}$ and $E_{\varphi,Reg_3}(\vec{r}') = \frac{\sqrt{2j}\, sin(\varphi)}{128\pi k_d}\frac{T_{VdW_{TE}}^{(4)}(0)}{(r')^3}e^{-jk_d r'}$.

While deriving the phase dependence of the higher order derivatives of the regularized part is not straightforward, their amplitude dependence with the radial distance can be explicitly extracted. In particular, as can be noticed from the above presented expressions, the first term $(T_{VdW}^{(0)}(0))$ features an $1/r'$ dependence, the second $(T_{VdW}^{(2)}(0))$ an $1/(r')^2$ dependence and so on. Considering this amplitude dependence with the radial distance (r'), it can be anticipated that the level of the higher order terms falls off as the observation grid moves away from the source, eventually leading to the description of the regularized part by only the first term of the expansion.

To also showcase the nature of the above presented terms with respect to the angular regions they influence, their contributions are isolated and visualized through Figure 3-27. The co polarized component is examined in the main planes, referring to a spherical observation gird with $2\lambda_0$ radius from the phase centre of the wideband structure. As a first step, this comparison is performed for the uniform phase centre choice (*2.14*), i.e., Δ_z=*0.42*λ_0.

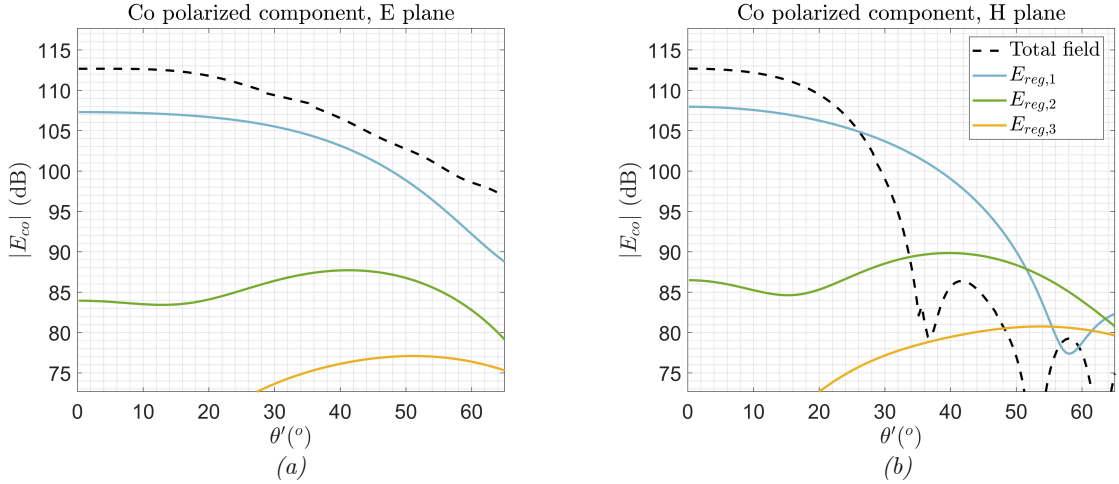

Figure 3-27. Regularized term decomposition for the wideband structure and $r' = 2\lambda_0$, using the uniform phase centre choice (2.14), (a) E-plane and (b) H-plane.

As visualized through the above presented figures, the first term of the regularized expansion $(E_{Reg,1})$, dominates the contribution of the regularized part along broadside with the higher order terms $(E_{Reg,2},\ E_{Reg,3})$ mostly contributing at larger angular regions. Similar

deductions can also be made for the resonant structure, as shown through Figure 3-28 for a spherical observation grid with radius $r' = 9\lambda_0$ from its phase centre position (Δ_z=*3.2*λ_0).

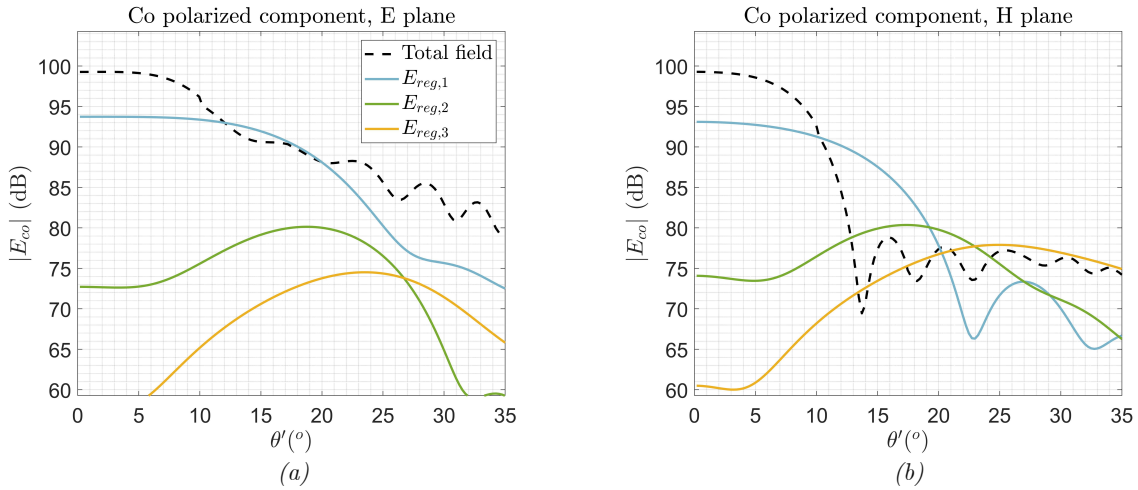

Figure 3-28. Regularized term decomposition for the wideband structure and $r' = 9\lambda_0$, using the uniform phase centre choice (2.14), (a) E-plane and (b) H-plane.

One important note refers to the contribution of the regularized component after the change of reference system (*3.23*). In particular, through the change of decomposition introduced by moving the reference system to the ground plane, the contribution of the regularized component is substantially diminished. To visualize this concept, the setup examined through Figure 3-27 is evaluated once more, employing the non-uniform phase center choice of (*3.23*). As evident through Figure 3-29, above the shadow boundary the contribution of all regularized terms is substantially reduced, meaning that essentially only the first term is important.

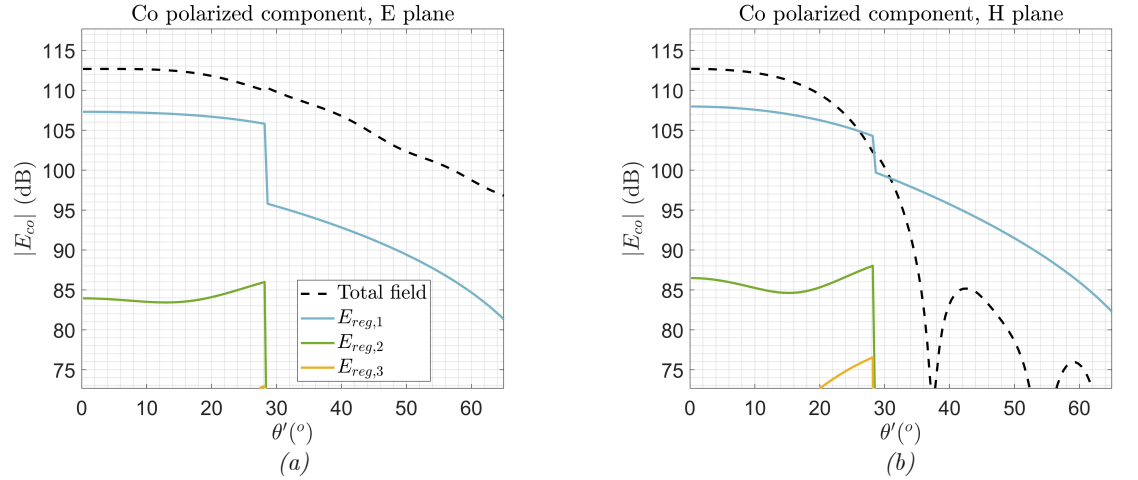

Figure 3-29. Regularized term decomposition for the wideband structure and $r' = 2\lambda_0$, using the non-uniform phase centre choice (3.23), (a) E-plane and (b) H-plane.

To summarize this comparison, while for the uniform phase centre choice the higher order terms of the regularized part can be used to better recover the larger angular regions of the near field; for the non-uniform approach the contribution of the higher order terms is mostly limited along broadside.

Having described the nature of the transition functions as well as that of the regularized component in the previous two sections, in the remaining of this chapter, the fundamental aspects resulting from the decomposition of the near field into a finite sum of terms will be showcased.

3.3c. Near field as a finite sum of terms

Employing the steps described in the introductory part of this section results into the asymptotic approximation of the near field through a small number of terms, as indicatively expressed in (*3.26*). These terms include the residue contributions, the transition functions resulting from the integral of the polar contributions and the terms of the expansion of the regularized part. The above terms are mostly analytical, with the only exception referring to the higher order derivatives of $T_{VdW}^{TE/TM}(s)$, which are acquired in a numerical manner as discussed in *Appendix H*. Substituting the integral expressions with such a small number of mostly analytical terms, has a significant effect in the computational efficiency of the near field evaluation, since it mitigates the need for any spectral integration.

As an indicative example, for a spherical observation grid at $r' = 2\lambda_0$ from the phase centre of the wideband structure featuring 361 φ and 140 θ points, the asymptotic approximation of the near field requires roughly *1.5 sec*, with very small deviation depending on the number of terms included in the expansion of the regularized part. For the same problem, the SDP integration approach described in Chapter 2, requires approximately *1* minute, being roughly forty times slower. This timing comparison is summarized through Table 3-II.

Evaluation method	**Numerical** (integration path of Figure 2-4 b)	**Numerical** (SDP)	**Asymptotic** (1 term)	**Asymptotic** (3 terms)
Time required	*9 min*	*1 min*	*1.4 sec*	*1.5 sec*

Table 3-II. Timing comparison between different near field evaluation methods.

One important comment regarding the time required for the derivation of the near field using the asymptotic approach, refers to it not being influenced by neither the spectral properties of the source nor directly by the distance from the phase centre (r'). In particular, the latter has an indirect impact since it determines the number of terms required in the expansion of the regularized part to maintain acceptable accuracy, but this effect is very small. The same cannot be said for the numerical methods of Chapter 2, for which both the spectrum of any potential source as well as the radial distance, significantly impact the convergence of the spectral integrals involved in the near field evaluation.

As a final remark regarding the near field decomposition into a finite sum of terms, it will be indicatively showcased for both the uniform (*2.14*) and non-uniform (*3.23*) phase centre choices. This is illustrated for an observation sphere of $2\lambda_0$ radius from the phase center of the wideband structure, through Figure 3-30 and Figure 3-31 respectively. Both asymptotic approximations employ three terms in the expansion of the regularized part.

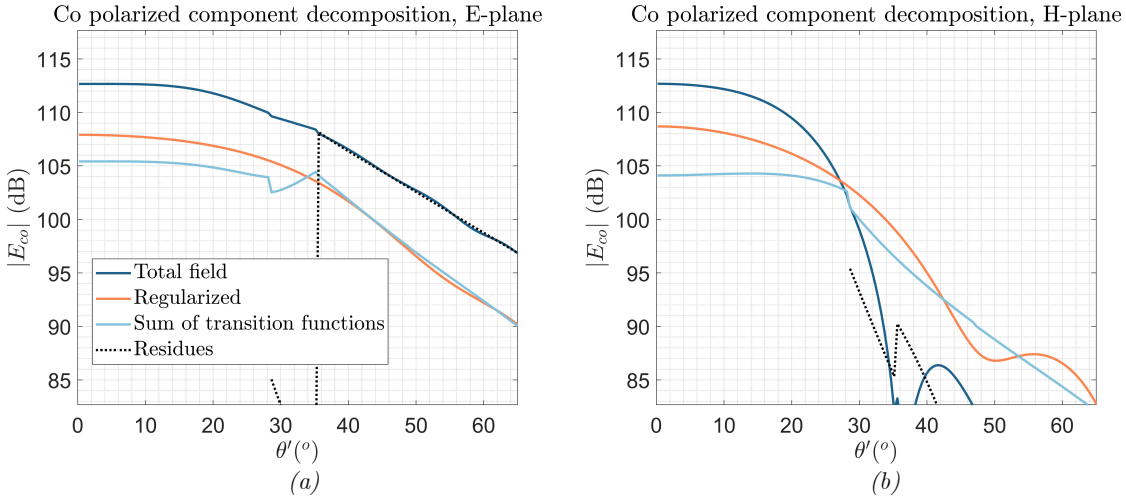

Figure 3-30. Field decomposition for asymptotic approximation with the uniform phase centre choice (a) E and (b) H-plane (150 GHz). The observation grid is a sphere of $r' = 2\lambda_0$ from the phase centre (wideband structure).

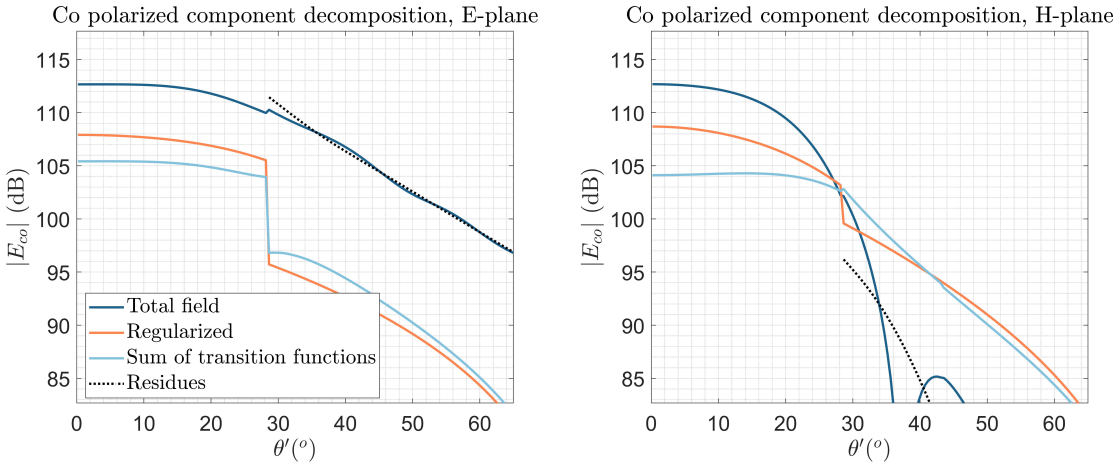

Figure 3-31. Field decomposition for asymptotic approximation with the non-uniform phase centre choice (a) E and (b) H-plane (150 GHz). The observation grid is a sphere of $r' = 2\lambda_0$ from the phase centre (wideband structure).

3.3d. Applicability region

The trade-off involved for this improvement of the computational efficiency through the asymptotic approximation of the near field, refers to the applicability region of the approximations introduced through *section 3.2c*. To visualize this impact in accuracy and how it changes with the radial distance, the co and cross polarized components of the near field (*3.25*) will be evaluated over spherical observation grids of different radii from the phase centre for both the wideband and resonant structures. For this comparison, the non-uniform asymptotic approach will be employed (*3.23*). Even so, it should be noted that for the region along broadside for which the main accuracy concerns will be expressed, both the uniform and non-uniform approaches are actually equivalent. Having said the above, as a first step for the following discussion the numerical and asymptotically approximated near field will be compared for the wideband structure and two observation grids of $r' = 2\lambda_0$ and $r' = 1.4\lambda_0$ from the phase centre through Figure 3-32 and Figure 3-33 respectively. In both cases, the asymptotic approximations is performed with three terms in the expansion of the regularized part.

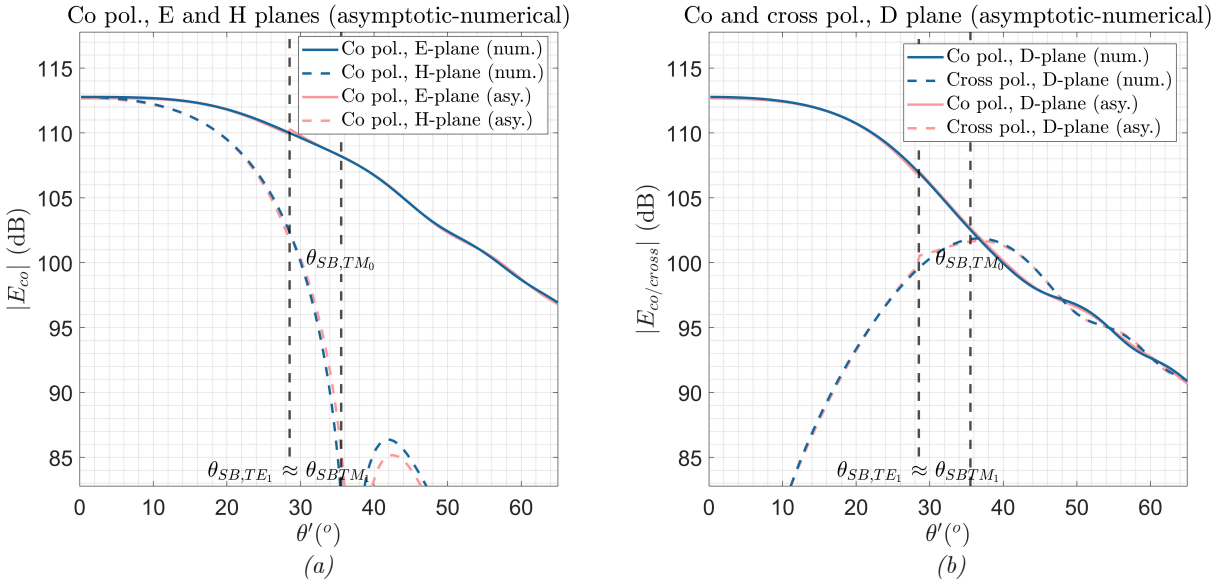

Figure 3-32. Field comparison for numerical integration and asymptotic approximation (3 term expansion of the regularized part), (a) co pol. at E and H planes, (b) co and cross pol. at D plane (150 GHz). The observation grid is a sphere with $r' = 2\lambda_0$ (wideband structure).

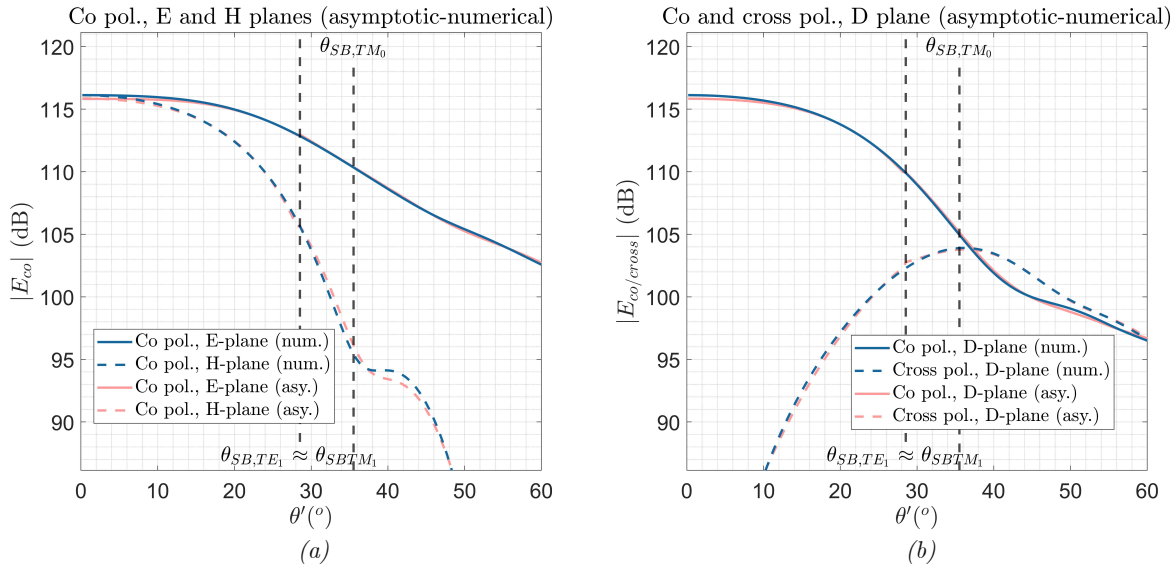

Figure 3-33. Field comparison for numerical integration and asymptotic approximation (3 term expansion of the regularized part), (a) co pol. at E and H planes, (b) co and cross pol. at D plane (150 GHz). The observation grid is a sphere with $r' = 1.4\lambda_0$ *(wideband structure).*

As visualized through the figures above, the approximations of *section 3.2c* result into slight discontinuities at all the shadow boundaries in the asymptotically approximated near field, due to the different treatment of the SDP integrals and the residue contributions. However, given the small level of those discontinuities, what in fact constitutes a limit for the applicability region of the asymptotic approach is the somewhat reduced accuracy along broadside with the reduction of the radial distance. This effect can be justified through the physical interpretation of the introduced approximations and the nature of the near field. In particular, as discussed through *section 3.2d* the approximations of (*3.21 a*) essentially implies the near field spherical wave formation for $\theta' < \theta_{SB}$. Consequently, the applicability region of this asymptotic approach is inherently limited to radial distances where the introduced definition of the phase centre enables this spherical wave formation around broadside.

In turn, the radial distance from the phase centre where this nature of the near field can be assumed for a leaky wave structure depends on its directivity, as hinted through the Poynting vector angles examined in the final section of Chapter 2 (Figure 2-11 and Figure 2-12 *(e)*, *(f)*). More specifically, given the relatively large attenuation constants (α_{LW}) for the significant leaky wave modes in the wideband structure, the near field spherical wave formation can be considered even at very small distances from the phase centre, as visualized through Figure 3-32 and 3-33. Contrary to the latter, due to the small attenuation constants of the significant modes in the resonant structure, the larger aperture field distribution formed by the leaky waves implies that the spherical wave formation occurs at larger distances from the phase centre as hinted through the Poynting vector angle depicted in Figure 2-12 *(e)* and *(f)*. In turn, this leads to the failure of the presented asymptotic approach for distances very close to the source. To visualize this concept, the numerical and asymptotically evaluated field for the resonant structure will be compared through Figure 3-34 and Figure 3-35, referring to observation grids of $r' = 8\lambda_0$ and $r' = 5\lambda_0$ respectively. Similar to the previous case of the wideband structure, three terms are included in the expansion of the regularized part.

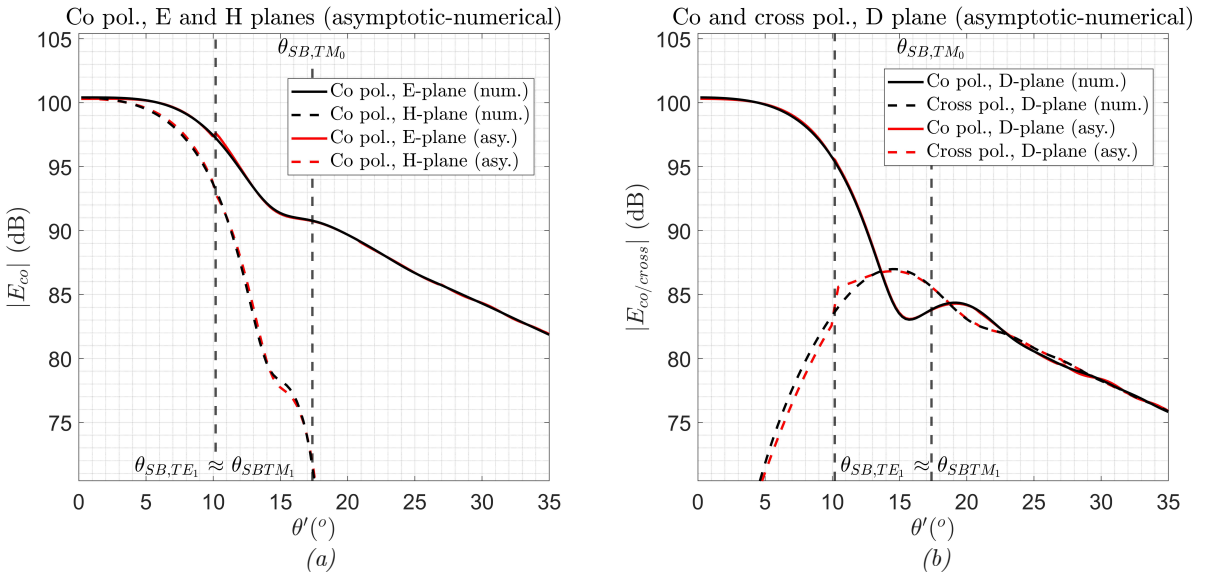

Figure 3-34. Field comparison for numerical integration and asymptotic approximation (3 term expansion of the regularized part), (a) co pol. at E and H planes, (b) co and cross pol. at D plane (150 GHz). The observation grid is a sphere with $r' = 8\lambda_0$ *(resonant structure).*

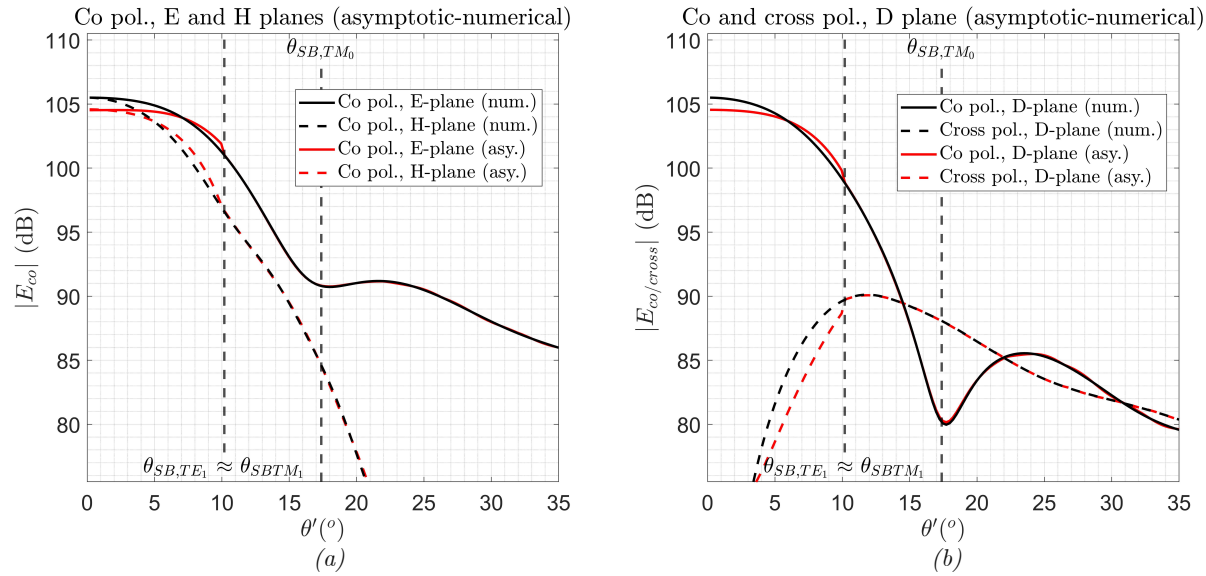

Figure 3-35. Field comparison for numerical integration and asymptotic approximation (3 term expansion of the regularized part), (a) co pol. at E and H planes, (b) co and cross pol. at D plane (150 GHz). The observation grid is a sphere with $r' = 5\lambda_0$ *(resonant structure).*

Following the above discussion one can deduce that accurately reconstructing the near field of the leaky wave structure through the introduced asymptotic approach, requires evaluating it at radial distances where the spherical wave formation around broadside can be assumed. Taking this into account, in the remaining part of this section a rough estimate of the region which satisfies this nature of the near field will be identified for both the examined structures. This is performed through deriving the percentage magnitude and absolute phase errors between the co polarized component obtained via the numerical and asymptotic approaches, as given below.

$$E_{rror,mag}(\theta',\varphi) = \frac{|E_{co}^{num}(\theta',\varphi)| - |E_{co}^{asy}(\theta',\varphi)|}{|E_{co}^{num}(\theta',\varphi)|} \tag{3.28}$$

$$E_{rror,phase}(\theta',\varphi)\,[deg] = \left|\left(\measuredangle E_{co}^{num}(\theta',\varphi) - \measuredangle E_{co}^{num}(0,0)\right) - \left(\measuredangle E_{co}^{asy}(\theta',\varphi) - \measuredangle E_{co}^{asy}(0,0)\right)\right|$$

Subsequently, the maximum errors are computed for both the wideband and resonant structures, using different number of terms in the expansion of the regularized part. The resulting comparison is illustrated through Figure 3-36, in terms of the electrical distance of the observation spheres from the respective phase centre positions. Given that the failure of the approximation (*3.21 a*) occurs along broadside, as seen through Figure 3-33 and Figure 3-35, this process is performed for $\theta' < min(\theta_{SB,TE_1}, \theta_{SB,TM_1})$.

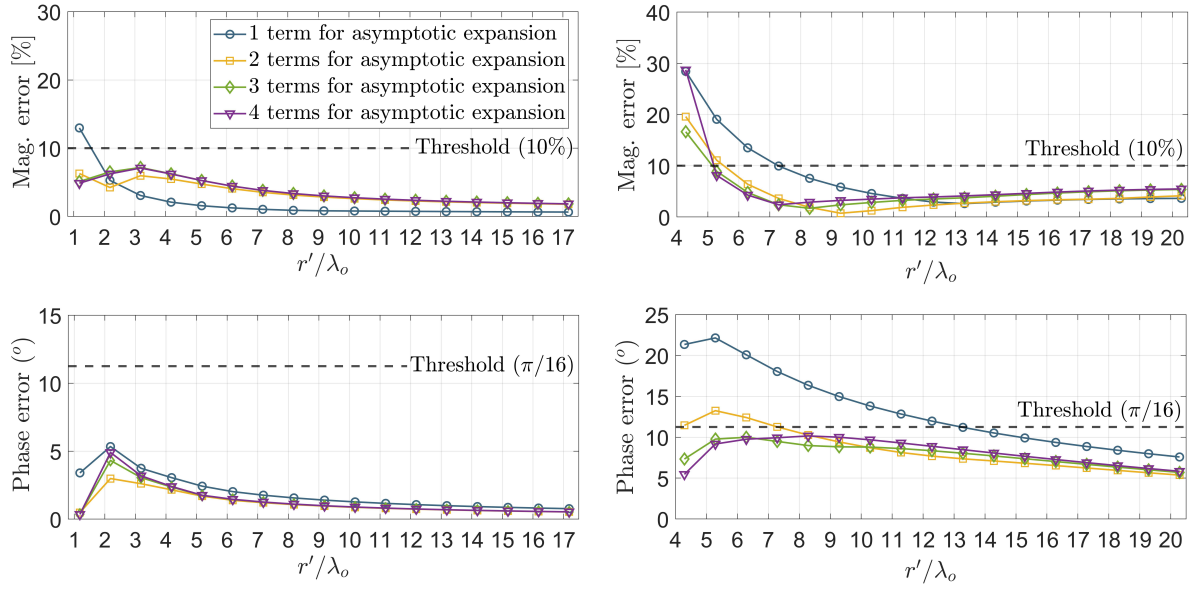

Figure 3-36. Maximum percentage magnitude and absolute phase errors between numerically and asymptotically evaluated co polarized component (E_{co}). The examined errors refer to the solid angle defined by the smallest shadow boundary angle (θ_{SB}), for (a) the wideband and (b) the resonant structure.

Through comparing the above presented maximum errors, the applicability limit of the asymptotic approach can be visualized. In particular, it can be noticed that increasing the number of terms above a certain point would not lead to any improvement in terms of recovering the field around broadside at small radial distances. This essentially constitutes the inherent limitation of the asymptotic approach, arising from the assumed nature of the near field. Taking this into account, for the remaining of this document three terms will be used in the expansion of the regularized part to obtain the asymptotically approximated near field.

Defining in a somehow arbitrary manner a maximum acceptable error of *10%* for the magnitude and *11.25^o* absolute error for the phase, the applicability region of the asymptotic approach can be identified as less than *1* and roughly *5.5* λ_0 for the wideband and resonant structures respectively.

Before proceeding further, it should be noted that the fundamental difference of leaky wave structures with different dielectric contrasts between the cavity and semi-infinite region, refers to the dispersion of the excited leaky wave modes. In turn, this determines the operational bandwidth of the respective structure. Therefore, examining the applicability region of the asymptotic approach only for the central frequency is somewhat lacking in terms of evaluating its actual utility. For this reason, the same maximum errors for the co polarized component will be derived for the lower and higher frequencies of the structures' bandwidths, assuming the central frequency at *150 GHz* and a *40%* and *15%* operational bandwidth for the wideband and resonant structures respectively. The resulting maximum magnitude and phase errors for both structures are presented through Figure 3-37. The errors are computed in spheres of progressively larger radii, centred at the phase centre position of the leaky wave structure for the central frequency. The normalizing free space wavelength on the horizontal axis refers to that of the central frequency ($\lambda_0 = \lambda_0^{150\ GHz}$).

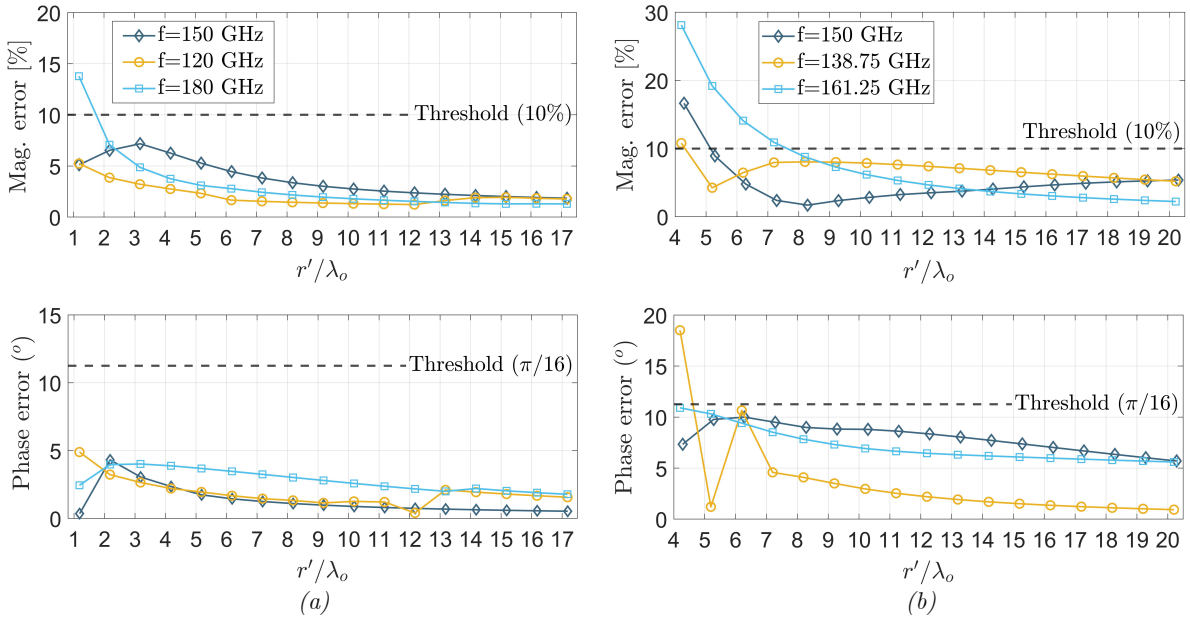

Figure 3-37. Maximum percentage magnitude and absolute phase error between the numerically and asymptotically evaluated co polarized component, for $\theta' < \theta_{SB}^{150\,GHz}$ and different frequencies (a) wideband and (b) resonant structure.

As visualized through the figures above, the change of the operational frequency has a notable impact in the applicability region of the asymptotic approach. In fact, this impact seems to be more significant at higher frequencies, given the larger aperture field distribution formed by the leaky waves (smaller α_{LW}) and thus the more directive nature of the structure. This in turn forces the previously discussed assumption for the nature of the near field further away from the source. Consequently, to extract a somewhat more conservative estimate for the applicability region of the asymptotic approach, the same maximum acceptable thresholds are introduced for the percentage magnitude and absolute phase errors. The resulting limits for the applicability region are roughly *1.5* λ_0 and *8* λ_0 for the wideband and resonant structures respectively, where λ_0 refers to the free space wavelength for the central frequency (*150 GHz*).

Apart from the larger directivity of the structure as the frequency increases, another noteworthy aspect regarding the applicability region refers to the accuracy of the phase centre definition presented through [20]. As a matter of fact, its derivation employs an approximation for the phase of the co polarized component, given in [34], which assumes a similar nature for the *TE₁* and *TM₁* leaky wave modes, as well as that for each mode the attenuation constant is almost equal to the propagation constant ($\alpha_{LW} \approx \beta_{LW}$) [40], something that fails away from resonance (i.e., when $h \neq \lambda_{cav}/2$).

To visualize this performance degradation of the asymptotic approximation with frequency, the numerically and asymptotically evaluated near field will be compared for the wideband structure and an observation grid of $r' = 3.2mm$ from the phase center at *150 GHz* (Δ_z=*0.84mm*), through Figure 3-38.

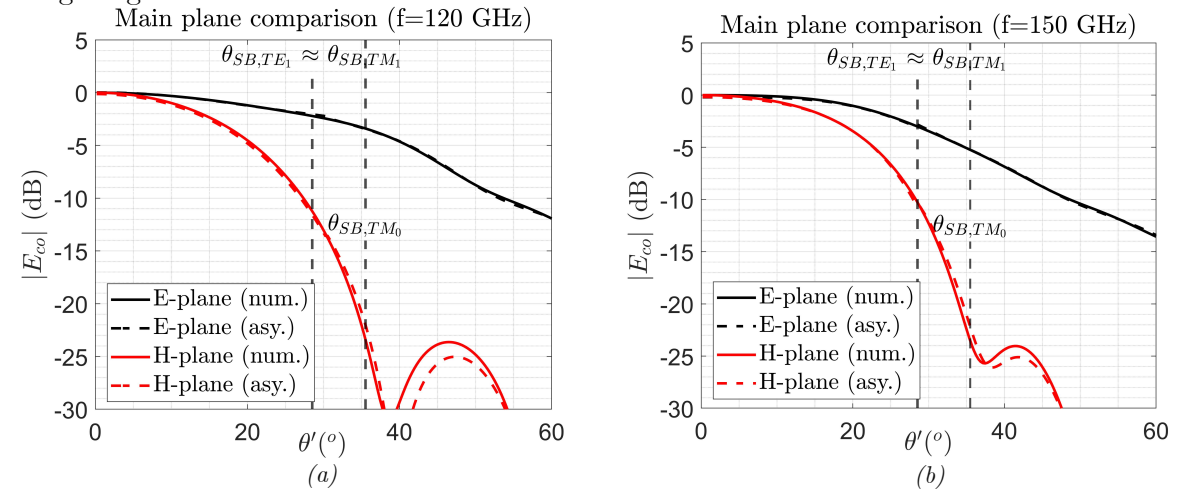

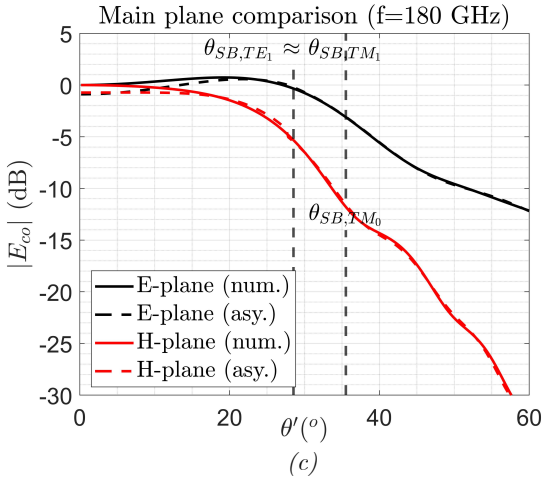

(c)

Figure 3-38. Field comparison for numerically and asymptotically evaluated near field (3 term expansion of regularized part), (a) 120 GHz, (b) 150 GHz and (c) 180 GHz. The observation grid is a sphere with $r' = 3.2mm$ *from the phase centre at the central frequency (*Δ_z*=0.84mm) and it refers to the wideband structure.*

Evidently, the more significant degradation of the asymptotic approximation's accuracy appears at the higher frequencies, due to the larger field distribution formed by the leaky waves inside the cavity and thus the higher directivity of the structure.

To conclude the discussion presented in this chapter, the asymptotic approximation of the SDP integral expressions allows for a much faster derivation of the near field for a leaky wave structure around resonance. Moreover, provided that the phase centre choice enables the assumption for a spherical wave formed in a region around broadside, the asymptotic approximation maintains good accuracy. At those regions, the only hint of any approximation appears through the discontinuities at the shadow boundaries arising from the different treatment of the residues and the SDP integrals. In addition, these discontinuities are a bit more evident in planes dominated by *TM* modes, due to neglecting the impact of the TM_0 in the phase centre choice of *section 3.2d*. It should be noted that while the above presented approach could be applied for the study of near field lenses, like that of the Fly's Eye antenna concept, a more generic asymptotic near field study would require a complete treatment of the Hankel function, instead of using the approximation of (*3.21 a*).

CHAPTER 4. NEAR FIELD LENSES

In the previous chapter, the approximations of the SDP integrals which enabled the asymptotic evaluation of the near field for elementary sources were introduced and the near field decomposition was discussed. To build upon this concept, the following chapter will briefly explore the use of the asymptotically approximated near field to illuminate small lenses. For this purpose, the additional considerations required to enable the asymptotic approximation of the near field when an actual current distribution is considered in the ground plane will first be presented. Following this, some indicative cases of small lenses will be examined. This study will showcase one potential benefit of putting a lens in the near field and also provide an indicative example on how the decomposition of the incident field into wave components can contribute to the analysis and design of small lenses.

4.1. Source inclusion

4.1a. Integral formulation

Considering an equivalent magnetic current distribution in the ground plane of a leaky wave supporting stratification similar to those of Figure 2-8, the near field can be evaluated through the following double spectral integral. This integral corresponds to the inverse Fourier transform of the convolution between the Spectral Green's function and the current distribution in the ground plane. Assuming an equivalent magnetic current distribution in the ground plane, the pertinent Green's function is the one relating electric fields and magnetic currents (i.e., $\bar{\bar{G}}^{em}(k_\rho, \alpha, z, z_s)$).

$$\vec{E}(\vec{r}) = \frac{1}{4\pi^2}\int_0^{+\infty}\int_0^{2\pi} \bar{\bar{G}}^{em}(k_\rho, \alpha, z, \Delta_z)\cdot \vec{C}_m(k_\rho, \alpha) e^{-jk_\rho \rho\, cos(\alpha-\varphi)} k_\rho d\alpha dk_\rho, \qquad (4.1)$$

Where $\vec{C}_m(k_\rho, \alpha)$ refers to the spectrum of the equivalent current distribution.

In order to resort to either the computationally efficient numerical methods for the near field evaluation (Chapter 2) or the asymptotic approach (Chapter 3), the α integral must first be closed, leading to the single complex integral expression in k_ρ similar to equation (*2.2 b*). When an elementary source was considered in Chapter 2, this step was performed through the use of the identities given in (*2.2 a*). However, for the case of an actual current distribution in the ground plane, this approach is not directly applicable.

To enable the closing of the integral in α in the same manner and end up with the single complex integral in k_ρ, the spectrum of the current distribution ($\vec{C}_m(k_\rho, \alpha)$) must first be extracted from the α integral. This can be performed through the stationary phase point approximation. In particular, considering the spectrum of the source slow varying in α compared to the exponential of the integrand ($e^{-jk_\rho \rho\, cos(\alpha-\varphi)}$), $\vec{C}_m(k_\rho, \alpha)$ can be evaluated on the saddle point $\alpha_{SP} = \varphi$ and subsequently extracted from the integral as shown below.

$$\vec{E}(\vec{r}) = \frac{1}{4\pi^2}\int_0^{+\infty} C_m(k_\rho, \varphi)\int_0^{2\pi} \bar{\bar{G}}^{em}(k_\rho, \alpha, z, \Delta_z)\cdot \hat{y} e^{-jk_\rho \rho\, cos(\alpha-\varphi)} k_\rho d\alpha dk_\rho, \qquad (4.2)$$

$$\text{assuming } \vec{C}_m(k_\rho, \alpha) = \hat{y} C_m(k_\rho, \alpha)$$

Following this step, the remaining α integral can be evaluate as was done for an elementary source in *section 2.2a* and subsequently the near field can be treated either numerically or asymptotically. One alternative to the above would be to represent a more complex current distribution through a number of elementary sources with different weights. This would enable directly employing the asymptotic approach of Chapter 3 but would require superimposing a potentially large number of sources, depending on the modelled current distribution. As such, this approach would end up being somewhat more time consuming and thus it will not be considered further at this stage.

4.1b. Slow varying spectrum on α

When the observation grid is far away from the source, the assumption for a slow varying spectrum of the current distribution on α can be employed without much consideration. This is attributed to the large radial distance of the observation points (r'), which make the exponential term ($e^{-jk_\rho \rho\, cos(\alpha-\varphi)}$) fast varying on the integration path compared to the spectrum of the source ($\vec{C}_m(k_\rho,\alpha)$). Having said the above, in the near field where the radial distance of the observation points is not that large, additional considerations must be made prior to this assumption in order to ensure the slow varying nature of the source's spectrum.

Considering an overview of the problem at hand, leaky lenses are usually illuminated by a pair of apertures in the ground plane which are spaced apart such that they suppress the TM_0 in its dominant plane [17]. More specifically, the suppression of the TM_0 is performed through forcing a null around its polar singularity ($k_{\rho,LW}^{TM_0}$) via the array factor of the employed apertures. While these can feature an iris shape to enhance the suppression in the diagonal planes, for the time being we will consider elementary sources for simplicity.

If the assumption for a slow varying spectrum is performed when the array factor is included in the spectral representation of the source ($\vec{C}_m(k_\rho,\alpha)$), its accuracy will degrade, especially around the angular region where the array factor contributes its null. Taking the above into account, such structures comprised of a pair of elements can be more conveniently treated through superposition, as indicatively illustrated in Figure 4-1.

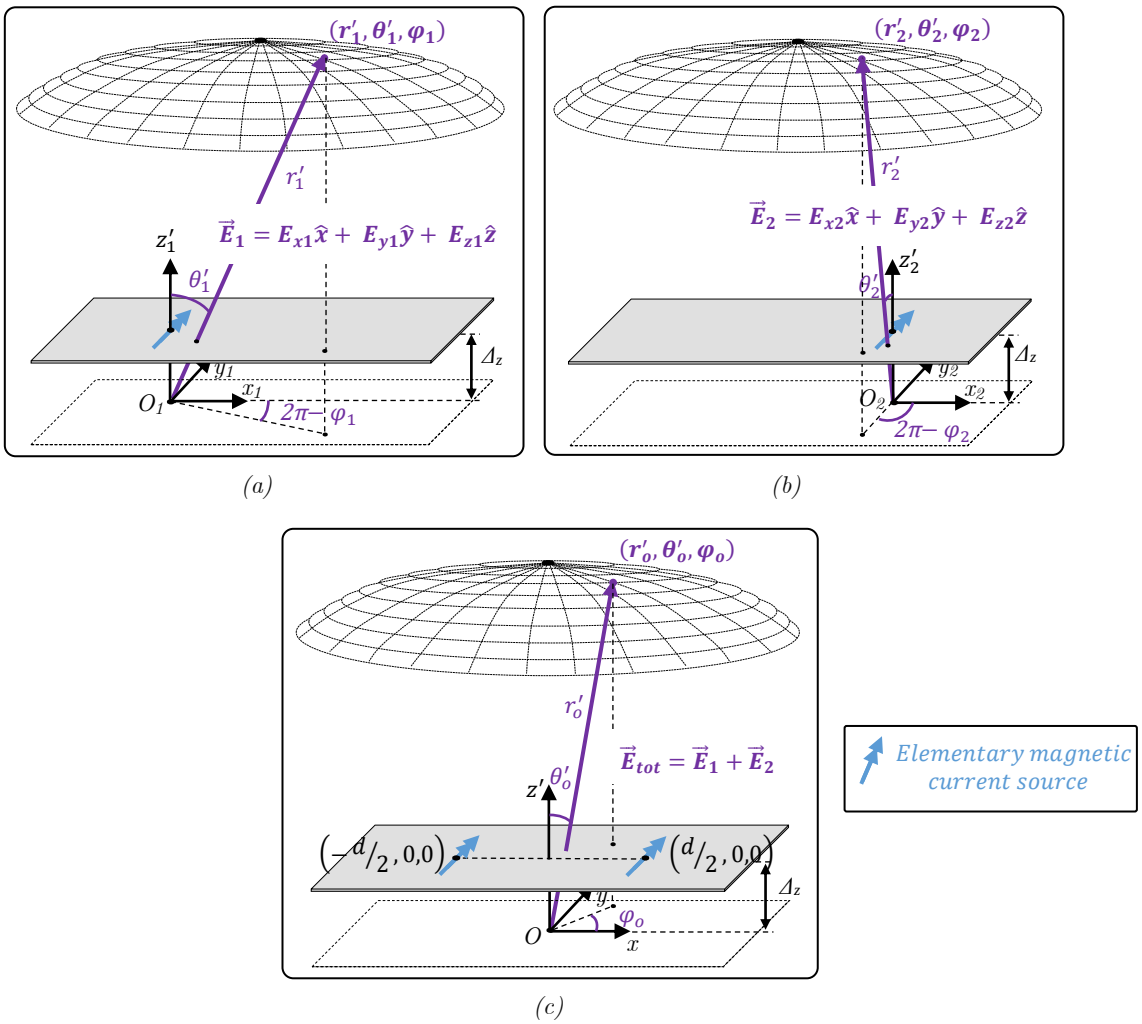

Figure 4-1. Combination of the fields from individual sources (a) and (b), for the derivation of the total field of a double elementary magnetic current source (c).

To showcase this improvement in accuracy resulting from the use of superposition, one indicative example is considered for the above presented double elementary structure. In particular, two y-oriented elementary sources are assumed in the ground plane of the wideband structure ($\varepsilon_{r,cav} = 3.8$ and $\varepsilon_{r,inf} = 12$), spaced along x by $d = 500\,\mu m \approx \pi/Re(k_{\rho,LW}^{TM_0})$, such that they suppress the TM_0 in the E-plane. In turn, the near field extracted through the superposition of the two elementary sources ($C_{m,ele}(k_\rho, \alpha) = 1$) is compared to that obtained by using their combined spectrum ($C_{m,double}(k_\rho, \alpha) = 2\cos(k_\rho\, cos(\alpha)\, d/2)$) and assuming it to be slow varying on α, as given through (*4.2*). The near field is evaluated numerically for both approaches at the central frequency (*150 GHz*) and in turn compared over a sphere close to the source ($r' = 2.5\,mm \cong 1.25\lambda_0^{150\,GHz}$). To illustrate which approach is more accurate, the near field extracted through of a full-wave simulation (CST) is also included in the comparison of Figure 4-2.

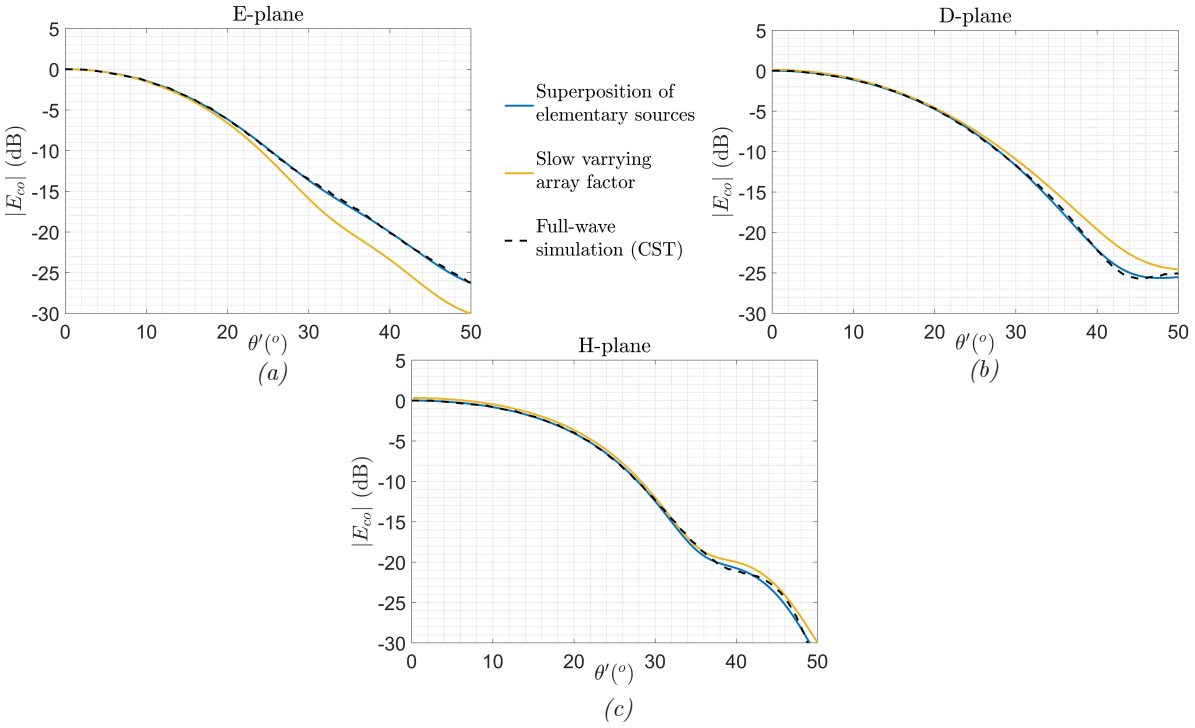

Figure 4-2. Near field comparison ($r' = 2.5\,mm$) for two y-oriented elementary magnetic current sources integrated in the ground plane of the wideband structure of Figure 2-8. The two elementary sources are spaced in x by 500μm, while the observation grid is drawn with respect to the phase centre of the structure (Δ_z=0.42λ_0). The resulting comparison is performed in the main planes with (a) E-plane, (b) D-plane and (c) H-plane.

As evident from the figures above, deriving the field through the superposition of the two sources improves the accuracy of the evaluated near field around angular regions where the array factor features its null. Having said that, it is without saying that the difference of the two approaches is reduced as the observation grid moves away from the source, owing to the faster varying exponential with the increasing of the observation distance (r'). Even so, to preserve the accuracy of the near field evaluation even for very small radial distances, structures of double straight or elementary sources will be treated through superposition for the remaining of this document.

To finalize this section, the co and cross polarized field components extracted through the full-wave simulation of the double elementary structure will also be compared to the asymptotically approximated near field, using three terms in the expansion of the regularized part. The comparison refers to the main planes over the same observation grid as Figure 4-2 and is depicted through Figure 4-3.

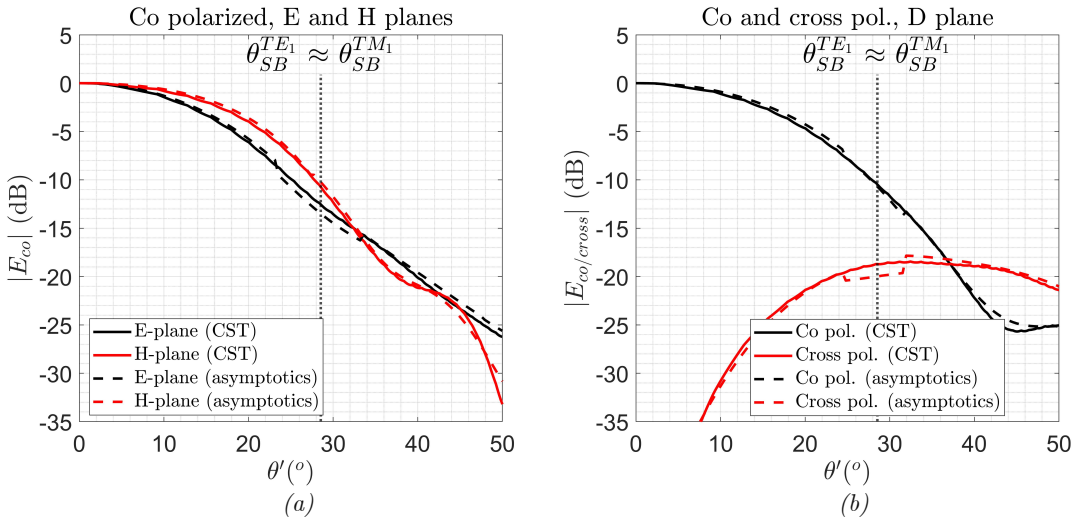

Figure 4-3. E-field comparison for double elementary structure (d = 500 μm), (a) co pol., E and H planes, (b) co and cross pol., D plane (150 GHz). The observation grid is identical to that of Figure 4-2.

Evidently the asymptotically approximated near field is in very good agreement with the full-wave simulation. The only notable difference refers to the discontinuities around the shadow boundary of the *TM1* mode ($\theta_{SB}^{TM_1} \cong 28^o$), mainly visible for the co polarized component in the E-plane and the cross polarized in the D-plane. These discontinuities arise from the different approximations introduced in the treatment of the SDP integral and the residue contributions. They are more evident in planes with significant impact from the *TM* modes due to the simplification employed for the phase centre choice in the *TM* integrals in *section 3.2d*.

4.1c. Straight slots as feeding elements

Further expanding on the above discussion, double straight slots will also be treated apart from pairs of elementary structures. The spectrum of the current distribution of a straight slot can be approximated as given below for y-oriented slots, where the effective wavenumber is chosen as $k_{eff} = (k_0 + k_{d,cav})/2$.

$$\vec{C}_{m,slot}(k_\rho, \alpha) = \hat{y}\frac{2k_{eff}sinc\left(\frac{k_\rho cos(\alpha)W_{slot}}{2}\right)\left(cos\left(\frac{k_\rho sin(\alpha)L_{slot}}{2}\right) - cos\left(\frac{k_{eff}L_{slot}}{2}\right)\right)}{\left(k_{eff}^2 - k_\rho^2 \sin^2(\alpha)\right) sin\left(\frac{k_{eff}L_{slot}}{2}\right)}, \qquad (4.3)$$

While pairs of straight slots will be treated through superposition, as described in the previous section, for each individual slot the slow varying assumption for its spectrum will still be employed ($\vec{C}_{m,slot}(k_\rho, \alpha) \cong \vec{C}_{m,slot}(k_\rho, \varphi)$). This step introduces an approximation with respect to the actual near field. However, for reasonable sized slots (i.e., L_{slot} around $\lambda_{eff}/2$), the impact of this approximation is negligible compared to the simplification it introduces. To illustrate this, the single slot depicted through Figure 4-4 will be indicatively examined.

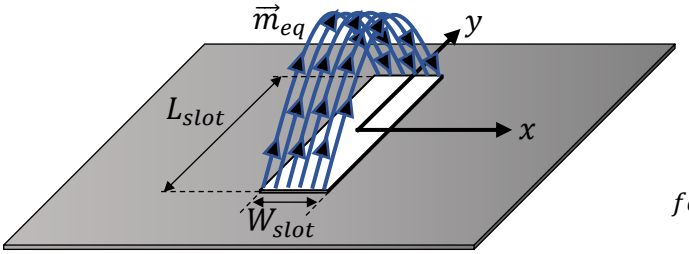

$$L_{slot} = \frac{\lambda_{eff}^{150\,GHz}}{2}$$
$$W_{slot} = \frac{\lambda_{eff}^{150\,GHz}}{20}$$
$$for \quad k_{eff} = \frac{k_0 + k_{d,cav}}{2}$$

Figure 4-4. Single straight slot used to evaluate the slow varying assumption for its spectrum.

In order to evaluate the impact of assuming a slow varying spectrum for the indicated straight slot, the field resulting from the double integral of (*4.1*) will be compared to that

obtained by using the slow varying spectrum assumption ($C_m(k_\rho,\alpha) \cong C_m(k_\rho,\varphi)$) and in turn employing the integral of (*4.2*). The resulting comparison for *150 GHz* is depicted in Figure 4-5, referring to a sphere of $r' = 3\,mm$ from the phase center of the wideband structure.

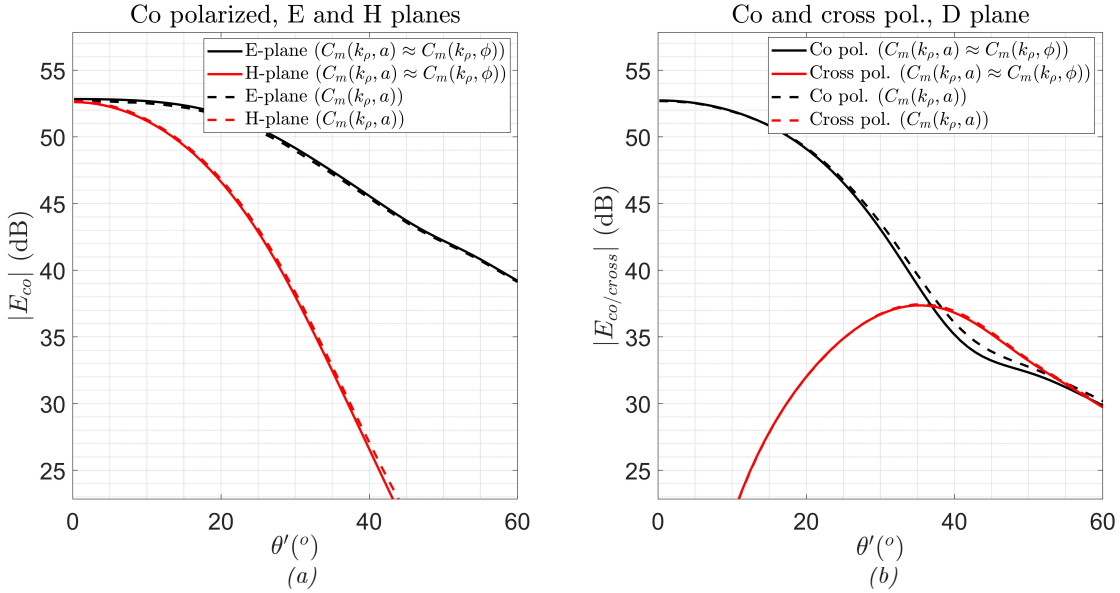

Figure 4-5. E-field comparison for double and single integral evaluation (150 GHz), (a) co pol. at E and H planes, (b) co and cross pol. at D plane. The observation grid is a sphere with $r' = 3mm = 1.5\lambda_0$ *(wideband structure).*

As visualized from the figures above, the assumption for a slow varying spectrum constitutes a very good approximation for the examined slot, even for observation points very close to the source. This is important since combining the above approximation with the array factor treatment of *section 4.1b* enables the subsequent evaluation of the near field of double straight slots through either the methods described in Chapter 2 or 3.

4.1d. Asymptotic analysis

Introducing the Fourier transform of the current distribution in the near field integral expressions slightly modifies the asymptotic approach described through Chapter 3. This section will explain this concept and describe the required treatment when a single slot is considered in the ground plane of the stratification. Towards this goal, the field decomposition resulting from the regularization of the SDP integral expressions is re-written below.

$$\vec{E}(\vec{r}') = \vec{E}_{Reg.}(\vec{r}') + \vec{E}_{Pole}(\vec{r}') + \sum_{i=1}^{3} U\left(\theta' - \theta_{SB,i}\right)\vec{E}_{LW,i}^{TE/TM}(\vec{r}'), \qquad (4.4\ a)$$

Where $\vec{E}_{Pole}$ is the part containing all the polar contributions of the SDP integrals.

Regarding the field decomposition presented above, the approaches used to evaluate the residue contributions of the polar singularities ($\vec{E}_{LW,i}^{TE/TM}(\vec{r}')$) as well as the regularized part of the SDP integral ($\vec{E}_{Reg.}(\vec{r}')$), are not modified by the presence of the source's spectrum in the integrand. Having said that, what does change is the treatment of the part of the SDP which contains all its singularities, i.e., $\vec{E}_{Pole}(\vec{r}')$. To showcase why this occurs and present an approach to resolve the problem, the integral expressions of $\vec{E}_{Pole}(\vec{r}')$ are first expressed for a y-oriented slot, as given below.

$$\begin{bmatrix} E_{\rho,Pole}(\vec{r}') \\ E_{\varphi,Pole}(\vec{r}') \\ E_{z,Pole}(\vec{r}') \end{bmatrix} = \frac{1}{4\pi}\sqrt{\frac{2k_d^3}{\pi r'}}\, e^{j\frac{\pi}{4}} e^{-jk_d r'} \int_{-\infty}^{+\infty} \begin{bmatrix} -cos(\varphi)\left(v_{apr,TM_1}^{+} + v_{apr,TM_0}^{+}\right) \\ sin(\varphi)\, v_{apr,TE_1}^{+} \\ \zeta_d\, cos(\varphi)\left(i_{apr,TM_1}^{+} + i_{apr,TM_0}^{+}\right) sin(\beta) \end{bmatrix} C_{m,slot}(k_\rho,\varphi)\, cos(\beta) \left(\frac{d\beta}{ds}\right) e^{-k_d r' s^2} ds \qquad (4.4\ b)$$

Where $C_{m,slot}(k_\rho,\varphi)$ as given in (*4.3*), $v_{apr,TM/TE}^{+} = v_{apr,TM/TE}^{+}(k_\rho,\Delta_z)$ and $i_{apr,TM/TE}^{+} = i_{apr,TM/TE}^{+}(k_\rho,\Delta_z)$. Also, while several spectral variables are included in the integrands to maintain a compact form, namely k_ρ, β and s, all are related as given in (*2.8*) and (*3.4*).

In *section 3.2b* it was described that at this stage the integrands must be expressed through four simple poles which in turn can be evaluated asymptotically, resulting into a sum of transition functions as given in (*3.17*). Following this mindset, the representation of $G_{pole}(s)$ is introduced in the integrands and subsequently expressed as given through (*4.4 d*).

$$\begin{bmatrix} E_{\rho,Pole}(\vec{r}') \\ E_{\varphi,Pole}(\vec{r}') \\ E_{z,Pole}(\vec{r}') \end{bmatrix} = \frac{1}{4\pi}\sqrt{\frac{2k_d^3}{\pi r'}}e^{j\frac{\pi}{4}}e^{-jk_d r'}\int_{-\infty}^{+\infty}\begin{bmatrix} -cos(\varphi)\left(G_{pole}^{v_{TM_1}}(s)+G_{pole}^{v_{TM_0}}(s)\right) \\ sin(\varphi)\,G_{pole}^{v_{TE_1}}(s) \\ \zeta_d\,cos(\varphi)\left(G_{pole}^{i_{TM_1}}(s)+G_{pole}^{i_{TM_0}}(s)\right) \end{bmatrix} C_{m,slot}(k_\rho,\varphi)e^{-k_d r' s^2}ds, \quad (4.4\ c)$$

$$G_{pole}^{(v/i)_{TE/TM}}(s) = \sum_{i=1}^{4}\frac{a_{pi}^{(v/i)_{TE/TM}}}{s-s_{pi}^{(v/i)_{TE/TM}}}, \quad \text{where} \quad a_{pi}^{(v/i)_{TE/TM}} = \lim_{s\to s_{pi}}\left(s-s_{pi}^{(v/i)_{TE/TM}}\right)G_{pole}^{(v/i)_{TE/TM}}(s), \quad (4.4\ d)$$

At first glance, one might consider that the spectrum of the straight slot ($C_{m,slot}(k_\rho,\varphi)$) should be included in $G_{pole}(s)$ and in turn the treatment of (*4.4 d*) can be applied without issue. However, as was mentioned at the end of *section 3.2b* (*3.17 c*), if the integrand function also features zeros which approach the saddle point for some observation angles, these must also be isolated and subsequently evaluated through the canonical forms describing simple poles and zeros (*3.10 b*). For the case of elementary slots, the only zeros in the integrands were caused by cosine and sine functions arising in the representation. However, the addition of the Fourier transform of the source changes this aspect. In particular, the spectrum of a straight slot (*4.3*) features a number of periodic zeros with their proximity to the saddle point determined by the electrical size of the slot, and most importantly its length.

An analytical way to resolve this issue would require all the important zeros (the ones that approach the saddle point) to be isolated and treated as described in equation (*3.17 c*). Even so, to simplify this process and make it a bit more generic, the spectral behaviour of the source can be included in the integral by simply evaluating its spectrum on the dominant integral's contribution, namely, the saddle point ($k_{\rho SP} = k_d sin(\theta')$). To showcase the performance of this approach, the resulting co polarized component from the asymptotic approximation of the integrals (*4.4 c*) will be derived for the *TE₁* and the *TM₁* leaky wave modes in their respective dominant planes and compared to the numerical result. The asymptotically approximated terms will be obtained through both approaches, i.e., including $C_m(k_\rho,\varphi)$ in $G_{pole}(s)$ and using (*4.4 d*) as well as evaluating $C_m(k_\rho,\varphi)$ on the saddle point. The above described comparison is presented through Figure 4-6, referring to a spherical observation grid of $r' = 3\,mm$ from the phase centre of the wideband structure, with the utilized slot being that of Figure 4-4. While the illustrated results correspond to the non-uniform phase centre choice described in *section 3.2d*, the same deductions can also be extracted for the uniform case.

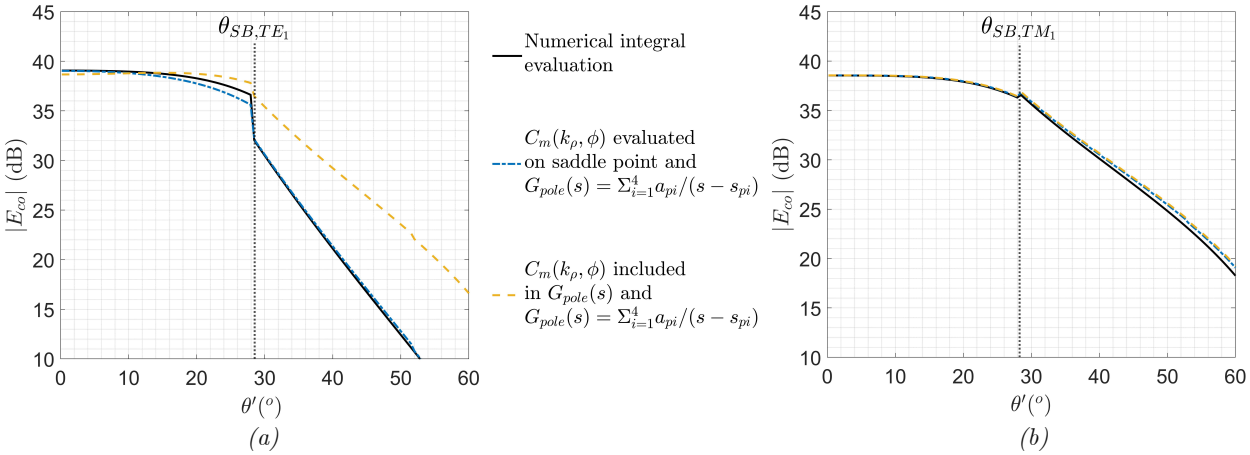

Figure 4-6. Co polarized component of polar contributions expressed in (4.4 c) for (a) TE₁ in the H-plane and (b) TM₁ in the E-plane, using different treatments for the spectrum of the source (f=150 GHz).

As visualized from the figure above, while for the TM_1 mode the presence of the source does not seem to impact the described treatment for its polar contributions, the same cannot be said for the case of the TE_1. This is due to the fact that the dominant zeros of the source's Fourier transform are attributed to its length. As such, for a y-oriented slot they appear at the H-plane and thus mainly impact the TE variants of the transmission line solutions. In order to increase the accuracy of the process, the source's spectrum around the saddle point can be represented through a power series expansion in terms of s. Given the electrical length of the examined slot ($L_{slot} = \lambda_{eff}/2$), in our case a two-term expansion is sufficient.

$$C_m(k_\rho, \varphi) \cong C_m(k_{\rho SP}, \varphi) + s\left(\frac{dk_\rho}{ds}\frac{dC_m(k_\rho,\varphi)}{dk_\rho}\right)_{k_\rho = k_{\rho SP}}, \tag{4.5}$$

To illustrate the impact of this step, the result of using (4.5) for the representation of the source is incorporated in the comparison of Figure 4-6. This is illustrated through Figure 4-7, showing improved agreement with the numerical integral in the region before the shadow boundary. It should be noted that, if necessary, a higher order expansion can also be employed instead of (4.5), to even better represent the spectrum of the source. However, as the source gets electrically larger and thus requires a higher order expansion, one should also consider evaluating the validity of the assumption for a slow varying spectrum on α.

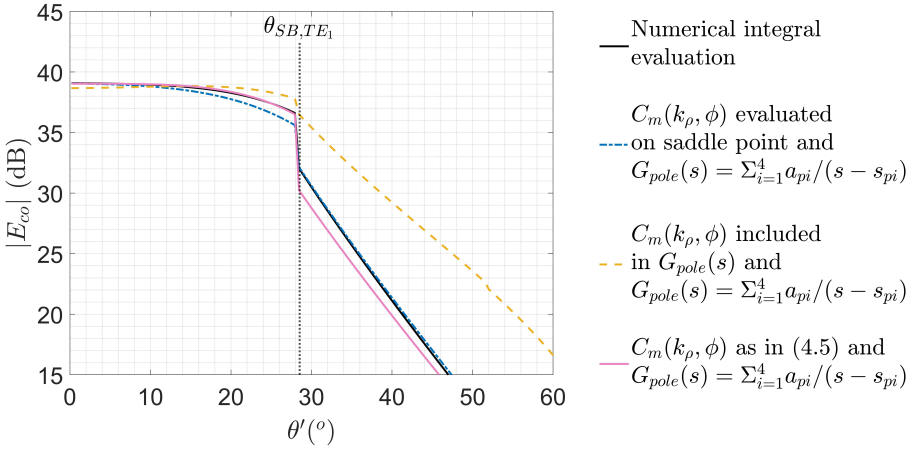

Figure 4-7. Co polarized component of (4.4 c) in the H-plane, considering only the TE_1 leaky wave mode.

To conclude this section, the performance of the described treatment in terms of modelling the behaviour of the source will be showcased by comparing the numerically and asymptotically evaluated near field for a pair of y-oriented slots. To do so, the co and cross polarized components of the field will be evaluated at spherical observation grids of different radii from the phase centre of the wideband structure, as illustrated through Figure 4-8 and Figure 4-9. Each slot is identical to that of Figure 4-4, with their spacing in x being d=500μm.

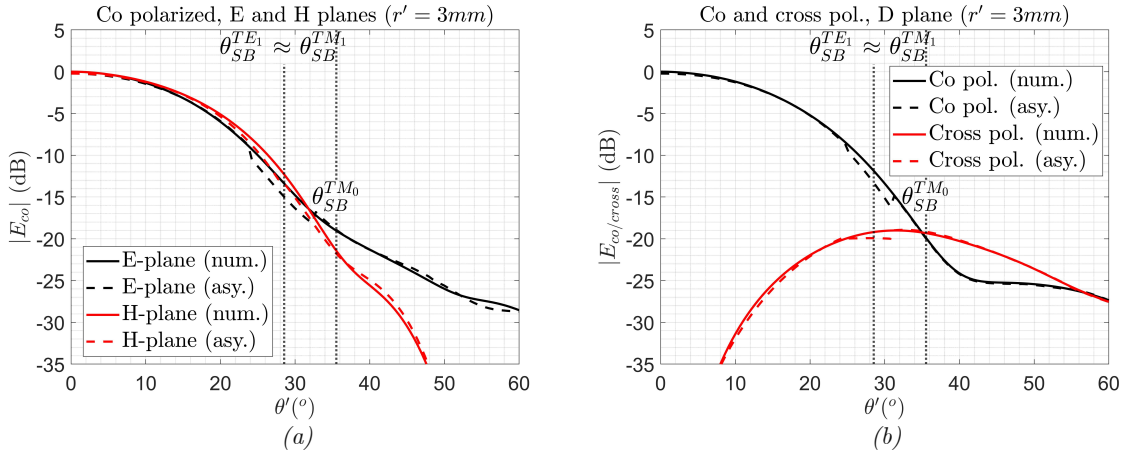

Figure 4-8. Numerical and asymptotic (3 term expansion of regularized part) comparison for $r' = 3mm = 1.5\lambda_0$ (wideband structure) (a) co pol. in E and H planes and (b) co and cross pol. in D plane (f=150 GHz).

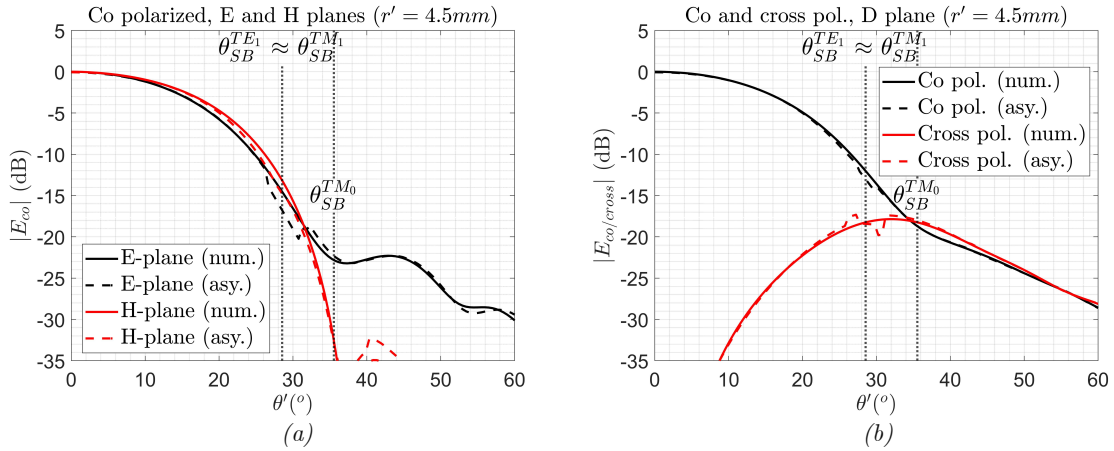

Figure 4-9. Numerical and asymptotic (3 term expansion of regularized part) comparison for $r' = 4.5mm = 2.25\lambda_0$ (wideband structure) (a) co pol. in E and H planes and (b) co and cross pol. in D plane (f=150 GHz).

As illustrated through the figures above, the numerical and asymptotically evaluated near field feature overall good agreement. Having said that, the superposition of the two individual elements forms a region around the shadow boundary angle of the TM_1 where the field is not that well represented. This region is situated between the crossings of the shadow boundary angle of the TM_1 for the individual elements from their respective reference systems. Given that this particular issue is somewhat reduced through the uniform phase centre choice described through *section 3.2d*, as indicatively visualized through Figure 4-10, it is reasonable to claim that in order to reduce its impact in Figure 4-8 and Figure 4-9, the phase centre choice for the TM integrals must be further improved to account for the presence of the TM_0.

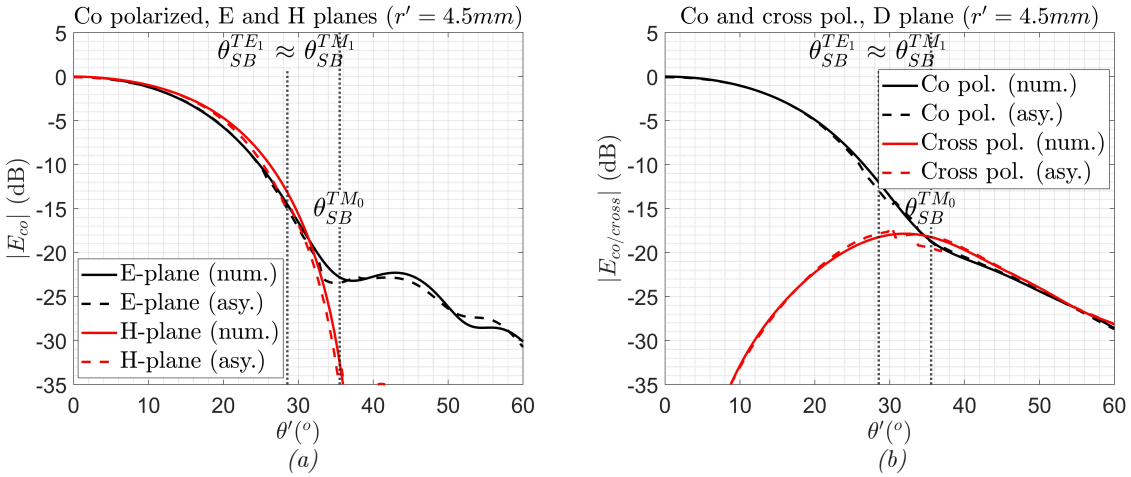

Figure 4-10. Numerical and asymptotic (3 term expansion of regularized part) comparison for $r' = 4.5mm = 2.25\lambda_0$ (wideband structure) using the uniform phase centre choice of section 3.2d, (a) co pol. in E and H planes and (b) co and cross pol. in D plane (f=150 GHz).

4.2. Small lenses in the near field

Having discussed all the complications involved with adding a double straight slot in the near field evaluation, in the following section the utility of the asymptotic approach will be showcased. This will be performed by examining small elliptical lenses, such that their surface approaches the near field of the source. For the illumination of those lenses, two y-oriented straight slots, each identical to that of Figure 4-4, are assumed in the ground plane of a leaky wave supporting stratification. The two sources are spaced in x such that the TM_0 is suppressed in the E-plane, i.e., $d \cong \pi / Re(k_{\rho,LW}^{TM_0})$, while the lens is truncated at the smallest shadow boundary angle $(\theta_{tru} = min\,(\theta_{SB}^{TE_1}, \theta_{SB}^{TM_1}))$ and its lower focus is centred at a distance Δ_z below the ground

plane, as illustrated through Figure 4-11. The truncation is introduced considering that elliptical lenses are optimally illuminated by spherical waves, whereas the near field of a leaky wave structure resembles a spherical wave only up to the shadow boundary.

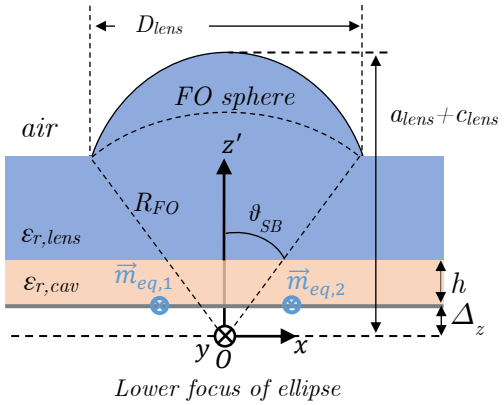

Figure 4-11. Elliptical lens integrated with leaky wave supporting stratification and fed by two y-oriented slots in the ground plane.

To evaluate the performance of the discussed asymptotic approach, the aperture efficiency of the examined lenses is computed using both the numerical and asymptotic methods for the derivation of the near field, with the resulting values subsequently being compared. In both approaches the field of the double slot is obtained through superposition in the Fourier Optics (FO) sphere, as was described through *section 4.1b*. Following this, the lens aperture efficiency is derived via evaluating the reaction integral between the Geometrical Optics (GO) fields in the FO sphere and the near field of the leaky wave structure at the same surface. The steps required for this analysis of lens antennas in reception, which in turn result in the evaluation of the aperture efficiency through the aforementioned reaction integral, can be found in the Appendix of [17].

The resulting comparison of the derived aperture efficiencies at the central frequency (*150 GHz*) for the resonant and wideband stratifications of Figure 2-8, is presented through Figure 4-12 and Figure 4-13, in terms of the electrical diameter of the elliptical lens together with the resulting radius of the FO sphere. For both structures a quarter-wave matching layer is considered between the elliptical lens aperture and the air region. For comparison purposes, the resulting aperture efficiency through assuming the far field of the feeding structure incident on the elliptical lens is also included.

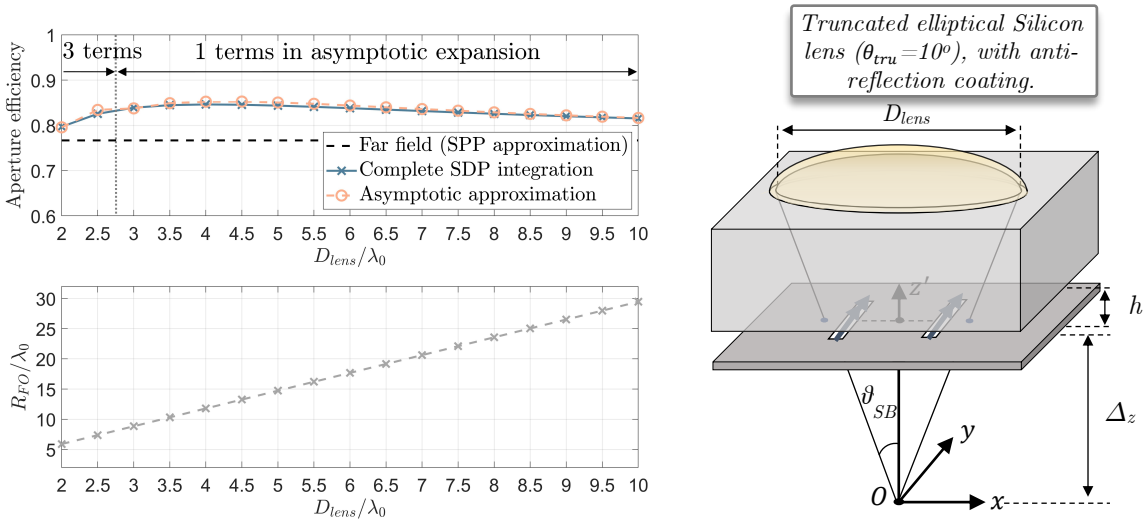

Figure 4-12. Aperture efficiency of elliptical lens integrated on resonant leaky wave structure (h=λ0/2).

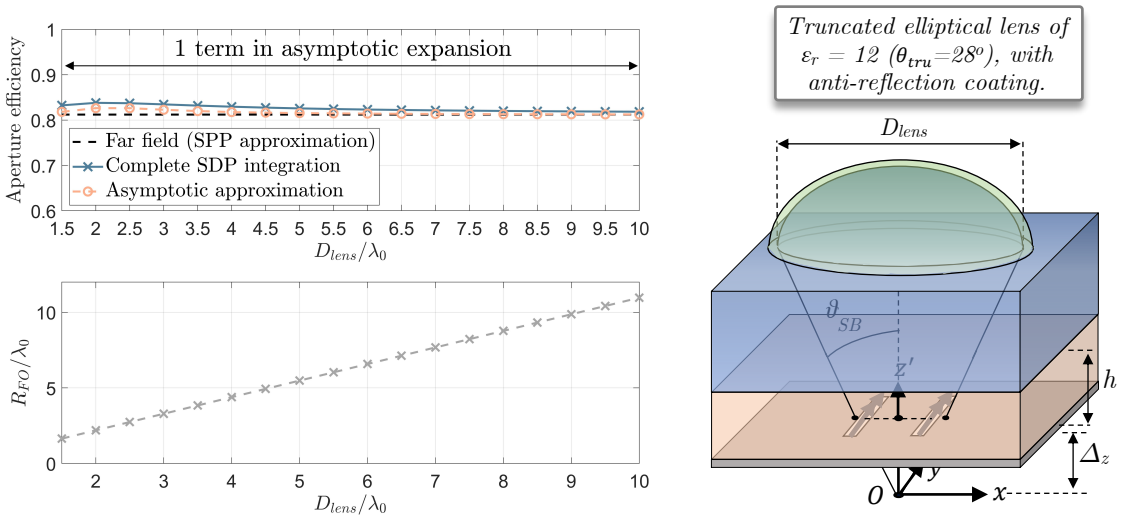

Figure 4-13. Aperture efficiency of elliptical lens integrated on wideband leaky wave structure ($h=\lambda_{cav}/2$).

The first noteworthy aspect of the above comparison refers to the performance of the asymptotic approach. More specifically, provided that lenses with FO spheres within the applicability region of the respective structures are examined, the asymptotic approach is in very good agreement with the numerical method. Having said that, the benefit of the asymptotic approach refers to the substantially improved computational efficiency. As an indicative example, for the study case referring to the wideband structure which considers *16* different elliptical lenses each with *60* θ and *361* φ points in the FO sphere, the timing comparison between the numerical and asymptotic approaches is given in Table 4-I.

Evaluation method	**Numerical** (SDP)	**Asymptotic** (3 terms)
Time required	*15 min*	*30 sec*

Table 4-I. Timing comparison between different near field evaluation methods

Apart from the difference in computational efficiency between the numerical and asymptotic approaches, two interesting remarks can also be performed regarding the resulting aperture efficiencies themselves. These are the convergence of the aperture efficiency to that of the far field for the wideband structure and the improved efficiency in the near field for the resonant structure. The following two sections will elaborate on these aspects.

4.2a. Far field convergence

Contrary to aperture antennas for which the far field distance depends on their electrical size, when apertures are etched on the ground plane of a leaky wave supporting stratification this is not the case. More specifically, the far field distance of leaky wave structures depends on the size of the aperture field distribution formed by the excited leaky waves inside the cavity. This is in turn determined by the attenuation constants (α_{LW}) of the significant modes, with smaller attenuation corresponding to larger field distribution.

Considering the significant modes of the examined structures, the one with the smallest attenuation constant which at first glance seems to determine the far field distance is the TM_0. However, when the feeding structure is designed such that this mode is suppressed, the size of the aperture field distribution formed by the leaky waves depends on the much weaker mode pair, namely TE_1 and TM_1. Given that the attenuation constants of these modes are smaller the larger is the dielectric contrast between the cavity and semi-infinite region, the far field distance of the resonant structure is much farther than that of the wideband.

To further build upon this concept, in [20] it was shown that given a proper definition of the phase centre position the near field up to the shadow boundary converges very fast to the

far field. This can be clearly observed for the wideband structure through Figure 4-13, given the resemblance of the far field aperture efficiency to that obtained when using the near field. To visualize this concept, the near and far field of the double slot pair will be compared for the case of the wideband structure in a sphere of $2\lambda_0$ radius through Figure 4-14.

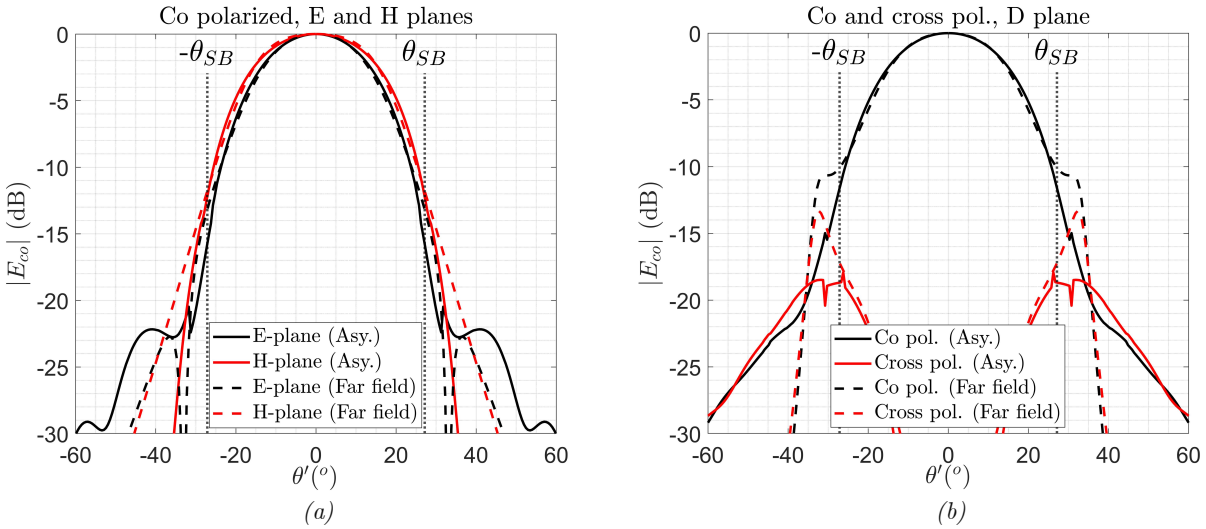

Figure 4-14. Near field and far field comparison for double slot, (a) co pol. at E and H planes, (b) co and cross pol. at D plane (150 GHz). The observation grid is a sphere of $r' = 4mm = 2\lambda_0$ radius (wideband structure), while the near field is approximated asymptotically using three terms in the expansion of the regularized part.

The converge to the far field up to the shadow boundary ($\theta_{tru} = min(\theta_{SB}^{TE_1}, \theta_{SB}^{TM_1})$) is very much evident through the E and H plane comparison of Figure 4-14 *(a)*. While this is a bit less noticeable for the D-plane due to the improper suppression of the TM_0, one might still consider that employing the far field would be sufficient for the design of small lenses in wideband leaky wave structures. However, the far field convergence can only be assumed up to the shadow boundary angle. As such, if the truncation angle of the lens is increased, using the far field would not be sufficient.

To illustrate this, an indicative test case will be considered resembling the core lens of the Fly's Eye antenna. More specifically a spherical lens of *4 mm* radius is assumed integrated in the wideband stratification ($\varepsilon_{r,cav} = 3.8$, $\varepsilon_{r,core} = 12$), radiating inside an infinite plastic medium ($\varepsilon_{r,shell} = 2.3$). The lens is coated with a matching layer ($\varepsilon_{r,match} = 5.25$), its truncation angle is chosen at *35°* (whereas $\theta_{SB}^{TE_1} \cong \theta_{SB}^{TM_1} \cong 28^o$) and the aforementioned slot pair is considered in the ground plane. To visualize the different nature of the near field above the shadow boundary angle, first, the ray picture of the transmitted field in the core-plastic interface is illustrated in Figure 4-15 at the H-plane, assuming far field and near field incidence on the spherical lens.

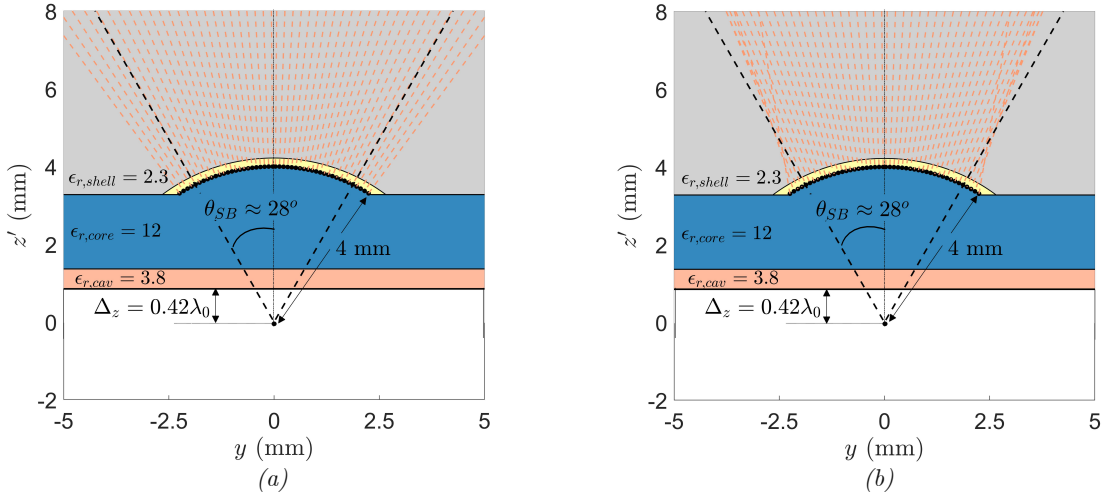

Figure 4-15. Ray picture of transmitted field after the core lens (H-plane) for (a) far field and (b) near field.

Evidently, while up to angles very close to the shadow boundary the spherical wave assumption for the near field holds, above this point the nature of the field is more complex. To further illustrated this concept, the far field inside the plastic region for the above example is depicted for two different truncation angles through Figure 4-16.

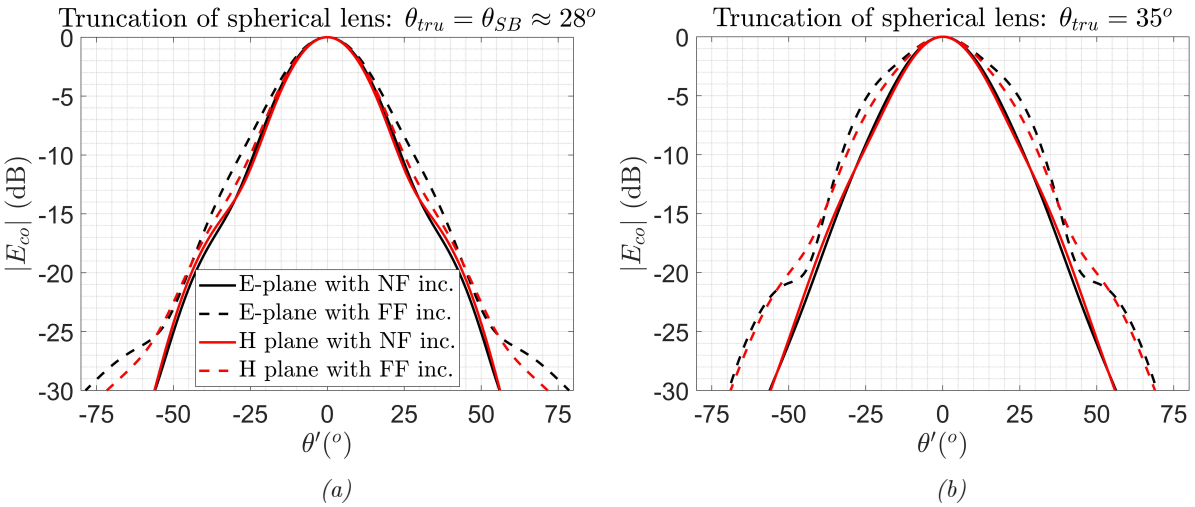

Figure 4-16. Far field comparison inside plastic region for far field and near field incidence on the core lens (150 GHz). In (a) the lens is truncated at 28º (roughly the smallest shadow boundary angle), while in (b) at 35º.

When the lens is truncated at the shadow boundary angle (Figure 4-16 *(a)*), its far field is quite similar either for far field or near field incidence. However, if the truncation angle is increased (Figure 4-16 *(b)*), this is no more the case. Essentially what this implies is that in a scenario where the lens is truncated above the shadow boundary, knowledge of the actual near field would be required. It should be noted that the modelling of the small spherical lens used for this example is performed through the Physical Optics techniques described in Chapter 5.

4.2b. Near field lens efficiency

The second noteworthy aspect regarding the results presented in the introductory part of *section 4.2*, refers to the improved aperture efficiency of the resonant structure when the lens surface is placed in the near field. In fact, the resulting efficiency seems to peak for lenses with diameters around $4\lambda_0$. To provide a physical interpretation of this effect, the aperture efficiency will first be decomposed into the tapper and spillover terms, as given through Figure 4-17.

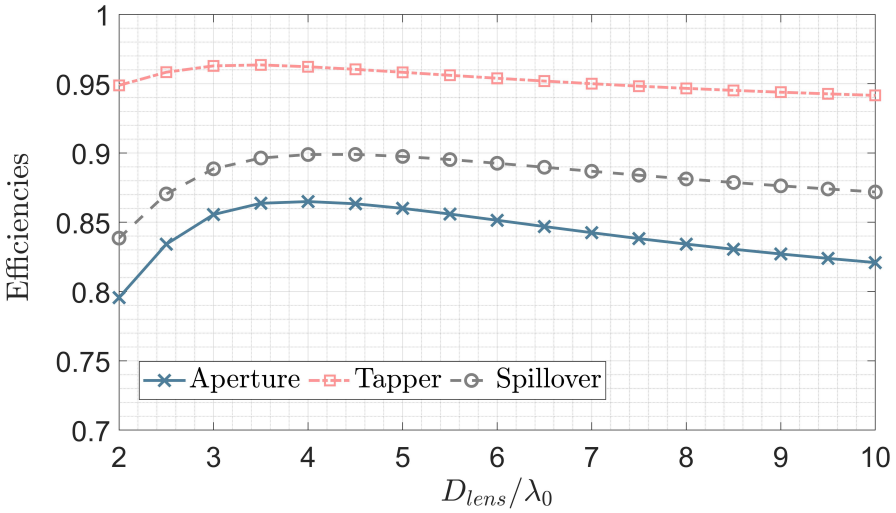

Figure 4-17. Efficiency term decomposition for resonant case. The reflection efficiency at the air interface is included in the spillover term.

As illustrated through the above figure, the term which provides the above-described nature of the aperture efficiency is the spillover. To realize the reason for this behaviour, the wave decomposition of the near field must be considered. More specifically, by evaluating the field through the path of steepest descent, it is decomposed into the SDP integral and the residue polar contributions. The residue contribution of each mode exists only above its shadow boundary angle, with its Poynting vector angle being constant and tending to the pointing angle of the leaky wave mode (*Appendix E*, $\theta_{LW} \cong \theta_{Poy.}^{Res.}$). Considering the structural aspects of the elliptical lens in the example of Figure 4-12, the ellipse is truncated at the shadow boundary angle of the main mode pair ($\theta_{SB,TE_1} \cong \theta_{SB,TM_1} \cong 10^o$), meaning that the residues exist only outside the solid angle defined by the elliptical surface.

Having said the above, to explain the behaviour of the spillover efficiency one must consider the relative value of the shadow boundary and Poynting vector angles for the main leaky wave mode pair (TE_1 and TM_1). As was shown in Figure 2-6 and is again depicted through Figure 4-18, the shadow boundary angles of the leaky wave modes are larger than their Poynting vector angles ($\theta_{Poy.}$). This means that the residues of the main mode pair progressively push power inside the shadow boundary cone as the radial distance from the phase centre is increased. This can be visualized through Figure 4-18 *(a)*, which illustrates the direction of the residue Poynting vector at different observation heights together with the limits of the shadow boundary cone. The latter essentially corresponds to the solid angle defined by the elliptical surface.

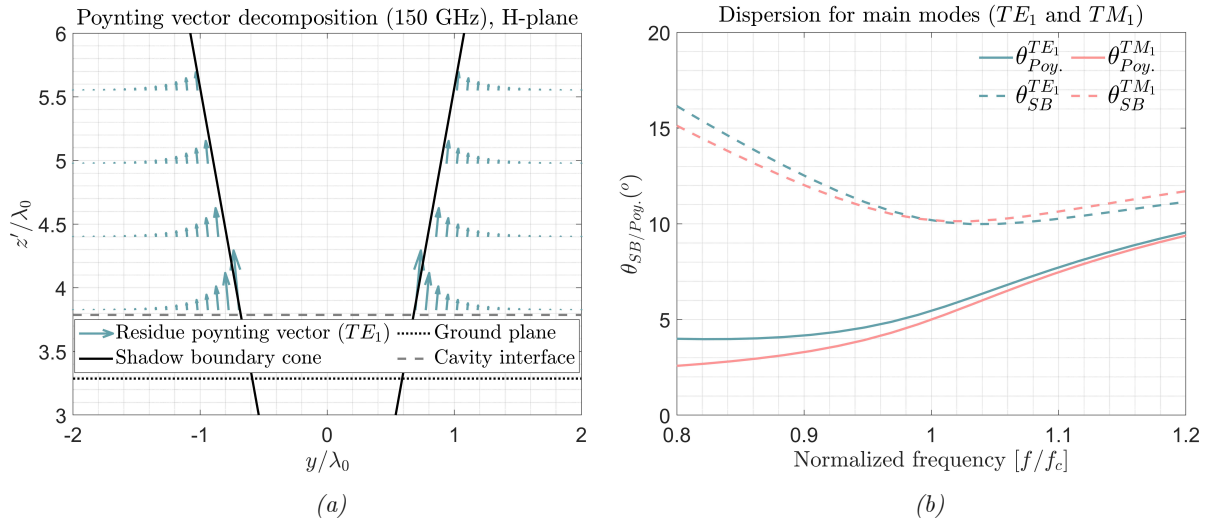

(a) *(b)*

Figure 4-18. (a) Poynting vector angle illustration in the H-plane with respect to the shadow boundary cone and (b) dispersion of the main leaky wave mode pair (TE1, TM1) in terms of their Poynting vector and shadow boundary angles.

To finalize this discussion, the attenuation of the residues at the rim of elliptical lenses with different diameters ($r' = R_{FO}$ and $\theta' = \theta_{SB}$), is computed and plotted together with the resulting aperture efficiency in Figure 4-19.

$$Attenuation\ [dB] = 20\ log_{10}\left(e^{Im(k_{z,LW})R_{FO}\ cos(\theta_{SB})} e^{Im(k_{\rho,LW})R_{FO}\ sin(\theta_{SB})}\right), \qquad (4.6)$$

It can be visualized through the following figure that the elliptical lens diameter for which the aperture efficiency is maximized corresponds to the one for which the average attenuation of the residues of the main modes at the edge of the shadow boundary cone is *-15 dB*. This essentially means that at the point of maximum aperture and thus spillover efficiency, most of the power of the residues has already entered the shadow boundary cone. This effect is directly related to the strength of excitation for the residues and thus it can be mainly observed in resonant structures.

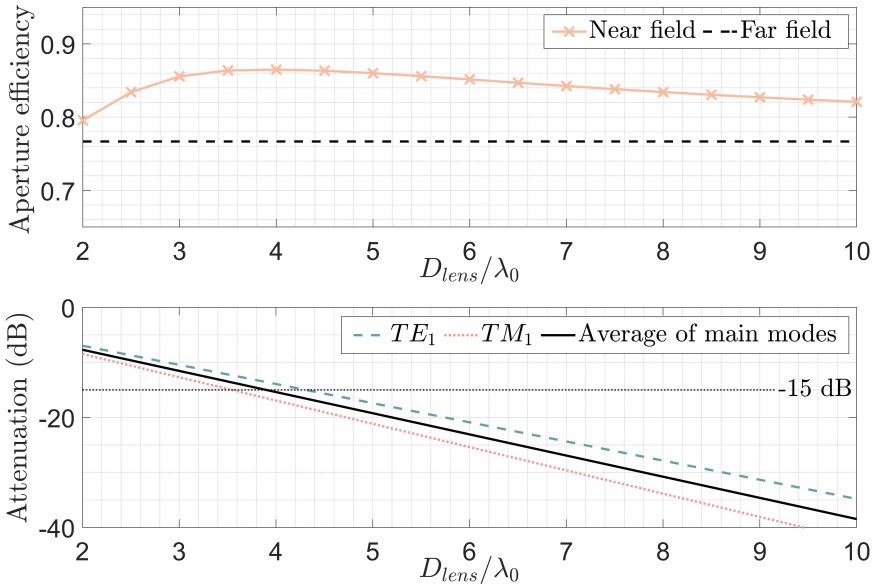

Figure 4-19. Aperture efficiency of Figure 4-12 together with the attenuation of the residues at the rim of the elliptical lens ($r' = R_{fo}$ and $\theta' = \theta_{SB}$) (4.6).

Having elaborated of the asymptotic approximation of the near field through Chapter 3 and 4, in the remaining of this document, the use of the asymptotically approximated near field to model the Fly's Eye antenna concept will be discussed. As a first step in this process, in the following chapter the Physical Optics techniques used to model the core-shell structure will be described.

CHAPTER 5. PHYSICAL OPTICS ANALYSIS

Having described the asymptotic method used to derive the near field of a leaky wave supporting stratification, the following chapter will discuss the Physical Optics techniques employed for the modelling of the integrated lens architecture of the Fly's Eye antenna (core-shell). Even though the same steps will be applied for both the core and shell lenses, the process will be separately presented for the two structures in their respective subsections. For the case of the core lens, the performance of the Physical Optics techniques will be evaluated through a full-wave simulation, while for the shell lens, it will be compared to an analysis in reception approach. To maintain the focus of this chapter only on the performance of the Physical Optics techniques, the feeding element will be simply represented by two elementary sources. In particular, two y-oriented sources are considered in the ground plane, displaced in x by $d_{ele} = 500\ \mu m$ such that they suppress the TM_0 leaky wave mode in its dominant plane. The modelling of the Fly's Eye antenna, employing additional considerations for the representation of the feeding element, will be presented in the following chapter.

5.1. Core lens

5.1a. Structure overview

In the context of the Fly's Eye antenna concept, the high permittivity core lens is primarily used to improve the front-to-back ratio of the feeding structure and thus facilitate chip integration. Simultaneously, it maintains low dielectric contrast with the resonant fused silica cavity, preserving the bandwidth of the leaky wave feeding structure. Its spherical shape allows the efficient illumination of the high eccentricity elliptical lens (shell), essentially simulating a leaky wave stratification with a high permittivity semi-infinite dielectric region. In terms of dimensions and dielectric properties, the synthesis of the core lens is done with a type of PPE plastic featuring a relative permittivity of *9.3* (PREMIX). To minimize the losses introduced by the core lens material, the size of the lens is maintained small, featuring a radius of *3.2 mm* and centred at the phase centre of the leaky wave structure (for *150 GHz*), displaced by *0.7 mm* below the ground plane. To improve the spillover on the core lens, i.e., minimize the power launched outside its truncation angle, the latter is chosen to be 44^o. Finally, to reduce the level of reflections in its surface, the core lens is coated with a matching layer. In the actual design this is done by drilling holes in the PREMIX such that a layer of the desired effective permittivity is formed. However, in the modelling process a uniform matching layer of quarter-wave thickness at *150 GHz* is considered for simplicity ($\varepsilon_{r,ML} = \sqrt{\varepsilon_{r,core}\varepsilon_{r,shell}}$). To visualize the above, the core lens with its physical dimensions is illustrated through Figure 5-1.

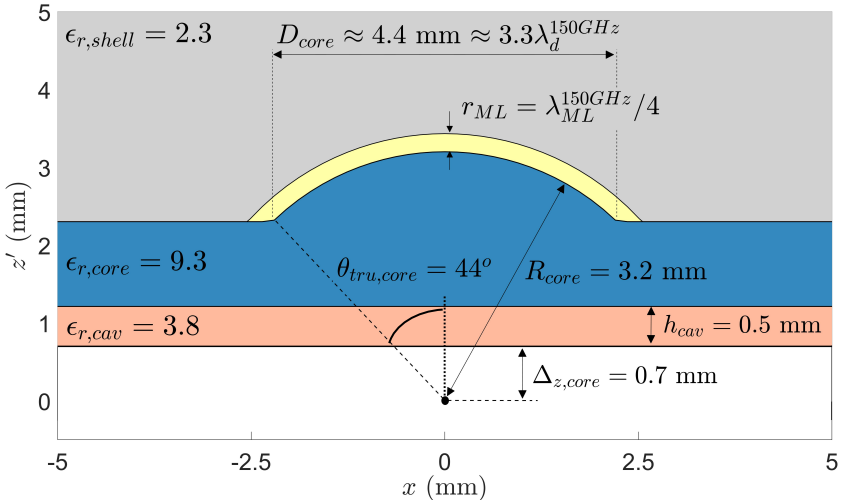

Figure 5-1. Core lens of the Fly's Eye antenna concept with its physical dimensions.

5.1b. Field on the core lens surface

One significant simplification for the analysis of the core lens refers to the derivation of the field on its surface, which in turn is required to obtain the field radiated inside the plastic region of the shell lens. Considering that the spherical core lens is centred at the phase centre of the leaky wave feeding structure, the near field incident on the latter can be assumed to resemble very well a spherical wave, conformal to the core lens surface [18]. Combining this fact with the presence of the matching layer between the PREMIX and plastic regions, enables the deduction that the level of reflections on the core lens is small. This means that a good approximation for the total field on the core lens surface can be derived by using only the field incident on the latter. As a result, the modelling of the near field can be significantly simplified by considering a leaky wave supporting stratification with an infinite PREMIX region, similar to those explored through Chapter 2 to 4. The core lens structure and the simplified stratification used to obtain the near field on its surface are visualized through Figure 5-2.

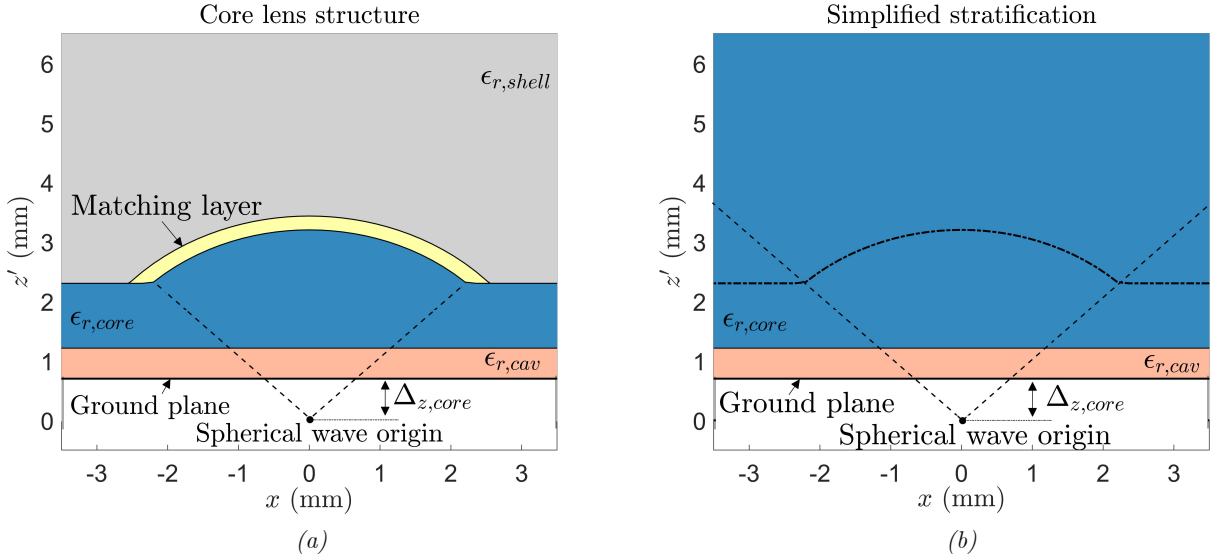

Figure 5-2. (a) Core lens structure and (b) simplified stratification employed to obtain the near field incident on the core lens.

To evaluate the validity of this assumption, both structures of Figure 5-2 are simulated in CST (full-wave simulation) and the field on the core lens surface is compared between the two cases. The resulting comparison, showcased through Figure 5-3, refers to the co polarized component produced by the double elementary source on top of the core lens surface.

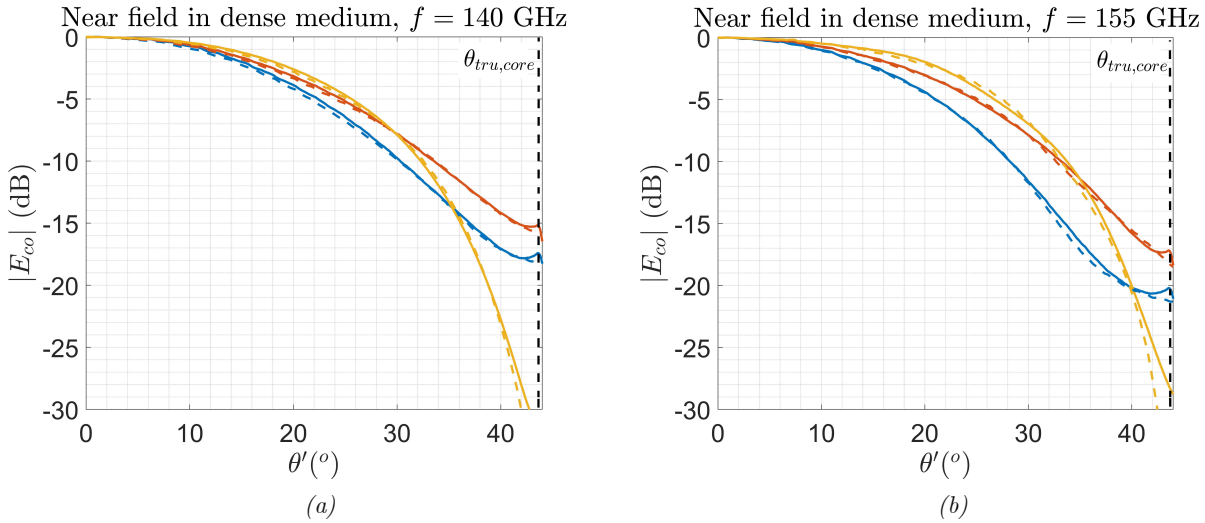

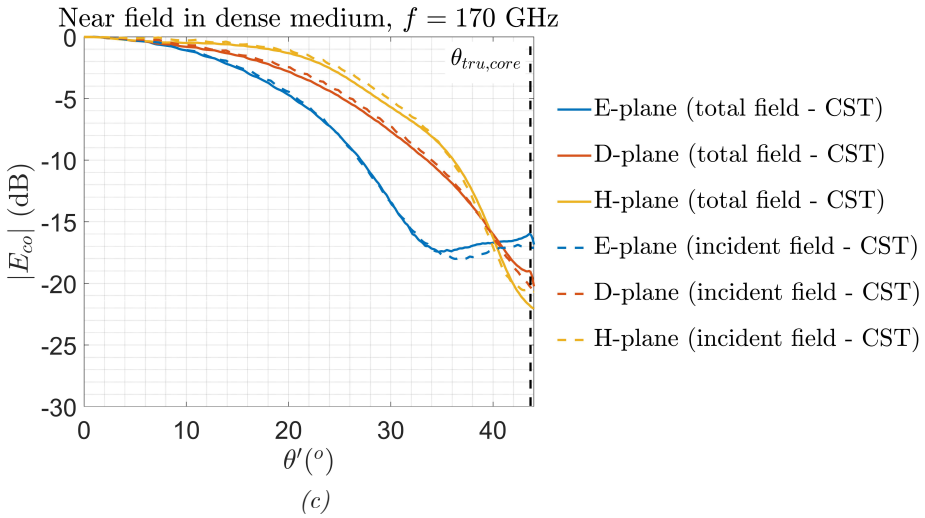

(c)

Figure 5-3. Comparison of total and incident near field on the core lens surface for (a) 140 GHz, (b) 155 GHz and (c) 170 GHz. The angle θ' corresponds to a reference system at the center of the core lens.

The very good agreement between the total field, derived through the stratification of Figure 5-2 *(a)*, and incident field, obtained using the stratification of Figure 5-2 *(b)*, justifies the above described simplification for the core lens structure.

5.1c. Modelling the core lens

Once the incident field on the core lens surface has been derived, the field transmitted through the core-plastic interface ($\vec{E}_{t,core}$, $\vec{H}_{t,core}$) can be obtained by the assumption of a locally flat interface at every point of incidence and the use of a transmission dyad. The presence of the matching layer can be included in the modelling process through the transmission dyad, by modifying the transmission coefficients for $\theta' < \theta_{tru,core}$, to those obtained from an equivalent transmission line model. Subsequently, the transmitted field can be employed to derive equivalent currents which radiate inside the plastic region, as illustrated through Figure 5-4.

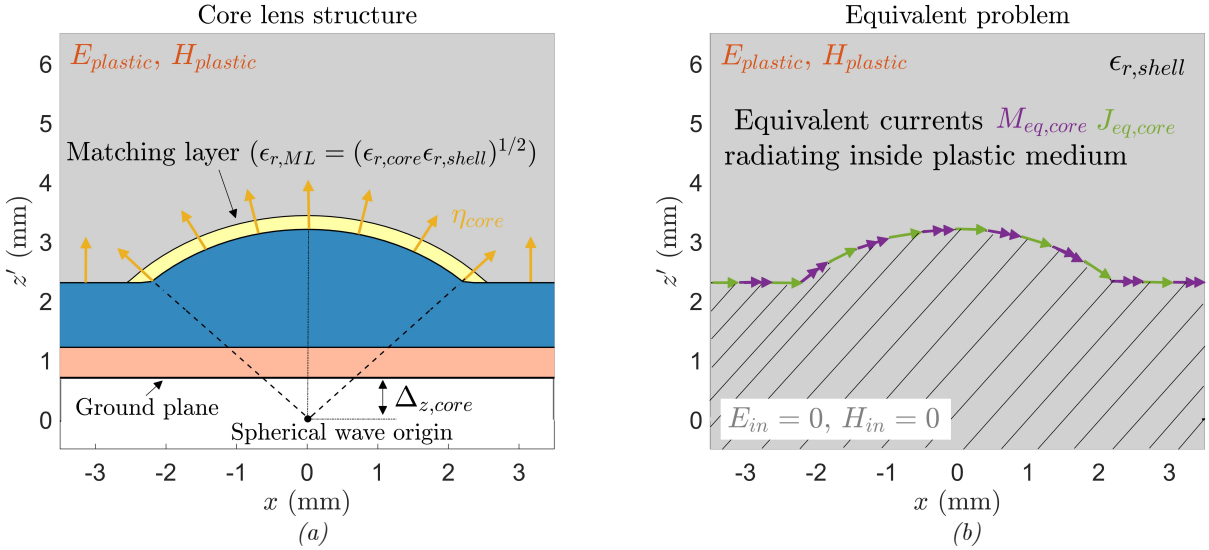

(a) *(b)*

Figure 5-4. (a) Core lens structure and (b) equivalent problem for the field inside the plastic region.

More specifically, employing the equivalence theorem [41], the field radiated by the core lens can be calculated through substituting the structure with an equivalent current distribution radiating in its absence. This current distribution is considered on top of a closed surface surrounding the core lens and infinitely extended laterally. Furthermore, using Love's formulation of the theorem, the equivalent current distributions are obtained through applying

the boundary conditions on the equivalent closed surface, such that the electric and magnetic fields are zero inside the surface and equal to the field produced by the actual source outside of it ($\vec{E}_{t,core}$, $\vec{H}_{t,core}$).

$$\vec{J}_{eq,core}(\vec{r}') = \hat{n}_{core}(\vec{r}') \times \vec{H}_{t,core}(\vec{r}') \quad \& \quad \vec{M}_{eq,core}(\vec{r}') = \vec{E}_{t,core}(\vec{r}') \times \hat{n}_{core}(\vec{r}'), \tag{5.1}$$

Where $\hat{n}_{core}$ refers to the normal vector of the core lens surface as indicated in Figure 5-4 *(a)*.

Once these equivalent current distributions are obtained, the field radiated by the core lens inside the surrounding medium can be evaluated through the convolution between the Green's function of the medium in question and the equivalent currents distributions ($\vec{J}_{eq,core}$, $\vec{M}_{eq,core}$). Considering an infinitely extended and homogeneous dielectric region of relative permittivity $\varepsilon_{r,shell}$ and maintaining only the radiative components of the dyadic Green's functions, since the field needs to be obtained on top of the shell lens which is far enough from the core structure ($R_{FO} \cong 24\,mm$); the resulting expressions for the field inside the plastic are given below, with $\vec{r}_{obs}$ and $\vec{r}'$ corresponding to the observation and the source grids respectively. The considered reference system is placed at the center of the core lens, i.e., displaced by Δ_z=*0.7mm* below the ground plane.

$$\vec{E}_{plastic}(\vec{r}_{obs}) = \iint_S jk_d\left[\hat{R} \times \vec{M}_{eq,core}(\vec{r}')\right]\frac{e^{-jk_dR}}{4\pi R}dS - \iint_S j\omega\mu\left[\vec{J}_{eq,core}(\vec{r}') - \left(\hat{R}\cdot\vec{J}_{eq,core}(\vec{r}')\right)\cdot\hat{R}\right]\frac{e^{-jk_dR}}{4\pi R}dS$$

$$\vec{H}_{plastic}(\vec{r}_{obs}) = -\iint_S jk_d\left[\hat{R} \times \vec{J}_{eq,core}(\vec{r}')\right]\frac{e^{-jk_dR}}{4\pi R}dS - \iint_S j\frac{k_d}{\zeta_d}\left[\vec{M}_{eq,core}(\vec{r}') - \left(\hat{R}\cdot\vec{M}_{eq,core}(\vec{r}')\right)\cdot\hat{R}\right]\frac{e^{-jk_dR}}{4\pi R}dS \tag{5.2}$$

Where $\hat{R} = \frac{\vec{r}_{obs}-\vec{r}'}{|\vec{r}_{obs}-\vec{r}'|}$, $k_d = k_0\sqrt{\varepsilon_{r,shell}}$ and dS describes the domain of integration.

Given the small electrical size of the core lens ($D_{core} \approx 3.3\lambda_d$ at *150 GHz*), one approximation that should be treated carefully refers to assuming a locally flat interface at every point of incidence. To evaluate the validity of this step in the modelling process, the far field inside the plastic obtained with (*5.2*) will be compared to that derived by a full-wave simulation (CST).

Before doing so, however, it should be noted that an aspect not modelled through the above procedure refers to the power trapped inside the PREMIX slab. In fact, by considering only the transmitted field on the core-plastic interface, all reflections are essentially completely neglected. For an actual source in the ground plane this approximation will provide reasonable results, since the source is designed such that the power launched outside the core lens is minimized. Even so, for the purpose of evaluating the validity of the Physical Optics techniques using the aforementioned double elementary source, additional considerations are required. More specifically, to enable the desired comparison the first step refers to adding a PEC plane on top of the PREMIX slab in the core lens model used for the full-wave simulation, as illustrated through Figure 5-5.

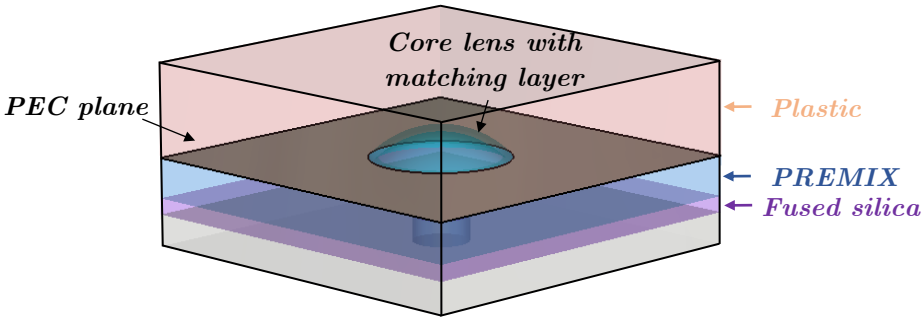

Figure 5-5. Core lens model in CST featuring a decoupling PEC plane above the PREMIX slab.

With the aim of isolating only the field radiated by the core lens in the full wave simulation, an additional step is needed. To obtain the far field inside the plastic region, CST derives equivalent currents on the bounding box surface, which in turn radiate in a uniform dielectric region, for this case with relative permittivity of $\varepsilon_{r,plastic} = 2.3$. While the presence of the PEC plane shown through Figure 5-5, limits the impact of the power trapped inside the PREMIX

slab to the region below said plane, the latter will still influence the equivalent currents on the boundaries and thus impact the far field. To avoid this issue, one can retain only the equivalent currents associated to the top box (plastic region), as illustrated through Figure 5-6, by using the decoupling plane option. This operation leads to neglecting the contributions to the far field arising from the lower box and thus isolate the field radiated by the core lens.

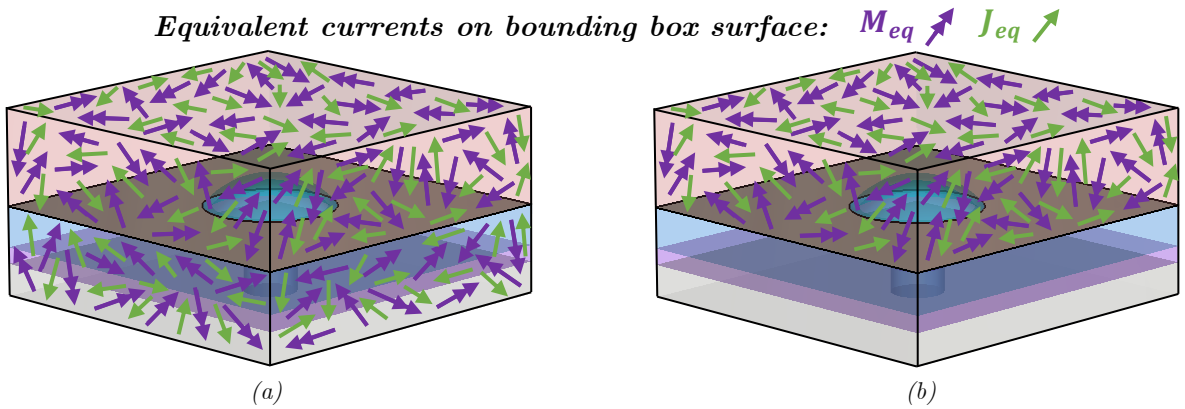

Figure 5-6. Illustration of (a) equivalent currents on bounding box surface of full-wave simulation and (b) equivalent currents maintained through the introduction of the decoupling plane.

Employing this approach, the far field inside the plastic obtained through the above discussed Physical Optics techniques, is compared to that extracted from the full-wave simulation by using the decoupling plane option. The resulting comparison of the far field is presented through Figure 5-7, showing very good agreement.

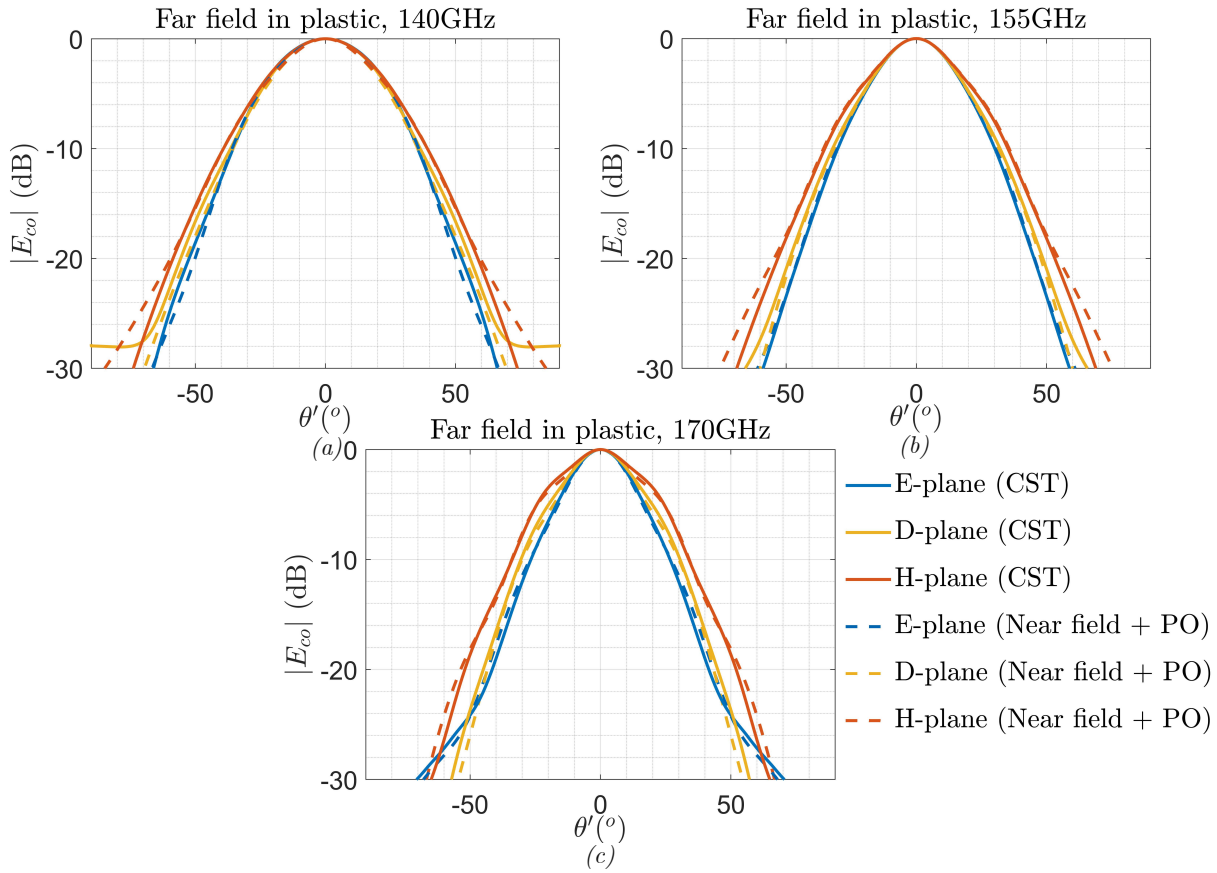

Figure 5-7. Far field in plastic comparison between full-wave simulation with decoupling plane and asymptotically approximated near field (3 term expansion of the regularized part) combined with Physical Optics techniques. The comparison is performed for three frequencies (a) 140 GHz, (b) 155 GHz and (c) 170 GHz. The observation angle θ' corresponds to the reference system at the center of the core lens.

5.2. Shell lens

5.2a. Structure overview

In the context of the core-shell structure, the elliptical shell lens aims to enable the implementation of a large radiating aperture capable of satisfying the gain requirements [5], through the use of low cost and low loss materials. An ideal candidate material satisfying the above is HDPE, which due to its low permittivity at the examined frequency range ($\varepsilon_{r,HDPE} \simeq 2.3$ [17]) does not feature significant reflections in the plastic-air interface, mitigating the need for a matching layer and thus reducing the overall complexity of the design. For the physical dimensions of the shell lens, a *3 cm* diameter (D_{shell}) aperture is chosen, with the lens truncated at 38^o. Regarding the lower focus of the ellipse, it is displaced by *0.27 mm* ($\Delta_{z,shell}$) above the ground plane of the core lens structure. As will be showcased in the final part of Chapter 6, the relative position of the lower focus with respect to the core lens structure is chosen to improve the antenna performance at the lower end of the desired band of operation (*140–170 GHz*).

5.2b. Modelling the shell lens

Having discussed the modelling of the core lens in the previous section, the free space patterns radiated by the shell lens can in turn be computed through a step-by-step implementation of the same Physical Optics techniques. In particular, due to its large extension in terms of the wavelength, the field on the shell lens will be obtained through the use of the equivalent currents derived via the modelling of the core lens ($J_{eq,core}$ and $M_{eq,core}$), radiating inside an infinite plastic region, as given in (*5.2*). In turn, approximating the total with the incident field on the shell lens surface, the field transmitted outside the interface can be derived through a transmission dyad and can be subsequently used to obtain equivalent currents radiating in free space.

$$\vec{J}_{eq,shell}(\vec{r}') = \hat{n}_{shell}(\vec{r}') \times \vec{H}_{t,shell}(\vec{r}') \quad \& \quad \vec{M}_{eq,shell}(\vec{r}') = \vec{E}_{t,shell}(\vec{r}') \times \hat{n}_{shell}(\vec{r}'), \tag{5.3}$$

Similar to the modelling of the core lens, the equivalent currents result from the implementation of the Love's formulation for the equivalence theorem [41] and can thus be utilized to derive the field only outside the modelled region, in this case being the shell lens. The set of equivalent problems employed for the modelling of the core-shell structure are jointly depicted through Figure 5-8.

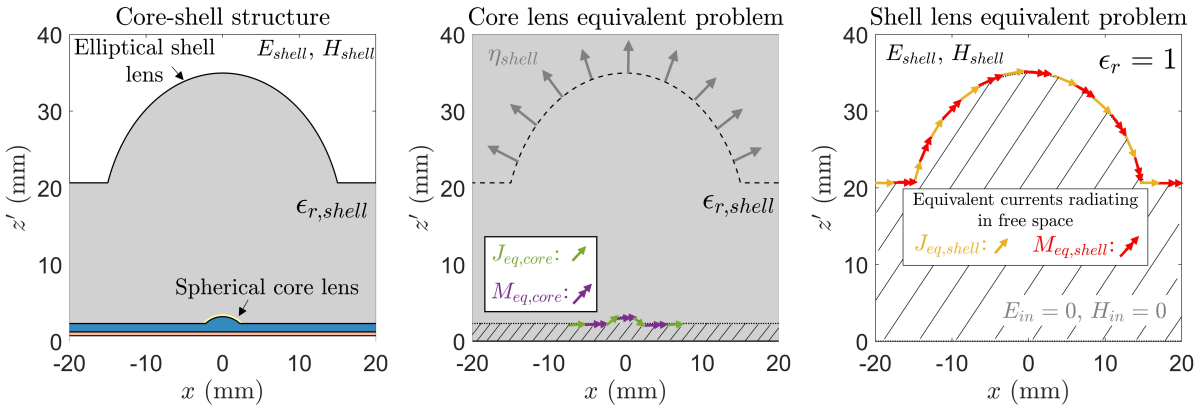

(a) *(b)* *(c)*

Figure 5-8. (a) Core-shell structure, (b) equivalent problem for the field on the shell lens surface and (c) equivalent problem for the field outside the shell lens.

Once the equivalent currents on the shell lens surface have been derived, the field radiated outside the elliptical lens can be evaluated through the convolution between the free space Green's function and the respective equivalent currents distributions ($J_{eq,shell}$ and $M_{eq,shell}$). In other words, the secondary patterns of the shell lens can be extracted through the integral expressions (*5.2*), where the current distributions and integration domain are modified to those of the shell lens and k_d is substituted with k_0.

To evaluate the described Physical Optics model of the shell lens, the free-space patterns obtained through this approach will be compared to those extracted by employing the far field inside the plastic from the full-wave simulation showcased in Figure 5-7 and the GO/FO tool of [42]. The resulting comparison of the secondary patterns is presented through Figure 5-9.

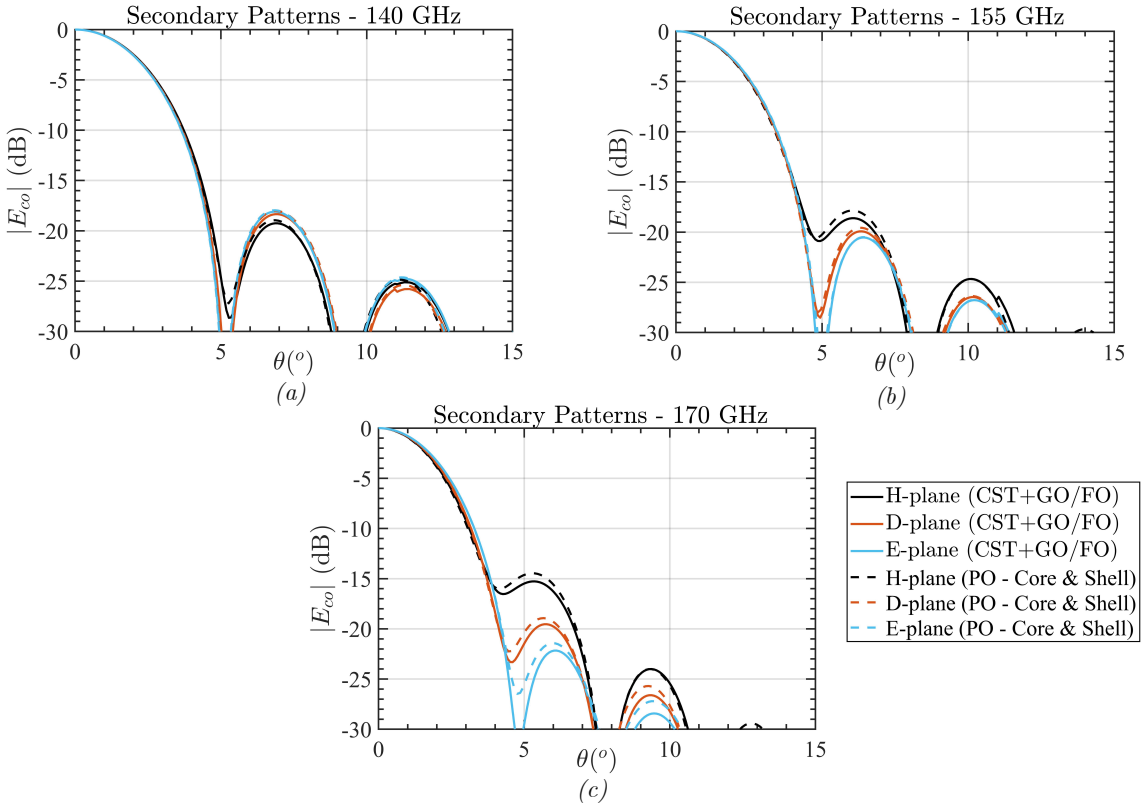

Figure 5-9. Secondary pattern comparison between full-wave simulation of core lens combined with a GO/FO tool [42] and Physical Optics combined with asymptotic techniques for core-shell modelling (a) 140 GHz, (b) 155 GHz and (c) 170 GHz. The observation angle θ refers to a reference system on the tip of the elliptical lens.

As evident through the comparison presented above, while the two methods are in overall very good agreement, a small difference can indeed be observed in the level of the first sidelobe, especially at higher frequencies. A reasonable explanation for the latter refers to the assumption for far field incidence on the shell lens when using the GO/FO tool, whereas no such assumption is employed through the integrals of (*5.2*). In fact, at the higher end of the operating frequency range (*170 GHz*), the assumption for the FO sphere being in the far field of the core lens degrades in accuracy given the core lens electrical dimensions ($R_{FF}^{170\,GHz} \cong 2D_{core}^2/\lambda_d^{170\,GHz} \approx 33.2\,mm$ whereas $R_{FO} \cong 24\,mm$).

CHAPTER 6. Application to the Fly's Eye Antenna

The following chapter presents a model for the Fly's eye antenna concept in matlab and elaborates on its contribution in terms of evaluating the measurements of the assembled prototype. The model is derived through a combination of asymptotic and Physical Optics techniques, with the former used for the modelling of the near field incident on the core lens, while the latter employed to enable the representation of the free space field radiated by the shell lens structure. The description of the modelling approach is followed by a discussion on the contribution of the derived model in the measurement campaign, and finally the chapter is concluded with a brief tolerance study.

6.1. Modelling the feeding element

6.1a. Double iris shaped slot

As already discussed through the introductory section of this document, when leaky wave feeds are used to illuminate lenses, the radiation properties of the feeding element are mostly determined by the nature of the excited leaky wave modes inside the cavity, rather than the apertures etched on the ground plane. Having said that, for stratifications around resonance ($h_{cav} \approx \lambda_{cav}/2$), not all the impactful leaky wave modes are desirable. In particular, while the TE_1 and TM_1 leaky wave mode pair can contribute to the efficient illumination of the integrated lens, since they enhance the radiation of the feeding element along broadside, TM_0 launches power at relatively larger angles and can thus constitute a significant spillover loss.

Taking this into account, several design approaches can be employed in order to suppress the undesired TM_0 leaky wave mode; with the most common being the choice of the feeding element such that its Fourier transform features a null near the spectral position of the leaky wave polar singularity of the undesired mode (TM_0). The simplest structure capable of the desired suppression is the double slot, as discussed in Chapter 4. However, while providing very good suppression for the E-plane, the double straight slot does not significantly impact the TM_0 in the diagonal planes. To also improve the suppression in those planes, several designs employ an iris shaped double slot [17], [20]. In turn, this leads to more symmetric patterns which provide an overall better illumination of integrated lenses.

Adhering to this thought process, a double iris shaped slot is used to illuminate the core lens of the Fly's Eye antenna. In terms of additional considerations for its design, in order to enhance its matching performance while also maintaining low levels of coupling between the two slots by limiting their angular size, the double iris slot is elliptically elongated [18], as illustrated through Figure 6-1.

6.1b. Modelling the near field of the iris

Having introduced the feeding element, the first step for the modelling of the Fly's Eye antenna refers to recreating the field on the core lens surface. Given the radius of the core lens, this essentially corresponds to the near field of the double iris shaped slot. Considering the discussion of *section 5.1b*, a good approximation for the total field on the core lens is the incident field, simplifying the core structure with one featuring an infinite dense region. To justify the reasoning behind the choice of representation used to model the double iris shaped slot, a brief overview of the deductions made in Chapter 3 and 4 will first be presented.

Obtaining the near field of a leaky wave supporting stratification can be performed in a straightforward manner through the following double spectral integral.

$$\vec{E}(\vec{r}) = \frac{1}{4\pi^2}\int_0^{+\infty}\int_0^{2\pi} \bar{\bar{G}}^{em}\left(k_\rho, \alpha, z, \Delta_z\right) \cdot \vec{C}_m\left(k_\rho, \alpha\right) e^{-jk_\rho \rho\, cos(\alpha-\varphi)} k_\rho d\alpha dk_\rho, \qquad (6.1)$$

While the derivation of the near field through (*6.1*) is feasible, it is a very computationally inefficient process due to the slow convergence of the integral in question. This is problematic

since a versatile modelling tool primarily needs to be fast such that the studies of interest can be performed in a reasonable time frame. Substantial reduction in the time required for the evaluation of the near field integral expression can indeed be achieved by exploiting the spectral properties of the Green's function ($\bar{\bar{G}}^{em}$), as described in [20] and summarized through the background Chapter 2. In this manner, the near field can be expressed through a much faster convergent integral ($\vec{E}_{SDP}$) and a finite sum of analytical terms which correspond to the leaky wave modes supported by the stratification. As extensively discussed in Chapter 3, to further enhance this concept, the polar singularities of the SDP integral can be isolated, separating the integral in question into two terms. Combining this decomposition with the approximation described in *section 3.2c*, allows each of the resulting integrals to be evaluated asymptotically. This essentially enables the evaluation of the initial integral expressions through a finite sum of analytical terms, negating the need for any spectral integration and thus constituting a very fast approach to obtain the near field.

While computationally efficient, one limiting aspect of the above-described process is that the manipulation of the integrals involved enforces certain requirements on the spectral properties of the current distributions considered in the ground plane, as described through *section 4.1.* The most fundamental of these requirements refers to a slow varying spectrum of the source ($\vec{C}_m(k_\rho,\alpha)$) in terms of α (*section 4.1b*). Consequently, this gives rise to certain considerations for the modelling approach employed to derive the near field of the double iris shaped slot of the Fly's Eye antenna. One option would be to model the actual current distribution in the ground plane through a number of elementary sources with different weights. This would in principle enable the representation of any current distribution, provided that a large enough number of elementary sources is used, but it would partly negate the computational efficient of the near field derivation approach due to the need of superimposing a large number of sources. To preserve the computational efficiency of the asymptotic near field evaluation, another approach could be to use a simplified model for the double iris shaped slot which satisfies the required spectral properties.

With the aim of maintaining the prospect for a fast-modelling tool, the second option is chosen. In particular, the employed model is comprised of two straight slots which are treated through superposition, since each of them satisfies the required spectral properties (*sections 4.1b* and *4.1c*). The Fourier transform of the equivalent current distribution used to model each of the employed slots was given in equation (*4.3*). Finally, the dimensions and spacing of the straight slots are tuned to those depicted in Figure 6-1 *(a)*, such that they provide a sufficient matching for the near field of the iris shaped structure.

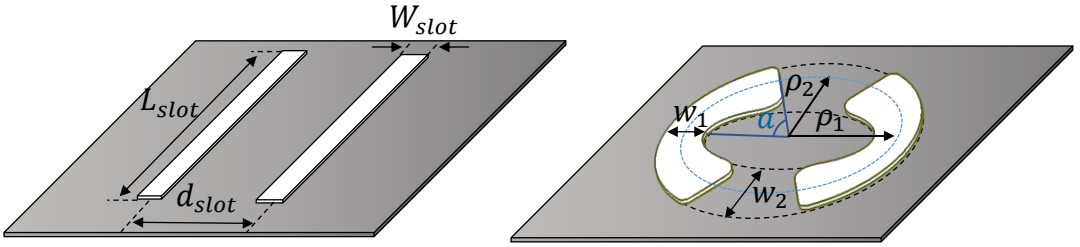

Figure 6-1. (a) Double straight slot used for the modelling of (b) the iris shaped slot of the Fly's Eye antenna.

As an indicative example to showcase the modelling of the double iris shaped slot, the near field inside the infinite dense region of the simplified stratification of the core lens (i.e., infinite dielectric of $\varepsilon_{r,core}$) will be compared for the two structures presented in Figure 6-1. The field comparison illustrated through Figure 6-2, is performed at a sphere of *3.2 mm* radius from the phase center of the leaky wave structure, which is displaced by $\Delta_{z,core}$*=0.7 mm* below the ground plane. The near field of the double iris shaped slot is obtained through a full-wave simulation (CST) while that of the double straight slot is derived asymptotically using matlab.

Considering the discussion of *section 3.3d*, the asymptotically approximated near field is extracted using three terms in the expansion of the regularized part.

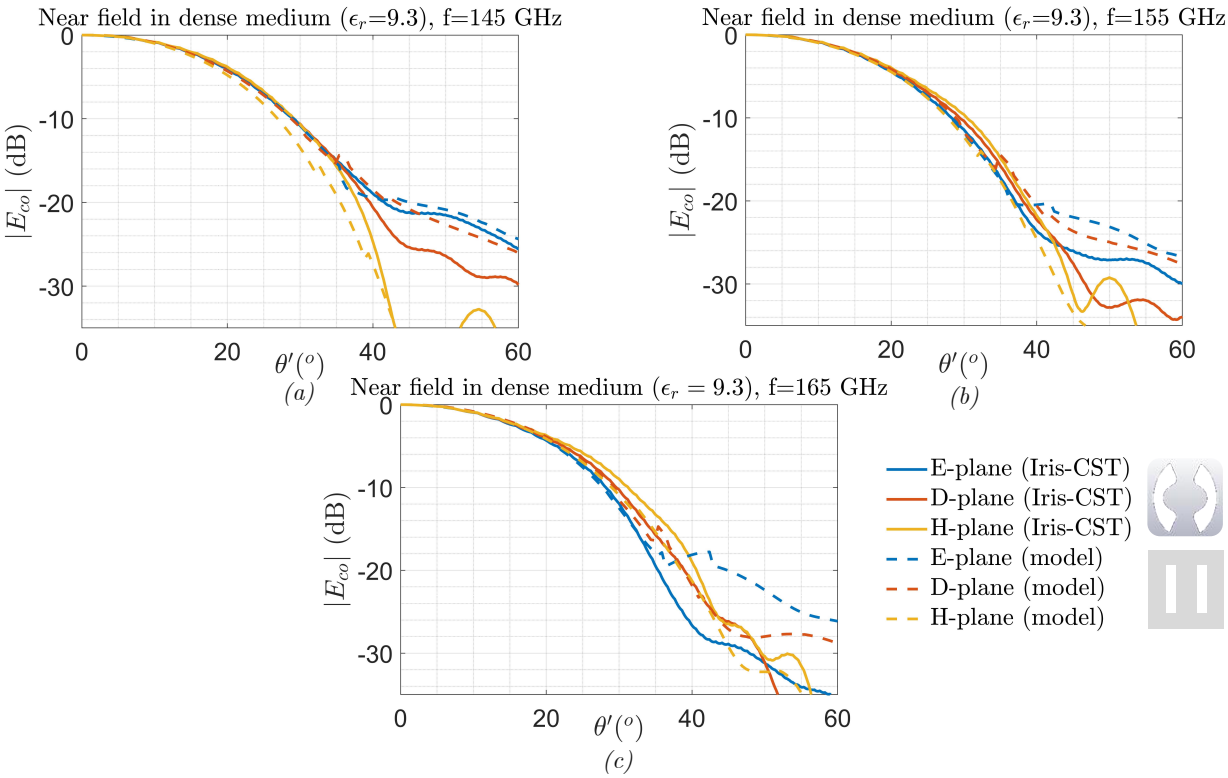

Figure 6-2. Near field comparison for the structures of Figure 6-1 (a) 145 GHz, (b) 155 GHz and (c) 165 GHz. The observation angle (θ') corresponds to the displaced reference system below the ground plane.

As visualized through the figures above, the model provides satisfactory agreement for angles up to roughly 35^o, with the main difference appearing for larger angles at the E and D planes. In those regions the double straight slot features higher field values compared to the iris shaped structure, due to the inadequate suppression of the TM_0 leaky wave mode.

It is important to note that while representing the double iris shaped slot with a simple double straight slot cannot lead to an exact recreation of the field incident on the core lens, it enables the development of a fast-modelling tool, which can be subsequently used to evaluate the antenna performance. Having said that, for the purpose of examining shaped variants of the core lens within the context of a future study, a more accurate model of the iris shaped structure would need to be derived as will be elaborated through *section 7.3*.

6.2. Core-shell model performance

Once the asymptotically approximated near field on the core lens has been obtained, the next step refers to combining the derived near field with the Physical Optics techniques described through Chapter 5, to model the Fly's Eye antenna.

6.2a. Core lens

The first step in this process refers to evaluating the near field model's performance when combined with the core lens. To accommodate the latter, a full-wave simulation (CST) is used to obtain the far field of the core lens fed by the double iris shaped slot of the Fly's Eye antenna, inside the plastic region of the shell lens. Subsequently, the resulting far field is compared to that obtained through combining the model of the near field presented in the previous section, with the Physical Optics techniques discussed in *section 5.1*. An indicative example of the resulting comparison is presented through Figure 6-3, with the black lines referring to the full-wave simulation of the core lens, while the colored lines corresponding to the developed model.

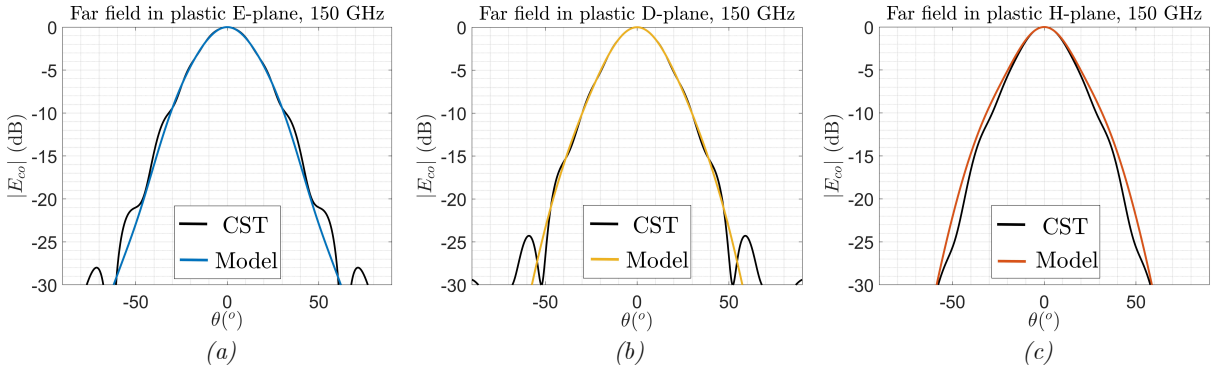

Figure 6-3. Comparison of the far field of the core lens inside the plastic ($\varepsilon_{r,plastic} = 2.3$) (a) E-plane, (b) D-plane and (c) H-plane.

While the model provides good agreement with the full-wave simulation, one noteworthy difference in the figures above refers to the ripples appearing in the E and D planes of the CST results. This effect can be attributed to power trapped inside the PREMIX slab of the stratification in the full-wave simulation. Since the modelling process for the core lens (*section 5.1*) considers only the transmitted field at the core-plastic interface, this effect is essentially neglected. Even so, given the good suppression of the TM_0 provided by the double iris shaped structure of the Fly's Eye antenna, the amount of power trapped inside the PREMIX slab is small; meaning that the model still provides a good representation of the field inside the plastic region. To showcase the model's performance with frequency, some additional comparisons for the far field inside the plastic are presented through Figure 6-4.

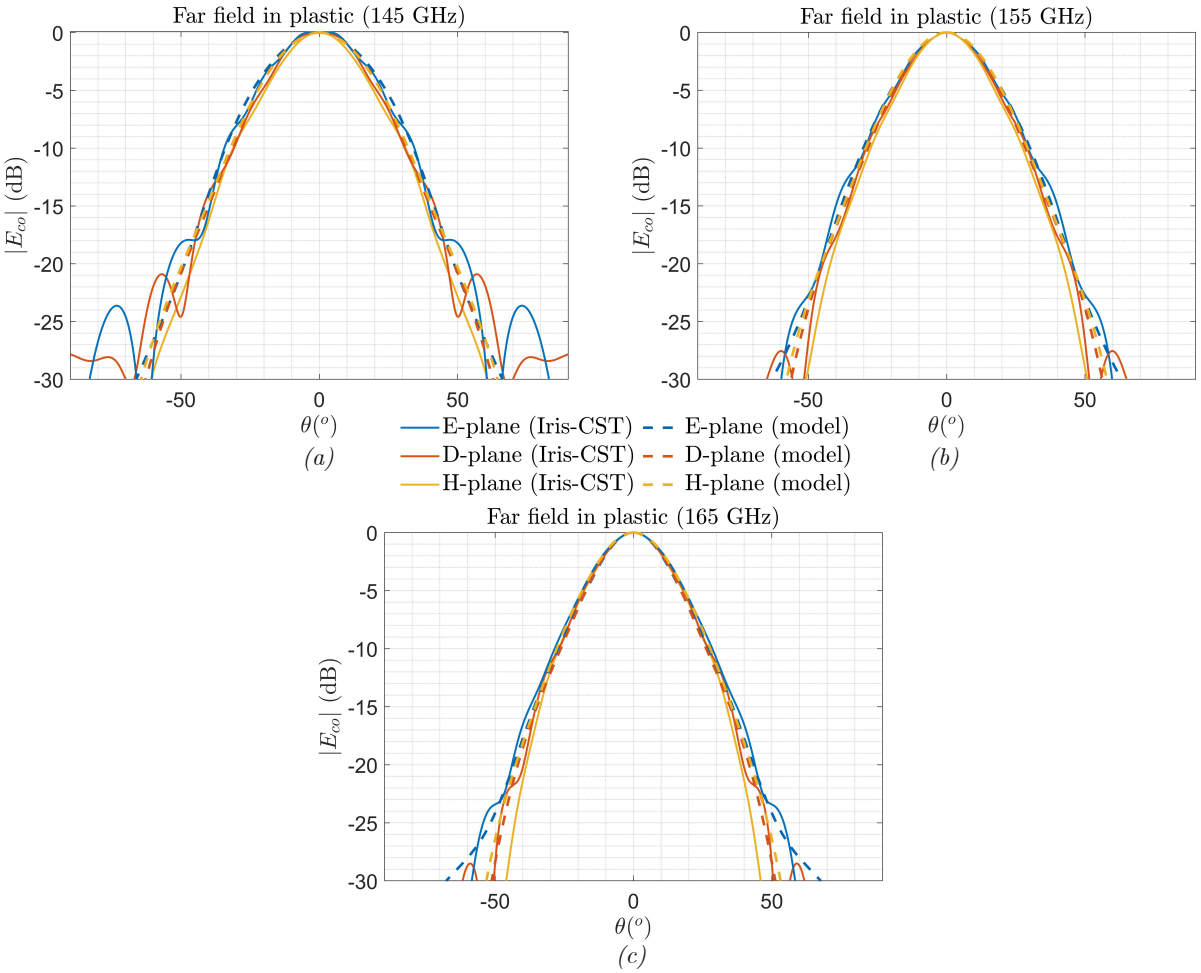

Figure 6-4. Comparison of the far field in the plastic ($\varepsilon_{r,plastic} = 2.3$) for (a) 145 GHz, (b) 155 GHz and (c) 165 GHz.

6.2b. Shell lens

Having evaluated the modelling of the core lens, the free space patterns of the shell lens can in turn be computed through the steps described in *section 5.2*. The performance of this part in the modelling process will be evaluated as described below.

First, the far field inside the plastic obtained by the full-wave simulation of the core lens is introduced into the GO/FO tool of [42], which computes the secondary patterns of the shell lens through performing an analysis in reception approach. Subsequently, these free space patterns (solid) are compared to those obtained by the modelling process for the shell lens through the Physical Optics techniques described in *section 5.2* (dashed). The resulting comparison is depicted for four frequencies through Figure 6-5.

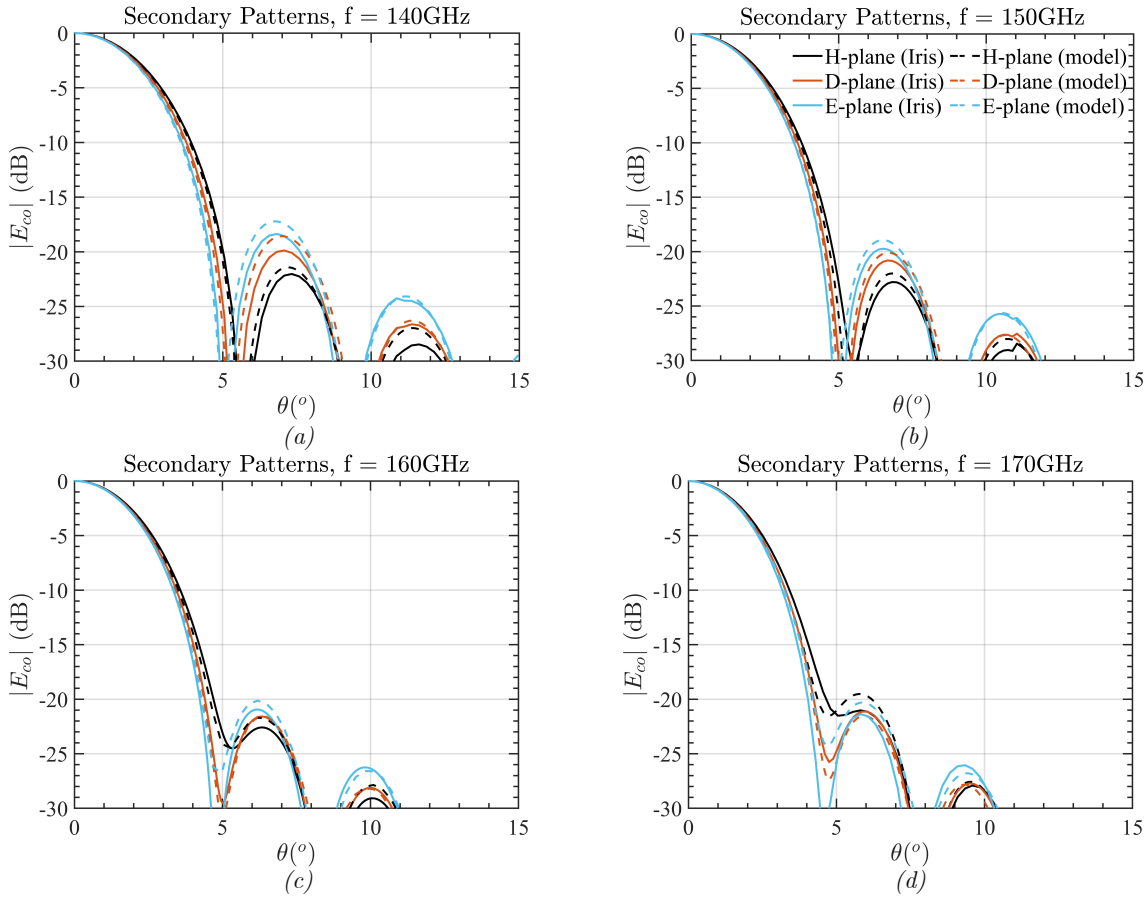

Figure 6-5. Shell lens pattern comparison for full-wave simulation of core lens combined with the GO/FO tool of [42] and Physical Optics techniques of Chapter 5, for (a) 140 GHz, (b) 150 GHz (c) 160 GHz and (d) 170 GHz.

Since the far field inside the plastic was recreated with significant accuracy by the utilized model, as visualized through Figure 6-4, the good agreement of this comparison is somehow anticipated. It is worth noting that while the secondary patterns illustrated through Figure 6-5 do not include the impact of a number of effects that will be present in a full-wave simulation, like secondary reflections from the plastic-air interface, they still provide a good first order model for the performance of the Fly's Eye antenna.

As a final note, the resulting efficiencies obtained through the described model will be compared to those of the actual Fly's Eye antenna concept. This is performed through extracting the far field inside the plastic and introducing it to the GO/FO tool of [42] which computes the efficiencies through an analysis in reception approach. The resulting comparison is illustrated through Figure 6-6 *(a)* and *(b)*. The difference between the two figures refers to the inclusion of the spillover and reflections on the core lens. In particular, in Figure 6-6 *(a)* the power radiated by the feed is considered as that launched into an infinite dielectric region

of relative permittivity $\varepsilon_{r,core}$, while for Figure 6-6 *(b)* only the power of the far field inside the plastic is considered for the efficiency derivation.

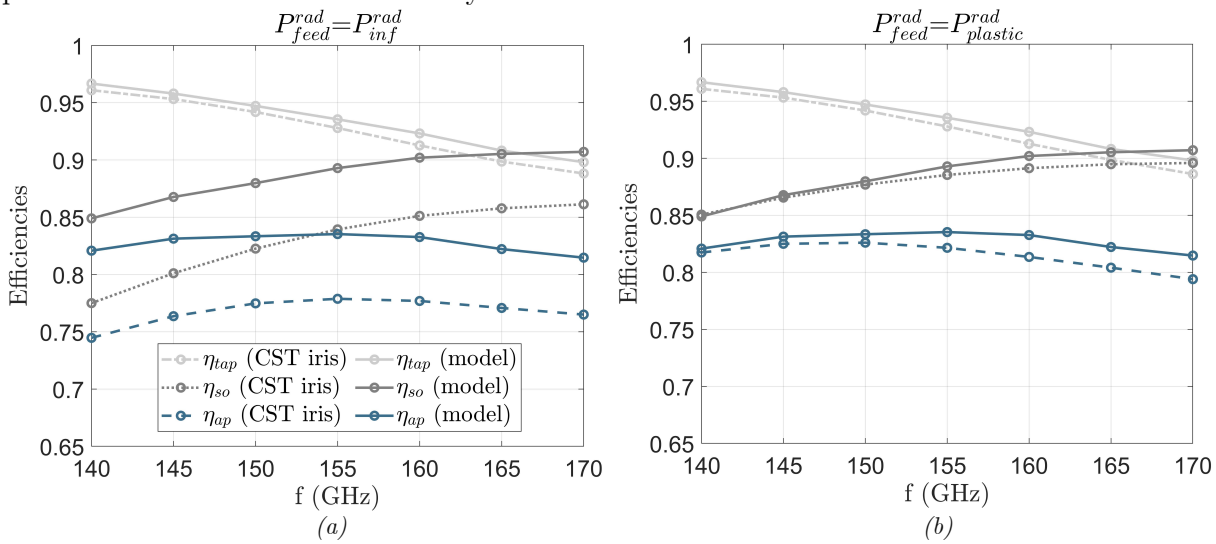

Figure 6-6. Aperture efficiency performance for the model of the Fly's Eye antenna using the far field inside the plastic and the GO/FO tool of [42], (a) with and (b) without spillover and reflections on the core lens.

The above presented comparison illustrates that the developed model features a similar trend with frequency as that of the Fly's Eye antenna concept but has a degraded performance in terms of spillover efficiency. Furthermore, through the comparison of Figure 6-6 *(b)* one can deduce that this difference in spillover is mainly attributed to the simplified modelling of the iris structure with a double straight slot. In particular, due to the worse suppression of the TM_0 in the diagonal planes, the power launched outside the core lens for the double straight slot is significantly more when compared with the iris, leading to a reduction in the spillover efficiency.

6.3. Contribution to measurement campaign

Having presented the modelling of the Fly's Eye antenna through a combination of Asymptotic and Physical Optics techniques, the following section will discuss the utilization of the described modelling tool for the purpose of examining the measurements of the assembled prototype. Within this context, the main deductions extracted from the measurements will be presented together with the thought process behind their subsequent study. Starting from the former, the phase profiles extracted from two distinct measurements are shown through Figure 6-7. These measurements correspond to two distinct 2D scans, one performed close to the tip of the elliptical lens, while the other derived from a farther distance.

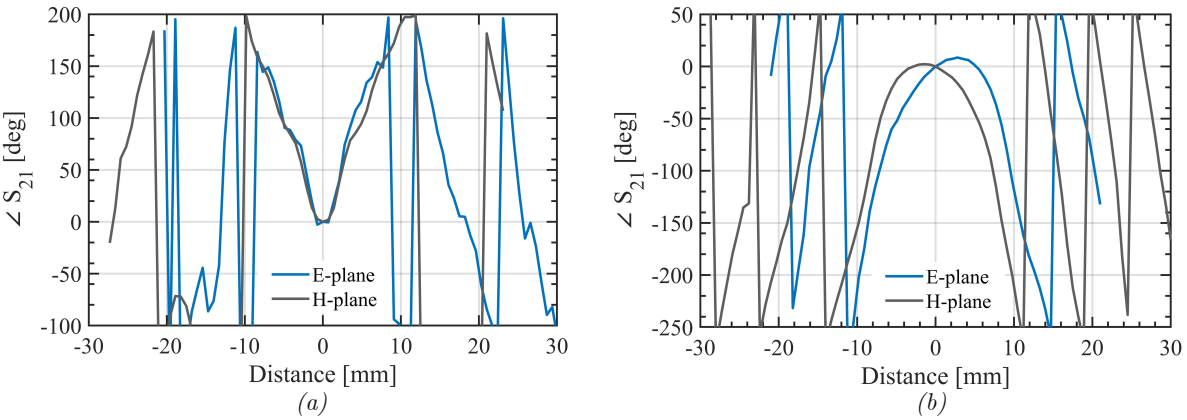

Figure 6-7. Phase profile of 2D scan (a) close to and (b) further away from the shell lens.

As clearly visible from the figures above, instead of a more or less flat phase profile within the area defined by the shell lens aperture ($D_{shell} = 30\ mm$), which would correspond to a beam focused in the far field; both measurements feature substantial phase variance, each relating to a different focusing behavior. More specifically, given the phase profile of the measurement close to the shell lens, the field at this position seems to converge, while considering the measurement farther away from the shell lens, the field seems to diverge. Combining these observations for the behavior of the field in the two measuring planes, the field picture produced by the shell lens seems to resemble that of Figure 6-8, instead of being collimated.

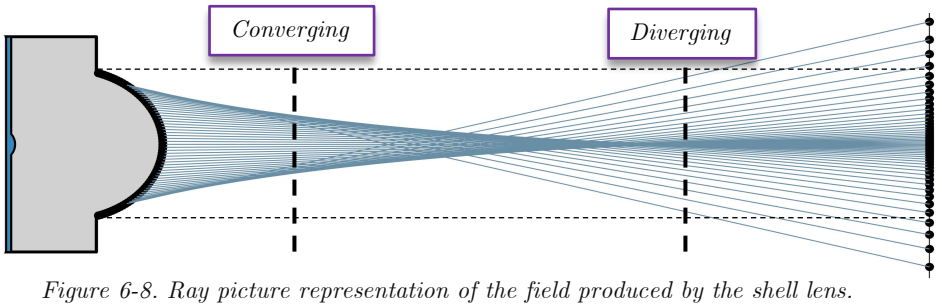

Figure 6-8. Ray picture representation of the field produced by the shell lens.

Using this insight derived from the examination of the measurements, the modelling tool presented in the two previous sections will be employed in an effort to identify the cause of the observed focusing effect.

6.3a. Physical displacement

Arguably the simplest reason which can lead to the replication of the observed focusing refers to simulating a physical vertical displacement between the origin of the spherical wave incident of the shell lens surface and the lower focus of the ellipse. More specifically, if the lower focus of the elliptical shell lens is displaced above the spherical wave origin, the produced ray picture starts to feature the observed focusing effect as illustrated through Figure 6-9.

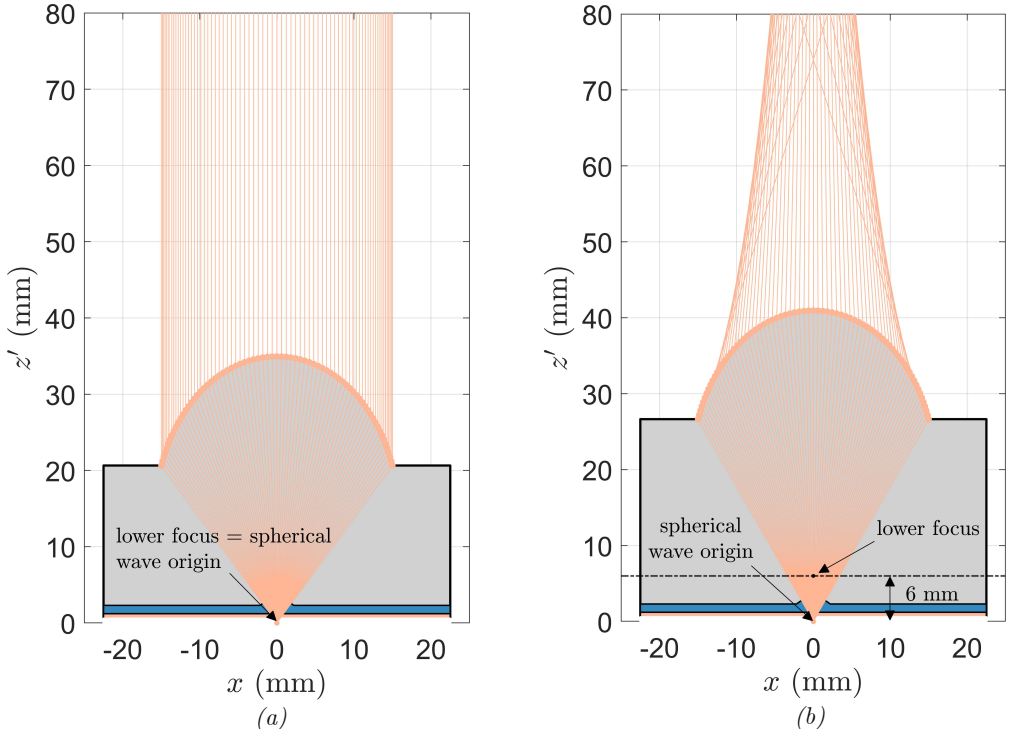

Figure 6-9. Ray picture of shell lens assuming $\hat{k}_{inc,shell} = \hat{r}$, for (a) lower focus of ellipse coinciding with origin of spherical wave and (b) lower focus displaced above spherical wave origin.

Even so, in order to begin to replicate the focusing observed in the measurements, the required displacement of the elliptical lens must be in the range of *7 mm*, as indicated through the phase profile comparison shown in Figure 6-10. Considering the physical size of the structures, such a difference in dimensions is unreasonable to assume since it would be easily identified in either the core or the shell lenses. As a result, this option can be ruled out.

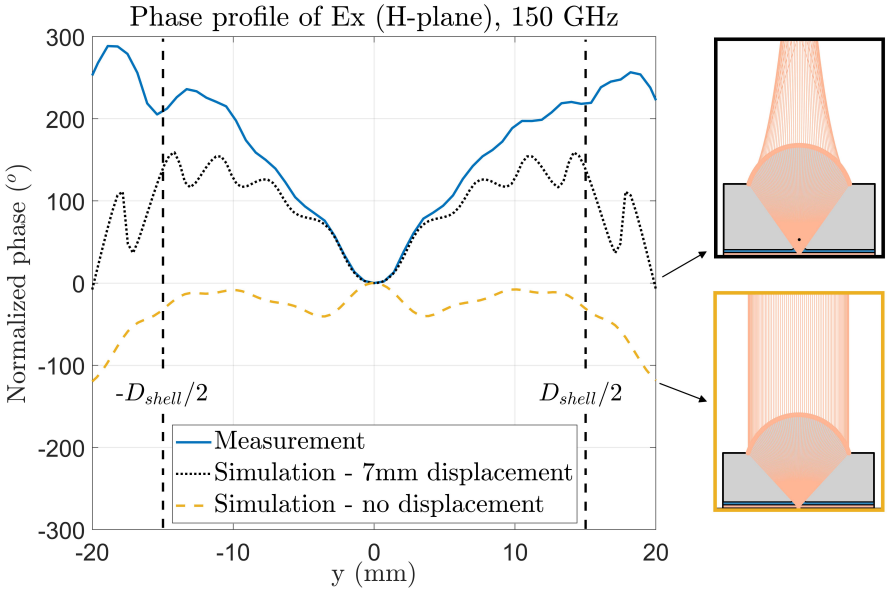

Figure 6-10. Phase profile comparison between measurement and recreated field close to the tip of the ellipse, with and without displacement of the shell lens.

6.3b. Core lens material permittivity

The next potential cause that can recreate the observed focusing refers to featuring a larger than anticipated permittivity in the core lens material. In this case, given the more resonant structure, the origin of the near field spherical wave would drop farther below the ground plane. In turn, this would cause the core lens to act as an extended hemispherical lens, thus forming a virtual focus even farther below the ground plane. Having said that, in order to create an impactful difference between the expected origin of the spherical wave and the virtual focus, the relative permittivity of the core lens material would need to be significantly increased ($\varepsilon_{r,core} \approx 20$), as indicatively showcased by the ray picture illustration of Figure 6-11.

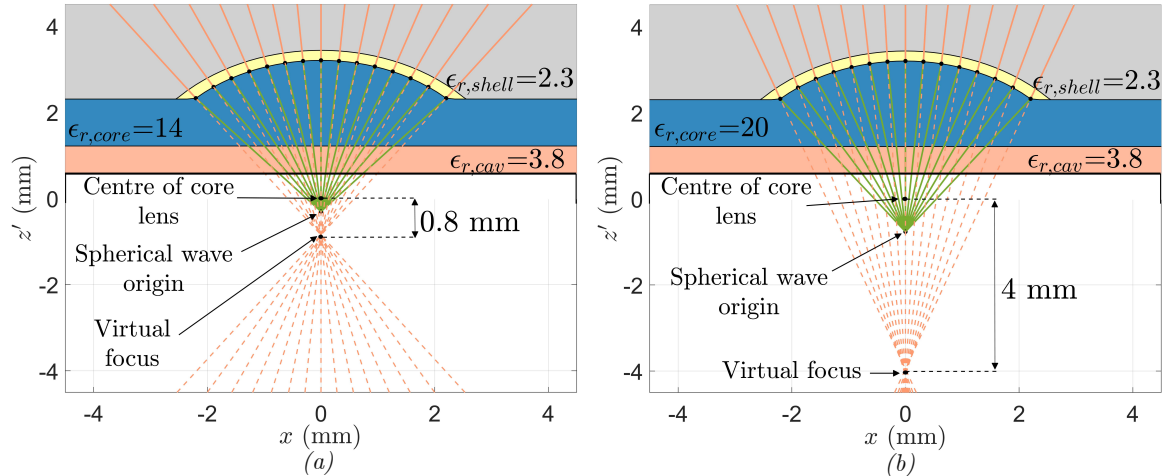

Figure 6-11. Ray picture for core lens assuming spherical wave incidence, for (a) $\varepsilon_{r,core}$=14 and (b) $\varepsilon_{r,core}$=20.

Similar to the previous case of the physical displacement, considering the permittivity values necessary to cause the required displacement together with the measured values for the permittivity of the PREMIX ($\varepsilon_{r,measured} \approx 9.3$), this effect can also be ruled out.

6.3c. Shell lens material permittivity

Having elaborated on the possibility of recreating the measured focusing effect through either a physical displacement or an increased permittivity for the core lens material, the next step in the examination process refers to considering the impact of changing the plastic material's permittivity. In particular, the elliptical structure of the shell lens is designed such that it transforms a spherical wave originating from its lower focus to a plane wave and vice versa. This process is very much dependent on the permittivity of the plastic, since its value determines the level of refraction at the plastic-air interface and as such the overall behavior of the elliptical structure. In fact, if the geometry of an elliptical structure is designed expecting a certain permittivity but the actual permittivity of the utilized material is larger; the refraction on the shell surface is increased, essentially causing a focusing effect as indicatively illustrated through the ray pictures presented in Figure 6-12.

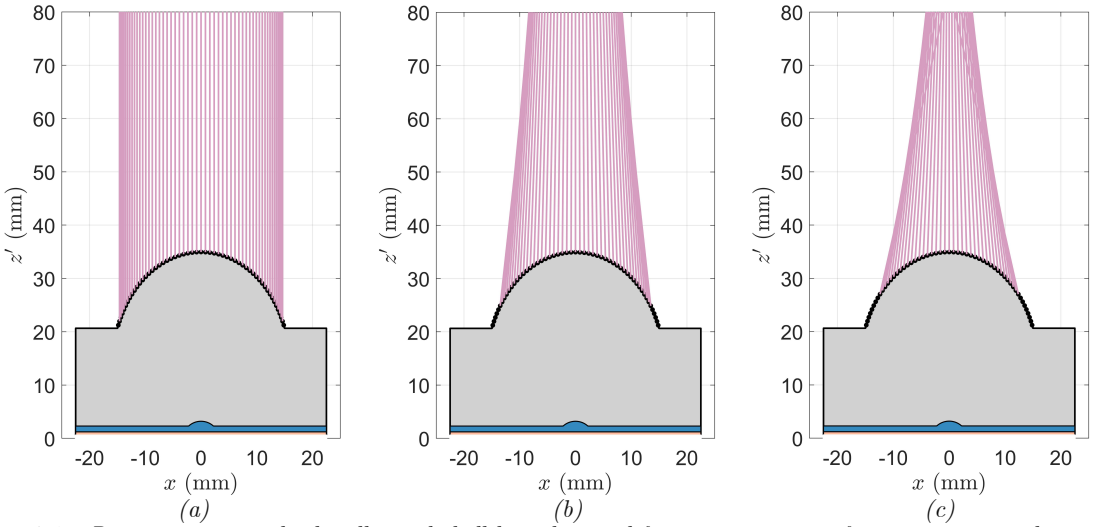

Figure 6-12. Ray picture outside the elliptical shell lens designed for a permittivity of 2.3, assuming spherical wave incidence ($\hat{k}_{inc,shell} = \hat{r}$), for (a) $\varepsilon_{r,shell}$=2.3, (b) $\varepsilon_{r,shell}$=2.5 and (c) $\varepsilon_{r,shell}$=2.8.

Using this insight, the model described through the previous sections will be employed in an effort to recreate the magnitude and phase profiles obtained from the measurements of the assembled prototype. Defining the geometry of the elliptical lens with the expected relative permittivity of HDPE ($\varepsilon_{r,shell}$=2.3) and testing different permittivity values for the plastic, we are able to reproduce the measured patterns with sufficient accuracy for permittivity values in the range of 2.8 to 2.9. This is indicatively showcased through the comparison presented in Figure 6-13, corresponding to a plastic permittivity of 2.85.

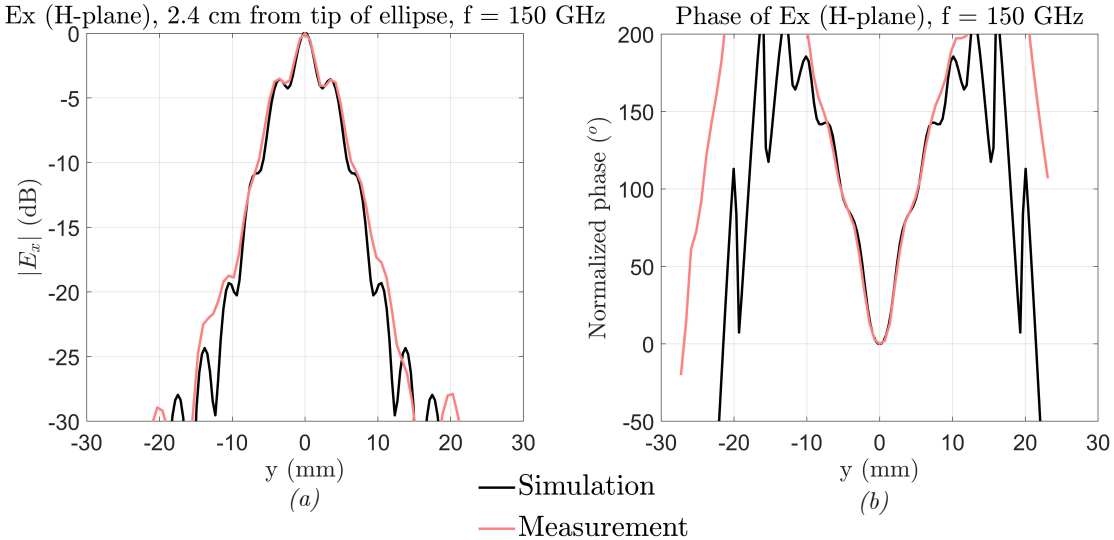

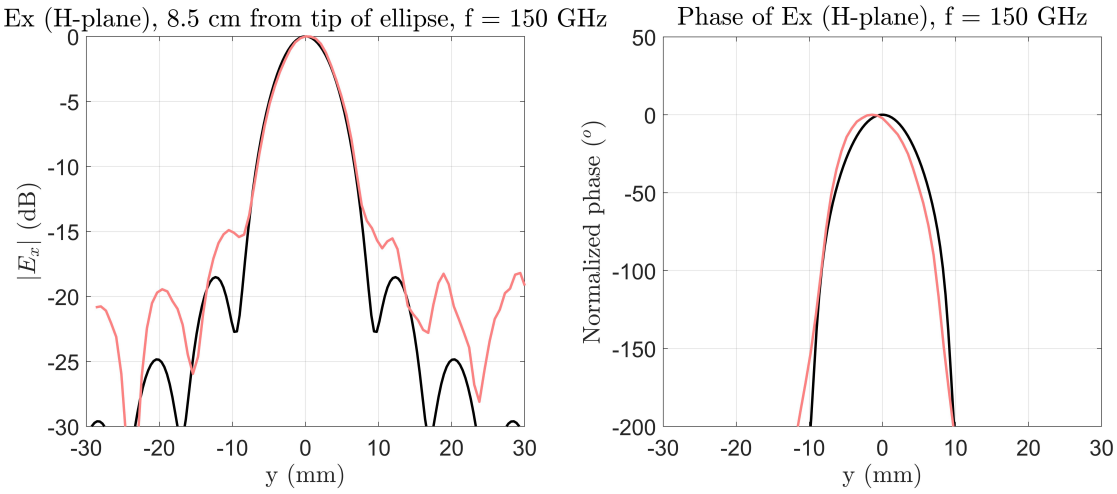

Figure 6-13. Measurement and simulation comparison for close position, (a) magnitude and (b) phase profile and for farther away position (c) magnitude and (d) phase profile.

As visualized through the figures above, the magnitude and phase profiles are recreated with significant accuracy for both the close and the farther away measurement setups. The impact of employing a plastic with such a different permittivity from its nominal value on the antenna performance, can be clearly indicated through either the above phase profiles or the illustration of the focusing effect in Figure 6-8. Even so, to showcase this even further, the directivity of the shell lens is presented versus frequency for large permittivity variation through Figure 6-14, considering that the value for which the elliptical lens is design is $\varepsilon_{r,shell}$=*2.3*. The illustrated directivity† is computed using the recreated free space patterns of the shell lens.

$$D_{ir,max} = \frac{4\pi R^2 |E_{max}|^2}{2\zeta_0 P_{rad,feed}}, \tag{6.2}$$

Where $P_{rad,feed}$ corresponds to the power radiated by the double slot described in *section 6.1* inside an infinite dielectric region with relative permittivity of $\varepsilon_{r,core}$ and R refers to the distance between the tip of the elliptical shell lens and an observation sphere in the far field.

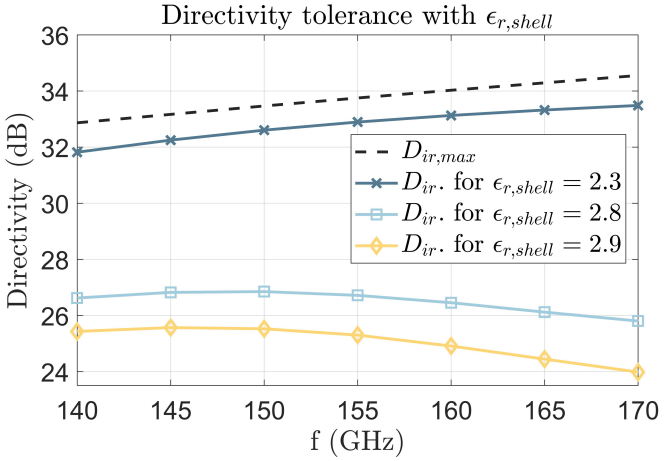

Figure 6-14. Directivity tolerance for significant permittivity variation of $\varepsilon_{r,shell}$.

To conclude this section, it is worth mentioning that the presented study and thought process led to the measurement of the permittivity of the plastic used in the assembled prototype of the Fly's Eye antenna, extracting its value to be very close to the estimated one ($\varepsilon_{r,measured} \approx 2.83$) and as such identifying it to be the issue of the assembled prototype.

† *The directivity includes both the spillover and reflection losses of the core-shell structure.*

6.4. Tolerance study

Having discussed the utilization of the developed model towards studying the measurements, this chapter will conclude with a brief tolerance study regarding the impact of the plastic's permittivity to the performance of the Fly's Eye antenna. For this purpose, a reasonable variation is considered for the relative permittivity of HDPE (± 0.1) with its nominal value, i.e., the one used for the definition of the elliptical structure, being $\varepsilon_{r,HDPE} = 2.3$. The resulting directivity comparison is presented through Figure 6-15. It is worth noting that this comparison refers to the developed model and thus it's not the exact directivity values that must be taken into account but the impact of changing the permittivity from its nominal value.

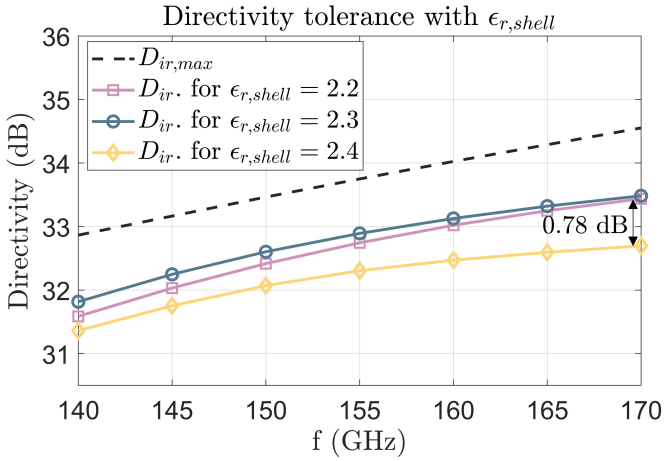

Figure 6-15. Directivity tolerance for reasonable permittivity variation of $\varepsilon_{r,shell}$.

One noteworthy question that arises from the comparison presented above, refers to the reason behind the bigger impact in the antenna directivity when using a larger permittivity plastic compared to that for a lower permittivity, especially noticeable at higher frequencies. To give an answer to this question the problem will be decomposed in two parts, separating the impact of the elliptical shell lens from the primary pattern of the core lens structure. To identify the former, the analysis in reception is employed to derive the Geometrical Optics (GO) fields in the Fourier Optics (FO) sphere produced by an incident plane wave from broadside, as illustrated through Figure 6-16 *(a)*. This process is repeated for the above examined permittivity values, with an elliptical lens geometry defined for $\varepsilon_{r,shell} = 2.3$. The impact of the different permittivity values can be clearly illustrated through the phase variance of the GO fields over the FO sphere, as shown in Figure 6-16 *(b)*.

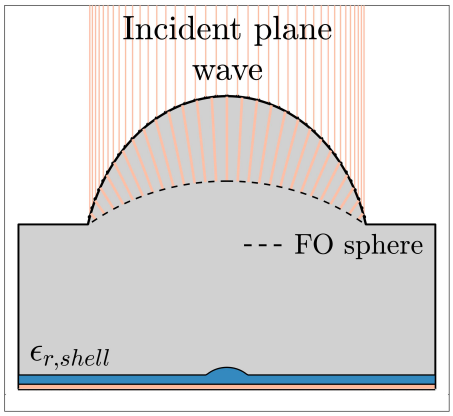

(a)

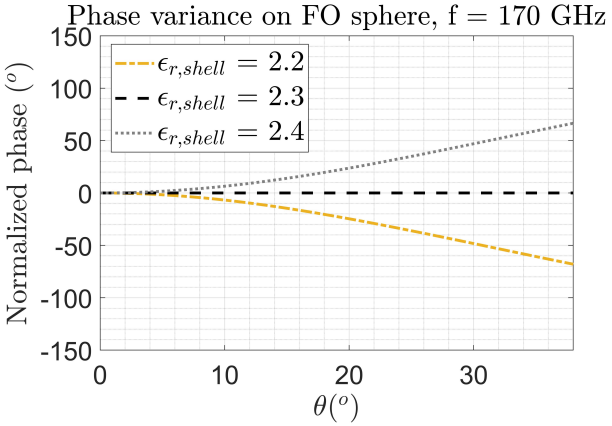

(b)

Figure 6-16. (a) Ray tracing of incident plane wave to FO sphere for $\varepsilon_{r,shell}$=2.3 and (b) phase variance of GO fields over the FO sphere for f=170GHz.

As visualized from the above phase variance, while for the nominal permittivity of the plastic ($\varepsilon_{r,shell} = 2.3$) the phase is constant over the FO sphere, the same cannot be said for the other two examined cases. However, given that the level of phase variance does not significantly change between the two cases ($\varepsilon_{r,shell} = 2.2$ and 2.4), one can anticipate that, on its own, the elliptical lens cannot justify the different impact of the two permittivity values observed through Figure 6-15. As such, to identify the reason behind the bigger impact of the larger permittivity, the behavior of the primary patterns illuminating the shell lens must also be considered.

Analyzing lenses in reception enables the evaluation of their performance in terms of the field matching between the GO fields and the field of the feeding structure in the FO sphere. In fact, when the GO and feed fields are conjugate matched, the component's aperture efficiency is maximized; meaning that the obtained directivity approaches the maximum possible one for the given aperture size. Having said the above, to evaluate the antenna performance in combination with the change in the structure's permittivity, the phase of the primary patterns will be compared to the conjugate of that of the GO fields in the FO sphere for the three different permittivity cases ($\varepsilon_{r,shell} = 2.2$, 2.3 and 2.4). The reference system used to derive the field is displaced by *0.27 mm* above the ground plane, corresponding to the physical position of the lower focus of the shell lens in the Fly's Eye antenna prototype. The resulting comparison of the phases over the FO sphere for a frequency of *170 GHz*, is presented through Figure 6-17.

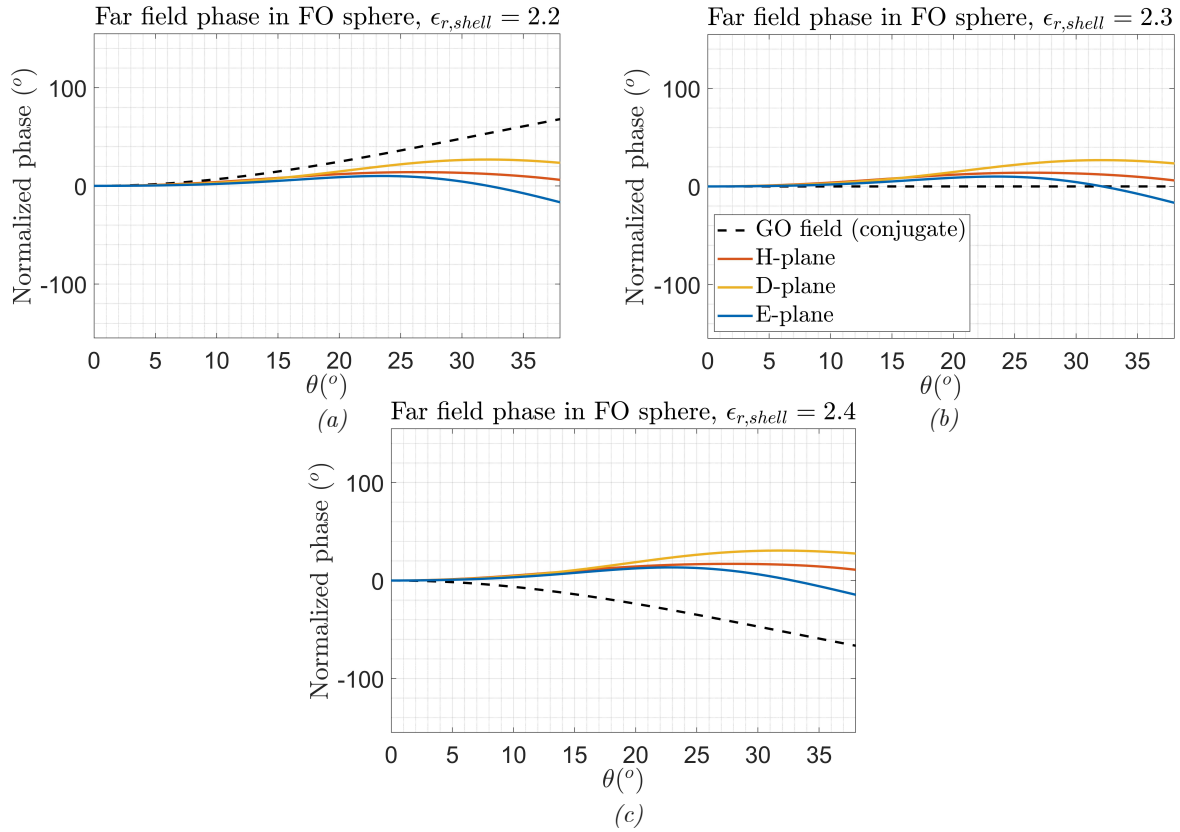

Figure 6-17. Phase comparison over the FO sphere between main planes of feeding structure and GO fields at 170 GHz, for (a) $\varepsilon_{r,shell}$=2.2, (b) $\varepsilon_{r,shell}$=2.3 and (c) $\varepsilon_{r,shell}$=2.4. The observation angle θ refers to a reference system displaced above the ground plane to the position of the lower focus of the elliptical shell lens ($\Delta_{z,shell}$=0.27mm).

Given the behavior of the phase of the primary pattern over the FO sphere relative to that of the GO fields, as illustrated through the figures above, it can be deduced that the phase matching is much more degraded for the larger permittivity of the plastic, compared to that for the smaller permittivity case. This essentially justifies the different impact in the directivity observed through Figure 6-15.

In order to provide a physical explanation of this effect in terms of the core-shell structure design, one must consider the relative position of the spherical wave origin compared to the lower focus of the elliptical structure. As a first step in this consideration, the ray tracing of the broadside incident plane wave is performed for the three different permittivity cases, as visualized through Figure 6-18.

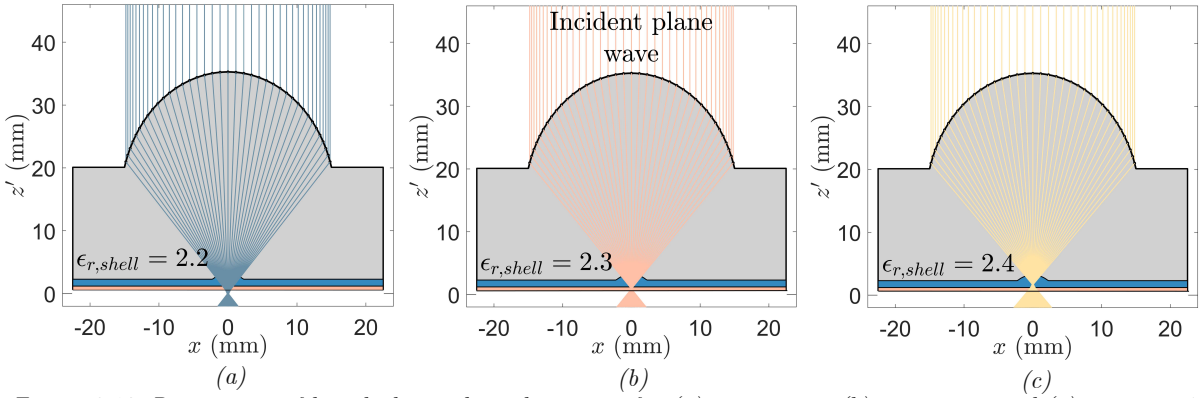

Figure 6-18. Ray tracing of broadside incident plane wave for (a) $\varepsilon_{r,shell}$=2.2, (b) $\varepsilon_{r,shell}$=2.3 and (c) $\varepsilon_{r,shell}$=2.4.

While the only structure for which the elliptical lens focuses the rays to a single point is the one with the nominal permittivity ($\varepsilon_{r,shell} = 2.3$), it is worth noting that for larger permittivity values in the plastic, the rays are focussed above the lower focus of the elliptical lens while for smaller values they are focussed below. Taking into account that the spherical wave origin of the primary patterns changes with frequency, together with the directivity comparison presented through Figure 6-15, one can deduce that the phase centre of the primary pattern at higher frequencies is below the chosen lower focus of the elliptical lens, approaching the focussing point for the lower permittivity (Figure 6-18 *(a)*). This can in turn be attributed to the choice of the lower focus placement in the design process such that it improves the Fly's Eye antenna performance at the lower frequencies of the desired band of operation (*140-170 GHz*). To showcase the latter, the field inside the plastic will be derived through a full-wave simulation (CST) of the core lens structure, considering the double iris shaped slot etched in the ground plane and a plastic permittivity of $\varepsilon_{r,shell} = 2.3$. Subsequently, the extracted far field will be introduced into the GO/FO tool of [42] to derive the resulting aperture efficiency for different positions of the lower focus of the elliptical lens relative to the ground plane. The improvement of the lens performance at lower frequencies for lower focus placements above the ground plane can be visualized through Figure 6-19.

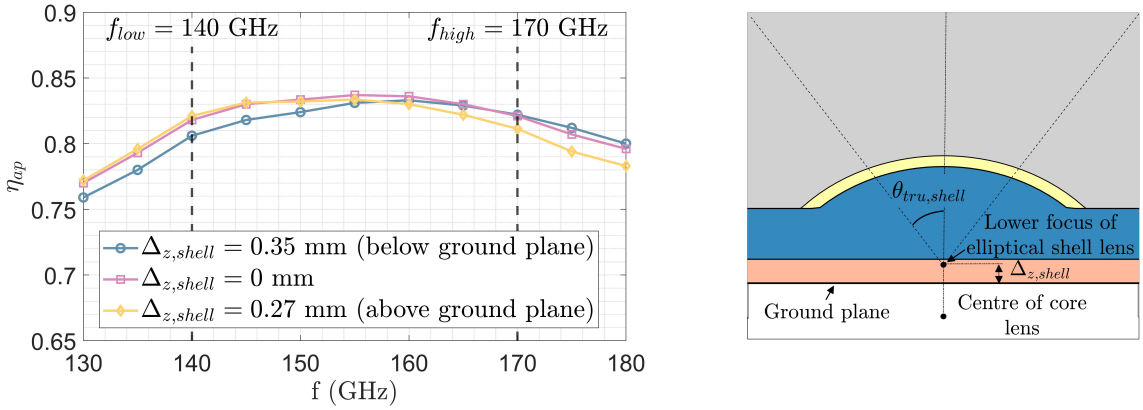

Figure 6-19. Aperture efficiency comparison for different positions of the lower focus of the shell lens. The displayed efficiencies are derived using the far field inside the plastic obtained by a full-wave simulation and the GO/FO tool of [42].

CHAPTER 7. Conclusions and future work

7.1. Summary

Excluding the introduction as well as the motivation for this work which were presented in Chapter 1, the content of this thesis can be neatly separated into two parts. The first, comprised of Chapter 2 and 3, provides an extensive description of the mathematical steps required for the efficient evaluation of the near field of a leaky wave structure. Following this, the second part which consists of Chapter 4 to 6, presents some basic implementations of small lenses and describes the development of a model for the Fly's Eye antenna concept as well as its utilization.

As discussed through Chapter 1, the motivation for developing a computationally efficient approach to evaluate the near field of a leaky wave structure lies on the potential of shaping the core lens of the Fly's Eye antenna. Towards this goal, Chapter 2 provides an extensive description of an efficient numerical method in which the involved complex integrals are evaluated over the path of steepest descent in the spectrum. Using this background, in Chapter 3, an approach for the asymptotic evaluation of the integral expression resulting from the steepest descent path method of integration is presented. While this method substantially improves the computational efficiency, essentially mitigating the need for any spectral integration; its accuracy is based on the applicability of the approximation described through *section 3.2c*. In a few words, the utilized approximations enable the derivation of the near field, provided that at the examined region the latter resembles a spherical wave around broadside. For a leaky wave structure around resonance, this assumption can be performed even very close to the leaky wave cavity given a proper choice of the phase centre position as described through [20] and elaborated in *section 3.2d*.

The complete discussion presented through Chapter 3 considered the evaluation of the near field for the case of an elementary source. To build upon this concept, the initial stages of Chapter 4 elaborate on the complications involved in the asymptotic evaluation process when an actual source is introduced, treating the case of a double straight slot in the ground plane. Following this, some basic small lens concepts are examined, showcasing the far field convergence in wideband structures up to the shadow boundary angle, as well as the potential improvement of the spillover efficiency for resonant structures when placing lenses in the near field. Subsequently, Chapter 5 describes the combination of Physical Optics techniques that can be used to replicate the impact of the core-shell structure, with Chapter 6 combining those techniques with a simplified representation of the iris shaped slot to develop a model of the Fly's Eye antenna. Finally, the last part of Chapter 6 describes the utilization of this model for troubleshooting during the measurement campaign of the Fly's Eye antenna prototype. Through this process it showcases how the model contributed to identifying the problem in the antenna prototype, by simulating different design alterations with the aim of recreating the measured patterns. This led to the identification of the problem as the shell lens material relative permittivity, which was substantially different from its nominal value.

7.2. Conclusions

To supplement the summary of the content of this thesis presented above, the most noteworthy concluding remarks will be outlined in the following section.

- The spherical wave nature of the near field of a leaky wave structure arising from the proper choice of phase centre [20], allows its asymptotic evaluation through an approximation that mitigates the branch singularity of the Hankel function (*section 3.2c*). This enables the subsequent asymptotic evaluation of the near field integral expressions, through treating

only polar singularities related to the leaky wave modes supported by the examined stratification.

- This approximation's accuracy can be enhanced through modifying the phase centre choice above and below the shadow boundary angles. This approach could be further improved by defining additional angular regions for the treatment of the *TM* integrals, in order to also account for the TM_0 leaky wave mode (*section 3.2d*).

- Since the introduced approximation is based on the spherical wave nature of the near field, it's accuracy along broadside progressively degrades as the observation point moves closer to the source. An indicative estimate for its applicability region identified it to be radial distances larger than $1.5\,\lambda_0$ for the wideband and $8\,\lambda_0$ for the resonant leaky wave structures (*section 3.3d*). However, it should be noted that the applicability region must be defined per individual case, considering the acceptable accuracy and the angular region of interest.

- Regarding the source inclusion, the treatment of the near field integral expression depends on the nature of the source's spectrum with respect to the principle exponential term of the integrand (*section 4.1*). To maintain an accurate representation of the near field for the distances of interest, the examined double straight slot was treated through superimposing two straight slots. In this manner, the source's spectrum could be assumed to be slow varying with respect to the exponential for each slot, allowing the closing of the α integral through the SPP approximation.

- The asymptotic approximation of the near field can be combined with a set of Physical Optics techniques to model the core-shell structure of the Fly's Eye antenna. This becomes useful when the structure needs to be simulated several times, since the asymptotic approximation negates the need for any spectral integration in order to calculate the near field, making it very computationally efficient. In particular, the asymptotic approximation of the near field is roughly forty times faster compared to the numerical evaluation of the same SDP integral expressions.

- The elliptically elongated double iris shaped slot of the Fly's Eye antenna has been approximated via a simple double straight slot to model the core-shell structure in an efficient manner. In turn, this provided a versatile tool that was employed to evaluate the antenna performance during the measurement campaign of the Fly's Eye antenna assembled prototype.

7.3. Future work

Asymptotic approach - elementary source

As was noted through several parts of this thesis report, the asymptotic approach presented through Chapter 3 for the evaluation of the near field, and more specifically the treatment of the Hankel function, is based on the nature of the near field. As such, its applicability is limited to regions where the near field spherical wave formation along broadside can be assumed. While this can indeed be employed for the study of small lenses in wideband stratifications, similar to the core lens of the Fly's Eye antenna, a neater approach would require asymptotically treating the branch of the Hankel functions similar to what was done in [43]. Even if this would substantially complicate the presented asymptotic analysis, requiring separate treatment for the branch singularity both in the regularized part as well as the polar contribution, while also

necessitating the separate treatment of the small and large argument representations of the Hankel function, it indeed constitutes an interesting aspect for future study. Essentially, if the approximation of *section 3.2c* is not employed, there would be no inherent limitation for the applicability region of the asymptotic approach, enabling further studies on the wave phenomena which drive the radiation process for leaky wave structures.

Asymptotic approach – source inclusion

Another important aspect that would be a significant improvement of the asymptotic approach, refers to the treatment of the source. In particular, the approach described through Chapter 4 considered as a given the closing of the integral in α in a similar manner to what was done for the case of elementary sources (*section 2.2a*). This approach led to the separation of pairs of sources into distinct elements (*section 4.1b*) and their subsequent treatment through superposition. Having said that, another potentially interesting alternative would be to expand the spectrum of the source in a Fourier series prior to closing the integral in α, as given below.

$$C_m(k_\rho, \alpha) = \sum_{n=-\infty}^{\infty} c_n(k_\rho) e^{-jn\alpha} \tag{7.1}$$

Where the coefficients $c_n(k_\rho)$ can be represented by the generalized pencil of function (GPOF) method [44], as in [21].

In this manner, the α integral can be closed analytically through a term-by-term integration into Bessel functions using the following identity.

$$\int_0^{2\pi} e^{-jn\alpha} e^{-jk_\rho \rho \cos(\alpha-\varphi)} d\alpha = 2\pi(-j)^n e^{-jn\varphi} J_n(k_\rho \rho), \tag{7.2}$$

This process would result into a sum of single complex integrals in k_ρ with Bessel and in turn, through the use of (*2.3*), Hankel functions of higher order. As a result, while it allows for a more generic treatment of any source, in terms of the asymptotic evaluation of the near field, this approach would necessitate dealing with Hankel functions of higher order in addition to those already presented in the integral representation.

Shaping of the core lens

While up till now the proposed future steps referred to the overall improvement of the asymptotics, in the following paragraph the future applicability of such a computationally efficient approach will be described. More specifically, having presented an asymptotic method able to evaluate very fast the near field on small lenses, the latter can be used in combination with an optimizer to further improve the performance of the Fly's Eye antenna via changing the core lens shape. For example, the core lens can be made conformal to the incident field, thus acting as an ideal transition; or alternatively it can be shaped with the aim of enhancing the aperture efficiency for displaced feeds, in turn improving the scanning capabilities of the core-shell structure. Such an approach can be employed in combination with laterally displacing the feeds for scanning cases, as in [45], in order to derive shaped variants of core lenses depending on their position in the focal plane, or in other words the scanning they produce.

It should be noted that in order to optimize the Fly's Eye antenna performance through shaping the core lens, the simplified model of the iris shaped structure presented through *section 6.1b* would not be sufficient. Instead, a simple approach to improve the modelling process would be to segment the iris structure and represent it through a superposition of elementary sources or straight slots, using the process described throughout this thesis.

To conclude, all the above presented ideas are yet to be further explored, with their analysis and implementation expected to be the continuation of the work presented in this thesis.

APPENDICES

Appendix A. Spectral Green's function

The Green's functions correspond to the impulsive response of the examined structure, i.e., the fields radiated by an elementary source, with distinct variants relating different kinds of sources (J_{eq} or M_{eq}) to different types of fields (E or H). For any stratified structure with an arbitrary number of planar and unbounded dielectric layers, obtaining the Green's function primarily requires solving for the voltage and current potentials of the equivalent transmission line problem. This equivalent problem is in turn constructed with respect to the examined structure, where E-field discontinuities in the stratification (i.e., magnetic currents) correspond to series voltage sources in the transmission line model, while H-field discontinuities in the stratification (i.e., electric currents), relate to parallel current sources. For the stratified structures presented through Figure 2-1, the equivalent transmission line models are depicted through Figure A-1. The only difference between the two refers to the dielectric properties of the cavity and semi-infinite regions, as well as the physical height of the cavity.

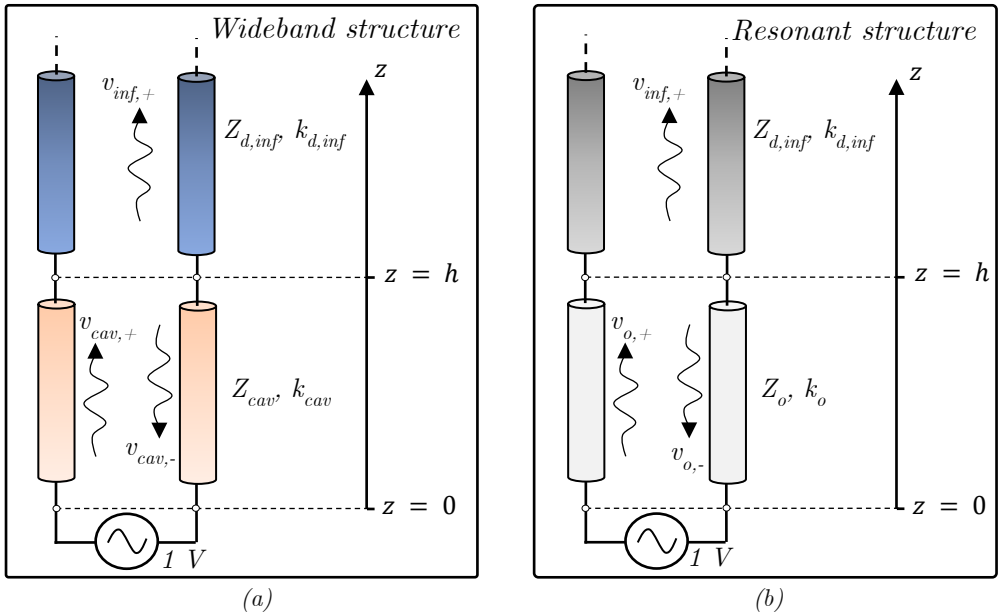

Figure A-1. Equivalent transmission line models for (a) wideband and (b) resonant structures of Figure 2-1.

Once the equivalent transmission line model has been extracted, the voltage and current potential functions can be obtained in a straightforward manner as will be presented through *Appendix B*. More specifically, two different types of potential functions can be derived, labelled as *TE* and *TM* solutions (v_{TE}, i_{TE} and v_{TM}, i_{TM}). These correspond to the fields produced by the different kinds of auxiliary potentials introduced for the derivation of the Green's function for the stratified structure, namely the *TE* solutions relates to the electric vector potential ($\vec{F}$), while the *TM* to the magnetic vector potential ($\vec{A}$). Having discussed the above, the voltage and current potential functions can be substituted into analytical expressions for the spectral Green's function of stratified media. Considering the examined structures which feature equivalent magnetic current distributions in the ground plane, the required dyadic spectral Green's function (G^{em}) for planar sources (i.e., along x or y), is given below.

$$\bar{\bar{G}}^{em}(k_x, k_y, z, z_s) = \begin{bmatrix} \frac{\left(v_{TM}(k_x,k_y,z,z_s) - v_{TE}(k_x,k_y,z,z_s)\right)k_x k_y}{k_\rho^2} & -\frac{v_{TE}(k_x,k_y,z,z_s)k_y^2 + v_{TM}(k_x,k_y,z,z_s)k_x^2}{k_\rho^2} \\ \frac{v_{TE}(k_x,k_y,z,z_s)k_x^2 + v_{TM}(k_x,k_y,z,z_s)k_y^2}{k_\rho^2} & \frac{\left(v_{TE}(k_x,k_y,z,z_s) - v_{TM}(k_x,k_y,z,z_s)\right)k_x k_y}{k_\rho^2} \\ -\frac{\zeta_d k_y i_{TM}(k_x,k_y,z,z_s)}{k_d} & \frac{\zeta_d k_x i_{TM}(k_x,k_y,z,z_s)}{k_d} \end{bmatrix}, \quad (A.1)$$

Since this work focuses on the derivation of the field in the semi-infinite region of the leaky wave structure, the potential functions can be written as follows, expressed in terms of the voltage and current wave amplitudes in the semi-infinite region ($v^+_{TM/TE}$ and $i^+_{TM/TE}$) together with the exponential term relating to the propagation inside the latter.

$$\begin{aligned} v_{TM/TE}(k_x, k_y, z, z_s) &= v^+_{TM/TE}(k_x, k_y, z_s)e^{-jk_z z} \\ i_{TM/TE}(k_x, k_y, z, z_s) &= i^+_{TM/TE}(k_x, k_y, z_s)e^{-jk_z z}, \end{aligned} \tag{A.2}$$

Introducing this notation to (*A.1*), allows for the extraction of the z dependence from the dyadic expression when examining the field in the semi-infinite region of a leaky wave structure.

$$\bar{\bar{G}}^{em}(k_x, k_y, z, z_s) = \bar{\bar{D}}^{em}(k_x, k_y, z_s)e^{-jk_z z}, \tag{A.3}$$

Where $\bar{\bar{D}}^{em}(k_x, k_y, z_s) = \begin{bmatrix} \frac{(v^+_{TM} - v^+_{TE})k_x k_y}{k_\rho^2} & -\frac{v^+_{TE}k_y^2 + v^+_{TM}k_x^2}{k_\rho^2} \\ \frac{v^+_{TE}k_x^2 + v^+_{TM}k_y^2}{k_\rho^2} & \frac{(v^+_{TE} - v^+_{TM})k_x k_y}{k_\rho^2} \\ -\frac{\zeta_d k_y i^+_{TM}}{k_d} & \frac{\zeta_d k_x i^+_{TM}}{k_d} \end{bmatrix}$ and $\begin{aligned} v^+_{TE/TM} &= v^+_{TE/TM}(k_x, k_y, z_s) \\ i^+_{TE/TM} &= i^+_{TE/TM}(k_x, k_y, z_s) \end{aligned}$.

Appendix B. Transmission line solution

The leaky wave supporting stratifications introduced in Chapter 2 and subsequently discussed in the remaining of this document, consist of a resonant cavity confined between a ground plane and a semi-infinite dielectric region, with all planar layers assumed infinite and untruncated. The equivalent transmission line models for both the wideband and resonant structures of Figure 2-1 were illustrated through Figure A-1 and their purpose of deriving the potential functions ($v_{TE/TM}$, $i_{TE/TM}$) to be subsequently introduced in the analytic expression of the spectral Green's function (*A.1*), has been discussed in *Appendix A*. In the following appendix section, the solution of this transmission line model will be extracted both for observation points inside the cavity and the semi-infinite region. Furthermore, the different treatment required for the *TE* and *TM* solutions will also be discussed.

Before proceeding to the transmission line solution itself, it should be noted that the spectral Green's function given through (*A.1*), is modified such that the transmission line voltages and currents solutions correspond to an equivalent problem with unitary amplitude sources. In other words, H-field discontinuities in the stratification are substituted by *1 A* parallel current sources, while E-field discontinuities are replaced by *1 V* series voltage sources. Consequently, assuming a generic planar magnetic current source in the ground plane (M_{eq}) of the examined stratification, a unitary amplitude voltage source is used in the equivalent model. This voltage source is placed in series with the short representing the infinitely extending ground plane, assumed to be a perfect electric conductor.

Having said the above, for the derivation of the analytical solution of the equivalent transmission line problem, the complete expressions for the voltage and current representations are formulated in each transmission line section and the voltage continuity is enforced at the interfaces (boundary conditions), resulting in all the necessary voltage wave amplitudes. As a first step, the derivation of the voltage and current transmission line solutions is performed for the structure of Figure B-1 *(a)*, featuring its reference system on the ground plane. The variable z_s included in the following expressions refers to the height of the source in the stratifications.

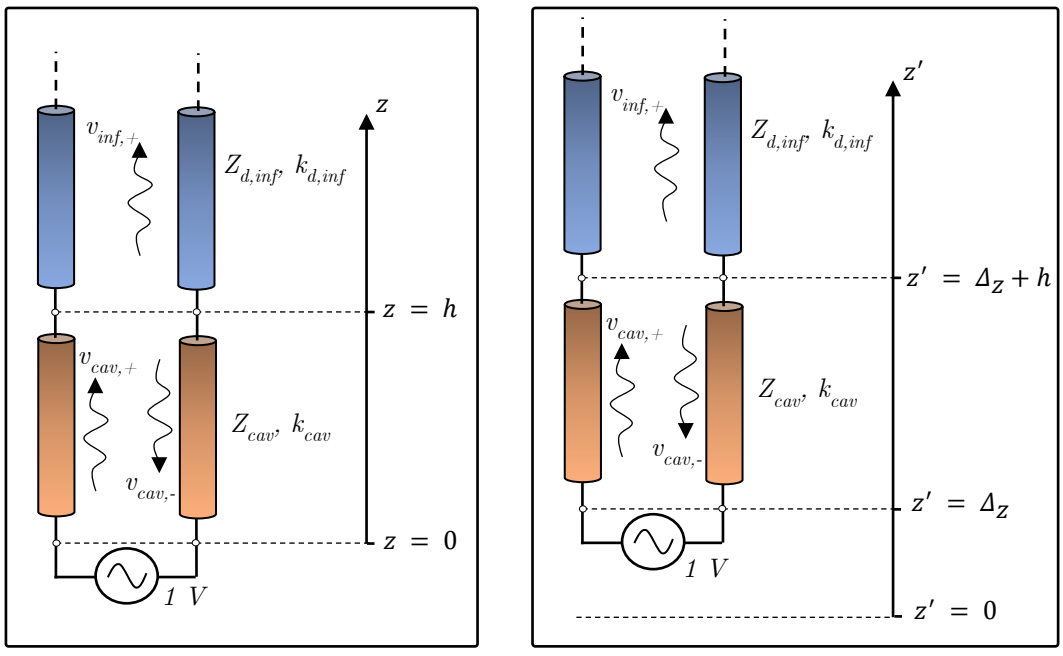

Figure B-1. Equivalent transmission line model of wideband structure for reference system (a) in ground plane and (b) displaced by Δ_z below the ground plane.

For section representing the cavity (0 ≤ z ≤ h)

$$v_{cav}(k_\rho, z, z_s = 0) = v_{cav,+}(k_\rho, z_s = 0)e^{-jk_{z,cav}z}\left(1 + \Gamma_1(k_\rho, z, z_s)\right), \tag{B.1}$$

Where $\Gamma_1(k_\rho, z, z_s = 0) = \frac{v_{cav,-}(k_\rho, z_s=0)}{v_{cav,+}(k_\rho, z_s=0)} e^{j2k_{z,cav}z}$.

Expressing the reflection coefficient at a height z inside the cavity ($\Gamma_1(k_\rho, z, z_s)$) in terms of its value at the interface $z = h$ (Γ_A):

$$\Gamma_A = \Gamma_1(k_\rho, h, z_s = 0) = \frac{Z_{inf} - Z_{cav}}{Z_{inf} + Z_{cav}} = \frac{v_{cav,-}(k_\rho, z_s=0)}{v_{cav,+}(k_\rho, z_s=0)} e^{j2k_{z,cav}h} \Rightarrow \Gamma_1(k_\rho, z, z_s = 0) = \Gamma_A e^{j2k_{z,cav}(z-h)}, \tag{B.2}$$

Enforcing boundary conditions (voltage continuity) for the voltage solutions at $z = 0$:

$$v_{cav}(k_\rho, 0, z_s = 0) = 1 \Rightarrow v_{cav,-}(k_\rho, z_s = 0) = 1 - v_{cav,+}(k_\rho, z_s = 0), \tag{B.3}$$

Combining (*B.2)* and (*B.3*) results in the required voltage wave amplitude.

$$v_{cav,+}(k_\rho, z_s = 0) = \frac{1}{1+\Gamma_A e^{-2jk_{z,cav}h}}, \tag{B.4}$$

The current solution can be expressed in a straightforward manner through the voltage wave amplitudes as given below, with both the transmission line solutions at a height z inside the cavity presented through (*B.5*).

$$i_{cav}(k_\rho, z, z_s = 0) = \frac{v_{cav,+}(k_\rho, z_s = 0)}{Z_{cav}} e^{-jk_{z,cav}z}\left(1 - \Gamma_A e^{2jk_{z,cav}(z-h)}\right)$$

$$\textit{Voltage \& Current solutions for the dielectric cavity } (z < h): \quad \begin{aligned} v_{cav}(k_\rho, z, z_s = 0) &= \frac{e^{-jk_{z,cav}z}\left(1+\Gamma_A e^{2jk_{z,cav}(z-h)}\right)}{1+\Gamma_A e^{-2jk_{z,cav}h}} \\ i_{cav}(k_\rho, z, z_s = 0) &= \frac{e^{-jk_{z,cav}z}\left(1-\Gamma_A e^{2jk_{z,cav}(z-h)}\right)}{Z_{cav}\left(1+\Gamma_A e^{-2jk_{z,cav}h}\right)} \end{aligned} \tag{B.5}$$

For the section representing the semi-infinite medium (z ≥ h)

Assuming an infinitely extended dielectric region, the voltage and current solutions can be expressed as follows.

$$v_{inf}(k_\rho, z, z_s = 0) = v_{inf,+}(k_\rho, z_s = 0)e^{-jk_{z,inf}z} \quad \& \quad i_{inf}(k_\rho, z, z_s = 0) = \frac{1}{Z_{inf}} v_{inf,+}(k_\rho, z_s = 0)e^{-jk_{z,inf}z}$$

Evidently the current solution (i_{inf}) can be directly derived through dividing the voltage solution (v_{inf}) with the characteristic independence of the transmission line section (Z_{inf}). This results from assuming no reflections at any height of the examined dielectric region, which in turn leads to the existence of a single propagating wave along positive z. Having said that, enforcing voltage continuity at the interface of the two regions ($z = h$), returns the required voltage wave amplitude.

$$v_{inf}(k_\rho, h, z_s = 0) = v_{cav}(k_\rho, h, z_s = 0) \Rightarrow v_{inf,+}(k_\rho, z_s = 0) = \frac{1+\Gamma_A}{1+\Gamma_A e^{-2jk_{z,cav}h}} e^{j(k_{z,inf} - k_{z,cav})h}, \tag{B.6}$$

$$\textit{Voltage \& Current solutions for semi infinite dielectric } (z > h): \quad \begin{aligned} v_{inf}(k_\rho, z, z_s = 0) &= \frac{1+\Gamma_A}{1+\Gamma_A e^{-2jk_{z,cav}h}} e^{j(k_{z,inf} - k_{z,cav})h} e^{-jk_{z,inf}z} \\ i_{inf}(k_\rho, z, z_s = 0) &= \frac{1}{Z_{inf}} \frac{1+\Gamma_A}{1+\Gamma_A e^{-2jk_{z,cav}h}} e^{j(k_{z,inf} - k_{z,cav})h} e^{-jk_{z,inf}z} \end{aligned}$$

(*B.7*)

As evident through equations (*B.6*) and (*B.7*), due to the existence of a single propagating wave in the semi-infinite region, the voltage and current potential functions can be decomposed into their respective wave amplitudes, featuring no z dependence, and the exponential term corresponding to the propagation inside the semi-infinite medium. For the examined structure of Figure B-1 (*a*), this decomposition is expressed through equation (*B.8*).

$$v_{inf}(k_\rho, z, z_s = 0) = v_{inf}^{+}(k_\rho, z_s = 0)e^{-jk_{z,inf}z} \quad \& \quad i_{inf}(k_\rho, z, z_s = 0) = i_{inf}^{+}(k_\rho, z_s = 0)e^{-jk_{z,inf}z}, \qquad (B.8)$$

$$\text{where} \quad \begin{aligned} v_{inf}^{+}(k_\rho, z_s = 0) &= \frac{1+\Gamma_A}{1+\Gamma_A e^{-2jk_{z,cav}h}} e^{j(k_{z,inf}-k_{z,cav})h} \\ i_{inf}^{+}(k_\rho, z_s = 0) &= \frac{1}{Z_{inf}} \frac{1+\Gamma_A}{1+\Gamma_A e^{-2jk_{z,cav}h}} e^{j(k_{z,inf}-k_{z,cav})h} \end{aligned}$$

This nature of the transmission line solution is what enables the extraction of the exponential term relating to the propagation inside the semi-infinite region from the dyadic part of the spectral Green's function, as was showcased in *Appendix A (A.3)*.

Regarding the distinction between the *TE* and *TM* cases, the above expressions for the transmission line solutions (*B.5*), (*B.7*) can be employed for both, with the only difference being the characteristic impedances of the transmission line sections as given below.

$$\begin{aligned} &\textit{For TE solution: } (Z_{cav}, Z_{inf}) \Rightarrow (Z_{TE,cav}, Z_{TE,inf}) \\ &\textit{For TM solution: } (Z_{cav}, Z_{inf}) \Rightarrow (Z_{TM,cav}, Z_{TM,inf}) \end{aligned} \quad \text{where } Z_{TE,i} = \frac{k_i \zeta_i}{k_{zi}} \ \& \ Z_{TM,i} = \frac{k_{zi}\zeta_i}{k_i}$$

<u>Displacing the reference system</u>

Considering the structure of Figure B-1 *(b)* with its reference system displaced by Δ_z below the ground plane ($\Delta_z > 0$), the voltage and current solutions in the semi-infinite region are transformed as follows, where $z' = z + \Delta_z$ as evident by Figure B-1.

$$\textit{Voltage \& Current solutions for semi infinite dielectric } (z' > h + \Delta_z): \begin{aligned} v_{inf}(k_\rho, z', z_s = \Delta_z) &= v_{inf}^{+}(k_\rho, z_s = \Delta_z)e^{-jk_{z,inf}z'} \\ i_{inf}(k_\rho, z', z_s = \Delta_z) &= i_{inf}^{+}(k_\rho, z_s = \Delta_z)e^{-jk_{z,inf}z'} \end{aligned}$$

(B.10)

$$\text{with} \quad \begin{aligned} v_{inf}^{+}(k_\rho, z_s = \Delta_z) &= \frac{1+\Gamma_A}{1+\Gamma_A e^{-2jk_{z,cav}h}} e^{j(k_{z,inf}-k_{z,cav})h} e^{jk_{z,inf}\Delta_z} \\ i_{inf}^{+}(k_\rho, z_s = \Delta_z) &= \frac{1}{Z_{inf}} \frac{1+\Gamma_A}{1+\Gamma_A e^{-2jk_{z,cav}h}} e^{j(k_{z,inf}-k_{z,cav})h} e^{jk_{z,inf}\Delta_z} \end{aligned}$$

With the aim of relating the displacement of the reference system with the spectral representation of the field in the semi-infinite region, presented through Chapter 2 and utilized in this document, the voltage wave amplitudes for the two structures of Figure B-1 can be associated as follows. The same expression applies for the current wave amplitudes.

$$v_{inf}^{+}(k_\rho, z_s = \Delta_z) = v_{inf}^{+}(k_\rho, z_s = 0)e^{jk_{z,inf}\Delta_z}, \qquad (B.11)$$

Appendix C. Mapping to the angular spectrum

The transformation to the angular spectrum is a very convenient step for integrals with similar form to that of (*2.4*), since it removes one branch pair (that at $\pm k_d$), facilitating substantially all the subsequent theoretical manipulations. A short discussion regarding the single valued nature of this transformation as well as the periodicity of the angular spectrum was presented through the second part of *section 2.2d*. For the completeness of this discussion, a brief description of the mapping from the rectilinear to the angular spectrum will be included through the following appendix section.

Due to the single valued nature of the transformation (*2.8*), both Riemann sheets of the rectilinear spectrum (k_ρ) are mapped into adjacent regions of a single Riemann sheet in the angular spectrum (β). This is illustrated through Figure C-1 *(a)* and *(b)*, where the horizontally shaded regions in the angular spectrum correspond to the top, while the vertically shaped regions refer to the bottom Riemann sheets of the k_ρ complex plane.

The depicted mapping can be derived in a simple manner by separating k_ρ and k_z into their real and imaginary parts through substituting the complex angle variable $\beta = \beta_r + j\beta_i$, as follows.

$$\begin{aligned} k_\rho &= k_d(sin(\beta_r)\,cosh(\beta_i) + jcos(\beta_r)\,sinh(\beta_i)) \\ k_z &= k_d\big(cos(\beta_r)\,cosh(\beta_i) - jsin(\beta_r)sinh(\beta_i)\big)' \end{aligned} \qquad (C.1)$$

As an indicative example, region 1 of Figure C-1 *(a)* features positive real and imaginary part of k_ρ. This corresponds to the sections of the angular spectrum with $0 < Re(\beta) < \pi/2$ and $Im(\beta) > 0$ as well as that with $\pi/2 < Re(\beta) < \pi$ and $Im(\beta) < 0$. In turn, these two regions feature different sign for the imaginary part of k_z with the former referring to the top while the latter to the bottom Riemann sheet of the k_ρ complex plane. The same process can be applied for all regions of Figure C-1 *(a)*, resulting to the mapping presented below.

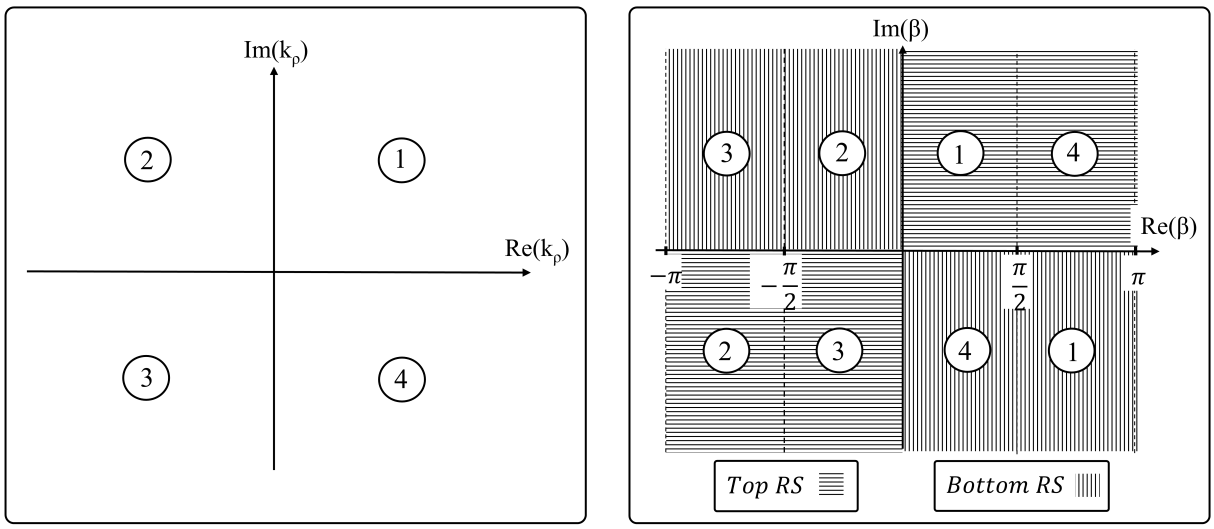

(a) *(b)*

Figure C-1. Mapping of the (a) four quadrants of the k_ρ complex plane, to the (b) principal strip (-π,π) of the angular spectrum.

Appendix D. Magnetic field components derivation

The integral expressions for the electric field in the semi-infinite region of a leaky wave structure fed by a y-oriented elementary magnetic current source in the ground plane, have been presented through *section 2.2a*. Considering those integrals, Chapter 2 and 3 elaborated on numerical and asymptotic methods for their evaluation. Regarding the magnetic field integral expressions, they can be formulated and subsequently evaluated in a similar manner as those of the electric field, with the only difference between the two cases being the employed Green's function of the stratified structure ($\bar{\bar{G}}^{em}$ for the electric field and $\bar{\bar{G}}^{hm}$ for the magnetic field). The required steps, starting from the expression of the magnetic field as the inverse Fourier transform (*D.1*), up to the formulation of the integral expression through a represenation which enables contour deformations (*D.5*), are presented below. It should be noted that the following expressions refer to the reference system displaced below the ground plane by Δ_z.

$$\vec{H}(\vec{r}') = \frac{1}{4\pi^2}\int_{-\infty}^{+\infty}\int_{-\infty}^{+\infty}\bar{\bar{D}}^{hm}(k_x,k_y,\Delta_z)\cdot\hat{y}e^{-jk_z z'}e^{-jk_x x}e^{-jk_y y}dk_x dk_y, \tag{D.1}$$

$$(D.1)\xrightarrow[k_y=k_\rho\sin(\alpha)]{k_x=k_\rho\cos(\alpha)}\vec{H}(\vec{r}') = \frac{1}{4\pi^2}\int_0^{+\infty}\int_0^{2\pi}\bar{\bar{D}}^{hm}(k_\rho,\alpha,\Delta_z)\cdot\hat{y}e^{-jk_z z'}e^{-jk_\rho\rho\cos(\alpha-\varphi)}k_\rho d\alpha\, dk_\rho, \tag{D.2}$$

The required projection of the dyadic part of the Green's function relating magnetic fields and currents ($\bar{\bar{D}}^{hm}$) for the semi-infinite region, to the y unitary vector, is given below. It should be noted that all the showcased expression corresponds only to the semi-infinite dielectric region, since the z dependence of the potential functions is explicitly extracted, with $v_{TE/TM}^{+}$, $i_{TE/TM}^{+}$ referring to the wave amplitudes as discussed in *Appendices A* and *B*.

$$\bar{\bar{D}}^{hm}(k_\rho,\alpha,\Delta_z)\cdot\hat{y} = \frac{1}{2}\begin{bmatrix}\left(i_{TM}^{+}(k_\rho,\Delta_z)-i_{TE}^{+}(k_\rho,\Delta_z)\right)\sin(2\alpha)\\ -\left(i_{TM}^{+}(k_\rho,\Delta_z)+i_{TE}^{+}(k_\rho,\Delta_z)+\left(i_{TM}^{+}(k_\rho,\Delta_z)-i_{TE}^{+}(k_\rho,\Delta_z)\right)\cos(2\alpha)\right)\\ \frac{2}{\zeta_d k_d}k_\rho\sin(\alpha)\,v_{TE}^{+}(k_\rho,\Delta_z)\end{bmatrix}, \tag{D.3}$$

Introducing the expression (*D.3*), into the inverse Fourier transform of (*D.2*) and evaluating the α integrals through the identities of (*2.2 a*), results into field expressions featuring a single complex integral in k_ρ.

$$\begin{bmatrix}H_x(\vec{r}')\\H_y(\vec{r}')\\H_z(\vec{r}')\end{bmatrix} = \frac{1}{4\pi}\int_0^{+\infty}\begin{bmatrix}-\sin(2\varphi)\,(i_{TM}^{+}-i_{TE}^{+})J_2(k_\rho\rho)\\ -\left((i_{TE}^{+}+i_{TM}^{+})J_0(k_\rho\rho)+\cos(2\varphi)\,(i_{TE}^{+}-i_{TM}^{+})J_2(k_\rho\rho)\right)\\ -j\frac{2}{\zeta_d k_d}\sin(\varphi)v_{TE}^{+}J_1(k_\rho\rho)k_\rho\end{bmatrix}e^{-jk_z z'}k_\rho dk_\rho, \tag{D.4}$$

Finally, the Bessel functions are transformed into Hankel functions of the second kind through the use of (*2.3*), resulting to integral expressions whose formulation facilitates contour deformations and thus the steepest descent path method of integration as well as the subsequent asymptotic evaluation.

$$\begin{bmatrix}H_x(\vec{r}')\\H_y(\vec{r}')\\H_z(\vec{r}')\end{bmatrix} = \frac{1}{8\pi}\int_{-\infty}^{+\infty}\begin{bmatrix}-\sin(2\varphi)\,(i_{TM}^{+}-i_{TE}^{+})H_2^{(2)}(k_\rho\rho)\\ -\left((i_{TE}^{+}+i_{TM}^{+})H_0^{(2)}(k_\rho\rho)+\cos(2\varphi)\,(i_{TE}^{+}-i_{TM}^{+})H_2^{(2)}(k_\rho\rho)\right)\\ -j\frac{2}{\zeta_d k_d}\sin(\varphi)v_{TE}^{+}H_1^{(2)}(k_\rho\rho)k_\rho\end{bmatrix}e^{-jk_z z'}k_\rho dk_\rho, \tag{D.5}$$

Where for both *(D.4)* and *(D.5)*, $v_{TE/TM}^{+} = v_{TE/TM}^{+}(k_\rho,\Delta_z)$ and $i_{TE/TM}^{+} = i_{TE/TM}^{+}(k_\rho,\Delta_z)$

The final integral expressions of (*D.5*) are in a similar form to those of the electric field (*2.4*) and thus can be evaluated through either of the numerical methods discussed in Chapter 2 or the asymptotic approach described in Chapter 3.

Appendix E. Poynting vector angles of residues

This appendix section will discuss the derivation of the Poynting vector angle for the residue contributions. This angle is obtained through projecting the active part of the time average Poynting vector to the z unitary vector, as given in the following steps for the *TE* and *TM* residue contributions respectively. The large argument approximation is used for the Hankel function (*2.5 a*) in order to simplify the resulting expressions, while the indicated voltage and current potentials refer to the wave amplitudes in the semi-infinite region of the structure with the displaced reference system, thus $v^+_{TE/TM} = v^+_{TE/TM}(k_\rho, \Delta_z)$ and $i^+_{TE/TM} = i^+_{TE/TM}(k_\rho, \Delta_z)$.

TE modes

$$\begin{bmatrix} E_{\rho LW,TE}(\vec{r}') \\ E_{\varphi LW,TE}(\vec{r}') \\ E_{zLW,TE}(\vec{r}') \\ H_{\rho LW,TE}(\vec{r}') \\ H_{\varphi LW,TE}(\vec{r}') \\ H_{zLW,TE}(\vec{r}') \end{bmatrix} = \begin{bmatrix} 0 \\ -\frac{j}{2} sin(\varphi) Res(v^+_{TE})_{k_\rho = k_{\rho,LW}} H_0^{(2)}(k_{\rho,LW}\rho) k_{\rho,LW} e^{-jk_{z,LW}z'} \\ 0 \\ \frac{j}{2} sin(\varphi) Res(i^+_{TE})_{k_\rho = k_{\rho,LW}} H_0^{(2)}(k_{\rho,LW}\rho) k_{\rho,LW} e^{-jk_{z,LW}z'} \\ 0 \\ -\frac{1}{2\zeta_d k_d} sin(\varphi)\, Res(v^+_{TE})_{k_\rho = k_{\rho,LW}} H_1^{(2)}(k_{\rho,LW}\rho) k^2_{\rho,LW} e^{-jk_{z,LW}z'} \end{bmatrix}, \tag{E.1}$$

Where $Res(i^+_{TE}) = \frac{Res(v^+_{TE})}{Z_{inf,TE}}$ and $Z_{inf,TE} = \frac{k_d \zeta_d}{k_z}$.

Using the field expressions of (*E.1*), the resulting Poynting vector angle can be extracted as given below, resulting into expression (*E.2*).

$$\vec{P}_{LW}(\vec{r}') = \frac{1}{2} Re\left(\vec{E}_{LW}(\vec{r}') \times \vec{H}^*_{LW}(\vec{r}')\right) = \frac{1}{2} Re\left(\begin{vmatrix} \hat{x} & \hat{y} & \hat{z} \\ E_x(\vec{r}') & E_y(\vec{r}') & E_z(\vec{r}') \\ H^*_x(\vec{r}') & H^*_y(\vec{r}') & H^*_z(\vec{r}') \end{vmatrix} \right) \xrightarrow{H_1^{(2)} = jH_0^{(2)}}$$

$$\Rightarrow \hat{P}_{LW}(\vec{r}') = \frac{\vec{P}_{LW}(\vec{r}')}{|\vec{P}_{LW}(\vec{r}')|} = \frac{\left(Re(k_{\rho,LW})(cos(\varphi)\,\hat{x} + sin(\varphi)\,\hat{y}) + Re(k_{z,LW})\hat{z}\right)}{\sqrt{Re(k_{\rho,LW})^2 + Re(k_{z,LW})^2}}$$

$$\theta_{Poy,TE} = acos\left(\hat{P}_{LW}(\vec{r}') \cdot \hat{z}\right) = acos\left(\frac{Re(k_{z,LW})}{\sqrt{Re(k_{\rho,LW})^2 + Re(k_{z,LW})^2}} \right), \tag{E.2}$$

TM modes

$$\begin{bmatrix} E_{\rho LW,TM}(\vec{r}') \\ E_{\varphi LW,TM}(\vec{r}') \\ E_{zLW,TM}(\vec{r}') \\ H_{\rho LW,TM}(\vec{r}') \\ H_{\varphi LW,TM}(\vec{r}') \\ H_{zLW,TM}(\vec{r}') \end{bmatrix} = \begin{bmatrix} \frac{j}{2} cos(\varphi)\, Res(v^+_{TM})_{k_\rho = k_{\rho,LW}} H_0^{(2)}(k_{\rho,LW}\rho) k_{\rho,LW} e^{-jk_{z,LW}z'} \\ 0 \\ -\frac{\zeta_d}{2k_d} cos(\varphi)\, Res(i^+_{TM})_{k_\rho = k_{\rho,LW}} H_1^{(2)}(k_{\rho,LW}\rho) k^2_{\rho,LW} e^{-jk_{z,LW}z'} \\ 0 \\ \frac{j}{2} cos(\varphi)\, Res(i^+_{TM})_{k_\rho = k_{\rho,LW}} H_0^{(2)}(k_{\rho,LW}\rho) k_{\rho,LW} e^{-jk_{z,LW}z'} \\ 0 \end{bmatrix}, \tag{E.3}$$

Using the field expressions of (*E.3*), the Poynting vector angle is obtained as given through (*E.4*), similar to the case of the *TE* modes.

$$\theta_{Poy,TM} = acos\left(\hat{P}_{LW}(\vec{r}') \cdot \hat{z}\right) = acos\left(\frac{Re(k_{z,LW})}{\sqrt{Re(k_{\rho,LW})^2 + Re(k_{z,LW})^2}} \right), \tag{E.4}$$

It should be noted that the Poynting vector angles derived above, tends to the one of (*E.5*), for cases where the mode's attenuation constant is not very large.

$$\theta_{LW} = asin\left(\frac{Re(k_{\rho,LW})}{k_d}\right), \tag{E.5}$$

Appendix F. Stationary Phase Point approximation

Arguably the simplest and most common method to asymptotically evaluate radiation integrals is the stationary phase point approximation. As an indicative example, the implementation of this method to derive the far field of a stratified structure will be presented in the following appendix section.

Taking into account that the far field is a spherical wave, it is reasonable to target the canonical integral of the inverse Fourier transform of the spherical spreading term (scalar Green's function) during the asymptotic evaluation of the complex integrals.

$$\int_{-\infty}^{\infty}\int_{-\infty}^{\infty} e^{-jk_x x}e^{-jk_y y}\frac{e^{-jk_z z}}{k_z}dk_x dk_y = \int_0^{\infty}\int_0^{2\pi} e^{-jk_\rho \rho\, cos(\alpha-\phi)}\frac{e^{-jk_z z}}{k_z}k_\rho d\alpha\, dk_\rho = 2\pi j\frac{e^{-jk_d r}}{r}, \quad (F.1)$$

Using as an example the structures of Figure 2-1, fed by a generic magnetic current source in the ground plane with spectrum $C_m(k_x, k_y)$, the total field in the semi-infinite dielectric region can be expressed as the inverse Fourier transform of the convolution between the Green's function ($\bar{\bar{G}}^{em}$) and the current distribution of the source.

$$\vec{E}(\vec{r}) = \frac{1}{4\pi^2}\int_0^{+\infty}\int_0^{2\pi}\bar{\bar{G}}^{em}(k_\rho, \alpha, z, 0)\cdot\vec{C}_m(k_\rho, \alpha)e^{-jk_\rho\rho\, cos(\alpha-\varphi)}k_\rho d\alpha dk_\rho, \quad (F.2\ a)$$

By multiplying and dividing the integrand with k_z, the inverse Fourier transform of the spherical spreading term can be formed inside the integral; together with an amplitude term comprised of the dyadic spectral Green's function ($\bar{\bar{D}}^{em}$), the spectrum of the current source (C_m) and the spectral variable k_z.

$$\vec{E}(\vec{r}) = \frac{1}{4\pi^2}\int_0^{+\infty}\int_0^{2\pi}\bar{\bar{D}}^{em}(k_\rho, \alpha, 0)\cdot\vec{C}_m(k_\rho, \alpha)k_z\frac{e^{-jk_z z}}{k_z}e^{-jk_\rho\rho\, cos(\alpha-\varphi)}k_\rho d\alpha dk_\rho, \quad (F.2\ b)$$

Employing the saddle point considerations for the double integral of (*F.2 b*), its dominant contribution can be identified as the point $k_{\rho SP} = k_d\, sin(\theta)$ and $\alpha_{SP} = \varphi$ (double saddle point), where (r, θ, φ) refers to the observation point. Assuming an observation point in the far field region of the source, i.e., a large enough radial distance (r), the integrand's phase term oscillates very fast on the integration path compared to the much slower varying amplitude. As a matter of fact, this behaviour of a rapidly oscillating phase and a slow varying amplitude, leads to destructive contributions in all regions of the integration path away from the saddle point, which can also be considered as the point of least phase variance (stationary phase point).

Since sections of the complex plane where the phase function is fast varying compared to the amplitude, would not contribute to the integral result, the latter can be asymptotically approximated by evaluating the slow varying amplitude at the stationary phase point and extracting it from the integral. Subsequently, the remaining infinite integral can be analytically closed, given that it corresponds to the inverse Fourier transform of the spherical spreading term. The aforementioned steps are indicated below together with the resulting far field.

$$(F.2\ b) \Rightarrow \vec{E}_{FF}(\vec{r}) = \frac{1}{4\pi^2}\bar{\bar{D}}^{em}(k_{\rho SP}, \alpha_{SP}, 0)\cdot\vec{C}_m(k_{\rho SP}, \alpha_{SP})k_{zSP}\int_0^{+\infty}\int_0^{2\pi}\frac{e^{-jk_z z}}{k_z}e^{-jk_\rho\rho\, cos(\alpha-\varphi)}k_\rho d\alpha dk_\rho \Rightarrow$$

$$\overset{(3.1)}{\Longrightarrow} \vec{E}_{FF}(\vec{r}) = jk_{zSP}\bar{\bar{D}}^{em}(k_{\rho SP}, \alpha_{SP}, 0)\cdot\vec{C}_m(k_{\rho SP}, \alpha_{SP})\frac{e^{-jk_d r}}{2\pi r}, \quad (F.3)$$

To visualize the previously described properties of the stationary phase point, the behavior of the fast-varying term of (*F.2 a*) is presented through Figure F-1 *(a)* and *(b)* for different observation points, considering the wideband structure of Figure 2-1.

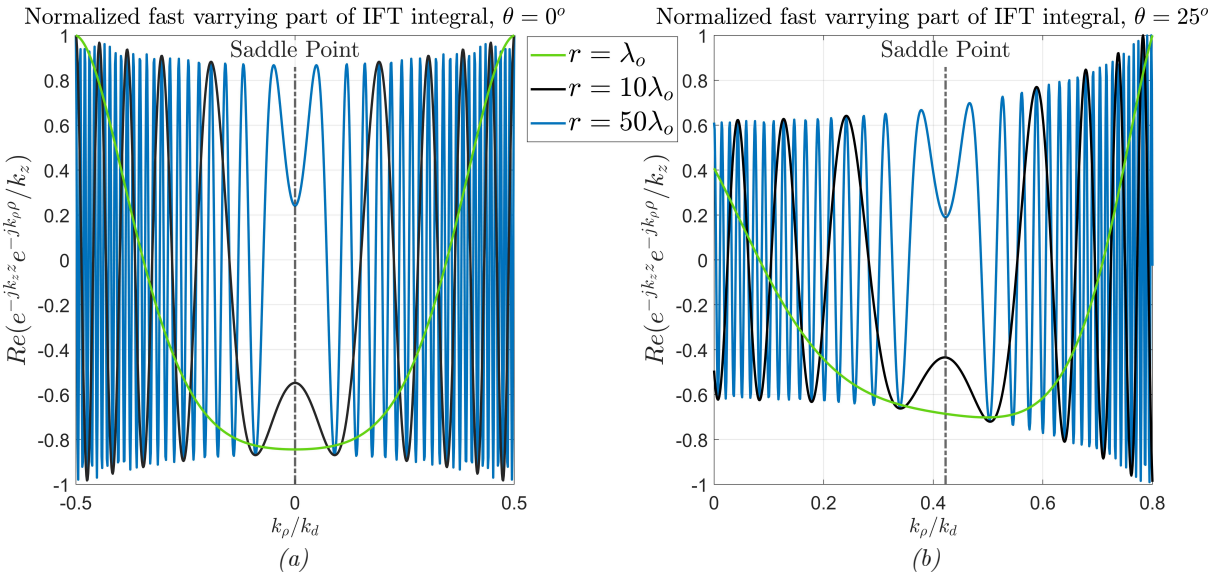

Figure F-1. Fast varying part of (F.2 b) along the real axis of k_ρ spectrum with $a_{SP} = \varphi$ and different radial distances of the observation point (r), for (a) θ=0^o and (b) θ=25^o.

As evident from the above figure, the larger is the radial distance (r), the oscillations away from the saddle point become more rapid thus the consideration for meaningful contribution of the amplitude only in the vicinity of the latter becomes increasingly neat, showcasing the applicability of the stationary phase point (SPP) method for the far field.

Appendix G. Regularization approach comparison

In *section 3.2b*, the necessary treatment for polar singularities approaching the saddle point of the integrand function was described. While two methods were introduced for the isolation of the integrand's polar singularities (regularization), only the additive approach was utilized for the purpose of the subsequent study. In this appendix section, the choice of the additive regularization approach will be justified through comparing the resulting formulation with that obtained by the multiplicative regularization approach. For this purpose, the same indicative integral treated in the example of *section 3.2b*, will be evaluated with the multiplicative approach.

$$\int_{SDP} v_{TE}^{+}(k_d\, sin(\beta)\,, \Delta_z)\, cos(\beta)\, e^{\Omega q_B(\beta)} d\beta = e^{-jk_d r'} \int_{-\infty}^{+\infty} G_p^{TE}(s) e^{-\Omega s^2} ds, \qquad (G.1)$$

Where $G_p^{TE}(s) = v_{TE}^{+}(k_d\, sin(\beta)\,, \Delta_z)\, cos(\beta) \frac{d\beta}{ds}$, $\Omega = k_d r'$ and $q_B(\beta) = -jcos(\beta - \theta')$.

Multiplicative pole treatment

In contrast to the additive method, in the multiplicative pole treatment introduced by Pauli-Clemmow for a simple pole and expanded by Bleisten [38], the function $G(s)$ is expressed as the product of two functions, namely $G(s) = T_{PC}(s)\, B(s)$, where $T_{PC}(s)$ is regular around the saddle point while $B(s)$ contains the poles of $G(s)$. Subsequently, similar to the additive method, the regular part can be expanded into a power series around the saddle point, while $B(s)$ needs to be decomposed into a summation of simple poles. In turn the product of these two expressions can be evaluated through term-wise integration, using either of the integrals given in *(3.10)*.

Whereas, for the additive regularization method a function describing the behaviour of the v_{TE} around the aforementioned polar singularities was needed *(3.13)*, for the multiplicative approach only the positions of these poles in the s-plane needs to be derived. The latter is obtained by using the mapping given in *(3.9)* considering that the positions of a polar singularity in the angular and rectilinear spectrum are related through $\beta_{LW} = asin(k_{\rho,LW}/k_d)$.

The regularized part derived through the multiplicative approach is given below, labelling the mapped singularities $\pm k_{\rho,LW}^{TE_1}$ to the s-plane as $s_{TE,+}$ and $s_{TE,-}$ respectively.

$$T_{PC_{TE}}(s) = v_{TE}^{+}(k_d\, sin(\beta)\,, \Delta_z)\big(s - s_{TE,+}\big)\big(s - s_{TE,-}\big)\, cos(\beta) \frac{d\beta}{ds}, \qquad (G.2)$$

To showcase the equivalent impact of this regurlarization approach compared to the additive case, the spectral regions depicted through Figure 3-3 and Figure 3-4 are also visualized for $T_{PC}^{TE}(s)$ in Figure G-1.

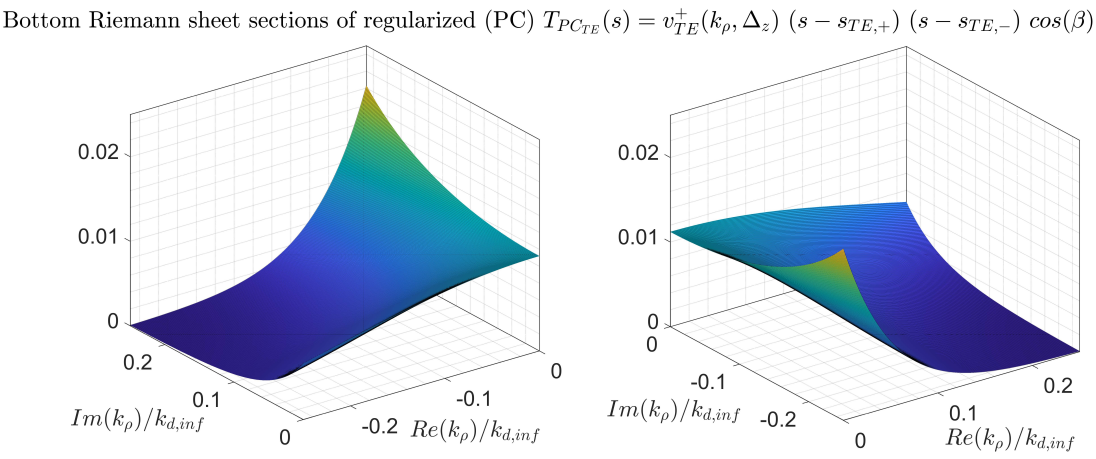

Figure G-1. Bottom Riemann sheet of the regularized part through the multiplicative method ($T_{PC}^{TE}(s)$). The depicted sections of the rectilinear (k_ρ) spectrum are indicated in the inset of Figure 3-3.

Resolving the remaining integral of (*G.1*), labelled $I_{SDP}(\Omega)$, through the additive regularization approach resulted in the following decomposition.

$$I_{SDP}(\Omega) = \sum_{n=0}^{\infty}\left(\frac{T_{VdW_{TE}}^{(2n)}(0)}{(2n!)}\frac{\Gamma\left[\frac{2n+1}{2}\right]}{\Omega^{\left(\frac{2n+1}{2}\right)}}\right) + \int_{-\infty}^{+\infty} G_{pole}^{TE_1}(s)e^{-\Omega s^2}\,ds, \qquad (G.3)$$

Where $G_{pole}^{TE_1}(s) = v_{apr,TE}^{+}(k_d\,sin(\beta)\,,\Delta_z)\,cos(\beta)\frac{d\beta}{ds}$ and $T_{VdW_{TE}}(s)$ as given in *(3.14)*.

For the purpose of comparing the additive and multiplicative regularization approaches, the same integral ($I_{SDP}(\Omega)$) is treated using the multiplicative approach as presented below.

$$I_{SDP}(\Omega) = \int_{-\infty}^{+\infty} G_p^{TE}(s)e^{-\Omega s^2}\,ds = \int_{-\infty}^{+\infty} \frac{(s-s_{TE,+})(s-s_{TE,-})G_p^{TE}(s)}{(s-s_{TE,+})(s-s_{TE,-})}e^{-\Omega s^2}\,ds = \int_{-\infty}^{+\infty} \frac{T_{PC_{TE}}(s)}{(s-s_{TE,+})(s-s_{TE,-})}e^{-\Omega s^2}\,ds \Rightarrow$$

$$\Rightarrow I_{SDP}(\Omega) = C_{TE,+}\int_{-\infty}^{+\infty}\frac{T_{PC_{TE}}(s)}{s-s_{TE,+}}e^{-\Omega s^2}\,ds + C_{TE,-}\int_{-\infty}^{+\infty}\frac{T_{PC_{TE}}(s)}{s-s_{TE,-}}e^{-\Omega s^2}\,ds, \qquad (G.4)$$

$$\text{using } \left(\prod_{i=1}^{N}(s-s_i)\right)^{-1} = \sum_{i=1}^{N}\frac{C_i}{s-s_i} \text{ with } C_i = \left(\prod_{\substack{j=1\\ j\neq i}}^{N}(s_i-s_j)\right)^{-1}$$

While the complete expression of (*G.4*) will not be included here to maintain some semblance of simplicity, in general, the integral of $I_{SDP}(\Omega)$ can be separated into a summation of simple pole integrals, as shown above. This in turn enables its evaluation through summing expressions of the following form.

$$I_{TE,i}^{SDP}(\Omega) = \int_{-\infty}^{+\infty}\frac{T_{PC_{TE}}(s)}{s-s_{TE,i}}e^{-\Omega s^2}ds = \int_{-\infty}^{+\infty}\frac{T_{PC_{TE}}(s)(s+s_{TE,i})}{s^2-s_{TE,i}^2}e^{-\Omega s^2}ds \xrightarrow{\substack{expanding\ T_{PC_{TE}}(s)\ around\\ s=0\ and\ using\ (3.10\ c)}}$$

$$\Rightarrow I_{TE,i}^{SDP}(\Omega) = -\frac{1}{s_{TE,i}}\sqrt{\frac{\pi}{\Omega}}T_{PC_{TE}}(0) + \cdots + \left(\frac{1}{s_{TE,i}}T_{PC_{TE}}(0) + T'_{PC_{TE}}(0) + \frac{s_{TE,i}}{2}T_{PC_{TE}}^{(2)}(0) + \cdots\right)\sqrt{\frac{\pi}{\Omega}}\left(1 - F\left(j\Omega s_{TE,i}^2\right)\right) \Rightarrow$$

$$\Rightarrow I_{TE,i}^{SDP}(\Omega) = -\frac{T_{PC_{TE}}(0)}{s_{TE,i}}\sqrt{\frac{\pi}{\Omega}} + \sum_{n=0}^{\infty}\left(\frac{T_{PC_{TE}}^{(n)}(0)}{n!}s_{TE,i}^{(n-1)}\sqrt{\frac{\pi}{\Omega}}\left(1 - F\left(j\Omega s_{TE,i}^2\right)\right)\right) + \frac{\Gamma\left[\frac{3}{2}\right]}{\Omega^{\left(\frac{3}{2}\right)}}\sum_{n=3}^{\infty}\left(\frac{T_{PC_{TE}}^{(n)}(0)}{n!}s_{TE,i}^{n-3}\right) + \frac{\Gamma\left[\frac{5}{2}\right]}{\Omega^{\left(\frac{5}{2}\right)}}\sum_{n=5}^{\infty}\left(\frac{T_{PC_{TE}}^{(n)}(0)}{n!}s_{TE,i}^{n-5}\right) + \cdots$$

(G.5)

Having resolved the test case integral ($I_{SDP}(\Omega)$) through both the additive (*G.3*) and multiplicative regularization approaches (*G.4*) and (*G.5*), the fundamental difference of the two can now be observed.

In the additive method, the integral of the polar contributions is not related with the expansion of the regular part. In contrast, in the multiplicative approach, each term of the power series of $T_{PC_{TE}}(s)$ is multiplied by a Fresnel integral (or equivalently an *erf* function). The fundamental property of the polar contributions is that they are comprised of a sum of transition functions, each corresponding to a distinct pole in the s-plane and introducing a discontinuity if the respective polar singularity crosses the SDP. Considering the latter, one can deduce that the two expressions would be completely equivalent only if an infinite number of terms is used in the expansion [46].

To visualize this concept, the two regularization approaches will be compared considering the integral of (*G.6*). In particular, the given integral in the k_ρ complex plane is transformed into the angular spectrum and subsequently deformed into the SDP passing through the saddle point ($\beta_{SP} = \theta'$). In turn, the resulting SDP integral is transformed into the s-plane and regularized with either of the previously discussed approaches. In both cases the regular part ($T_{VdW_{TE}}(s)$ or $T_{PC_{TE}}(s)$) is expanded around the saddle point, with the resulting integrals evaluated numerically. The only reason for using (*G.6*) instead of directly comparing the two methods for the integral of (*G.1*), is that the former also includes the residue contribution above the

shadow boundary angle, something that will facilitate the evaluation of the difference between the two regularization approaches.

$$I(\theta') = \frac{1}{k_d}\int_{-\infty}^{+\infty} v_{TE}^{+}(k_\rho, \Delta_z) e^{-j(k_z z' + k_\rho \rho)} dk_\rho = I_{SDP}(\theta') + U(\theta' - \theta_{SB,TE1}) I_{res}(\theta'), \quad (G.6)$$

where

$$I_{SDP}(\theta') = \int_{SDP} v_{TE}^{+}(k_d\, sin(\beta), \Delta_z)\, cos(\beta)\, e^{-jk_d r' cos(\beta - \theta')} d\beta$$

$$I_{res}(\theta') = -\frac{1}{k_d} 2\pi j Res\left(v_{TE}^{+}(k_\rho, \Delta_z) e^{-j(k_z z' + k_\rho \rho)}\right)_{k_\rho = k_{\rho,LW}^{TE_1}}$$

Considering as an indicative example the wideband structure of Figure 2-8 for the derivation of the voltage wave amplitude (v_{TE}^{+}) and a spherical observation grid at $r' = 2.5\lambda_0$ from the phase centre, the resulting comparison is presented through Figure G-2 for different number of terms in the expansion of the regularized parts ($T_{VdW_{TE}}(s)$ and $T_{PC_{TE}}(s)$).

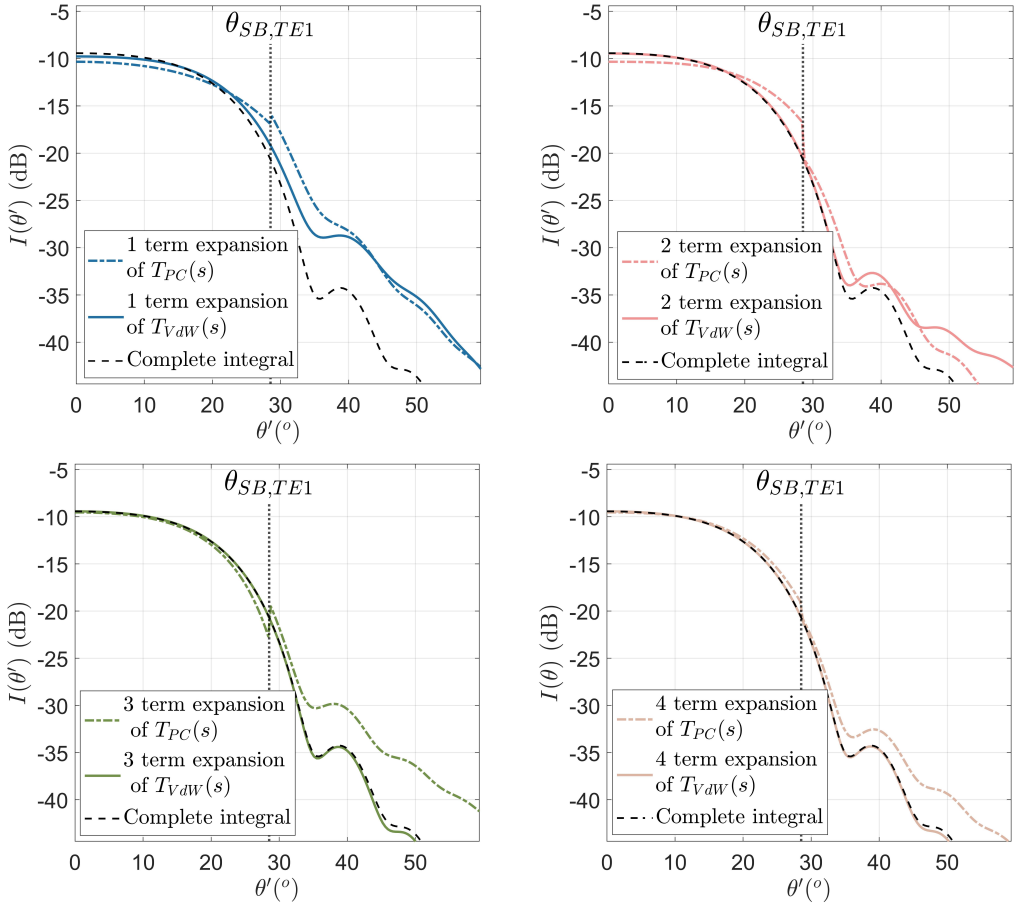

Figure G-2. Comparison of the additive and multiplicative regularization approaches for the integral of (G.6) at 150 GHz, with different number of terms in the expansion of the regular part, as noted in the respective legends.

As evident through comparing the figures above, while after a certain number of terms both approaches converge to the same result, their difference can be identified through observing the shadow boundary angles. In particular, if an insufficient number of terms is used in the expansion of the regularized part for the multiplicative approach ($T_{PC_{TE}}(s)$), the result is discontinuous. This impact is related to the nature of the SDP integral, which is discontinuous at the shadow boundaries with the exact level of the featured discontinuity compensated by the inclusion of the residue contribution, making the total result continuous. Having said that, it can be intuitively realized that for the case of the multiplicative approach where each term of the power series expansion of $T_{PC_{TE}}(s)$ is multiplied by a Fresnel integral (or equivalently an *erf* function), if an inadequate number of terms is used in the expansion, the total result would be discontinuous. The actual number of terms deemed sufficient for the expansion of the regularized part depends on the value of Ω.

Appendix H. Power series expansion of T(s)

As discussed through *section 3.2*, the asymptotic evaluation of complex integrals requires the approximation of their integrant functions around the saddle point (integral's dominant contribution), such that the resulting expressions can be evaluated through canonical integrals. The simplest manner, in which to describe the spectral properties of an analytical function around a certain point is to obtain its power series expansion as indicatively shown below for the saddle point at $s = 0$.

$$T(s) \cong T(0) + sT'(0) + \frac{s^2}{2}T^{(2)}(0) + \frac{s^3}{3!}T^{(3)}(0) + \frac{s^4}{4!}T^{(4)}(0) + \cdots, \qquad (H.1)$$

Given that $T(s)$ does not feature any singularities around the origin, the radius of convergence of the power series expansion, or equivalently the spectral region for which (*H.1*) describes the function in question ($T(s)$), depends only on the number of terms included in the expansion. Considering the encountered integrals throughout this work, their regularized parts can be expressed in terms of a function which depends on the complex angle variable β and the Jacobian transform $d\beta/ds$ in terms of s, as indicatively shown through (*H.2*) for the integral of the E_φ component of (*3.26*).

$$\int_{-\infty}^{+\infty} T_{VdW}(s)e^{-\Omega s^2}ds = \int_{-\infty}^{+\infty} F_{VdW}(\beta)\frac{d\beta}{ds}e^{-\Omega s^2}ds, \qquad (H.2)$$

Where $F_{VdW}(\beta) = \left(v_{TE}^{+}(k_d\, sin(\beta), \Delta_z) - v_{apr,TE}^{+}(k_d\, sin(\beta), \Delta_z)\right) cos(\beta)$ and $\frac{d\beta}{ds} = \frac{\sqrt{2j}}{\sqrt{1-j\frac{s^2}{2}}}$.

Setting the Jacobian transform as the function $\varphi(s)$ to facilitate the subsequent formulations, the higher order derivatives of $T_{VdW}(s)$ can be obtained through the chain rule, as indicatively given through (*H.3*) for derivatives up to the 3rd order.

$$\begin{gathered} T'_{VdW}(s) = \frac{d}{ds}\left(T_{VdW}(s)\right) = \frac{d}{d\beta}\left(F_{VdW}(\beta)\right)\frac{d\beta}{ds}\varphi(s) + F_{VdW}(\beta)\varphi'(s) = F'_{VdW}(\beta)\left(\varphi(s)\right)^2 + F_{VdW}(\beta)\varphi'(s) \\ T^{(2)}_{VdW}(s) = \frac{d}{ds}\left(T'_{VdW}(s)\right) = F^{(2)}_{VdW}(\beta)\left(\varphi(s)\right)^3 + F_{VdW}(\beta)\varphi^{(2)}(s) \\ T^{(3)}_{VdW}(s) = \frac{d}{ds}\left(T^{(2)}_{VdW}(s)\right) = F^{(3)}_{VdW}(\beta)\left(\varphi(s)\right)^4 + 3F^{(2)}_{VdW}(\beta)\left(\varphi(s)\right)^2\varphi'(s) + F'_{VdW}(\beta)\varphi(s)\varphi^{(2)}(s) + F_{VdW}(\beta)\varphi^{(3)}(s) \end{gathered}, \qquad (H.3)$$

The higher order derivatives of the Jacobian transform ($\varphi(s)$ or $d\beta/ds$) around the saddle point can be obtained analytically given that its expression is both simple and known. In contrast, for the case of $F_{VdW}(\beta)$ which includes either the voltage or the current wave amplitudes ($v_{TE/TM}^{+}$, $i_{TE/TM}^{+}$), to mitigate the complexity involved, the higher order derivatives are obtained numerically through the finite difference method. This approach refers all higher derivatives to values of $F_{VdW}(\beta)$ allowing for their numerical extraction. The resulting expressions for the first four derivatives using the central difference formula are indicatively given below. It should be noted that different formalisms can also be obtained using the forwards or backwards difference formulas.

$$\begin{gathered} F'(\beta) = \frac{F\left(\beta+\frac{\Delta\beta}{2}\right) - F\left(\beta-\frac{\Delta\beta}{2}\right)}{\Delta\beta} \\ F^{(2)}(\beta) = \frac{F(\beta+\Delta\beta) - 2F(\beta) + F(\beta-\Delta\beta)}{(\Delta\beta)^2} \\ F^{(3)}(\beta) = \frac{F\left(\theta+\frac{3}{2}\Delta\beta\right) - 3F\left(\theta+\frac{\Delta\beta}{2}\right) + 3F\left(\theta-\frac{\Delta\beta}{2}\right) - F\left(\theta-\frac{3}{2}\Delta\beta\right)}{(\Delta\beta)^3} \\ F^{(4)}(\beta) = \frac{F(\beta+2\Delta\beta) - 4F(\beta+\Delta\beta) + 6F(\beta) - 4F(\beta-\Delta\beta) + F(\beta-2\Delta\beta)}{(\Delta\beta)^4} \end{gathered}, \qquad (H.4)$$

CHAPTER 8. REFERENCES

[1] T. S. Rappaport, Y. Xing, O. Kanhere, S. Ju, A. Madanayake, S. Mandal, A. Alkhateeb and G. C. Trichopoulos, "Wireless Communications and Applications Above 100 GHz: Opportunities and Challenges for 6G and Beyond," *IEEE Access,* vol. 7, pp. 78729 - 78757, Jun. 2019.

[2] M. Alsabah, M. A. Naser, B. M. Mahmmod, S. H. Abdulhussain, M. R. Eissa, A. Al-Baidhani, K. N. Noording, S. M. Sait, K. A. Al-Utaibi and F. Hashim, "6G Wireless Communications Networks: A Comprehensive Survey," *IEEE Access,* vol. 9, pp. 148191 - 148243, Nov. 2021.

[3] H. Tullberg, P. Popovski, Z. Li, M. A. Uusitalo, A. Hoglund, O. Bulakci, M. Fallgren and J. F. Monserrat, "The METIS 5G System Concept: Meeting the 5G Requirements," *IEEE Commun. Mag.,* vol. 54, no. 12, pp. 132 - 139, Dec. 2016.

[4] A. Osseiran, F. Boccardi, V. Braun, K. Kusume, P. Marsch, M. Maternia, O. Queseth, M. Schellmann, H. Schotten, H. Taoka, H. Tullberg, M. A. Uusitalo, B. Timus and M. Fallgren, "Scenarios for 5G mobile and wireless communications: the vision of the METIS project," *IEEE Commun. Mag.,* vol. 52, no. 5, pp. 26 - 35, May 2014.

[5] N. Llombart, D. Emer, M. A. Campo and E. McCune, "Fly's Eye spherical antenna system for future Tbps wireless communications," in *Proc. Eur. Conf. Antennas Propag. (EuCAP)*, Paris, France, 2017.

[6] S. Elmeadawy and R. M. Shubair, "6G Wireless Communications: Future Technologies and Research Challenges," in *International Conference on Electrical and Computing Technologies and Applications (ICECTA)*, Ras Al Khaimah, United Arab Emirates, 2019.

[7] W. Hong, Z. H. Jiang, C. Yu, J. Zhou, P. Chen, Z. Yu, H. Zhang, B. Yang, X. Pang, M. Jiang, Y. Cheng, M. K. Taher Al-Nuaimi, Y. Zhang, J. Chen and S. He, "Multibeam Antenna Technologies for 5G Wireless Communications," *IEEE Trans. Antennas Propag.,* vol. 65, no. 12, pp. 6231 - 6249, Jun. 2017.

[8] D. Muirhead, M. A. Imran and K. Arshad, "A Survey of the Challenges, Opportunities and Use of Multiple Antennas in Current and Future 5G Small Cell Base Stations," *IEEE Access,* vol. 4, pp. 2952 - 2964, May 2016.

[9] G. Minatti, M. Faenzi, M. Sabbadini and S. Maci, "Bandwidth of Gain in Metasurface Antennas," *IEEE Trans. Antennas Propag.,* vol. 65, no. 6, pp. 2836 - 2842, Apr. 2017.

[10] A. Hosseini, F. D. Flaviis and F. Capolino, "Design Formulas for Planar Fabry–Pérot Cavity Antennas Formed by Thick Partially Reflective Surfaces," *IEEE Trans. Antennas Propag.,* vol. 64, no. 12, pp. 5487 - 5491, Sep. 2016.

[11] P. I. Theoharis, R. Raad, F. Tubbal, M. U. A. Khan and A. Jamalipour, "Wideband Reflectarrays for 5G/6G: A Survey," *IEEE OJAP,* vol. 3, pp. 871 - 901, Aug. 2022.

[12] M. H. Dahri, M. H. Jamaluddin, M. I. Abbasi and M. R. Kamarudin, "A Review of Wideband Reflectarray Antennas for 5G Communication Systems," *IEEE Access,* vol. 5, pp. 17803 - 17815, Aug. 2017.

[13] W.-L. Guo, G.-M. Wang, K.-Y. Liu, Y.-Q. Zhuang and Q.-C. Ge, "Design of Single-Layered Ultrawideband High-Efficiency Circularly Polarized Reflectarray," *IEEE Antennas Wirel. Propag. Lett.,* vol. 17, no. 8, pp. 1386 - 1390, Jun. 2018.

[14] Z.-W. Miao, Z.-C. Hao, Y. Wang, B.-B. Jin, J.-B. Wu and W. Hong, "A 400-GHz High-Gain Quartz-Based Single Layered Folded Reflectarray Antenna for Terahertz Applications," *IEEE Trans. Terahertz Sci. Technol.,* vol. 9, no. 1, pp. 78 - 88, Nov. 2018.

[15] L. Zhang, S. Gao, Q. Luo, W. Li, Y. He and Q. Li, "Single-Layer Wideband Circularly Polarized High-Efficiency Reflectarray for Satellite Communications," *IEEE Trans. Antennas Propag.,* vol. 65, no. 9, pp. 4529 - 4538, Jul. 2017.

[16] S. Bosma, N. v. Rooijen, M. Alonso-delPino and N. Llombart, "A Wideband Leaky-Wave Lens Antenna With Annular Corrugations in the Ground Plane," *IEEE Antennas Wirel. Propag. Lett.,* vol. 21, no. 8, pp. 1649 - 1653, Aug. 2022.

[17] M. A. Campo, D. Blanco, S. Bruni, A. Neto and N. Llombart, "On the Use of Fly's Eye Lenses with Leaky-Wave," *IEEE Trans. Antennas Propag.,* vol. 68, no. 4, pp. 2480 - 2493, Apr. 2020.

[18] N. v. Rooijen, M. A. delPino, M. Spirito and N. Llombart, "Core-Shell Leaky-Wave Lens Antenna for 150GHz Fly's Eye Communication Systems," in *47th International Conference on Infrared, Millimeter and Terahertz Waves (IRMMW-THz)*, Delft, Netherlands, 2022.

[19] M. A. Campo, G. Carluccio, D. Blanco and S. Brun, "Dielectric-Grating In-Lens Polarizer for Beyond 5G Communications," in *44th International Conference on Infrared, Millimeter, and Terahertz Waves (IRMMW-THz)*, Paris, France, 2019.

[20] S. Bosma, A. Neto and N. Llombart, "On the Near-Field Spherical Wave Formation in Resonant Leaky-Wave Antennas: Application to Small Lens Design," *IEEE Trans. Antennas Propag.,* vol. 70, no. 2, pp. 801 - 812, Dec. 2021.

[21] S. Skokic, M. Casaletti, S. Maci and S. B. Sorensen, "Complex Conical Beams for Aperture Field Representations," *IEEE Trans. Antennas Propag,* vol. 59, no. 2, pp. 611-622, 2011.

[22] R. R. Boix, A. L. Fructos and F. Mesa, "Closed-Form Uniform Asymptotic Expansions of Green's Functions in Layered Media," *IEEE Trans. Antennas Propag.,* vol. 58, no. 9, pp. 2934-2945, 14 June 2010.

[23] E. Martini and S. Maci, "Generation of Complex Source Point Expansions from Radiation Integrals," *Prog. Electromagn. Res.,* vol. 152, pp. 17-31, January 2015.

[24] M. Casaletti and S. Maci, "Aperture Beam Expansion by Using a Spectral 2D-GHOF Method," *Prog. Electromagn. Res.,* vol. 28, pp. 245-257, January 2013.

[25] M. Casaletti, S. Skokic, S. Maci and S. Sørensen, "Beam expansion in multi-reflector quasi-optical systems," in *Proc. Eur. Conf. Antennas Propag. (EuCAP)*, Barcelona, Spain, 2010.

[26] L. Felsen and N. Marcuvitz, Radiation and Scattering of Waves, New York: IEEE Press, 1994.

[27] A. Polemi and S. Maci, "On the Polarization Properties of a Dielectric Leaky Wave Antenna," *IEEE Antennas Wirel. Propag. Lett.,* vol. 5, pp. 306 - 310, Jul. 2006.

[28] S. Maci and A. Neto, "Green's Function of an Infinite Slot Printed Between Two Homogeneous Dielectrics - Part II: Uniform Asymptotic Solution," *IEEE Trans. Antennas Propag.,* vol. 52, no. 3, pp. 666-676, 2004.

[29] A. Neto and N. Llombart, "Wideband Localization of the Dominant Leaky Wave Poles in Dielectric Covered Antennas," *IEEE Antennas Wirel. Propag. Lett.,* vol. 5, pp. 549 - 551, 2006.

[30] N. Llombart, A. Neto, G. Gerini, M. Bonnedal and P. D. Maagt, "Leaky wave enhanced feed arrays for the improvement of the edge of coverage gain in multibeam reflector antennas," *IEEE Trans. Antennas Propag.,* vol. 56, no. 5, pp. 1280 - 1291, May 2008.

[31] A. Neto, M. Ettorre, G. Gerini and P. J. D. Maagt, "Leaky Wave Enhanced Feeds for Single Aperture Multi Beam Reflectors," in *38th European Microwave Conference*, Amsterdam, Netherlands, 2008.

[32] L. M. Brekhovskikh, Waves in Layered Media, New York: Academin Press, 1960.

[33] A. Baños, Dipole radiation in the presence of a conducting half-space, New York: Pergamon Press, 1966.

[34] P. Burghignoli, "A Leaky-Wave Analysis of the Phase Center in Fabry-Pérot Cavity," *IEEE Trans. Antennas Propag.,* vol. 60, no. 5, pp. 2226 - 2233, Mar. 2012.

[35] R. Rojas, "Comparison between two asymptotic methods," *IEEE Trans. Antennas Propag.,* vol. 35, no. 12, pp. 1489 - 1492, Dec. 1987.

[36] B. L. van der Waerden, "On The Method Of Saddle Points," *Appl. Sci. Res.,* vol. B2, p. 33–45, 1951.

[37] H. E. Salzer, "Formulas for Calculating the Error Function of a Complex Variable," *Math. Tables Aids Comp.,* vol. 5, no. 34, pp. 67 - 70, 1951.

[38] N. Bleistein, "Uniform asymptotic expansions of integrals with stationary point near algebraic singularity," *Commun. Pure Appl. Math.,* vol. 19, no. 4, pp. 353 - 370, 1966.

[39] H. L. Beltoni, A. C. Green and L. B. Felsen, "Shadowing of an Inhomogeneous Plane Wave by an Edge," in *EuMC*, Copenhagen, Denmark, 1977.

[40] A. Ip and D. Jackson, "Radiation from cylindrical leaky waves," *IEEE Trans. Antennas Propag.,* vol. 38, no. 4, pp. 482 - 488, Apr. 1990.

[41] C. A. Balanis, Advanced Engineering Electromagnetics, John Wiley & Sons, Inc., 1989.

[42] H. Zhang, S. O. Dabironezare, G. Carluccio, A. Neto and N. Llombart, "A GO/FO Tool for Analyzing Quasi-Optical Systems in Reception," in *44th International Conference on Infrared, Millimeter, and Terahertz Waves (IRMMW-THz)*, Paris, France, 2019.

[43] A. Neto and S. Maci, "Green's Function for an Infinite Slot Printed Between Two Homogeneous Dielectrics - Part I: Magnetic Currents," *IEEE Trans. Antennas Propag,* vol. 51, no. 7, pp. 1572-1581, 2003.

[44] T. K. Sarkar and O. Pereira, "Using the matrix pencil method to estimate the parameters of a sum of complex exponentials," *IEEE Antennas Propag. Mag.,* vol. 37, no. 1, pp. 48-55, 1995.

[45] S. O. Dabironezare, G. Carluccio, A. Freni, A. Neto and N. Llombart, "Coherent Fourier Optics Model for the Synthesis of Large Format Lens-Based Focal Plane Arrays," *IEEE Trans. Antennas, Propag.,* vol. 69, no. 2, pp. 734-746, 2021.

[46] K. A. Michalski and J. R. Mosig, "On the Deficiency of the First-Order Ott–Clemmow Saddle Point Method as Applied to the Sommerfeld Half-Space Problem," *IEEE Trans. Antennas Propag.,* vol. 70, no. 11, pp. 10820 - 10827, Jun. 2022.